Title	Chamber investigations of atmospheric mercury oxidation chemistry
Author(s)	Darby, Steven B.
Publication date	2015
Original citation	Darby, S. B. 2015. Chamber investigations of atmospheric mercury oxidation chemistry. PhD Thesis, University College Cork.
Type of publication	Doctoral thesis
Rights	© 2015, Steven B. Darby http://creativecommons.org/licenses/by-nc-nd/3.0/
Item downloaded from	http://hdl.handle.net/10468/2076

University College Cork, Ireland
Coláiste na hOllscoile Corcaigh

Chamber investigations of atmospheric mercury oxidation chemistry

Steven Ben Darby

Contents

List of Figures

List of Tables

I, Steven Ben Darby, certify that this thesis is my own work and I have not obtained a degree in this university or elsewhere on the basis of the work submitted in this thesis.

Steven Ben Darby

Acknowledgements

Firstly I would like to acknowledge my supervisor, Dean Venables, for all the opportunities he has given me over the past few years. The bulk of the data in this work was collected in the labs of Daniel Obrist and Hans Moosmüller in the Desert Research Institute in Reno, Nevada, USA, and I would like to thank them for allowing me to work there for so many months. I worked with many people while I was there. The operation of the Hg CRDS laser and processing to Hg concentrations were conducted entirely by Ashley Pierce. Also important to the chamber work were Ian Arnold and Chris Moore who were always around to help out. To get an environmental chamber up and running on such a tight schedule is due in no small part to the work of the in-house engineers and technicians of the DRI, especially Rick Purcell and Dana Schatz. I have never before asked in the afternoon about the possibility of having a job done some time in the future, and then arrived at 0700 the next morning to find it completed. Without the efforts of these and other people at the DRI, this thesis could not have been completed..

Abstract

Mercury is a potent neurotoxin even at low concentrations. The unoxidised metal has a high vapour pressure and can circulate through the atmosphere, but when oxidised can deposit and be accumulated through the food chain. This work aims to investigate the oxidation processes of atmospheric $Hg^0(g)$.

The first part describes efforts to make a portable Hg sensor based on Cavity Enhanced Absorption Spectroscopy (CEAS). The detection limit achieved was $66\,ng\,m^{-3}$ for a 10 second averaging time.

The second part of this work describes experiments carried out in a temperature controlled atmospheric simulation chamber in the Desert Research Institute, Reno, Nevada, USA. The chamber was built around an existing Hg CRDS system that could measure Hg concentrations in the chamber of $<100\,ng\,m^{-3}$ at 1 Hz enabling reactions to be followed. The main oxidant studied was bromine, which was quantified with a LED based CEAS system across the chamber. Hg oxidation in the chamber was found to be mostly too slow for current models to explain. A seven reaction model was developed and tested to find which parameters were capable of explaining the deviation. The model was overdetermined and no unique solution could be found. The most likely possibility was that the first oxidation step $Hg + Br \longrightarrow HgBr$ was slower than the preferred literature value by a factor of two. However, if the more uncertain data at low $[Br_2]$ was included then the only parameter that could explain the experiments was a fast, temperature independent dissociation of HgBr some hundreds of times faster than predicted thermolysis or photolysis rates.

Overall this work concluded that to quantitatively understand the reaction of Hg with Br_2, the intermediates HgBr and Br must be measured. This conclusion will help to guide the planning of future studies of atmospheric Hg chemistry.

Chapter 1

Introduction

1.1 Background

Mercury (Hg) has been in use by humans for many thousands of years. It occurs in the ground mostly as mercury sulfide (HgS) in the mineral known as cinnabar, but the free metal is also abundant in the same deposits. Powdered cinnabar—better known as the pigment vermilion—has been found in paintings in Çatalhöyük, a neolithic city in Turkey occupied from around 9500–7500 years ago.[6] There also is evidence of cinnabar being used used as preservative 5000 years ago.[7] The world's largest reserve of Hg, around a third of the global total, in Almadén, Spain was already being mined industrially by Celts and Romans 2000 years ago. Mining of the reserve ceased in 2001 due to lack of demand.[8–10] It is estimated that worldwide some 950 million kg have been extracted from the ground since Antiquity.[11] Put into one place this would fill about 30 Olympic-sized swimming pools. Through mining and other human activities such as coal combustion there are now many thousands of tonnes of Hg in global circulation today that would not otherwise be in the environment.

Despite the long history of usage by humans, mercury is very toxic. Recently levels in some environments have been rising, especially the Arctic where animals have been affected by high loadings of Hg.[12,13] As an element with a high vapour pressure the elemental gas, $Hg^0(g)$, has a long atmospheric lifetime of months and can be transported globally.[14] The precise mechanisms that cause it to deposit are not quantified well enough to predict its fate accurately.[15]

It is important to know the fate of $Hg^0(g)$: where it accumulates, why it does so

and how it may affect humans and the rest of the global ecosystem. This work aims to contribute to the understanding of the oxidation processes of $Hg^0(g)$ that allow it to deposit from the atmosphere.

1.2   Mercury as a toxin

The toxicity of Hg depends heavily on its form. The liquid metal, $Hg^0(l)$, is not absorbed through the skin but the vapour, $Hg^0(g)$, is readily absorbed through the lungs. Inorganic mercury, such as calomel (Hg_2Cl_2) can be absorbed through skin due to its higher solubility, so is more toxic. Some forms of organic mercury, especially $HgMe_2$, are exceedingly toxic and can readily pass through gloves, skin and then penetrate the brain.[16] Ethyl- and phenyl-mercuric cations are less toxic, and are still widely used as preservatives in medicines.[17]

There have been many fatalities of workers exposed to $MeHg^+$ and $HgMe_2$ both in research and industry.[18,19] The most famous victim of $HgMe_2$ is Karen Wetterhahn,[20] who, after spilling a few drops onto her gloved hand, fell into a coma and died 10 months after the accident. The total body burden of Hg at the time of diagnosis was 330 mg,[20] equivalent to absorbing just 130 µL of $HgMe_2$. Since the exposure occurred 150 days before diagnosis, the actual absorbed dose would have been several times larger (0.5 mL), which implies a spillage volume considerably larger than the 'single drop' often quoted. Delayed onset of symptoms is common with mercury poisoning, but is not fully explained.[17]

Miners would often die young from mercury poisoning, but historically the most prominent victims were alchemists. Hair analysis and historical records support the view that Michael Faraday,[21] Tycho Brahe[22] and Isaac Newton[23] all suffered from Hg poisoning, though none fatally. In more modern times much of the publicity of Hg poisoning is owed to Alfred Stock, who spent so much time using mercury in laboratories he was poisoned by it.[21]

As with many environmental toxins, the effects of Hg exposure can cause social and psychological problems in excess of its toxicity. In one case an artist's cooperative converted a disused factory into apartments and studio space.[24] After the discovery that the factory was contaminated with large pools of metallic Hg, the residents were evicted into temporary housing. Although there was a correlation between urine Hg levels and poor hand eye coordination, the most prevalent symptom in the residents was psychological distress unrelated to the urinary [Hg]. The distress was

induced not by the poisoning specifically but by the mandatory eviction. Several subjects had in fact diluted their urine samples in the hope of avoiding being torn from a project into which they had invested so much time and money.

Those who worked with Hg in mines or labs were exposed to large levels through the air or contact with their skin. For most people however the chief exposure route is consumption of predatory fish.[25,26] Zhang et al.[27] found that in polluted regions of inland China the main source was rice. Even with relatively small consumption, bioaccumulation can raise the concentration to harmful levels. Large arctic predators suffer from the toxic effects of mercury,[13,28] but so do smaller animals such as birds[29] and fish.[30] However, in a study of arctic foxes the correlation of poor health with hair [Hg] was thought to be caused by a non-ideal marine food source rather than Hg toxicity.[31]

Exactly what dietary Hg level is acceptable is not easy to define. Fish in particular are a source of polyunsaturated fatty acids, the consumption of which is probably necessary to maintain many body functions such as hormone production, cell membrane formation, brain function etc.[32] Consumption of fish can therefore have health benefits as well as health costs. Mackerel and sardines, for instance, contain little Hg but a lot of these fatty acids, so are recommended. Shark and swordfish are the opposite.

A meta-review of studies of low-level exposure to $MeHg^+$ (e.g. $4\,\mu g/g$ total [Hg] in maternal hair) found a link to neurological performance.[33] A review of studies with higher Hg levels came up with a correlation of -0.18 IQ points for each $\mu g/g$ increase of [Hg] in maternal hair.[34] The effect of a small drop in IQ becomes very large when experienced by a whole population. Using a value of € 17 363 lost lifetime earnings for each decrement in IQ point,[35] Bellanger et al.[36] found that $MeHg^+$ exposure reduction measures would have a net economic benefit in the EU of 8000–9000 M€ per year, albeit using a higher sensitivity of -0.46 IQ per $\mu g/g$. Sundseth et al.[37] found a global benefit of around 2000 M$ per year if Hg emissions were halved.

1.2.1 Mechanism of toxicity

Mercury is thought to be toxic by several mechanisms. Though it can bind to sulfur-containing enzymes in non specific ways, there are several more specific causes of toxicity.

It is thought that Hg^0 is not very toxic in comparison to Hg^{2+}, but is however much more mobile. Unfortunately they are inter-converted by various mechanisms in cells.[17] $MeHg^+$ is particularly dangerous as it is both toxic and easily transported across cell membranes by complexation with the amino acid cysteine, allowing it to use the same transport mechanisms that methionine uses. The antioxidant glutathione is another target, whose complexation leads to oxidative stress. $MeHg^+$ can also be demethylated, and under long-term low level exposure, it is probably the less mobile Hg^{2+} form that is the toxic agent.[38] Both Hg^{2+} and $MeHg^+$ disrupt the function of calcium channels, and may alter the structure of cell membranes through interaction with -COOH, $-NH_2$ and -SH groups.[39] $MeHg^+$ can function as an endocrine disruptor.[40] Selenium and zinc are important factors in mediating Hg toxicity.[38] Animal experiments showed that dietary selenium could be protective against measures of Hg toxic effects. This was, however, not borne out in epidemiological surveys,[41] nor was selenium supplementation found to be an effective treatment of Hg poisoning.[38]

1.2.2   Minamata

The most famous case of large-scale mercury poisoning occurred in the rural seaside village of Minamata in Japan, where the Chisso chemical company pumped industrial $HgMe^+$ waste into the sea. The local population was poisoned, resulting in hundreds of deaths and disabilities. The poisoning continued for a decade. Although a waste treatment plant was installed, it did nothing to reduce Hg levels. More than a thousand patients were certified for compensation.[42,43]

1.2.3   Iraq

One of the worst mass poisonings of any kind occurred in Iraq in 1971. After years of poor harvests and famine, thousands of tons of wheat and barley were imported. Nearly all of the wheat and more than half of the barley was treated with a $HgMe^+$ based fungicide.[44] The seed was delivered late and, with many fields already sown, it was milled to make bread and fed to livestock. Warnings that the seed was not for consumption were written only in Spanish and ignored. Mass poisoning ensued. The first official study of the poisoning noted over 6530 hospital admissions and 459 deaths. All of these occurred in rural areas where bread was home-made, as the bakeries in the cities used only government-inspected flour.[44] The authors note

that the typical poisonous dosage resulted from eating a few kg of wheat, yet 73 million kg of HgMe$^+$ coated wheat were distributed. The first author of that report was in fact the personal physician to Saddam Hussein, and later fled the country fearing for his safety.[45] Outbreaks of Hg poisoning caused by seed dressing had occurred previously in Iraq,[46] and HgMe$^+$ based fungicides were already banned elsewhere.

1.2.4 Hg Regulation

The Minamata Convention on Mercury[47] was adopted on October 2013, and as of December 2014, 128 countries had signed and 9 had ratified it. Parties to the convention are obliged to make efforts to monitor and control emissions, as well as to reduce and eliminate the use of Hg in all but essential applications.

There have already been efforts to reduce Hg releases for some time, e.g. scrubber units for coal power plants,[48] and education strategies for artisanal and small-scale gold mining.[49] It is too early to say what impact the treaty will have, as many countries were already adopting control measures anyway. Selin[50] forecasted that the effect of the treaty would be to avoid a rise in global atmospheric [Hg], which may instead decrease by a percent or two per year. Other treaties provide examples of the success of such measures. For instance the Stockholm convention to limit emissions of persistent organic pollutants was signed 14 years ago, yet its effects are unknown for many reasons.[51] Lead (Pb) pollution provides a case where legislation did have a large effect on the environmental burden, and its consequences may be instructive for the future of Hg.

Lead Pollution

The use of tetraethyl-lead (TEL) additive in petrol led to large scale Pb pollution. Unlike mercury, Pb is emitted from vehicles in an oxidised form and deposits nearby. Only a small fraction, bound to ultrafine particle, travels globally. After legislation and other factors eliminated leaded fuel, Pb pollution fell dramatically in the local environment. It has been suggested that trends in the rate of crime can be explained by changes in lead pollution as car usage first increased then leaded fuels were phased out,[52] and this idea has received intense media coverage. There does indeed exist a strong correlation between the childhood blood lead concentration and the tendency to commit crime later in life.[53,54] While spurious correlations abound in ecological

studies, the trend is replicated between US cities as they implemented leaded fuel bans at different times,[55] and across different countries.[53] The only peer reviewed article[56] refuting the statistics was funded by the Ethyl Cooporation, the distributors of TEL.* There are, of course many factors that could cause simultaneously lower lead emissions and crime rate—ordinary socio-economic development being one that is not easy to tease out, but the fact that lead is such a potent neurotoxin does make the hypothesis more noteworthy.

The idea that environmental legislation can have societal benefits well beyond its original scope is gaining currency, but even when there is a substantial quantity of data, the cause-and-effect relationships are near impossible to establish. As the Minamata convention comes into force and diminishes the anthropogenic emissions of Hg, we may discover similar correlations, but establishing causation will not likely be possible.

1.3   Sources and Sinks

As an element Hg can be neither created nor destroyed without nuclear reactions. It can only be moved from one place to another. There is no chemical form which is completely stable, so burial in sediments on land or under the ocean is necessary to keep it out of circulation. The current trend is that atmospheric [Hg] is decreasing slightly,[58] while oceanic [Hg] is increasing.[59] The processes that drive the cycling are not well understood, but in order to quantify the fluxes we need an inventory of the Hg circulation. The most recent assessment is shown in Figure 1.1. In this scheme a distinction is made between direct emissions of Hg from new sources and those which were recently deposited. A full discussion of the numbers and methods is outside the scope of this work, only a few items are noted below.

Natural sources   Any disturbance of Hg-containing ground will release some to the air or into waterways from where it can be deposited somewhere else. Thus volcanoes and fires are natural sources of Hg. For the year 2008, Pirrone et al.[60] estimated total natural emissions to be 5207 Mg. Volcanoes and geothermal activity contributed 90 Mg while biomass burning (usually counted as a natural source, even if carried out by humans) added 675 Mg of Hg to the atmosphere. In addition there

---

* Interestingly the only remaining manufacturer of TEL, Innospec, and four of its executives were convicted of corruption for giving bribes to Indonesian and Iraqi officials between 2002 and 2008 in order to delay TEL's phase out.[57]
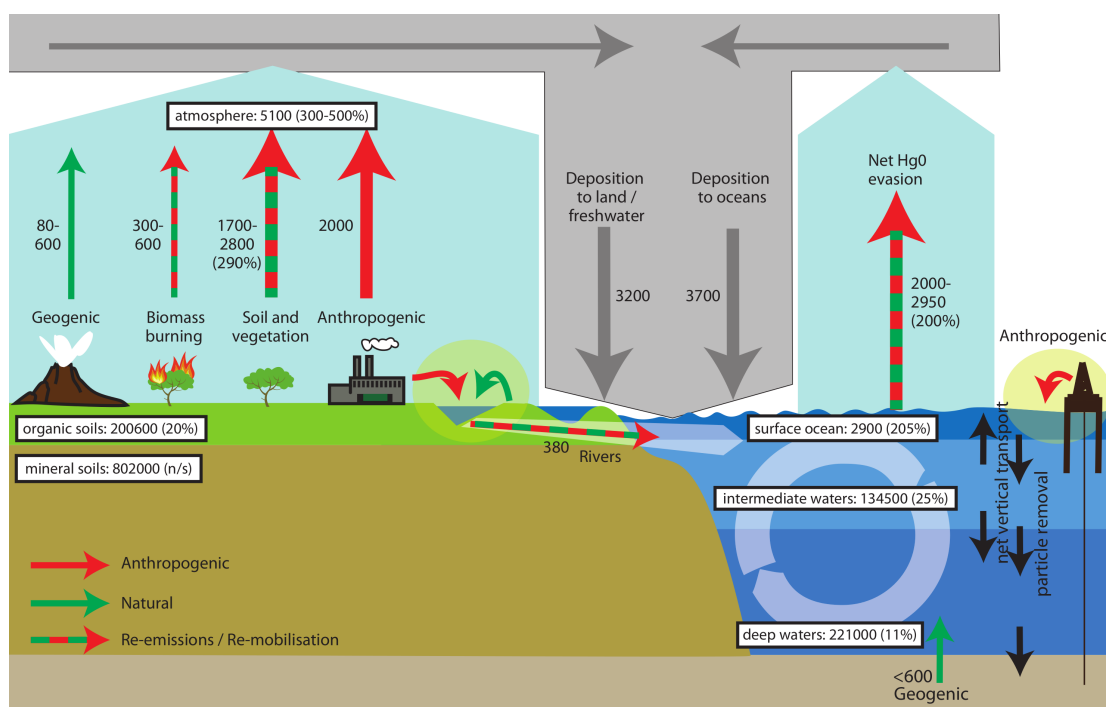
FIGURE 1.1: The global mercury budget. Total inventories (numbers in white boxes) are in Mg, and fluxes in Mg yr^{-1}. The percentage values in brackets are the estimated increases in inventories in the past 100 years due to anthropogenic activities. Image taken from the Technical Background to the Global Mercury Assessment, UNEP.[1]

is also re-emission following Hg deposition events, which contributed 200 Mg. By far the largest natural source was net evasion from the ocean at 2682 Mg. The ocean in fact acts as a reservoir of Hg. Emissions can be deposited there, then re-emitted and deposited on land some decades later. However, it is estimated that only 17% of the Hg in the ocean would be there in the absence of human activities, and 60% of the Hg deposited had already been re-emitted from a surface reservoir.[61]

Anthropogenic sources   Estimated total anthropogenic sources were 2200 Mg in the year 2000[62] and 2320 Mg in 2008.[60] The most common use of Hg for most of history has been for mining gold and silver. In the past this was the only available method and today it is practised on a small scale but by a vast number of people, nearly all of whom are in the developing world and rely on it as their only income. Estimates for atmospheric emission are 400 Mg for the year 2008[60] to over 1000 Mg in more recent years when the surveys are probably more accurate.[1]

The most common source of Hg where Hg is not deliberately used is coal combustion. Coal contains on the order of 0.01 to 1 g of Hg per Mg of coal.[63] Combustion of coal for power generation releases large quantities of Hg, around 300–700 Mg yr^{-1}.[2]
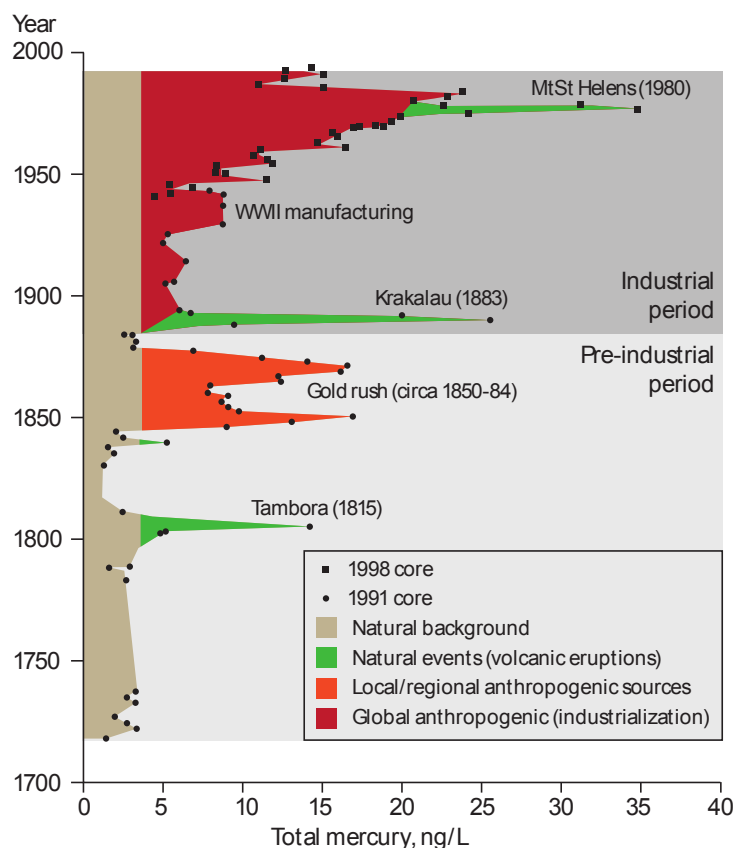
FIGURE 1.2: [Hg] with ice depth in a North American glacier. Image from the Global Mercury Assessment, UNEP.[2]

Streets et al.[11] and Horowitz et al.[64] have modelled how emissions have changed over time. The North American Gold and Silver Rush led to vast releases of Hg to the environment, much of which remains in circulation today. During the second world war there was increased usage for munitions, and as electronics became more common during the 1970 batteries were a significant source to the environment. Batteries and other Hg sold commercially may not be fully accounted for in other inventories, as they do not release to the environment by design but by accidental discharge.[64] There is a net 310 Gg in circulation of which 110 Gg is airborne.

Sinks   Ice cores from a glacier in North America show deposition events from both local, global, natural and anthropogenic sources (Figure 1.2).[65] The same anthropogenic sources predicted by the inventory models are also visible as depositions in the ice core. In addition there are three spikes from volcanoes, one of them local and the other two from the Southern Hemisphere.

Because deposition is a largely chemical process it is more difficult to predict from existing records than the emissions are. Ice and sediment cores provide historical

insight but there are few direct measurements of the day-to-day fluxes. The global budget in Figure 1.1 indicated that soil and vegetation were a net source of Hg, yet field measurements suggest that in fact soil may be able to sequester Hg permanently.[66] The same is true of the oceans. Anthropogenic emissions may take on the order of 1000 years to be permanently reincorporated into oceanic sediment.[51,67] Recent measurements found the oceans contained 59 Gg of anthropogenic Hg,[59] This amounted to a tripling of the background level in surface waters, a figure in broad agreement with the 17% being natural of the inventory based model from Amos et al.[61] The extra loading means that the oceans are a net source of Hg even if on a longer timescale they are also a sink.

To better quantify the deposition and re-emission new types of instrumentation are desired. The various measurement techniques and their applicability to flux determination are described in Chapter 2. The next section will give an overview of Hg chemistry.

1.4   Mercury the element

Mercury is the only metal present in the atmosphere in its elemental form. To understand why, it is necessary to look at its chemical properties. Although Hg is famous for being a liquid metal, the heavier alkali metals rubidium, caesium and francium all have melting points below 40 °C, and the relatively benign gallium melts at 30 °C. Alloys of these metals have melting points below room temperature. Unlike all other metals however Hg has a significant vapour pressure at room temperature. This is a result of several factors which combine at the lower right of the periodic table to produce some remarkable properties.

Valence shell   The electronic ground state of Hg is $[\text{Xe}]4\,\text{f}^{14}5\,\text{d}^{10}6\,\text{s}^2$. Like the other elements in its group there are no partially filled orbitals, so there is much less opportunity to react chemically.

F-block contraction   The presence of the lanthanides means that Hg has an 14 extra electrons compared to cadmium above it. The extra electrons lie in the f-orbitals, which do not shield the outer electrons from the nuclear charge as effectively as those in the d-orbitals. This leads to a contraction, causing the valence shell to be more inert.

9

Relativistic contraction   In the heavy elements the electrons move so quickly that relativistic effects must be considered. This effect brings the electrons closer to the nucleus, and renders the valence electrons more inert. It was suspected for many years that this was responsible for mercury's unusually high melting point,[68] but it was only recently that a high level computational study found the melting point would be 105 K higher without relativity effects.[69]

These effects make the valence electrons lie close to the nucleus and have high ionisation energies—1st 1006, 2nd 1799 and 3st 3309 kJ mol^{-1}. The +1 state therefore has a tendency to disproportionate, and all known +1 compounds are actually of the form Hg_2^{2+}. From these energies the +3 state should be available too, but the energies are too high for it to be common.[70] The Hg_2^{2+} ion is a compromise between the high ionisation energy and the instability of an unpaired electron. These factors also apply to copernicium ($^{283}_{112}Cn$) and one would expect it to be even more volatile. Experiments—with only two atoms—have supported this.[71]

Vapour Pressure   The anomalously high vapour pressure of metallic Hg is understood to be a consequence of the above effects. However, there exists a large and currently unexplained uncertainty in the actual value of the vapour pressure. The relation known as the Dumarey equation is the one most often used to calculate the temperature dependence of the vapour concentration.[72] The vapour concentration ought to correspond to the vapour pressure in accordance with the perfect gas law, including some small corrections.[73] However, the actual pressure above the vapour measured by manometer has been determined as some 7% higher than suggested by the Dumarey equation.[74] Detailed thermodynamic calculation also supports this higher vapour pressure. Either all the pressure measurements are flawed to the same extent, or the methods of vapour sampling with a syringe are systematically too low. Efforts are under way to link [Hg] to fundamental units to give calibrations traceability back to national standards.[75–77] The most recent isotope-ratio mass-spec results are consistent only with the vapour pressure measurements, not the Dumarey equation.[78]

Isotope fractionation   Hg exists as seven stable isotopes. The ratio of these isotopes is not constant and some sources such as coal[79] or compact fluorescent lamps[80] have unique signatures. The isotopes can also react slightly differently, and the effects are grouped into two categories.[81] The Mass Dependent Fractionation (MDF) arises because heavier isotopes react differently, for both thermodynamic and kinetic

reasons. Mass Independent Fractionation (MIF) affects the odd to even isotope ratio and arises due to the nonlinear scaling of nuclear volume with atomic mass, and to the faster spin conversion of odd numbered isotopes due to hyperfine coupling of the radicals with the non zero nuclear spin. The MIF is particularly prevalent in photochemical reactions as they often proceed via radicals. By measuring the ratio of all the isotopes, information on the history of the sample can be extracted.[25] For example, the sign of the MIF of $Hg^0(g)$ will be different depending on whether the source of Hg was organic or inorganic. The area of Hg isotope fractionation research is only a few years old and is sure to be useful in evaluating the biogeochemical cycles of mercury.[82]

1.4.1   Mercury Detection

There are many kinds of gaseous mercury analysers available, each one designed for a specific application. Aqueous Hg and its speciation are not considered here. The largest market for Hg monitors is for industrial emissions monitoring, so most instruments are built to handle high levels of $Hg^0(g)$ in a dirty sample. Hand-held analysers are also available for moderate concentrations in relatively clean air. There is also a significant demand for long term environmental air monitoring, where samples are much cleaner but extremely dilute. The different techniques employed to measure Hg are reviewed in Chapter 2, but common to all these instruments is that the only species they can measure directly is $Hg^0(g)$, usually referred to as Gaseous Elemental Mercury (GEM). To detect low concentrations it is accumulated on gold traps for several minutes. Other Hg species are pre-concentrated and converted to $Hg^0(g)$. Two types of filter are used to collect non-$Hg^0(g)$, giving rise to the two non-elemental fractions commonly measured. Unfortunately these fractions are often referred to as 'species' or 'speciated measurements' when in fact they comprise a wide, largely unknown, range of compounds.

Reactive Gaseous Mercury (RGM)   The terms Reactive Gaseous Mercury (RGM) and Gaseous Oxidised Mercury (GOM) are used interchangeably. RGM is used here. It is defined as all the mercury which is collected onto a KCl coated annular denuder. This definition is due to the near universal use of such denuders for atmospheric measurements. It is well-known that denuder method is not completely robust. Lyman et al.[83] reported that O_3 caused the RGM to be released from the KCl denuder. There is also a lower collection efficiency of $HgBr_2$ in humid air.[84,85] Despite these

shortcomings, the alternative methods such as mist chambers or cation exchange membranes have not yet been commercialised.[86]

Particulate Mercury (PHg) Particulate Hg (PHg) or Particle Bound Mercury (PBM) is defined as mercury which is collected onto a particle trap, usually quartz fibre. The form can be elemental or oxidised, condensed or adsorbed to some other material, e.g. sea salt aerosol. The filter is usually downstream of the KCl denuder, so that RGM can be removed first and then the particulate matter filtered out. In the Tekran system large particles ($>1\,\mu$m) are trapped in an elutriator before entering the instrument, so are not collected into PHg.

The sum of all the fractions is here referred to as simply Hg. This total Hg is the quantity measured by many digestion and derivatisation measurements which convert all Hg species into Hg^0(g).

The lack of chemical detail in these fractions has impeded our understanding of environmental Hg chemistry. One of the original aims of this work, described further in Chapter 2, was to construct an instrument that could measure Hg species more specifically.

1.4.2   Environmental Chemistry

During the 1960s in Sweden it was noticed that fish in remote lakes contained a surprisingly large concentration of $MeHg^+$. While industrial waste and seed dressings explained the high levels found in some areas, only long range atmospheric transport could lead to high levels in isolated lakes.[87] Since then there has been much work in measuring the atmospheric [Hg], and finding the mechanisms by which Hg is emitted and deposited.

Unlike lead or other heavy metals Hg has considerable vapour pressure at room temperature. It has little tendency to dissolve in water or condense onto surfaces without first being oxidised. Typical background concentrations are on the order of $1\,\mathrm{ng\,m^{-3}}$ or 0.1 ppt. Due to the long lifetime of several months to a year[14] it is quite evenly distributed within hemispheres, with slightly higher concentrations in the northern hemisphere (1.5–$1.7\,\mathrm{ng\,m^{-3}}$) than the southern (1.1–$1.3\,\mathrm{ng\,m^{-3}}$) due to the extra industrial emissions there.[88]

1.4.3   Mercury Depletion Events

In the 1990's Schroeder et al.[89] noticed that the background mercury levels drop suddenly during springtime in the Arctic.[89] These events occur after polar sunrise and have been dubbed Atmospheric Mercury Depletion Events (AMDEs).[90] They were the subject of over 200 papers in the years after the discovery was announced.[15] Analysis of lake sediments show that these events have been happening for somewhere between 90 and 200 years in the Arctic.[91] AMDEs have also been documented in the Antarctic[92,93] and at mid latitudes in the northern[94] and southern[95] hemispheres. If the Hg is oxidised in the free troposphere it will remain there,[96] until it is deposited through mixing with the boundary layer[97] or by washout.[98]

Elemental Hg does not significantly adhere to ice surfaces,[99] whereas oxidised forms such as $HgBr_2$ have low vapour pressures and deposit rapidly on many surfaces and dissolve in water.[100,101] The mechanism underlying AMDEs was initially thought to involve oxidation by O_3 and HO,[100] similar to hydrocarbons. Later BrO radicals were proposed as the main oxidant in the air[102] as both O_3 and Hg are depleted during so-called bromine explosion events. During these events bromine is released from sea ice at sunrise and O_3 concentrations soon drop to zero.[103] The cause is a sequence of auto-catalytic reactions that convert Br^-(aq) into Br_2, Br˙ and BrO while using up O_3.[104] The BrO-rich air and O_3-depleted air can be transported to other areas.[105]

Although BrO itself is probably unable to initiate the oxidation of Hg^0(g) on thermodynamic grounds,[106] AMDEs are highly correlated with halogen concentrations[107] and the only species now thought to be both reactive and present in high enough concentrations to oxidise Hg is Br˙.[14] This applies not only to AMDEs but also to possibly all dry deposition of Hg^0(g).

Re-emission of the deposited Hg is often observed within 24 hours of deposition. The proportion of Hg re-emitted varies from only a few percent[108] to over 40%.[109,110] Re-emission is facilitated mainly by UV-B (< 320 nm) light as opposed to UV-A or visible wavelengths.[109,111] Humic substances,[112,113] dicarboxylic acids,[114] and alkanethiols[115] can reduce Hg^{2+}(aq) to Hg^0. Low pH, high $[Cl^-]$ or dissolved oxygen inhibit the process.[112,116] Dissolved Hg^0 can also be oxidised under freezing conditions.[117] The mechanism of remission is so uncertain that in models it is parametrised with a fixed value.[14,118]

The net effect of AMDEs is to transfer Hg from its emission source to polar terrestrial and aquatic environments, from where it can be incorporated into the food chain.

Understanding when and how the transfer happens is crucial to quantifying the problems caused by Hg emissions, and forecasting where on the planet will be worst affected in the future. A quantitative understanding of the gas-phase reactions of Hg with Br is therefore important to model the global biogeochemical cycle of Hg. There is, however, little experimental data on most of the reactions, and what data exists was collected in very different conditions to the environment. Further investigation of the Hg and Br chemistry is the main subject of Chapter 4.

1.5 Units used in this thesis

Concentrations in the gas phase can be expressed in absolute number or mass densities ($\mathrm{molec\,cm^{-3}}$ or $\mathrm{\mu g\,cm^{-3}}$), but these units suffer from the disadvantage that as a parcel of air warms up, for example, it expands and reduces in density. The absolute concentration will have decreased without any chemical transformation taking place. To correct for this, relative concentration are often used, and the unit is always relative to the number of air molecules (molar or mixing ratio), as opposed to the mass or volume fractions commonly used for liquids. In kinetics, the absolute concentrations of each species determine the rate so knowledge of the relevant air temperature and pressure is required when using relative units. In Chapter 2 all data refers to approximately sea level pressure of $100\,\mathrm{kPa}$. All the experimental data in Chapters 3 and 4 is collected at an altitude of $1500\,\mathrm{m}$, where the air density is about 15% lower than at sea level ($2.0\times10^{19}\,\mathrm{molec\,cm^{-3}}$ at $300\,\mathrm{K}$).

Most instruments detect the absolute concentration of a substance, and conversion to relative units can introduce significant errors.[119] Flow rates are at local temperature and pressure, i.e. not 'standard' litres per minute, as only the actual volumes in the experiment are relevant. Since all wavelength dependent quantities are processed as vectors they are written in bold $\boldsymbol{E}$ rather than as a function of wavelength $E(\lambda)$. Time dependent quantities have a subscript to denote the time they refer to, e.g. T_0 for the baseline and T_t for a general time t.

Chapter 2

Development of atmospheric mercury detectors

For more than 40 years there has been much interest in measurements of atmospheric Hg in all its forms, yet there are still large systematic uncertainties in Hg measurement.[120] As described in the introductory chapter, the toxicity of Hg and its compounds means that we must measure its emission and deposition fluxes, and find what mechanisms interconvert the oxidised and elemental forms. $Hg^0(g)$ has a lifetime of months in a typical atmosphere, yet will deposit very rapidly when oxidised. Understanding the oxidation process is critical to predicting where Hg pollution will end up and what consequences it may have.[15] Unfortunately existing instruments have unsatisfactory performance in a number of aspects. They are too slow to measure fluxes by the preferred technique of eddy covariance. No commercial instrument can measure oxidised Hg directly, and the oxidised fraction collected by the common denuder method does not yield any information about chemical speciation.

Described in this chapter are efforts to build a detector capable of measuring $Hg^0(g)$ with improved performance over commercial instruments, and the suitability of the new detector to determining fluxes.

The part of this chapter dealing with the atomic line source CEAS has been published.[121]

2.1 Atmospheric mercury measurement techniques

The commonly used Hg fractions were defined in Section 1.4.1. Briefly, Gaseous Elemental Mercury (GEM) is $Hg^0(g)$, Reactive Gaseous Mercury (RGM) is Hg that deposits rapidly to a KCl coated denuder, and Particulate Hg (PHg) is Hg that is filtered on a particulate trap. Clevenger et al.[122] provides an overview of the state of the art of Hg detection in 1997. This section will describe the detection mechanisms in more detail, and discuss how they can be applied to flux measurement.

2.1.1 Detection of GEM

Spectroscopy is at the heart of almost every commercial Hg detector. The transition from the ground to the first excited state at 253.7 nm, $^1S_0 \rightarrow {}^3P_1$, is ideal for sensitive and specific Hg detection. It was one of the lines used to investigate many of the fundamental theories of electronic structure.[123] The transition is spin forbidden, which gives the $^3P_1$ state comparatively long lifetime of 114 ns.[124] The cross section is large, on the order of 1×10^{-14} cm^2 atom^{-1} at 254 nm. Literature values of the absorption cross-section vary by an order of magnitude[125,126]—from 1.9×10^{-14} cm^2 atom^{-1} to 5.3×10^{-15} cm^2 atom^{-1}—due mainly to the different pressures it is measured at and the relative overlap with the linewidth of the source. Atomic transitions have a narrow linewidth and if the source has a larger linewidth than the absorption, the cross-section will appear smaller. Low pressure discharge lamps have a much narrower linewidth than most UV lasers.

Light at 254 nm can be generated by many designs of lamp. Most commonly a current is passed through a Hg-Ne or Ar gas to excite the Hg atoms, which then decay by emitting light at 254 nm. If the pressure is high the atoms can be collisionally deactivated before emission, which creates a layer of ground state atoms away from the electrodes at the edge of the lamp envelope. This cold layer of atoms absorbs the emission from the hot atoms closer to the centre, with the result that the strong emission lines are absorbed but weaker ones become dominant. High currents through the lamp make this self-absorption more severe, which places a limit on the achievable brightness of an atomic line. At high frequencies however, the magnetic field produced by the current pushes it to the edge of the lamp away from the centre of current flow. High-frequency discharge lamps utilise this so-called skin effect to produce brighter sources,[127] and many commercial atomic absorption spectrometers use this type of lamp.

There are several different implementations of Hg spectroscopy, outlined below.

Absorption Atomic absorption Spectroscopy (AAS) has been the mainstay of routine Hg detection for decades. It usually employs an Hg lamp as the light source. The Limit Of Detection (LOD) is around 100 ppt, but this can be improved with careful design. There are variations such as pre-concentration, cavity ring-down, Zeeman absorption, long path, and LED light source:

Pre-concentration By pre-concentrating the Hg on a gold trap and releasing it with heat the LOD can be reduced to atmospheric levels with an accumulation time of several minutes. It also filters out any interfering species. Nearly all environmental monitors use this technique.

Cavity Ring Down Cavity Ring-Down Spectroscopy uses a high-finesse optical cavity to extend the effective path length by a factor of several thousand. There have been many attempts to create a CRDS instrument for Hg.[125,128–132] Of these efforts, the system of Pierce et al.[128] was the most recent and successful with a reported LOD of $0.1\,\mathrm{ng\,m^{-3}}$ over 10 s. All the CRDS instruments had problems with laser stability and background correction. With very high Q cavities, there may also be difficulties with cavity mode hopping and radiation trapping, where the long lifetime of excited Hg leads to optical transparency.

Zeeman absorption The narrow absorption line of Hg makes for very sensitive detection, but it is not specific. Many trace species such as VOC's, SO_2, O_3 or particulate matter will absorb or scatter strongly at 254 nm. Some sort of background correction is required, and this is conveniently achieved by Zeeman shifting the emission wavelength of an atomic line source with a magnetic field. One example of a commercial device is the Lumex RA-915, which uses a permanent magnet to Zeeman shift the emission of a single-isotope Hg lamp. One of the lines coincides with the Hg spectrum and the other falls outside, and since lines have opposite polarisations their intensities can be compared easily at high frequency.[133] The LOD has been reported to be as low as $0.5\,\mathrm{ng\,m^{-3}}$, averaged over 10 s.[134]

Long path Another way to obtain the required sensitivity is to measure absorption over a long distance. A pathlength of 220 m has been applied to Hg.[135]

LED source Since Hg atoms absorb at a very precise wavelength, the light source must be equally precise to be absorbed effectively. Multimode absorption uses cheaper diodes to produce a frequency comb, which can also be used

for spectroscopy but at much lower sensitivity.[136] Lou et al.[137] achieved a sensitivity of $1\,\mu g\,m^{-3}$ for a 1 m path length and 30 s integration time.

Resonance fluorescence For the low concentrations encountered in environmental monitoring, fluorescence is preferred over absorption. It is the method of operation of the Tekran 2537 monitor, which has been used in most measurements of Hg in the field. Fluorescence is also less susceptible to interferents such as O_3 and SO_2 and usually has a lower baseline signal than absorption. Gold trap pre-concentration is nearly always used in tandem with fluorescence. The greatest sensitivity requires an argon gas supply, something which is not always available in remote regions.[15]

Non-resonance fluorescence For Hg non-resonant fluorescence entails multi-photon excitation, and detection at some other wavelength. Because of the lack of background from Rayleigh scattering, powerful lasers can be used and very low LODs can be reached. Bauer et al.[138] reported $0.1\,ng\,m^{-3}$ at a sample rate of 10 Hz, which is the fastest and most sensitive instrument known. It has recently been deployed in the field with moderate success,[139] and has potential to measure fluxes by eddy covariance.

Ionisation spectroscopy Ionisation spectroscopy is inherently more sensitive than optical since ions can be collected and detected with greater efficiency,[140] although it is also possible for a single atom to emit many photons. Clevenger et al.[141] achieved a detection limit of 15 atoms, in an atmosphere of argon and methane to prevent quenching. The required laser apparatus is similar to non-resonance fluorescence since both involve multi-photon absorption, but the technical barriers for ion detection are much greater than for photon detection. Such sensitive ion detection might not be viable with atmospheric Hg samples.

Mass spectrometry Whereas ionisation spectroscopy selectively ionises the species of interest, mass spectrometry ionises the whole sample and the products are separated by mass-to-charge ratio and detected. This is most useful for analysis of mixtures or isotopes, where information on all the species present is desired. It is commonly used for analysis of liquids or solids, but Hg is too dilute in the gas phase for mass-spec to be useful without pre-concentration. See sections on RGM and PHg below for details.

Plasma excitation Inductively Coupled Plasma (ICP) and Microwave Induced Plasma (MIP) Optical Emission/Atomic Fluorescence (OES/AFS) use radio or microwaves instead of lasers to excite the atoms, which then emit their characteristic wavelengths. The ability to measure many elements simultaneously is an advantage in clinical and industrial test laboratories, but the technique is not sensitive enough to detect ambient $Hg^0(g)$ without pre-concentration.[122]

Metastable Energy Transfer Atomic Luminescence (METAL) Dodge and Allen[142] used metastable excited N_2 molecules to excite Hg, which then chemiluminesced at 254 nm. The claimed detection limit was 10^7 atoms cm^{-3} at a pressure of 1 torr, which is mixing ratio of 300 ppt and not 3 ppq as the authors of the review[122] miscalculated. No effort was made to improve the LOD, but it seems unlikely that an improvement of 1000 could be forthcoming with such a complex instrument.

Solid state sensors The only commercial non-spectroscopic detection method in common usage is amalgamation of a gold film,[143] which is detected by an increase in electrical resistance. This measurement principle gives a LOD of 50 pg, which would be contained in 50 L of typical ambient air. A commercial detector based on this principle has been used for ppb level measurements in the atmosphere.[144] Other types solid state sensors have been developed. All have some type of gold surface to collect the Hg, and the sensor can be based on a quartz crystal microbalance,[145] piezoelectric microcantilever,[146] MOS capacitors and MOS-FETs,[147] carbon nanotubes[148] or gold nanowires.[149] None of these sensors have achieved better than ppb-level detection of $Hg^0(g)$, so are not useful for ambient monitoring.

2.1.2 Detection of RGM

Typical concentrations of RGM are of the order of 1-100 pg m^{-3}, so some kind of accumulation is essential.[15,150] There is no standardised method to measure oxidised Hg. The following paragraphs outline the approaches so far developed.

Potassium Chloride Annular Denuder The most common technique is pre-concentration onto an annular denuder coated with KCl followed by pyrolysis to release $Hg^0(g)$ after some accumulation time. This is the only commercially available non-passive method and prevails only because no better technique exists.[84] Its

collection efficiency of all oxidised Hg can be as poor as 20% in humid conditions or with elevated O_3 levels.[83,85]

Continuous Pyrolysis   There is a research instrument that does not rely on RGM accumulation but instead uses two Tekran units to simultaneously measure the difference between channels with and without a pyrolyser, providing higher time resolution.[96,151,152]

Temperature Programmed Pyrolysis (TPP)   A similar concept to temperature programmed desorption, TPP employs the usual accumulation but the pyrolysis step is conducted slowly in order to release species at different temperatures, enabling some kind of separation. This has been used to test the Hg content of meteorites,[153] finding that the Hg was probably contained as HgS. Kocman and Horvat[134] also used thermal release to show that the speciation in their soil samples was not identical, but could only report that it was either more or less oxidised. Some work has been carried out on atmospheric samples near coal-fired power plants, but results have been qualitative or inconclusive.[154–156]

Chemiluminescence   Dreiling and Setser[157] studied chemiluminescence from the formation of HgX compounds. They used an $[Hg^0(g)]$ of 150 ppb, but their objective was spectroscopy rather than detection.

Laser Induced Fluorescence (LIF)   Donohoue[158] used excitation at 256 nm and fluorescence at 500 nm to detect high $[HgBr]$ inside a reaction cell. The technique was used to follow the course of a reaction, and would not be sensitive enough to use in ambient air.

Mass spectrometry   Laboratory studies have employed ICP-MS and MALDI-TOF for analysis of deposited reaction products.[159,160] Chemical ionisation may not work well as some Hg compounds have a lower electron affinity than common ionisation reagents.[106] Ambient levels of RGM are not high enough to detect directly with mass-spec. Accumulation for 24 hours onto a trap, followed by thermal desorption and chemical ionisation with isobutane has been used recently to detect $HgBr_2$ and $HgCl_2$ in urban air.[161] A patent application has been filed on this technique,[162] and such methods hold promise for identifying the products of ambient Hg oxidation.

Passive filters   Passive samplers consist of an adsorbent which is exposed to the air for a period of days or weeks and then taken back to a laboratory for analysis. Huang et al.[163] reviewed them recently. Analysis usually involves wet digestion or pyrolysis and gold trap collection. Any of the many analytical techniques for solid samples could also be applied, such as neutron activation analysis, particle induced X-ray emission,[164] energy-dispersive X-ray spectroscopy[160] and X-ray photoelectron spectroscopy.[165] Due to the very low time resolution of filters (weeks for static filters but can be hours for moving tape) they are not useful for dynamic flux measurements.

Ontario Hydro method   For emissions monitoring of coal fired power plants the most common method of oxidised Hg analysis, named after the Ontario Hydro energy company, is to pass the flue gas through a set of solutions to selectively scrub different components. This method is vulnerable to interference from NO_2 and SO_2, and does not provide more detailed fractionation than solid KCl denuders.[166]

2.1.3   Detection of PHg

PHg presents a special detection challenge since the Hg is bound within an unknown and variable matrix. As for RGM, the normal approach is to accumulate on a filter and then bake off the Hg, but there have been several attempts to use aerosol mass-spectrometry.

Aerosol Mass Spectrometry   One campaign detected Hg in stratospheric aerosols just above the detection limit with an aerosol mass-spec.[167,168] Ionisation of Hg is challenging in a solid sample due to the high ionisation potential of Hg.[167]

2.2   Flux measurement techniques

When trying to establish whether Hg or indeed any species has a source or sink the flux has to be measured. The deposition reactions investigated in Chapter 4, even if known accurately, would give only half the picture if re-emission is not taken into account. There are several possible ways to do this and most of them have been used for Hg. Research into these field based techniques has progressed rapidly in

the past 20 years.[169] Sommar et al.[170] have reviewed every known field study of Hg flux measurement, so only an overview is given here.

2.2.1 Dynamic Flux Chamber

The least expensive approach to measuring fluxes employs a small transparent box over the ground. The difference in [Hg] between air pumped into and out of the box yields small scale and high time resolution flux information. The results can be heavily influenced by poor box design and uneven flow.[171] The data is also collected from a small patch ($< 1\,m^2$) which may not be representative of the wider area. The disturbance and greenhouse heating of the surface may also lead to bias.[169]

2.2.2 Micrometeorological Methods

On rough surfaces wind generates vertical eddies of wind. Micrometeorological (MM) methods measure the small difference in concentration of the species between air moving away from the surface and towards it. If there are no eddies, or no wind at all, the technique fails. It measures fluxes from an area of the same scale as the eddies, around 10 m. There are several different MM techniques.

Eddy Covariance   The most direct MM technique is to simultaneously measure the wind speed and direction and the concentration of the analyte. This requires instruments that can measure at a high frequency, about 10 Hz, and with enough precision that small concentration differences between up and downdrafts can be detected. Pre-concentration is not suitable as it slows the measurement rate. As yet no instrument has achieved eddy covariance for Hg. The CRDS instrument of Pierce et al.[128] was noisy at the required time resolution, so could only detect emission from contaminated surfaces.[172] The non-resonance fluorescence instrument of Bauer et al.[139] may be deployed for flux measurement soon.

Relaxed eddy-accumulation   This is similar to eddy covariance but a pre-concentration step is added. There are at least two traps and a fast valve switches between them depending on the wind direction. Then an average concentration can be measured over all updrafts and all downdrafts, and the difference is the flux. The advantage of this technique is that all the components are readily available as Hg analysers already use pre-concentration. The difficulties include setting up

the system in a tower while still maintaining fast and accurate switching between the two traps. This technique has been used over Arctic snow,[173] forests[174] and crops.[175]

Flux gradient   The flux gradient approach makes measurements at different heights simultaneously to obtain the concentration gradient. Together with knowledge of the wind the flux can be calculated. Alternatively the modified Bowen ratio method correlates the flux to another species whose flux can be measured at one point, such as CO_2. This has been used many times, and compares well to relaxed eddy accumulation.[170]

2.2.3   Differential absorption LIDAR

Differential absorption LIDAR (DIAL) measures the differential scatter from the air at wavelengths absorbed and not absorbed by Hg. The beam can be pointed at any angle which allows a full 3D snapshot of [Hg] in the atmosphere, from which fluxes can be calculated. Due to the expense of these systems, only a few have been built[176–178] and one has been used in several field studies at chlor-alkali plants,[179] other polluted industrial sites,[180] and an attempt was made at measuring fluxes from a whole volcano.[181] The advantage of this technique is the long 100–1000 m path length over which it can measure, and still retain some rough spatial resolution. Apparently only one system has ever been deployed in the field, and no system has been employed with MM methods.

2.2.4   Radon Flux Correlation

In some regions there is a very steady flux of ^{222}Rn from the soil due to radioactive decay in the ground. Since ^{222}Rn is radioactive its concentration can be measured easily, and the ratio ^{222}Rn/Hg^0 can be used as a measure of Hg flux from the soil. This method can only work where there is steady ^{222}Rn emission, but it is especially suited to very stable atmospheres where MM methods fail.[182]

2.3   Instrument Development

The goal of this section was to produce an instrument capable of measuring Hg fluxes, and of quantifying speciated mercury with more detail than the instrumentally defined fractions. To determine fluxes by eddy covariance, the instrument would have to detect sub-ppt levels of $Hg^0(g)$ at 10 Hz. Ideally, the instrument would also achieve the same sensitivity with various known and unknown oxidised species of mercury. The only light source bright enough to realise such fast and sensitive measurements is a laser. However, lasers emitting at 254 nm are not widely available so the system was custom designed.

The laser system was based on an existing design.[183–185] Two diode lasers are frequency summed to give laser light at 253.7 nm. This was done in two studies[183,185] to showcase the frequencies accessible by the relatively new violet diodes when frequency-summed, while Anderson et al.[184] developed it into a coal stack emissions monitor for Hg. The benefit of this laser design is the relative ease of tuning the wavelength. By scanning over the Hg absorption the signal can be discriminated from the background scatter. At a reduced pressure, the Hg isotopes can also be resolved. The LOD of Anderson et al.[184] varied between 300 and 10 ppt for acquisition times between 1 and 10 s respectively with a path length of 1 m. At our desired acquisition rate of 10 Hz, the LOD would increase by $\approx \sqrt{10}$ or to 1 ppb.

Optical cavities can increase the sensitivity by a factor of up to $1/(1-R)$ (R is mirror reflectivity, more details in Section 2.4). For our instrument R would have to be 99.98% to make rapid atmospheric detection feasible. With such large reflectivities very little light escapes the cavity, and the increase in shot-noise lowers the enhancement factor to $\sqrt{2/(1-R)}$. To use such high-R mirrors the light source would have to be several orders of magnitude more intense than feasible, so lower reflectivity mirrors with $R = 99\%$ were used for the prototype.

To fractionate RGM, an accumulation and pyrolysis unit was to be placed before the detector in a similar manner to Swartzendruber et al.[186] but with the addition of a temperature programmed pyrolysis step in order to identify individual species (Section 2.1.2).

2.3.1   Laser system

Figure 2.1 shows the intended setup. Two diode lasers are frequency summed in a BBO crystal (described in more detail later). The wavelength is monitored with
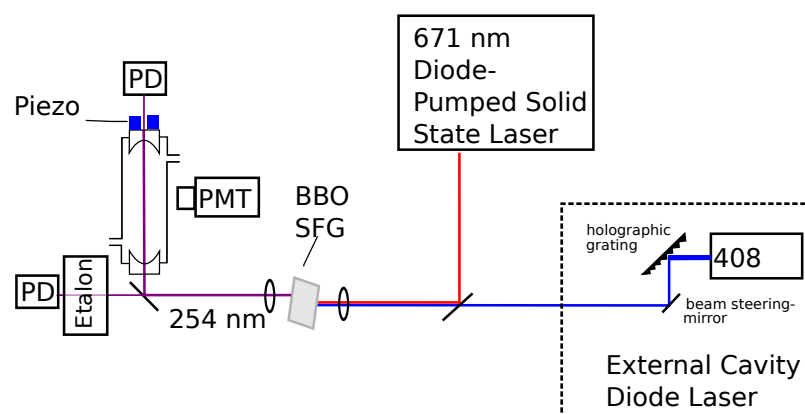
FIGURE 2.1: Optical design of the proposed Hg monitoring instrument.

an etalon. The 254 nm light is directed into an optical cavity, described in Section 2.4. The cavity length was to be adjusted with piezo stacks linked to the etalon, to achieve mode locking of the cavity with the laser wavelength. The Hg concentration was to be extracted from two signals: a photodiode (PD) at the rear of the cavity to measure absorption and a photomultiplier tube at the side to measure fluorescence.

There is no laser that emits 254 nm light directly but the wavelength can be obtained by summing two other wavelengths together. It is usually accessed with a combination of OPAs or dye lasers.[125,138,141,179,187] These are complex, delicate and expensive systems and for field use a more robust and compact system is desired. The use of diode lasers is a step toward a more practical field instrument.

Diode lasers have many beneficial properties for spectroscopy.[188] They are small and draw little power. They have a narrow Schawlow-Townes (fundamental) linewidth, and in practice the linewidth is limited by noise in the power supply. Linewidths below 100 kHz are readily achievable,[189] enabling the isotope-induced spectral shifts to be resolved. The success of CD, DVD and more recently Bluray players have made certain wavelengths readily available very cheaply. The growth in fibre-optic communications has also led to the development of especially high performance diodes for the infra-red. There are, however, many wavelengths for which no diode exists. Frequency conversion gives access to other wavelengths. The 532 nm of green laser pens is the most common example of a frequency converted system, although recently diodes that emit green wavelengths directly have become commercially available. The availability of diode wavelengths is growing all the time as new markets develop. While custom wavelength diodes cost of the order 1 k€, the common wavelengths cost mere cents. The wavelength required in this instrument, 254 nm, can be obtained by frequency doubling 508 nm or quadrupling 1016 nm. Custom diodes at these wavelengths are available, and a ready built system with

frequency quadrupling would cost of the order $10^5 \, €$ to purchase ready built, which
was not within the budget of this project. The approach proposed here was to sum
together two diode lasers using a non-linear crystal. [183–185]

2.3.2 Frequency control

Frequency or wavelength control of the diodes is important to be able to distinguish
absorption due to Hg and broadband extinction from aerosols and gases such as
VOCs and O_3. Only a small shift is required to tune the wavelength off the Hg
absorption lines, but the shift must be achieved without large changes in the diodes'
performance.

Diodes can be tuned by three mechanisms: optical feedback and modulation of cur-
rent or temperature. Increasing the temperature expands the diode cavity, making
the resonant wavelengths longer. Increasing the current also increases the tempera-
ture but also increases the density of charge carriers, which decreases the refractive
index of the lasing material so that overall the wavelength increases. Feedback
of a particular wavelength into the diode from a reflection encourages lasing on
that wavelength. Of these three methods, current can be modulated the fastest
(MHz), but it also changes the output intensity. Temperature can be modulated
slowly (0.1 Hz) and has a small range, depending on the power of the temperature
controller and the limitations of the diode. Selective feedback can be achieved with
a grating and several configurations are possible. There are IR diodes available
which have a grating integrated into the diode itself (Distributed Bragg Reflector,
DBR, or Distributed FeedBack, DFB) which have very narrow and tunable emission,
but such diodes are only available for the IR.

An External Cavity Diode Laser (ECDL) has the grating positioned at some angle to
feedback a particular wavelength. The simplest design of ECDL uses a transmission
grating placed in the path of the laser emission. While the mechanics of this
design are simple, the grating must be custom-made since commercial gratings have
excessive losses. [190] The design was not considered further.

There are two common configurations of ECDLs. [191] The Littrow design is simple
but tuning the wavelength changes the direction of the output beam. The Littman-
Metcalf design has a fixed output direction but lower emitted power. A compromise
is to add a beam steering mirror to the Littrow design to convert the angle change
into a lateral shift. The choice of the grating pivot point is crucial for maximising the
Mode-Hop Free Tuning Range (MHFTR), so a design which uses three piezoelectric

actuators instead of a pivot was chosen to simplify the mechanics and maintain flexibility. This design has achieved a MHFTR of 100 GHz,[192] which is 5 times wider than the range of the isotope lines of Hg.

The wavelength was to be monitored with an etalon and a photodiode. The isotope lines of Hg are spread over 20 GHz, so a free spectral range double this would allow a continuous change in intensity over the scan, which would be simpler to deal with than counting the fringes produced by scanning through a narrowband etalon. Unfortunately a range of 40 GHz corresponds to a glass thickness of 25 mm, and over 50 mm for an air spaced etalon, which would cost several k€. A stock 15 GHz solid etalon (Light Machinery, Canada) was used instead and the wavelength could be monitored by counting fringes.[184]

2.3.3   Laser performance

Violet ECDL   No tunable sources could be found within budget, so the ECDL was constructed in-house. Laser diodes are sold for use in ECDLs. They usually include an anti-reflective coating to increase the MFHTR, although the effectiveness of this has been disputed.[193] A relatively inexpensive and powerful violet diode (120 mW, Roithner LaserTechnik) was mounted in a temperature controlled laser diode mount (laser diode starter set, Thorlabs). A grating (1200 lines/mm, 400 nm blaze) was mounted on an aluminium holder opposite a small beam steering mirror, placed in a 3-axis piezo controlled kinematic mount (Thorlabs). Figure 2.2 shows the ECDL in operation. A short focal length lens (f = 1.45 mm) was chosen in order to collimate the beam into a less elliptical profile.[194] The smaller lens was also curved instead of flat on the rear side, which would prevent another cavity forming between the diode and the lens. The lens was AR-coated for the violet region, but the shape was designed for 780 nm so the lens was slightly astigmatic at 408 nm. However, the lens was near impossible to focus by hand so was replaced with a larger one (f = 3.1 mm) for easier operation. The grating was aligned by placing a pinhole in front of the lens and adjusting the vertical axis until the tuning effect of horizontal movement was maximised (range of ≈ 2 nm), using a spectrograph (SR163, Andor) to see the changes in wavelength.

The modes of the ECDL were too closely spaced to be resolved by a normal grating spectrometer. To see the mode structure the beam was passed through a slit (100 μm) and lens (f = 100 mm) onto a grating (3600 lines/mm), from where the diffracted beam was projected onto fluorescent fabric at a distance of 9.3 m, to create an
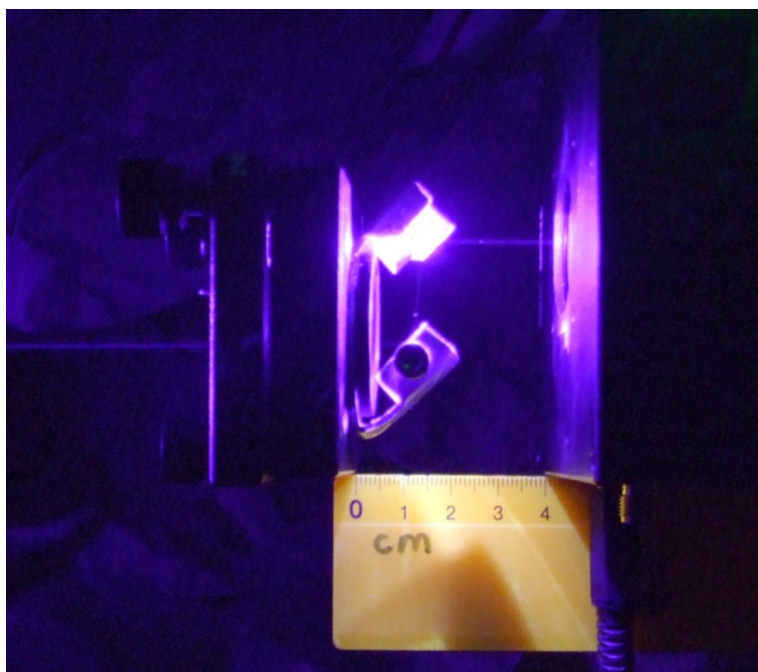
FIGURE 2.2: Photograph of the ECDL in operation. Laser diode is on right, grating and beam steering mirror in centre and tuned wavelength output on left.
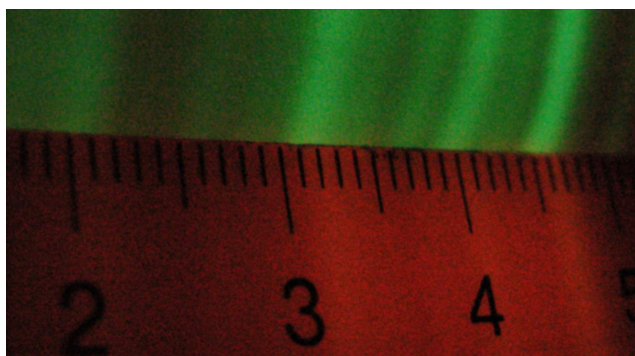
FIGURE 2.3: Highly dispersed modes of the ECDL projected onto a fluorescent screen. Contrast and brightness are adjusted to see modes more clearly. Scale in cm.

extremely high resolution spectrometer. The ECDL mode structure could be clearly seen (Figure 2.3), but attempts to derive quantitative results from this setup were unsuccessful.

A Bruker 70 Fourier Transform Spectrometer was used to obtain high resolution spectra ($0.7\,\text{cm}^{-1}$, $0.01\,\text{nm}$), with an acquisition time of $30\,\text{s}$ and Happ-Genzel apodisation to flatten the baseline. The temperature of the diode was set to $22\,°\text{C}$ for all spectra shown below.

The emission of the ECDL at high output power ($30\,\text{mW}$) is shown in Figure 2.4. It consists of about 16 narrow modes and not of the single mode required for efficient frequency conversion and spectroscopy. It was not known if all of these modes were
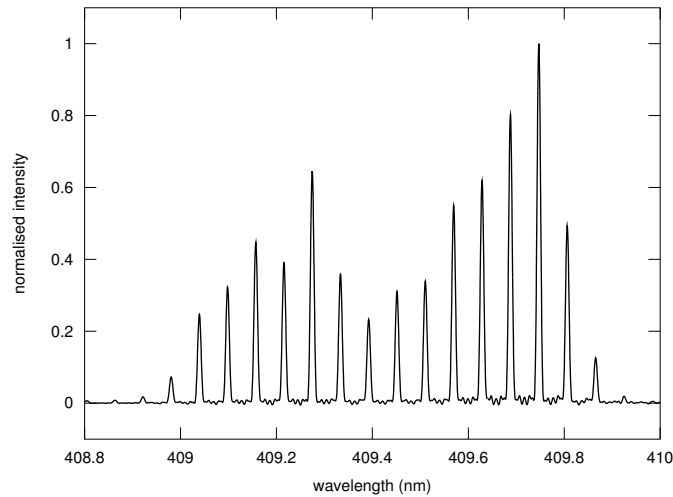
FIGURE 2.4: ECDL emission spectrum at 120 mA injection current and 30 mW output power, showing 16 dominant modes spread over 1 nm.
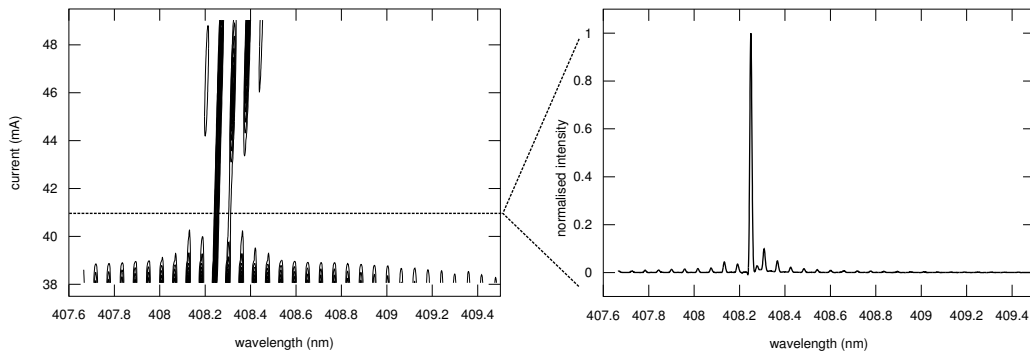
FIGURE 2.5: (a) Free running diode emission with no feedback grating or lens at different currents. (b) Diode emission at 41 mA, showing close to SLM operation.

active simultaneously, or if they were emitted in rapid succession following tiny fluctuations in the power supply.

To find the source of the modes, spectra were taken of the bare diode with no grating or collimating lens. The light was collected by a parabolic mirror about 30 cm from the diode and the metal bench was covered with black fabric to eliminate back reflections as even small reflective surfaces could cause feedback into the diode. Figure 2.5 shows how the emission spectrum of the free-running diode changed with current. At very low currents the diode has the broad emission of an LED, but when the lasing threshold is reached (41 mA) one mode dominates at 408.25 nm. The current range where one mode dominates is only 3 mA. Increasing the current further red-shifts the output and also stimulates more modes. At the maximum injection current of 120 mA, beyond the range of this plot, the spectrum was similar to that of the ECDL in Figure 2.4.
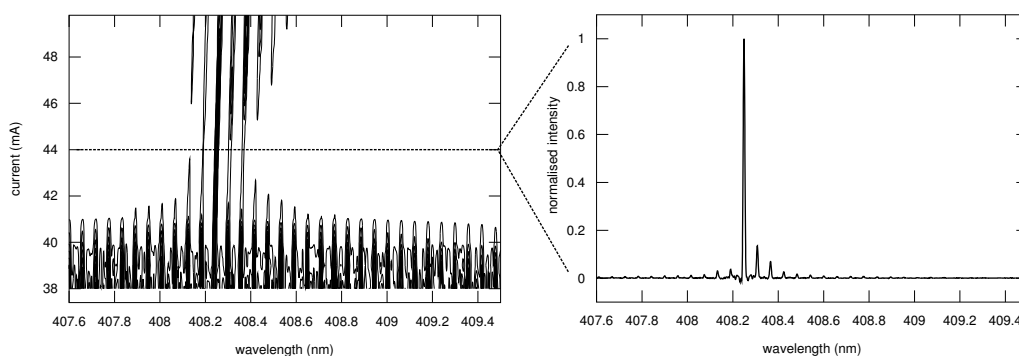
FIGURE 2.6: (a) Diode emission with a collimating lens at a range of currents. (b) Diode emission at 44 mA, showing close to SLM operation.

Positioning a collimating lens (f=3.1 mm, plano-aspheric) in front of the diode caused some feedback, and this changed the emission to that in Figure 2.6. The lasing threshold is higher at 44 mA, and the current range over which one mode dominates is even smaller (1 mA). Lancaster et al. [195] observed that the feedback from their lens encouraged single longitudinal mode (SLM) operation; this was not the case for our diode.

The ideal current for operation of the diode is at the point where it approaches SLM, as this gives the greatest wavelength selectivity. Spectra of the diode with grating-selected feedback (i.e. the ECDL in operation) could not be collected at such low currents in this setup because the output was too weak (8 μW). While it would have been possible to obtain spectra by rearranging the apparatus to collect more light, and possibly replacing the beamsplitter of the spectrometer with one designed for blue light, the spectrum at such low output is of little interest as it would be too low for the Hg monitor. No further effort was made to obtain SLM output of the ECDL.

Red DPSS   In place of a red diode (and a second ECDL, which would be too expensive) a 300 mW Diode-Pumped Solid-State (DPSS) laser (Roithner LaserTechnik) was tested. The red DPSS was intended to be a powerful fixed wavelength. The maximum power output was 350 mW at 671 nm. Unfortunately the power supply was highly unstable. Even after warming up for 4 hours it still flickered on and off. Figure 2.7 shows the output at full power and at slightly reduced power. The shift of wavelength is probably due to heating effects. It was also extremely sensitive to feedback, with significant changes in both longitudinal and transverse modes with tiny changes in reflections from apparatus or the optical bench. This laser was therefore unsuitable for use in atomic spectroscopy as it was too unstable.
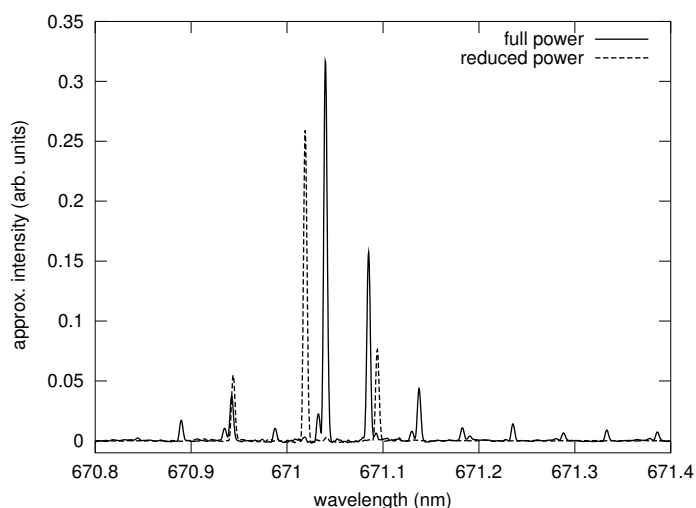
FIGURE 2.7: Emission spectrum of the red DPSS laser

2.3.4 Sum Frequency Generation

The Sum Frequency Generation (SFG) unit is the part that sums two different laser frequencies to get a third. SFG is always inefficient ($\approx 10^{-4}$ % at best)[185] so it is usually done inside a cavity designed such that light will not escape until it is converted. Such optical resonators are either expensive to buy or complex to engineer,[191] so one was not considered for this project. For SFG, two conditions must be satisfied:

Frequency matching: The generated frequency is always the sum of the two input frequencies. The output is self-adjusting, and it is this property that allows the sum frequency to be tuned by tuning one of the inputs.

Phase matching: The phases of all the waves must match over the length of the crystal. If the crystal is too long the phases become mismatched and the process operates in reverse, which reduces the intensity of the desired wavelength. Phase matching can be achieved by using the dependence of the crystal's refractive index on angle, wavelength and temperature. Either the angle or temperature can be altered to achieve phase-matching for the desired frequency. For this particular system only angle tuning has been used.

The optimum angles for β-Barium Borate (BBO) were calculated with the program SNLO.[196] To satisfy phase matching, the angle of propagation through the crystal must be 49.2° to the optical axis. Ideally, the faces of the crystal should be cut to the Brewster angle to minimise the reflection losses, but custom cut crystals cost on the

31

order of k∈. A stock crystal cut for 44.3° (Eksma Optics, Lithuania) was selected as it would have only a few percent reflection losses.

A misalignment of 0.01° is enough to reduce the SFG efficiency by half. When adjusting an optical mount this angle is equivalent to $^1/_{40}$ of a turn of a normal adjustment screw, or $^1/_3$ of an ultra-fine one. This angle tolerance must be satisfied in three rotation axes. The two input lasers must also have a precise angle between them since the non-oblique incident angle refracts them resulting in a poor interaction length. By using a thinner crystal ($6 \times 6 \times 1$ mm) the angle tolerances would be increased, but at the cost of lower conversion efficiency.

Despite the poor performance of the UV-ECDL and red-DPSS, several attempts were made to frequency-sum them to generate 254 nm. Initially a bare silicon diode (S130VC, Thorlabs) with a 254 nm bandpass filter (Schott) was used to detect the SFG emission. It had a large area and acceptance angle, which made it easy to align, but stray light was always too bright to detect the small 254 nm output. A spectrograph was then used as it would be only slightly less sensitive than the photodiode but much more specific. However the narrow acceptance angle and area of the slit required careful alignment to the expected location of the 254 nm output. Alignment of the crystal was attempted by bouncing another laser off the crystal and triangulating the spot with the source, but even at a spot distance of 5 m, the FWHM would still be less than 1 mm. Despite many attempts, no UV emission was detected. Given the poor quality of the diode lasers this was not surprising. The principle of building our own laser for Hg studies had to be abandoned. Since lasers were not feasible as a light source a low pressure Hg-Ne lamp was used instead.

2.4   Cavity Enhanced Absorption Spectroscopy

Absorption spectroscopy has long been a fundamental analytical tool and much effort has gone into increasing its sensitivity. Optical cavities are one such approach and have found recent application in the detection of trace gases.[197–199] An optical cavity is usually formed by two concave, opposing mirrors though other configurations such as triangles and bow ties are sometimes employed. Light is injected directly through the back of one mirror and the small proportion of light that penetrates into the cavity is trapped and reflected many times, with only the same small proportion of light leaking out of the cavity on each reflection. Due to the self focussing nature of a stable cavity and high reflectivities of dielectric mirrors, extremely long pathlength

enhancements of several thousand can be obtained. Compared to Herriott or White multipass cells,[200] optical cavities generally require smaller sample volumes and have longer potential pathlengths through the sample.

The first optical cavity technique was cavity ring-down spectroscopy (CRDS), in which a short laser pulse is injected into the cavity and the decay or ring-down of the light exiting the cavity is measured.[201] CRDS systems attain path lengths of the order of kilometres with a 1 m cavity, thus achieving very high sensitivity but at the cost of a complex setup.

A simpler method is to directly measure changes in the light intensity transmitted through the cavity, a technique variously known as cavity-enhanced absorption spectroscopy (CEAS),[202] integrated cavity-output spectroscopy (ICOS),[203,204] or Cavity-Enhanced Differential Optical Absorption Spectroscopy (CE-DOAS).[205,206] CEAS is the term used here.

Because the cavity mirrors are highly reflective at their operating wavelength, the light source must be bright enough to be detectable after penetrating the mirrors. Lasers are ideal for this, and a wide range of reliable, tunable and affordable diode lasers is available with output at visible and near-IR wavelengths. Using such near-IR lasers, CEAS systems have provided excellent selectivity and sensitivity to numerous small molecules, and devices for monitoring CH_4, CO_2, H_2O and other compounds are now commercially available. Certain instruments can also measure isotope ratios by detecting the slightly different absorptions of molecules containing different oxygen or carbon isotopes. Such instruments are fully competitive with isotope-ratio mass-spectrometry for measuring H_2O isotope ratios.[207] As yet, high power single mode diode lasers are not available below 300 nm in the deep-ultraviolet.

Although CRDS has been performed down to 197 nm,[208] and CEAS down to 308 nm,[209] the high power, non-linear, deep-UV laser systems are too costly and complex for widespread adoption. An unsuccessful effort to build such a system was described in Section 2.3.3.

Broadband light sources such as arc-lamps,[202] LEDs[210] and tungsten-halogen bulbs[211] have been used for trace gas detection, and supercontinuum sources[212,213] for analysis of liquid samples.[214] LEDs have also been used to measure fluxes by eddy-covariance,[215] the same objective as here but in the visible region. As low vapour pressure Hg lamps are known for their intense 253.7 nm emission line, these lamps also have potential as light sources for use with optical cavities.

CEAS model

When a beam is focussed through a mirror into an optical cavity most of the light is immediately reflected off the mirror and lost, but the portion that penetrates the mirror becomes trapped in the cavity. In an empty cavity formed by mirrors with a reflectivity of R, light will on average travel through the cavity $(1-R)^{-1}$ times. By solving an infinite series and assuming highly reflective mirrors with small losses, it can be shown that the intensity of light transmitted through the cavity in the presence (I) and in the absence (I_0) of a single absorbing species are related:

$$N = \left(\frac{I_0 - I}{I}\right)\left(\frac{1-R}{l\sigma}\right) \tag{2.1}$$

where l is the length of the cavity, N is the number density of molecules and σ is the absorption cross-section.[202] The enhancement factor—the increase in observed absorption over the single pass configuration—is defined for small absorptions as $E = (1-R)^{-1}$. Because the atomic line source is essentially monochromatic, only one value needs to be considered for all the wavelength dependent quantities. For the mirrors used here ($R = 0.98$), an enhancement factor of approximately 50 is expected. Equation 2.1 describes a linear relationship. This is accurate for small to quite large cavity extinctions, $I/I_0 \geq 0.1$, but after that the assumption of low loss per pass starts to break down, necessitating a more detailed analysis.[205]

2.4.1   Experimental

This section describes the development and evaluation of a CEAS setup at 254 nm, using an Hg lamp as the light source for the first time. Figure 2.8 shows a diagram of the setup. The output of a Hg-Ne pencil lamp (Oriel 6034) was focussed into an optical cavity formed by two dielectric mirrors (Laseroptik) separated by 252 mm. The cavity mirrors had a 200 mm radius-of-curvature and were approximately 98% reflective between 254 and 320 nm. These mirrors were housed in lens tubes held by mirror-mounts and sealed to the PTFE detection cell (i.d. = 33 mm, volume = 190 cm^3) with a thin rubber tube. In the first design (not shown) the light transmitted through the cavity was reflected off a 248 nm dielectric mirror into an SR-163 spectrograph with DV420 BU CCD camera (Andor). The camera was very sensitive, however the wavelength discrimination was not necessary for the setup. In the second setup in Figure 2.8 the output of the cavity was received directly by a magnetically shielded CsTe photomultiplier tube (Hamamatsu H10784 with a C9744
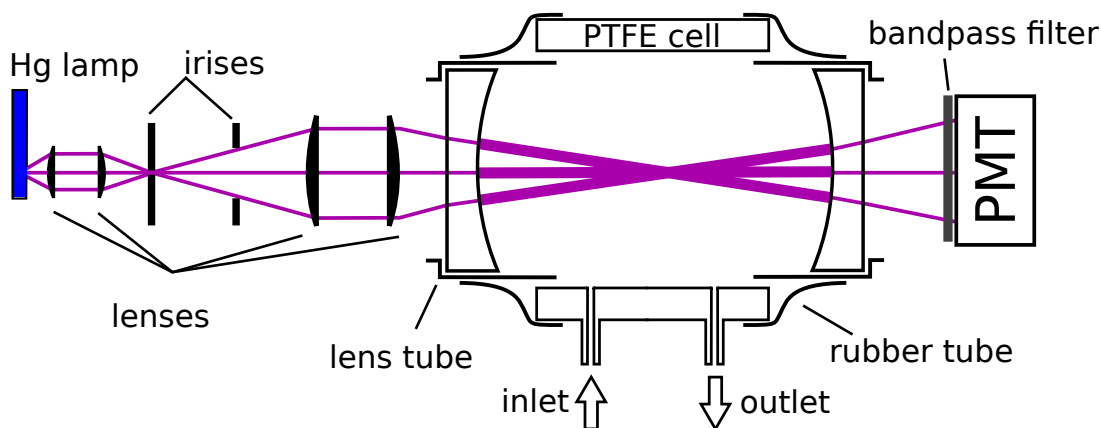
FIGURE 2.8: Diagram of the atomic line CEAS system

pulse discriminator unit). The counter was a DAQ board (Measurement Computing USB-1208HS-4AO) read with a LabVIEW program every 5 s, and averaged over 10 s in post-processing. Other atomic emission lines and out-of-band wavelengths were removed by a Schott 254 nm bandpass filter. The intensity was adjusted with irises to around $3{\times}10^6$ counts over the 5 second interval, including the 10-fold downscaling by the discriminator.

One of the problems of diode laser CEAS is that cavity mode-structure must be removed, usually through temporal averaging.[202,203] The free spectral range of the cavity here was 600 MHz, so the 253.7 nm Hg emission line would excite around 30 longitudinal cavity modes as well as numerous transverse modes. No evidence of mode structure was observed in our experiments. The system was stable to knocks and vibration, but a drift of a few percent was observed over several hours, probably due to changes in the lamp output. No attempt was made to correct for the drift in this study. Temperature and humidity were monitored with a Vaisala DM70 meter.

2.4.2 Results and Discussion

To compare the cavity-enhanced and the single-pass absorption directly, the cavity mirrors were replaced by fused silica windows and the intensity was attenuated to a similar value to that found with the cavity to avoid saturating the PMT. As shown in Figure 2.9, in the CEAS configuration a moderate Hg concentration of 140 ng m^{-3} (equivalent to a mixing ratio of 18 pptv under ambient conditions) produces a comparable absorption to that by a much higher Hg concentration of 7000 ng m^{-3} in the single-pass setup. In this example, the cavity increases the fractional intensity change by around 30–50 times without affecting the baseline noise.
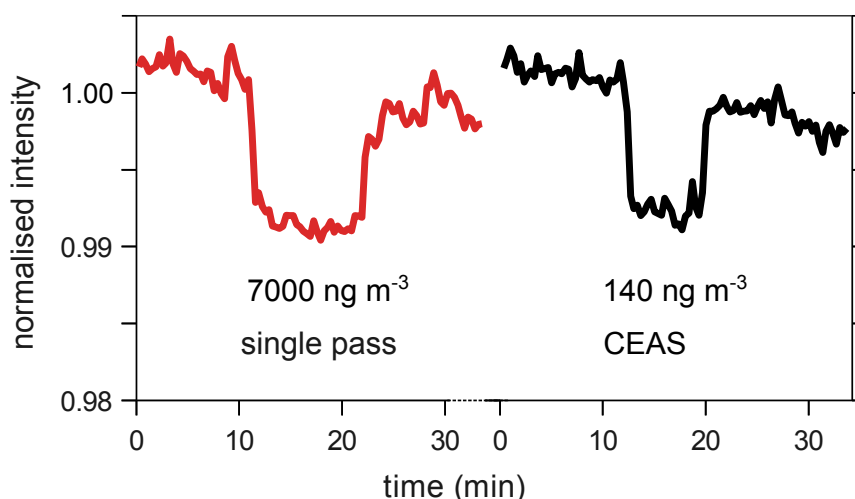
FIGURE 2.9: Comparison of the intensity changes arising from different concentrations of Hg in the single pass (red) and CEAS configurations (black).
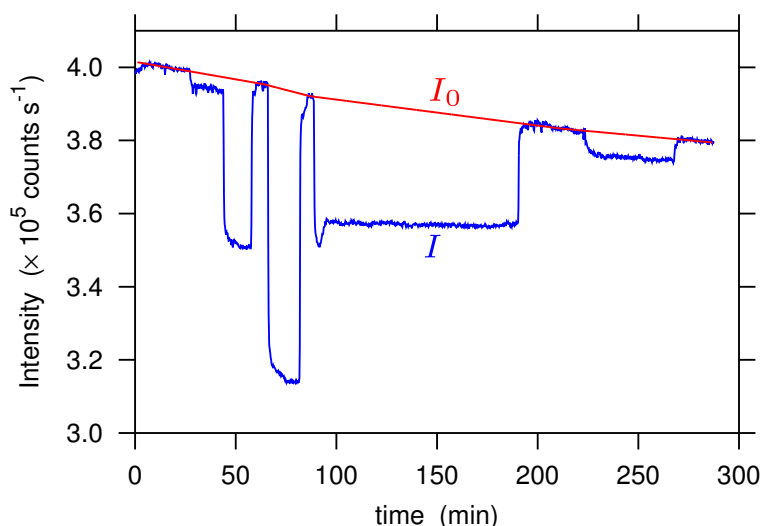
FIGURE 2.10: Time profile of the CEAS intensity at different O_3 concentrations. The estimated baseline, I_0, is shown in red.

Calibration curves were produced for both O_3 and Hg, to determine the enhancement factor more precisely. O_3 was introduced into a $2.2\,m^3$ atmospheric simulation chamber[216] with an Ozone Services O_3 generator. The chamber air was continuously extracted ($600\,cm^3\,min^{-1}$) to the CEAS cell and then to an O_3 monitor (2B Technologies model 202). We assumed that our cell was at atmospheric pressure. Figure 2.10 shows the intensity changes with varying concentrations of O_3 in the cell. At several points laboratory air was sampled through an O_3 scrubber to determine the baseline. The overall baseline, I_0, was estimated by linear interpolation and shows that the lamp output decreased by 5% over a period of 5 hours. The CEAS absorption rose linearly with the O_3 mixing ratio ($R^2 = 0.9995$, Figure 2.11). The slope of the
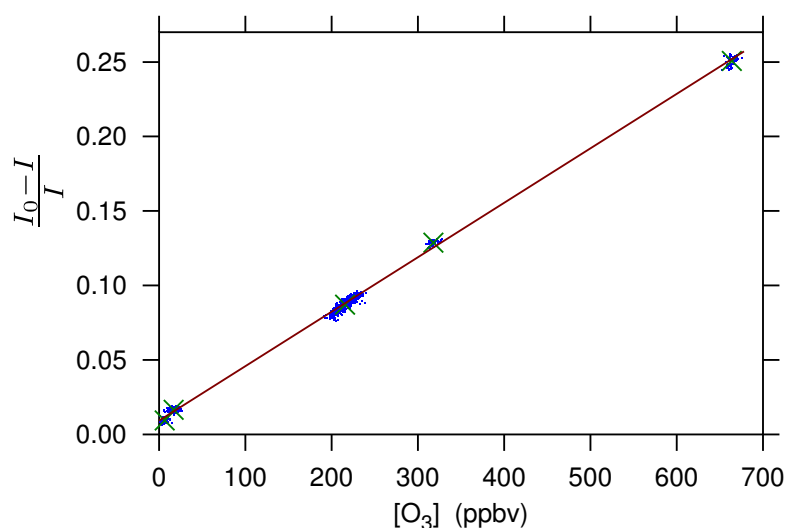
FIGURE 2.11: Calibration curve of CEAS absorption against O_3 in a flowing sample stream. O_3 concentrations were measured using the commercial monitor.

linear regression through the centroid of each concentration cluster is proportional to the product of the O_3 absorption cross-section ($1.15 \times 10^{-17}\,cm^2\,molecule^{-1}$ at $253.7\,nm$)[217] and the enhancement factor. For our cavity the slope gives an enhancement factor of 50.5 ± 0.6, corresponding to a mirror reflectivity of 0.9802 ± 0.0003 at a relative humidity of 38.6%. The small non-zero intercept arose because air for the baseline was taken from outside the chamber where the humidity was slightly higher (40.6%) than the O_3 source of the chamber. Water vapour adsorbed to the mirror coating reduces both the absorption and, to a lesser extent, the reflectivity of the mirror,[218] so that a change in humidity causes a change in cavity transmission. In the O_3 calibration the small difference resulted in the baseline signal (I_0) being too high. This is accounted for in the calibration as an offset equivalent to 25 ppb O_3. Drying the mirrors with a flow of dehumidified air (0.4% RH) reduced the signal by 12%, corresponding to about 360 ppb O_3. Practical applications will require either the mirrors to be kept dry by heating, purging with dry gas (already common in atmospheric applications)[197] or use of a different mirror coating.

The calibration curve for Hg vapour was obtained by injecting aliquots of between 2 and 200 μL of vapour from an Hg containing vessel (thermally equilibrated with the room and the gas-tight syringe) into the static volume ($190\,cm^3$) of the cavity. The Hg concentration was calculated from the Dumarey equation.[72] I and I_0 were estimated as previously. The relationship between the absorption and the concentration was again linear ($R^2 = 0.9993$, Figure 2.12). Radiation trapping and saturation effects by the Hg atoms were assumed to be negligible at the low concentrations and lamp intensities in these experiments, and no dependence of the absorption on the optical
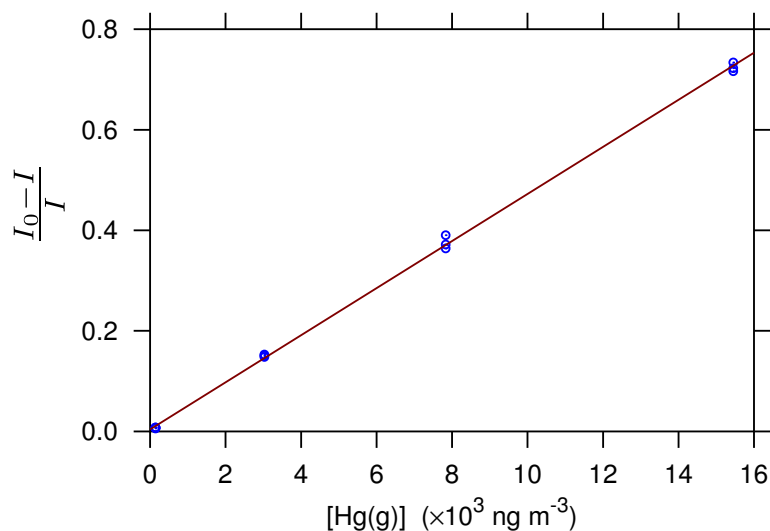
FIGURE 2.12: Calibration curve of CEAS absorption against Hg vapour in a static cell. Hg concentrations were obtained from injections of known volumes of saturated vapour.

power was observed.

Using the enhancement factor from the O_3 calibration (50.5) gives an Hg cross-section of $1.23 \times 10^{-14}\,cm^2\,molec^{-1}$. This value is instrumentally defined because it depends on the precise overlap of the emission profile of the lamp and the pressure-broadened and pressure-shifted absorption of Hg in the sample cell. Because an atomic line source has good overlap, the cross-section is at the upper end of the spread in literature values.[125,219] The detection limit for Hg in a single pass is $3300\,ng\,m^{-3}$ compared to $66\,ng\,m^{-3}$ in the cavity.

There are many improvements that could be made to the setup described here. Use of an electrodeless discharge lamp that is more stable than the pencil lamp used here would improve the signal-to-noise ratio. The minimum Allan deviation is only a third lower at the optimum averaging time of 1 minute (Figure 2.13), so there is little to be gained by longer averaging times.

An improvement could be gained by extending the cavity,[220] or using cavity mirrors of higher reflectivity. Both of these would reduce the light reaching the detector, but would still improve the detection limit as the system is still far from the shot-noise limit. Extremely high mirror reflectivities are probably not feasible in the deep-ultraviolet owing to increased scatter and absorption by the dielectric mirror coatings. The cavity mirrors in our system were fabricated using electron-beam evaporation coating because it produces coatings with lower scatter and absorption than alternative methods. These coatings are, however, porous and sensitive to humidity changes as illustrated above. Incorporating features such as alternative
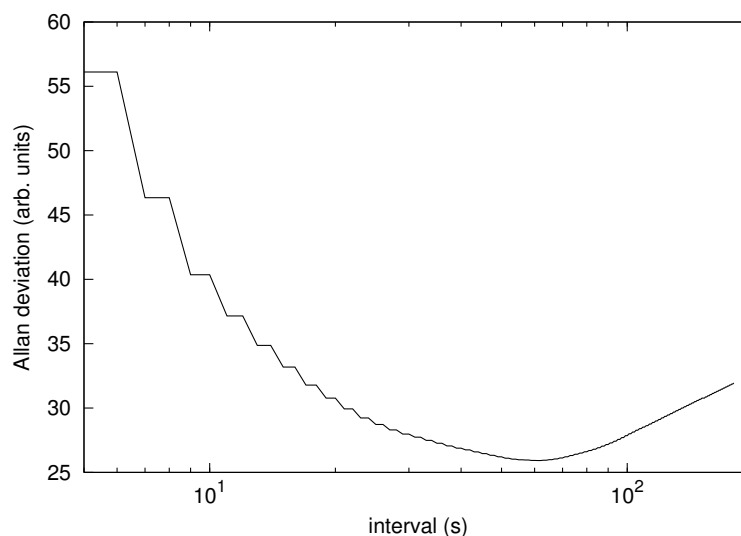
FIGURE 2.13: Overlapping Allan deviation of signal from PMT, calculated with the algorithm of Czerwinski et al.[3]

mirror coatings, or heated or gas-purged mirrors in the system design, would minimise the issue.

Although much better detection limit have been achieved with CRDS[128] or non-resonance fluorescence,[139] these systems require powerful pulsed lasers in complex setups. The CEAS detection limit is slightly better than some commercial single-pass optical absorption based devices for monitoring elevated Hg levels. Such commercial instruments use stabilised light sources and electronics, which our instrument does not. Nevertheless, our detection limit of $66\,\mathrm{ng\,m^{-3}}$ is better than the $0.1\,\mathrm{ppb}$ ($800\,\mathrm{ng\,m^{-3}}$) detection limit reported by Anderson et al.[184], using sum-frequency generation and two diode laser systems, or the $200\,\mathrm{ng\,m^{-3}}$ estimated by Thiebaud et al.[126] with a Hg vapour lamp combined with a UV LED.

2.4.3 Application to other gases

Further applications include O_3 monitoring, acetone in breath analysis and use as a non-specific detector in chromatography. Based on the smallest detectable change in signal (around 0.3% at 3σ, Figure 2.9), the estimated limits of detection to Hg, O_3 and several other compounds are presented in Table 2.1.

For O_3, the detection limits of the system are $420\,\mathrm{ppb}$ (single pass) against $8.4\,\mathrm{ppb}$ in the cavity. Commercial absorption instruments (such as our O_3 monitor, $\mathrm{LOD} = 3\,\mathrm{ppb}$, 2σ) already attain this level of sensitivity in a single-pass measurement. The dual beam version of the same monitor (model 205) attains a LOD better than $1\,\mathrm{ppb}$.

TABLE 2.1: Estimated LOD of our system to several species based on their absorption cross-sections at 254 nm, obtained via the MPI Spectral Database.[5]

Species	Cross-section ($cm^2\,molec^{-1}$)	LOD ppb	reference
Mercury	1.2×10^{-14}	0.0081	this work
Ozone	1.15×10^{-17}	8.4	Bogumil et al.[217]
Xylene	5.9×10^{-19}	160	Etzkorn et al.[221]
Toluene	3.9×10^{-19}	250	Etzkorn et al.[221]
Benzene	2×10^{-19}	350	Etzkorn et al.[221]
Acetone	3×10^{-20}	3300	Koch et al.[222]

Other applications include detectors for chromatography, for which both CRDS[223,224] and CEAS[225] have previously been proposed. Although this work has focussed on gases, the approach is also feasible for liquid samples. In this case, scattering by the liquid limits the performance, although useful enhancements are still possible.[214] These multiple applications of a single wavelength absorption measurement highlight the low specificity of the detector and the need to account for confounding absorptions. Existing strategies for Hg include pre-concentrating the target analyte, or selectively removing interferents with filters. Background extinction can be quantified and accounted for by measurement at another wavelength as in Zeeman corrected AAS, or by broadband measurement with a deuterium lamp or UV LED.[126]

2.4.4 Summary

In summary, this section demonstrated that CEAS is feasible with an atomic line source and greatly improves the absorption sensitivity over a single-pass configurations. The low vapour pressure Hg lamp allowed us to extend the approach into the deep-ultraviolet without requiring a complex laser system. The deep-UV wavelength region is particularly attractive for a number of compounds of environmental, analytical, and medical importance. The same approach is feasible with other atomic line sources, such as sodium vapour lamps and hollow cathode lamps, although alternative light sources should have a high radiance to offset the large losses to the optical cavity. As our results with Hg demonstrate, the combination of an atomic line source with an optical cavity is useful for elemental analysis and may have potential to enhance the sensitivity of atomic absorption spectroscopy. Further improvements to the cavity sensitivity are possible, although some care is necessary to maintain a stable mirror reflectivity. Owing to poorer mirror reflectivities and larger Rayleigh scattering losses in the UV, the sensitivity of this approach will never

match the sensitivities of optical cavities at longer wavelengths. Nonetheless, this work demonstrates a practical approach to exploit the large absorption enhancement of such cavities in the deep-UV.

2.5   Conclusions

In this chapter the existing methods for Hg detection were reviewed, and a new CEAS Hg sensor described. The laser light source was based on frequency summing of two diode lasers to generate 254 nm light. Laser emission at 254 nm was not achieved due to lack of equipment and other resources. Instead an Hg-Ne pencil lamp was used as the light source. This was the first known example of an atomic line source used in a CEAS system. Ultimately the performance of the instrument was not good enough for use in subsequent Hg experiments, either in the lab or in the field. In the following chapters, experiments will be carried out using the CRDS system of Pierce et al.[128]

Chapter 3

Chamber setup for study of mercury oxidation kinetics

In the second part of this work, the potential reactions that cause $Hg^0(g)$ oxidation and depletion were investigated in a simulation chamber. As the sensitivity and specificity of the Hg detector described in Chapter 2 were inadequate for this work, we used instead the existing Hg CRDS system in the Desert Research Institute, Reno, Nevada, USA.[125,128] The laser had already been used for eddy covariance studies,[172] so the objective was to measure the reaction rate with various species of interest, primarily Br_2. This chapter will describe the chamber setup and characterisation.

3.1   Introduction

Simulation chambers play a vital role in atmospheric research. The trace species in a gas are so dilute that a large volume is often required to be able to detect them. Many of these species are reactive intermediates and have a high affinity for surfaces, which also means chambers have to be large. The use of high-volume 'fumigation' chambers began in the 1950s as photochemical smog became a major concern for human and crop health.[226] Previous smog epidemics, such as the London 'pea-soupers', were caused mainly by particulates (smoke) and SO_2 formed directly from combustion of coal. The source was easy to identify. The photochemical smog of Los Angeles involved more complex gas-phase chemistry with many variables such as sunlight, Volatile Organic Compound (VOC) emissions, NO_x, O_3, and only controlled studies in simulation chambers could separate them.[227,228]

Chambers vary widely in size, temperature, pressure, instrumentation, material and illumination. The structural material can be stainless-steel,[229] aluminium[230,231] or glass[232] with or without[233] an inert fluoropolymer lining. Such inert linings are used to reduce surface reactions, but can also contribute to the VOC content of the chamber. Fluoropolymer lined chambers will always have a VOC content of a few ppb due to outgassing.[234]

When pressure variation is not required, the usual design is a fluoropolymer bag suspended from a metal frame. Fluorinated ethylene propylene (FEP) is the standard choice as its melting point (260 °C) is much lower than that of PTFE (327 °C), or PFA (306 °C) making it much easier to weld the panels together. This construction is especially suited to very large chambers[235,236] and it also allows the chamber to contract without any pressure change when gas is extracted for analysis.[237]

Cooling and heating systems can control the temperature inside the chamber. Illumination in very large outdoor chambers is usually provided by the sun. Fluorescent strip lights, both UV and white, are common, and large arc-lamps are also used.[216] Heating effects from the lighting can require a separate cooling system.[238] The instrumentation can be either extractive or *in situ*. Extractive analysis is only suitable in large chambers to avoid excessive dilution losses.

There exists a scheme to share the use of large simulation chambers (Eurochamp) as there is for laser facilities (LaserLab Europe). This project however depended on the existing laser system at the DRI in Reno, USA so a new chamber was designed and built for the available laboratory space there. Also, the hazards of Hg mean that it is safer to use on a small scale.

3.1.1   Mercury Chamber Studies

The chambers or vessels thus far used for Hg kinetics have had volumes between 0.65 L and 17 m^3.[159,239] The volume range is large and reflects the fact that $Hg^0(g)$ does not have high wall losses so can be studied in small reactors. The atmospheric concentrations of Hg however, are some of the lowest of any commonly measured species, so most studies of Hg chemistry have used an [Hg] well above ambient levels to make detection simpler. The high concentration of the saturated vapour is easily detectable, as even at room temperature the vapour pressure of Hg is 10^7 times higher than the natural background. The dominant reactions at very high concentrations can differ from those in the environment, so it is important to study the reactions in conditions comparable to those the derived rates are to be employed
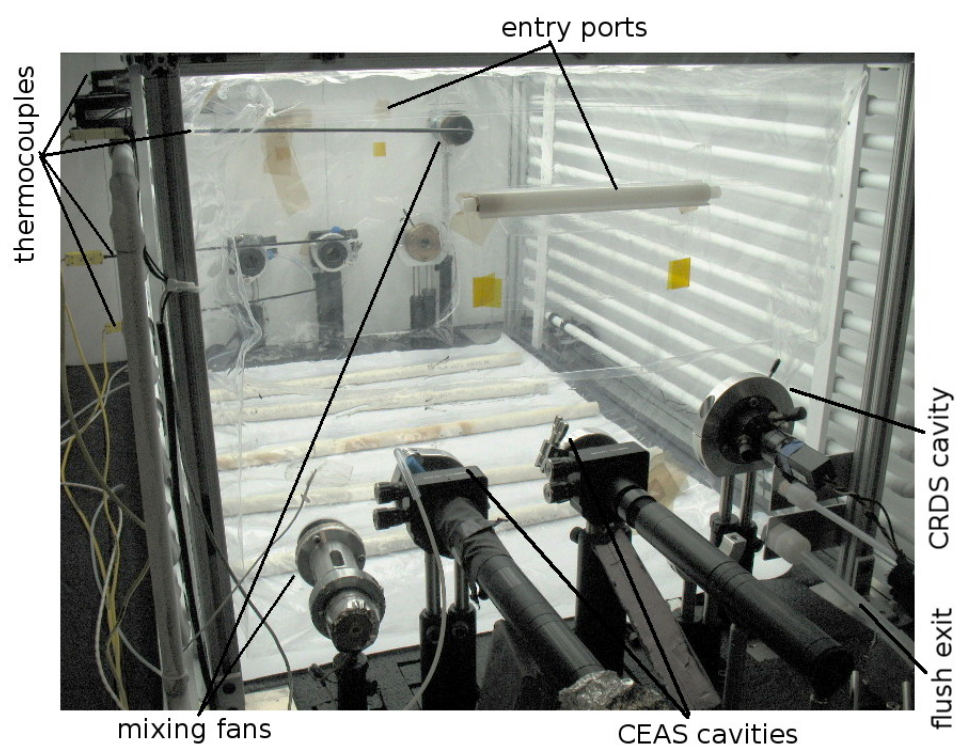
FIGURE 3.1: Photograph of the chamber with two walls removed

in. The chamber size here was chosen due to constraints of the laser setup and
available space.

3.2   Chamber Description

The chamber was a $0.5 \times 0.6 \times 1$ m FEP ($0.127\,\mu$m thickness) rectangular box
(Ingeniven, Hampton, NH, USA) suspended from an aluminium frame placed on an
optical bench. Figure 3.1 is a photograph of the chamber with two walls removed
and the illumination on. On top of the frame was a bank of four 40 W fluorescent
white strip lights (spectrum shown later in Figure 3.22), insulated from the chamber
by a single thin sheet of film to keep the cool air inside. Light was excluded from
the chamber by a shutter made from cardboard and black cloth. The walls of the
chamber comprised 50 mm thick polyurethane foam, spray painted on the inside
with white latex paint. The volume of the chamber was $0.3\,\text{m}^3$ with a surface area
of $2.8\,\text{m}^2$. Mixing was provided by two fans powered by two 12 V batteries either in
series or in parallel, allowing control over mixing time (typically 30 s). On either
side of the chamber were copper cooling coils. Copper absorbs blue light strongly,
so to maintain an even photolysis flux across the chamber the cooling pipes were
coated with a highly reflective polyurethane-based coating (Avian Technologies,

Table 3.1: Chamber Instrumentation. See text for more details.

Measurement	Instrument
[Hg]	CRDS at 254 nm
	Tekran 2537
[Br$_2$]	IBBCEAS at 365 and 440 nm
Temperature	3 internal PTFE coated K-type thermocouples,
	1 between bag and insulation
Light intensity	Thorlabs PM100/S130VC photodiode
[O$_3$]	2B Technologies 205
[NO], [NO$_2$]	Horiba APNA-360 NO$_x$ monitor

Sunapee, NH, USA). This coating was chosen as it would be more resistant to condensation than most water based paints, and would better tolerate thermal cycling. Four small brushless fans circulated the cooled air between the chamber and the insulation. Underneath the chamber was 12 mm insulation on the metal optical table covered with white paper and several pipes to aid air circulation. The chamber instrumentation is summarised in Table 3.1.

The only non-commercial components are the IBBCEAS system, described below in Section 3.3, and the CRDS system described elsewhere.[125,128] Briefly, the CRDS laser consisted of a Q-switched Nd:YAG (5 ns pulses, 50 Hz) which pumped a dye laser, the output of which was frequency doubled to 254 nm. The output was sequentially tuned on and off the absorption of Hg using a cell containing ^{200}Hg as a reference. The cavity was 1 m long and used 99.895% reflective mirrors. The cavity ring-downs were recorded with a PMT and data acquisition board and fitted with an exponential decay. The resulting [Hg] were then averaged to a 1 s time resolution.

3.2.1   Chamber cooling

The temperature control of the chamber was provided by a Neslab ULT-95 re-circulator, capable of 1650 W of heating and 350 W of cooling. The coolant was a potassium acetate based airfield de-icing mixture, which was rated to work down to −70 °C. This fluid was pumped via a well-insulated hose to the cooling coils around the chamber. An external PTR thermistor was attached to the chamber wall to provide PID control of temperature. In practice, the chiller was not used for room temperature studies to avoid the extra heating of the room air. The cooling coils could go down to 250 K, but the coldest temperature achieved inside the chamber was 265 K. The lower limit was due to heat flow into the chamber through the thin
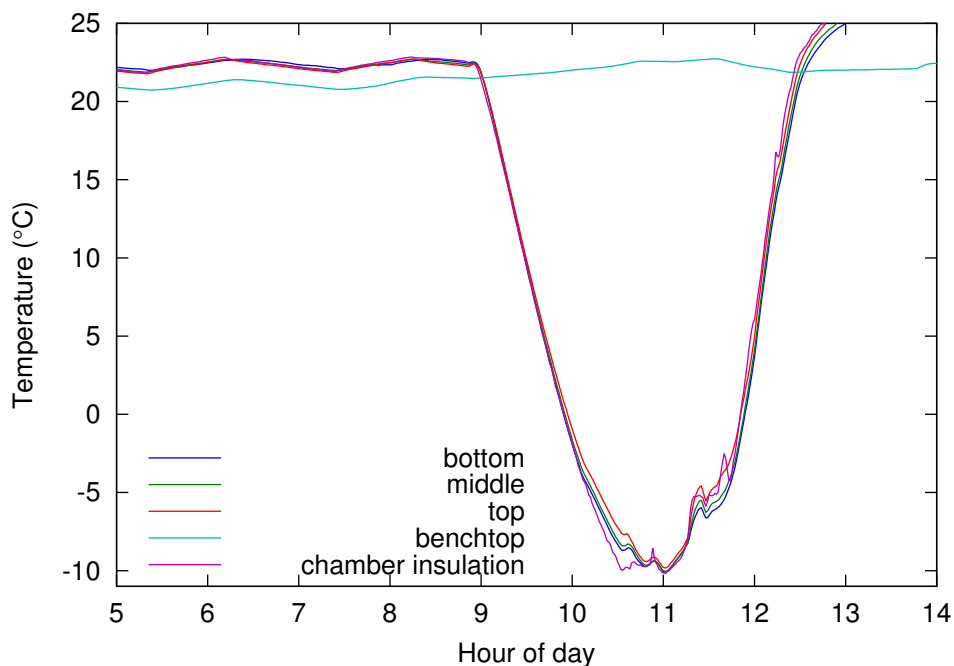
FIGURE 3.2: Typical temperature profiles of a cooled experiment. The slight 1 °C oscillation at the start is due to the building HVAC. The cyan line of the benchtop temperature warms slightly when the cooler is switched on at 0900, but the chamber temperatures go rapidly to −10 °C. The chamber is illuminated at 1110 and the cooling switched off at 1130 once the reaction had finished.

plastic window and shutter on top, the metal table underneath, and leaks between panels. Due to the very low ambient humidity during winter in Reno (dew point of -10 °C, RH 5%), icing on pipes or optics was not a problem except during one period of stormy weather when the dew point rose above 0 °C. External purge lines to keep the optics ice-free were therefore not necessary even at 265 K. During experiments the temperature was homogeneous between all three probes inside the chamber and the one between the insulation and FEP wall (Figure 3.2). The chamber typically took 1 hour to cool down, but at the coldest temperatures the temperature could not be maintained for longer than 1.5 hours, due to thickening of the cooling fluid causing pipe blockage.

3.2.2 Volume determination and flush rate

The volume of the chamber must be known to calculate concentrations of introduced species, and to estimate the time required to flush them out of the chamber even when the species cannot be measured. The geometrical volume of the chamber, found by measuring its dimensions and assuming a rectangular box shape, was
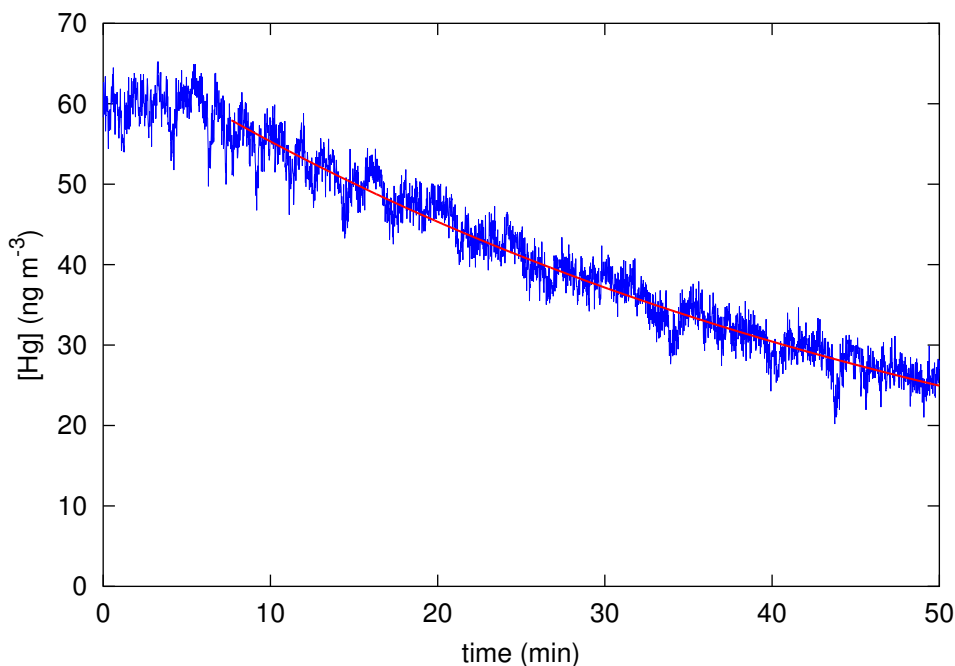
FIGURE 3.3: Decay of [Hg] in the chamber while flushing at a rate of 6.7 L/min. Red line is a best fit exponential decay.

297 ± 8 L. The flexible walls of the chamber could easily inflate, so a more accurate figure was obtained by measuring the loss rate of a stable gaseous species when flushing with a known flow rate. This measurement gives the volume at the inflated state, which is more relevant to the experiments. The flush rate was measured with a BIOS Definer 220 flow meter (MesaLabs). In a well mixed box with a constant flush rate the drop in concentration of a species, in this case Hg, follows a first order decay:

$$-\frac{d[Hg]}{dt} = \frac{f[Hg]}{V}$$
$$\ln[Hg]_t = \ln[Hg]_0 - \frac{f}{V} \cdot t$$

where the flow, f, is in L/min and V is the chamber volume in L. A plot of $\ln[Hg]_t$ against t gives a straight line with a gradient equal to $-f/v$.

Figure 3.3 shows the decay of [Hg] when the chamber is flushed at a rate of 6.7 L/min. The red line is the result of a linear best fit, replotted on the linear axes. The value of the gradient yields an inflated volume of 330 ± 10 L (2σ). This is 30 L more than the planar-sided rectangular box, which is expected due to the slight positive pressure in the chamber during the flush. Because the chamber could likely deflate as much as inflate with no change in pressure, a volume of around 60 L could be removed

from a newly flushed chamber without stressing the chamber and affecting optical alignment. At the flush rate from the Tekran zero-air generator, the half-life of a gas in the chamber was 34 minutes. With the faster flush from tanks of UltraZero air the half-life was 15 minutes, so to dilute the concentration of any species not present in the UltraZero air by a factor of 1000 would take 2.5 hours, neglecting any off-gassing from the walls.

3.2.3   Mixing time

The mixing time was determined by injection of Hg vapour. After some oscillation a steady state of Hg vapour was reached within 20 to 30 s. In experiments with the fans off or very slow, the mixing time increased to two minutes. The brush noise of the mixing fan motors interfered strongly with the laser wavelength locking system. To alleviate the interference extra metal shielding was installed around the fans and they were powered from batteries. The voltage applied to the fan closest to the laser was reduced to 12 V while the fan more distant to the laser was powered with 24 V.

3.2.4   Wall Losses

The loss of reactive gases to the walls of a chamber is unavoidable inside a simulation chamber. These wall losses must be well characterised. The larger the chamber, the smaller the surface-to-volume ratio. The use of inert fluoropolymer materials reduces the wall loss to a minimum. Care was taken to cover almost every internal surface of the chamber with PTFE, PFA or FEP. The chamber walls were FEP, the thermocouples and fan blades were purchased with PTFE coatings, the gas fittings were PFA, and any exposed metal was coated with PTFE adhesive tape. The only non-fluoropolymer surface were the CEAS and CRDS mirrors and the internal metal wall that the mirrors were in contact with. Purging of the mirrors could have eliminated even these as a reactive site, but this was not done to prevent dilution of the chamber contents and turbulence effects in the cavities.

The mechanism of wall loss is best explained by a reaction with a homogeneous surface yielding a non-volatile product. The kinetics are assumed to be first order in the depositing species, and that the supply of reactive surface is unlimited.[240] This means that if losses are seen to be negligible for a high concentration, they will also be negligible for a low concentration. If, however, the wall loss depended on a specific type of defect on the FEP surface (e.g. some porous structure), the
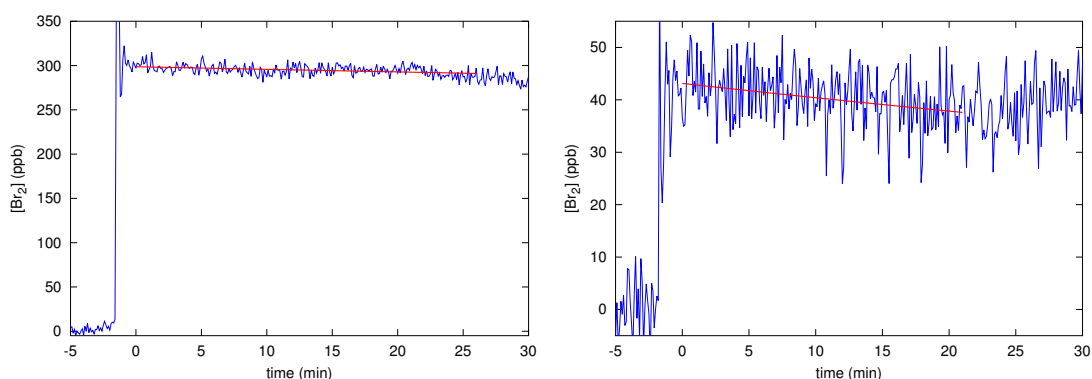
FIGURE 3.4: Decay of $[Br_2]$ due to wall loss at (a) $-8\,°C$ and (b) $-7\,°C$ at a large (300 ppb) and small (45 ppb) initial $[Br_2]$. Losses (red line) are 1.6 and $11\times10^{-5}\,s^{-1}$ respectively. The chamber is illuminated at the end of the red line.

rate could then be limited by the number of those defects present instead of the concentration of the depositing species. Such zero-order kinetics would lead to high losses at low concentrations, whereas at high concentration all the reactive sites would be occupied and the wall loss would be negligible. This consideration is relevant for the chamber as the $[Br_2]$ measurements were very uncertain, and at low concentrations the signal was so unstable that the wall loss could not be measured. However, the wall loss rate at mid and high-$[Br_2]$ (45 and 300 ppb) were the same, so it is assumed that first order kinetics predominates and the rate was also the same at the lowest $[Br_2]$.

Br_2 wall loss Br_2 was used in large excess in all the experiments, meaning that its concentration was not expected to change significantly during the reaction. Large Br_2 wall losses could violate the steady-state assumption used in the kinetic analysis. If the actual $[Br_2]$ were lower at the end of the reaction than the beginning, there could exist a systematic bias to slower rates for the presumed $[Br_2]$.

The wall loss shown in Figure 3.4(a) shows a rate of $1.6\times10^{-5}\,s^{-1}$, which translates to a decay of less than 2% over a 15 minute decay. The concentration here is quite large ($6\times10^{12}\,molec\,cm^{-3}$, 300 ppb), and it could be supposed if there were reactive sites on the surface they become saturated very quickly. If all the Br_2 in the chamber were to deposit to the surface, it would take a $[Br_2]$ of several ppm to form a monolayer over the walls. In the second example in Figure 3.4(b), starting at 45 ppb, the wall loss is higher at $11\times10^{-5}\,s^{-1}$, corresponding to a 15 minute decay of 10%. This is large enough to weaken the steady state assumption used in the kinetic analysis, but due to the large uncertainty associated with these low $[Br_2]$ the effect on the derived rate would be minimal. At the beginning of the measurement

49
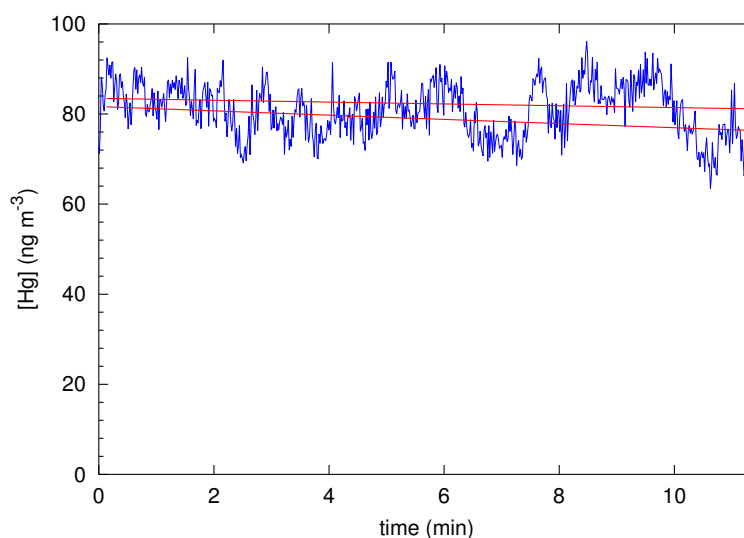
FIGURE 3.5: Decay of [Hg] in the chamber at $-7\,°C$ from wall losses. Red lines are the 95% confidence limits for the gradient and intercept of the fit to the $\ln[\mathrm{Hg}]$, yielding wall losses of 7.0×10^{-5} and $4.1 \times 10^{-5}\,\mathrm{s}^{-1}$.

campaign the retrieved $[\mathrm{Br}_2]$ were so noisy that no wall loss could be measured. As a result it is not clear whether there was any change in the wall loss rate as the chamber became increasingly contaminated.

Hg wall loss Elemental Hg is unreactive and was present in concentrations less than 10^{-5} of its vapour pressure. It should have negligible wall losses and experiments confirmed this. The losses that were observed were probably caused by reaction with residual Br_2 or $\mathrm{NO_x}$ adsorbed to the chamber walls. The [Hg] was so far below its vapour pressure that cooler temperatures were not expected to increase the wall loss, and this too was confirmed. Figure 3.5 shows the wall loss of Hg at $-7\,°C$. The red lines are the 95% confidence limits for the gradient and intercept of the fit to $\ln[\mathrm{Hg}]$, replotted on linear axes. The wall loss rates corresponding to these lines are 7.0×10^{-5} and $4.1 \times 10^{-5}\,\mathrm{s}^{-1}$, equivalent to an Hg lifetime in the chamber of between 170 to 400 minutes. The slowest reactions with $\mathrm{Br}^{\cdot}$ had Hg lifetimes at least 10 times shorter, so the direct loss of Hg to the walls was an insignificant source of error in the derived reaction rate.

3.2.5 Reagent introduction

Hg Typically, 2.5 mL of saturated Hg vapour was taken from a Tekran 2505 vapour unit set to $19.0\,°C$ with a glass syringe, PTFE plunger and metal needle (Hamilton).

The reservoir temperature was set a few degrees below room temperature to avoid condensation and volume contraction effects.[241] The resulting [Hg] in the chamber were close to $100 \, \mathrm{ng \, m^{-3}}$ ($3 \times 10^8 \, \mathrm{atoms \, cm^{-3}}$ or 15 ppt) which is 50 times the typical ambient concentration. The injections were not always quantitative, but mostly achieved at least 70% of the expected [Hg]. All Hg injections were carried out by Ashley Pierce.

NO$_\mathrm{x}$ NO$_2$ or NO were introduced by filling a 3 L polythene bag with bottled gas at an [NO$_2$] or [NO] in N$_2$ of $\approx$5 ppm. The filled bag was then emptied into the chamber. The flexible walls of the chamber could accommodate the extra gas without any pressure increase.

Br$_2$ injection   Liquid Br$_2$ (Alfa-Aesar) was stored in a FEP bottle with a PFA gas-tight fitting and septum attached to the lid. The bottle was initially stored in a water bath at a temperature slightly below ambient temperature underneath the chamber. After it became clear that the temperature control did not improve the repeatability of the injections the Br$_2$ vessel was kept in a fume hood at ambient temperature. The Br$_2$ vapour in the bottle was injected into the chamber by syringe, using three different techniques.

The initial method was a glass syringe with a metal needle, used to inject vapour volumes of 25 to 50 μL at a time. This method had extremely poor repeatability, with the resulting [Br$_2$] in the chamber varying from 0 to 30% of the expected concentration. Smaller volumes were especially variable. When the chamber was cooled this method did not inject any detectable Br$_2$ at all, presumably due to condensation inside the metal needle as it was inserted into the chamber. To achieve smaller concentrations a more reliable method had to be used.

The second method was to dilute liquid Br$_2$ in water and evaporate a portion into the chamber in a stream of hot air. This method was ineffective as the Br$_2$ did not reform from its dissolved state of HOBr and HBr. HOBr absorbs strongly at 254 nm and was easily detected by the Hg CRD system. Interestingly, no fast reaction was observed between the HOBr or HBr and Hg, but this experiment was only attempted once. Organic solvents could have been used in place of water but not tested due to fears of side reactions between the solvent and Br˙, HO˙ or photosensitised Hg present in the chamber.[242] These reactions would be particularly problematic at the low [Br$_2$] for which these experiments were intended, where the Hg lifetime would be long and side reactions more influential.

The third and most successful method was to use a 5 mL plastic syringe with internal surfaces coated with adhesive PTFE tape. Rather than inject with a metal needle, the syringe was emptied directly into the end of a short FEP line and then blown into the chamber with UltraZero air. As the syringe could only measure large volumes, dilutions were made by drawing 1 mL vapour, then aspirating and purging the syringe with ambient air repeatedly to reach effective $Br_2(g)$ volumes of 20 μL. This dilution would inject 1 mL of lab air into the chamber—containing up to 20 ppb NO_2—but as the sample is diluted in the chamber by a factor of $3{\times}10^5$, it would not add significantly to the lab air contaminants already present. This method gave $[Br_2]$ of 50 to 90% of those expected.

Amylene   2-Methyl-2-butene (Acros Organics) (99+%, boiling point 39 °C) was injected with a glass syringe into a stream of hot lab air from a heat gun directed into the chamber via a small glass fitting.

Ozone   Ozone was produced from a custom made ozone generator (based on UV photolysis of O_2) with a source gas of UltraZero air. No detectable NO_x was produced from this generator.

3.3   Cavity Enhanced Absorption Spectrometers

Incoherent Broadband Cavity Enhanced Absorption Spectroscopy (IBB-CEAS) is a type of extinction spectroscopy commonly used in trace gas studies. It was described in Section 2.4. Briefly, the CEAS model is

$$\frac{\boldsymbol{I_0}-\boldsymbol{I}}{\boldsymbol{I}} = N\boldsymbol{\sigma}l\boldsymbol{E} \tag{3.1}$$

where $\boldsymbol{I}$ and $\boldsymbol{I_0}$ are the cavity output spectra in the presence and absence of the analyte respectively, N is the number density of molecules, l is the length of the cavity, $\boldsymbol{\sigma}$ is the absorption cross-section, and $\boldsymbol{E}$ is the enhancement factor.[202] The chamber had two CEAS cavities monitoring the absorption in the blue and UV, and one CRDS cavity at 254 nm. The CRDS system was operated and maintained by Ashley Pierce and is described elsewhere.[128] The optical setup is shown in Figure 3.6. The two CEAS systems were coupled into the ends of a pigtailed fibre so they could be read with the same spectrometer. The blue and UV cavities were intended to provide complementary measurements, however the blue cavity was soon disabled
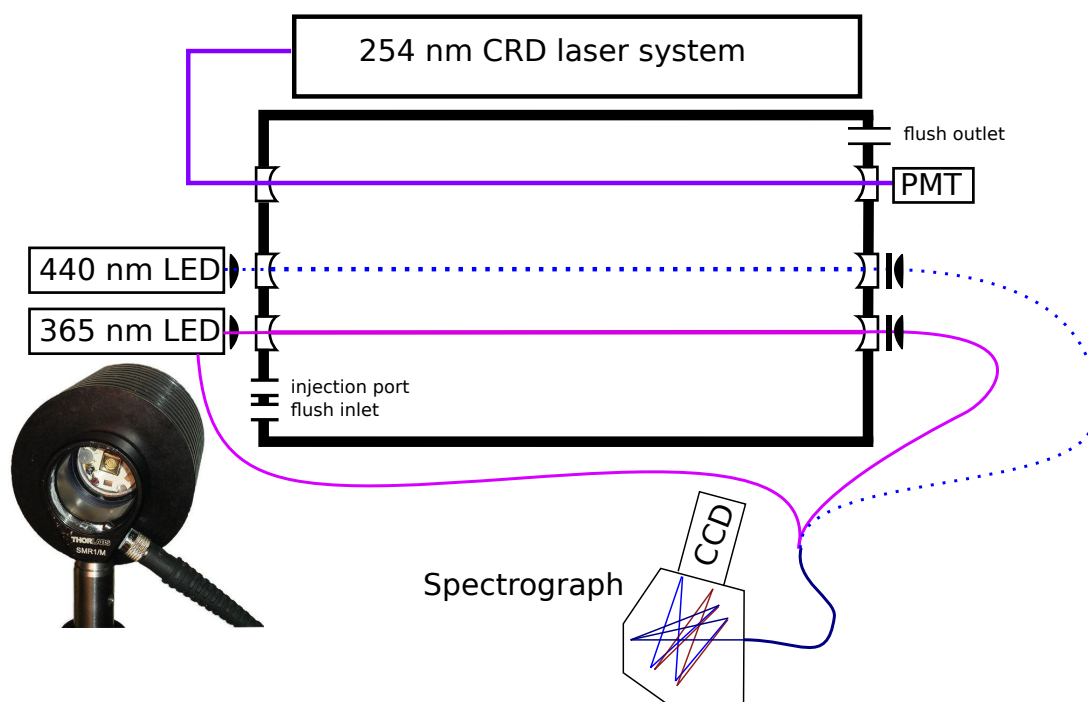
FIGURE 3.6: Diagram of optical cavities spanning the length of the chamber. The blue cavity shown with a dotted line was not used for most of the experiments. Instead the fibre was attached to the UV LED directly to provide a reference. A photograph of the attachment is inset.

in order to provide a separate baseline channel for the UV cavity. The older routing is shown with a dashed line.

The UV cavity used to measure $[Br_2]$ comprised a 365 nm LED (250 mW, Roithner LaserTechnik), powered by an LED driver (LEDD-1B, Thorlabs) focussed by an uncoated fused silica lens (f = 75 mm) into a cavity formed by two highly reflective curved mirrors (360–380 nm, reflectivity = 99.75%, radius of curvature (r) = 2 m, Layertec 109048), the output of which was filtered with a bandpass filter (357 ± 44 nm, Semrock) and focussed (uncoated fused silica lens, f = 100 mm) into one end of a pigtailed fibre (Andor) and into a spectrograph (Andor SR-163 with 600 lines/mm grating (500 nm blaze) with DV420-BU2 CCD camera). The blue cavity comprised a 435 nm LED (380 mW, Roithner LaserTechnik), powered by an LED driver (LEDD-1, Thorlabs), focussed by a coated BK7 lens (f = 75 mm) into a cavity formed by two mirrors (440 nm, R = 99.80%, r = 2 m, Layertec 107426), the output of which was filtered with a bandpass filter (440 ± 40 nm, Semrock) and focussed (coated BK7 lens, f = 100 mm) into the other pigtail of the fibre. The two fibre groups were arranged at the output in a line, acting as a 100 μm slit and enabling their images to be separated on the camera sensor.

A common problem with broadband cavities is that the light source is often wider
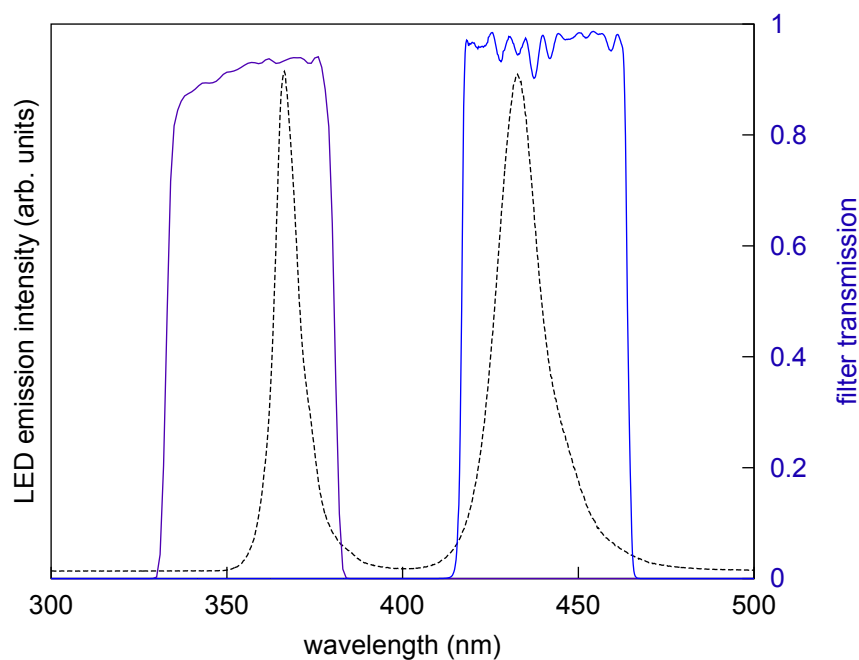
FIGURE 3.7: Plot of LED emission and filter transmissions

than the reflectivity range of the mirrors. This out-of-band light is not reflected by the mirrors and is focussed into the spectrograph where it can saturate the detector. In this setup the LEDs had an emission range similar to the mirror reflectivities, so there is less out-of-band light to start with. Nevertheless a bandpass filter in each channel was essential to avoid saturating the camera. The filter was initially placed immediately after the LED in order to avoid allowing more light than necessary into the chamber, which could have led to extra photolysis. However the filters also acted as mirrors and when the chamber lights were on a large background signal was observed due to the reflection of the white chamber wall travelling through the optical system. The filters were thereafter placed between the exit of the cavity and the fibre coupling lens.

Shortly after the beginning of experiments a small piece of reflective coating of a blue mirror became dislodged. The exposed area transmitted a large portion of the cavity light and reduced the enhancement factor of the cavity. Placing a mask on the damaged area eliminated the stray light but deformed the mirror enough to drastically reduce the cavity transmission and the enhancement factor. Further efforts to construct a mask at the front and rear of the mirror were unsatisfactory. The blue cavity was therefore disabled and the spare end of the fibre was used to measure directly the output of the UV-LED. The lack of a blue cavity did not hinder the $[Br_2]$ determination as it could only measure transmission in a region with very
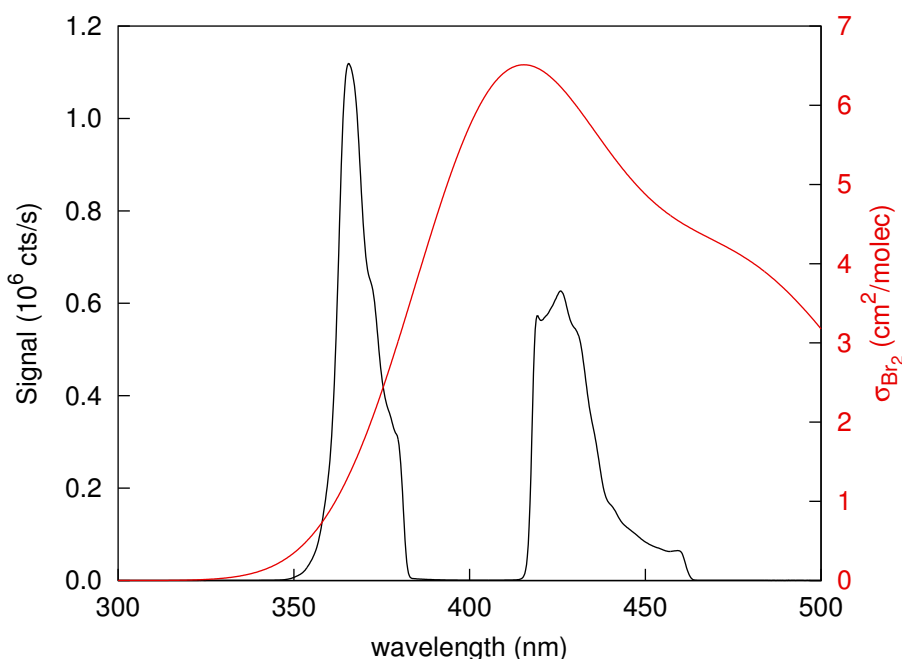
FIGURE 3.8: Example of typical signal measured by the CCD. In red is the Br_2 absorption cross-section reference spectrum from Maric et al.[4].

flat Br_2 absorption (Figure 3.8). Such a flat absorption meant background intensity changes were indistinguishable from actual $[Br_2]$ changes. The large absorption cross-section in the blue region also led to undesirable photolysis, creating an apparently large dark reaction (see Section 4.4.1). Because the two UV signals had the same wavelength range they had to be separated on the camera CCD with a focussing adapter so the two spectra could be read separately. There was no shutter in the system so to avoid smearing on the sensor the LED emission was triggered by the spectrometer's shutter signal. The acquisition time was then set at 31 spectra per 6 seconds (0.1 minutes), which were summed together before saving. Small adjustments to the acquisition rate were made every few weeks to keep the signal in range. Most of the data in the campaign was collected with the UV cavity alone.

3.3.1 Cavity enhancement factor calibration

The reflectivity of the mirrors is often considered to define the enhancement factor of the cavity. In Section 2.4 the enhancement factor was defined as $E = \frac{1}{1-R}$, meaning the mirror reflectivity defines the enhancement factor precisely and vice-versa. In experimental systems however the alignment of the optics and beampath can severely reduce the E defined on the basis of reflectivity. For instance the cavities in the chamber are much shorter than the radius of curvature of the mirrors, so it is likely

that the enhancement factor is much less than half of the maximum determined by the actual mirror reflectivity.[243] A direct measurement of the reflectivity in a UV-Vis spectrometer indicates the actual E was a third of the maximum possible. Instead of referring to reflectivity, it is more phenomenologically correct to use the enhancement factor as an experimentally calibrated fudge factor, incorporating all the alignment, focussing, and reflectivity parameters together. The calibration procedure can then confirm the linearity of the cavity enhancement, something which can become problematic with high extinctions.[205] Historically, the most important technique to calibrate cavities is to measure the ring-down time of a pulse of light injected into the cavity. This method was originally invented to measure very high reflectivity mirrors.[201] It requires fast detectors that are not part of a typical IBB-CEAS setup, so is inconvenient to use.

Instead the enhancement factor, E, can be measured directly by placing a standard absorber in the cavity. Low-loss optics have been used for this, but this was inconvenient as there was no easy access to the cavity inside the chamber. In our chamber the most appropriate method was to inject an absorbing gas whose concentration could be determined by other methods. Since the chamber was small the gas could be added and removed relatively quickly. The calibration gas was NO_2, quantified with a recently calibrated Horiba APNA 360 NO_x monitor. The absorption spectrum of NO_2 is similar to Br_2 so it provides a suitable reference to calibrate E.

Experimentally, the chamber was flushed from tanks of UltraZero air to remove any detectable NO_2 or anything that might interfere with the calibration. After a background baseline reading was taken with both the CEAS and NO_x detectors, about $1\,L$ of $5\,ppm$ NO_2 in N_2 was introduced into the chamber via a flexible plastic bag. A further two additions gave three calibration points. The volume of each addition was not intended to be quantitative as the actual $[NO_2]$ was measured by the NO_x monitor. The NO_x monitor extracted $0.8\,L/min$, totalling $30\,L$ over the course of a calibration. The walls of the chamber could collapse enough to accommodate this change without putting stress on the mounts and affecting the alignment. The $[NO_2]$ data could not be automatically logged due to a malfunction of the analogue output, so all $[NO_2]$ were were recorded by hand at predetermined intervals. At least three recordings spaced by two minutes each were used for each $[NO_2]$, and the value used for the calibration was the average of these three readings (or of the two readings closest to one another if one reading was clearly an outlier). The NO_2 cavity absorption spectra were checked for linearity with the $[NO_2]$ readings, and any values that clearly did not match were discarded. Such outliers were due to transcription errors or resulted from readings being taken when the displayed
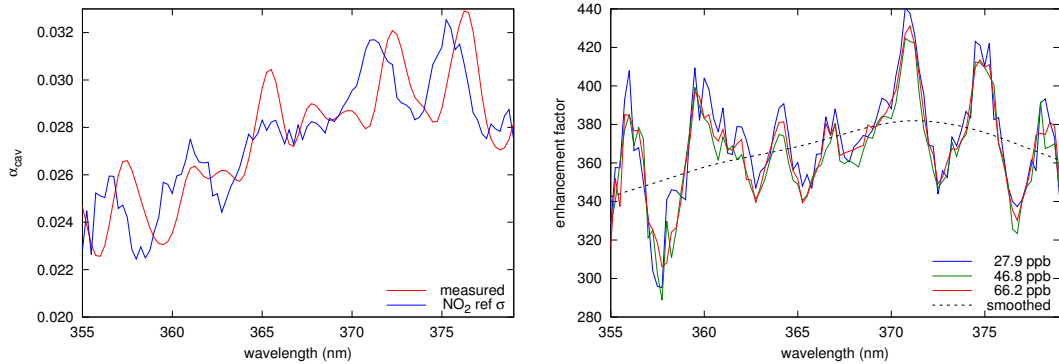
FIGURE 3.9: (a) Spectra of NO_2 reference σ (red) and cavity absorption (blue). (b) Resulting E curves from 3 $[NO_2]$ calibration points. The smoothed mean of all three is the dashed line.

$[NO_2]$ was fluctuating from its actual value.

Fitting the spectra The reference $[NO_2]$ spectrum was fitted to the measured spectrum in two ways. The most straightforward method is to find the ratio of the observed cavity absorption ($\frac{I_0 - I}{I}$) to the expected single-pass cavity absorption ($N\sigma L$), which yields E directly. Because the spectrum of NO_2 has a periodic structure a simple division of the measured and reference spectra leads to residual structures resulting from the inevitable slight mismatch of wavelength calibration (Figure 3.9(a)). These were smoothed over by Tikhonov regularisation [244] (`datasmoothing` package in Octave)(Figure 3.9(b)). This direct method could potentially lead to bias depending on how the peaks and troughs align.

A more advanced approach is to use an iterative method to stretch and shift the spectrum together with a polynomial function. The polynomial is then the enhancement factor. This approach begins with a similar CEAS equation:

$$\frac{I_0 - I}{I} = N\sigma_{ss}lE \tag{3.2}$$

where

$$E = a_0 + a_1\lambda + a_2\lambda^2 + a_3\lambda^3 + a_4\lambda^4 + a_5\lambda^5 \tag{3.3}$$

$$\sigma_{ss} = stretch(\sigma_{NO_2} + shift). \tag{3.4}$$

The parameters $a_n, stretch$ and $shift$ are the terms to be fitted. The term λ is the pixel to wavelength calibration vector, and σ_{ss} is the NO_2 absorption cross-section σ_{NO_2} interpolated on the adjusted wavelength scale. The initial wavelength calibration
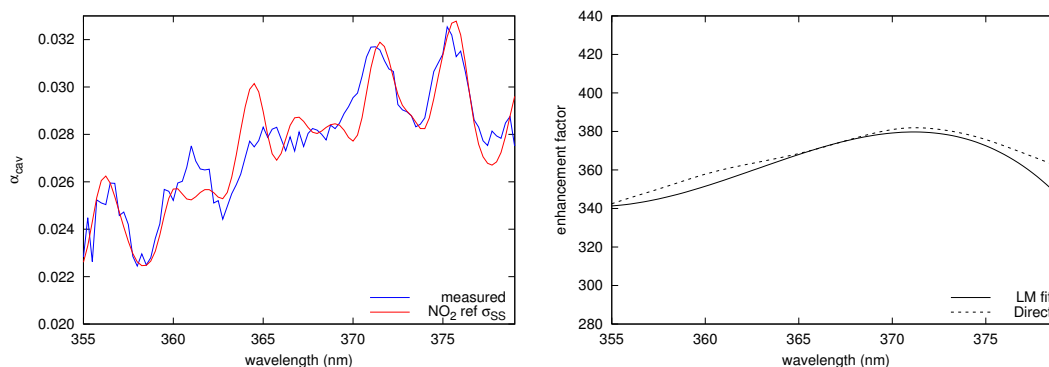
FIGURE 3.10: (a) Calculated NO$_2$ σ_{SS} (red), including a 1.00 nm shift and 0.975 squeeze, showing match with measured spectrum (blue). (b) Shapes of the E curve derived from LM fitting (solid), and smoothed direct division (dashed)

was carried out daily by directing the output of a Hg-Ar lamp into the I_{LED} fibre. This was always done at the end of the day as the lab cooled overnight, and the fibre took a few hours to settle and give a stable signal after unscrewing it.

Every term in these equations is known except for the stretch, shift and polynomial coefficients. The equation was solved for these with the Levenburg-Marquardt (LM) algorithm (`leasqr`). The residual was much smaller than that from the direct fit. The polynomial describing the enhancement factor is limited to order 5 so the resulting E curve is already smooth. Figure 3.10(a) shows the improved alignment of the reference and observed spectra, and Figure 3.10(b) compares the shapes of the direct fit and the LM fit. The two methods are in generally good agreement, with the difference smaller than 5%. The LM fit was the one used for [Br$_2$] retrieval.

The residual structures were mostly consistent within each calibration. The structure may have been caused by some residual contaminant—possibly HONO for instance—but it is more likely to have arisen from the temperature effects described later in Section 3.4. The E from the different [NO$_2$] differed by less than 10%, confirming the linearity of E with the extinction in the cavity (Figure 3.9(b)). Calibrations were taken at least every week and for each temperature point studied, and after any realignment. It was not possible to take a new calibration every time the chamber changed temperature, so it was assumed that the calibration would remain valid across temperature cycles. In fact the difference in E between the extremes of temperature was quite small ($\approx$10%) compared to the variation over months ($\approx$30%), during which there were setup alterations and realignments.

3.3.2   Retrieving $[\mathrm{Br}_2]$

The cavity absorption α is defined as

$$\alpha_{cav} = \frac{I_0 - I_t}{I_t} = [\mathrm{Br}_2]\sigma_{\mathrm{Br}_2} l E \qquad (3.5)$$

where I_0 is intensity of each wavelength band leaving the clean chamber, and I_t is the same with the addition of Br_2. $[\mathrm{Br}_2]$ is in $\mathrm{molec\,cm^{-3}}$ and the absorption cross-section σ_{Br_2} is in $\mathrm{cm^2\,molec^{-1}}$, l is the length of the cavity in cm and E is the enhancement factor of the cavity. Since the real I_0 at time t cannot be known, it was initially extrapolated from a period of several minutes immediately before the Br_2 injection. Unfortunately the emission of the LED was not stable enough to assume as constant. An example of a change of 0.5% is shown later in Figures 3.16 and 3.17. A second channel measured the intensity of the LED (I_{LED}) directly from its housing, which enabled intensity drifts to be compensated. The I_0 was corrected by a factor of the ratio between the present and initial LED spectra, and the corrected I_0^{corr} used in place of I_0 thereafter:

$$I_0^{corr} = I_0 \frac{I_{LEDt}}{I_{LED0}} \qquad (3.6)$$

Where I_{LED} was unavailable—such as in the few measurements before the blue cavity was disabled—I_t was estimated by assuming that the I_0 measured before the injection was constant throughout the $[\mathrm{Br}_2]$ measurement period. The uncertainty of those measurements was accordingly increased.

The absorption spectra of Br_2 were fitted to the reference with a linear model. The reference spectrum, σ_{Br_2}, was taken from Maric et al.[4] via the online MPI-Mainz spectral database.[5] The reference spectrum was interpolated to the λ-calibration scale and then convoluted to the slit function of the spectrometer, which was well-approximated by a Gaussian curve with a full-width at half-maximum (FWHM) of 0.8 nm. The normal DOAS routine of separating the broadband structure from the spectral details cannot be used, since Br_2 has only broadband structure over the wavelength region studied. Neither could iterative stretching and shifting be used since there are no obvious features on the Br_2 spectrum for the algorithm to fit. The permuted spectrum could shift and stretch until stopped by whatever, mostly arbitrary, constraints were used by the model. Instead the model fitted was

$$\alpha_{cav} = \sigma_{\mathrm{Br}_2} l E [\mathrm{Br}_2] + \epsilon \qquad (3.7)$$
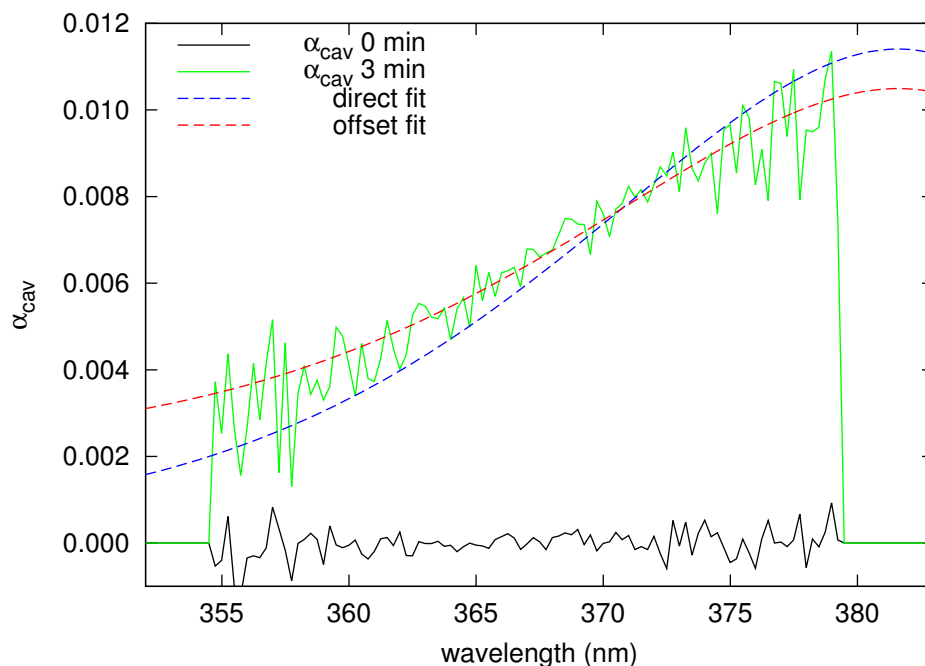
FIGURE 3.11: Example of Br_2 spectrum fitting. The direct fit yields 55 ± 2 ppb, and the offset fit 41 ± 4 ppb with an offset of $+0.002$. The difference between the fits here is about twice that typically observed.

where ϵ is the fit residual. Solving this simple linear model is equivalent to ordinary least squares regression, except instead of fitting a straight line it fits the Br_2 reference spectrum. For every experiment the $[Br_2]$ was calculated in two ways. The first assumed that when $\alpha = 0$ then $[Br_2] = 0$ at each wavelength, and the second allowed a constant offset that could accommodate broadband, wavelength-constant changes in α with no concomitant change in apparent $[Br_2]$. Such broadband offsets could be caused by transmission changes due to mechanical disturbance or drifts. Usually the difference between these two fits was small, so the offset-fit was used as it gave a larger, more realistic $[Br_2]$ uncertainty. An example of the fitting is shown in Figure 3.11. An example time profile can be seen later in Figure 3.12. The ratio of the direct and offset fits provided a metric that aided in interpretation of the fit quality. The poorest quality fits were those done with both UV and blue cavities, with greater than 50% difference between the fits. The offset fit was otherwise nearly always within $+5$ to -14% of the direct fit, unless influenced by an easily identifiable factor (heating effects, disturbance of the optics etc). In ideal circumstances any poor quality fits would be discarded and the experiment repeated. However for the low $[Br_2]$ there was only poor quality data, so the suspect data was included in the analysis with larger error bars. If it was not clear which value was more likely to be accurate, the range of both was used as the uncertainty. Two examples are
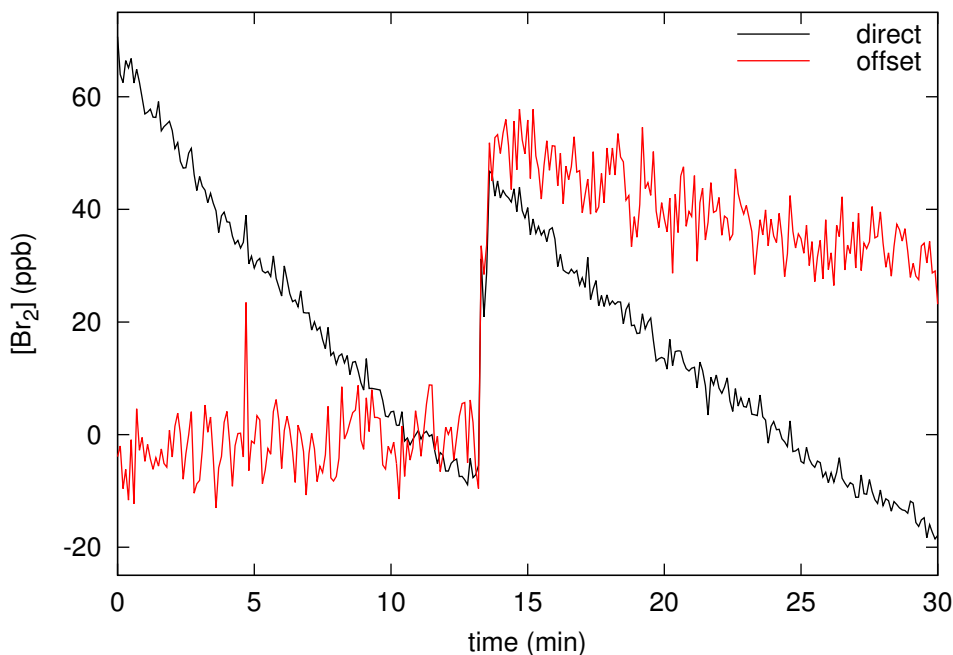
FIGURE 3.12: Time profile of $[Br_2]$ retrievals during a Br_2 injection using direct (black) and offset (red) fits in the presence of a decreasing concentration of sea salt aerosol. The direct fit is heavily influenced by the aerosol, whereas the spectral fit allowing an offset yields a more robust and realistic $[Br_2]$.

given below where, with some understanding of the cause of the discrepancy, the data could be reliably included. In particular, a temperature-induced artefact was present in a large proportion of the data, so it is discussed in depth.

3.3.3 $[Br_2]$ Artefacts

There were a number of spectral features that made the interpretation of the retrieved $[Br_2]$ problematic. A judgement had to be made on which of the fits—direct or baseline-offset—was more likely to give the correct $[Br_2]$.

Broadband-absorption artefact   Figure 3.12 shows the effect of aerosols on $[Br_2]$ retrieval. For this experiment sea salt aerosol was introduced into the chamber some minutes before the start of the graph. The $[Br_2]$ is derived from an I_0 taken immediately before the Br_2 injection. The black line shows a direct fit with no other absorbers or polynomial offsets permitted. It is heavily influenced by the aerosol extinction, and this is obvious since the aerosol concentration would be decreasing over the whole period. The red line is a fit which includes a flat baseline offset, and this correlates much better with the actual $[Br_2]$. It would be incorrect to interpret

the decrease in the direct fit $[Br_2]$ as a wall loss. If there was a trend before the injection, then it is quite probable that trend continued after the injection and its effects can be ignored.

Although aerosol was only used in three experiments, similar broadband intensity changes were quite frequently observed. Sudden drops in I were sometimes seen when injecting either Hg or Br_2 into the chamber. These were caused by disturbance of the foam housing of the chamber, causing it to scatter a small portion of the beampath. The fits that included an offset were not affected by such broadband intensity changes. However, the offset-fit was less robust when the unintended absorption was structured.

Structured-absorption artefact   Many experiments had a spurious absorption that was structured or sloping. In these cases the offset fit could be more affected than the direct fit. Temperature changes could cause such a structured absorption, and the worst case observed is shown in Figure 3.13(a). The cavity was clean throughout this example. The α_{cav} at $t = 0$ min is zero by definition. Some noise is observed at $t = 4$ min, but at 10 through 60 min a large structure appears. The apparent $[Br_2]$ retrieved from this structure is shown in Figure 3.13(b), and it is clearly well correlated to temperature. The periodicity of the structure is not important to $[Br_2]$ retrieval as the absorption of Br_2 has no structure. However, the slope of the structure produces a very severe artefact of more than 200 ppb over 60 minutes. The derived $[Br_2]$ are four times larger when the fit includes an offset. The fact that the artefact produces both a negative and positive apparent absorption indicates that it is not caused by a species offgassing inside the chamber, as an absorbing species could only reduce the cavity transmission.

The consequence of this artefact was that, if present, the direct fit was used and any large trend in apparent $[Br_2]$ before the injection was removed visually and the uncertainty for the $[Br_2]$ increased. However, the chamber was used over wide temperature range and the existence of a temperature-dependent artefact cast suspicion on all of the data at cooler temperatures, even if the artefact was not observed directly. The next section details the effort to find and remove the cause of the artefact.
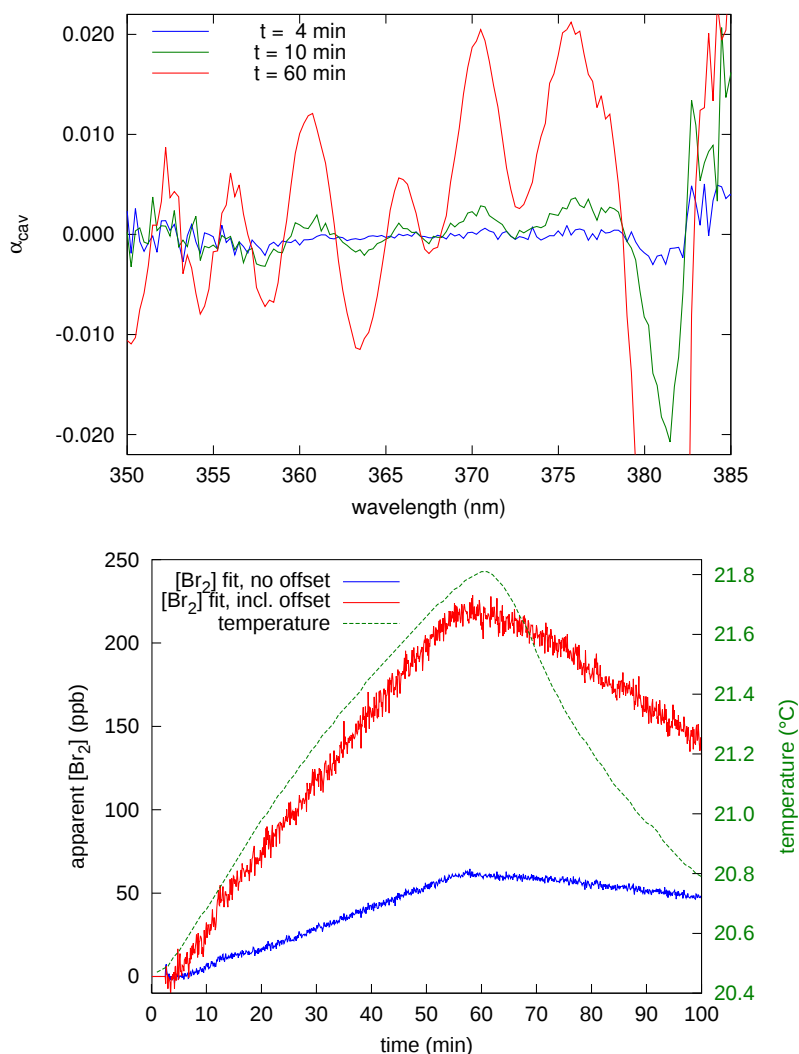
FIGURE 3.13: Correlation of temperature with apparent $[Br_2]$. (a) shows the cavity absorption α_{cav} changing in a clean chamber over 1 hour and (b) shows the time profile of the apparent $[Br_2]$ with temperature.

3.4 Origin of the temperature-induced artefact

The spectral structure shown in Figure 3.13 appeared only sporadically. As it seemed to be correlated to temperature changes, attention was focussed on the temperature performance of the system.

During the cold experiments the cooling coils of the chamber were cooled to $-20\,°C$. All the instrumentation had to be insulated or immune to temperature shifts of up to $40\,°C$ between days and up to $5\,°C$ within experiments. Day-to-day stability was necessary to maintain the validity of the NO_2 calibration, and within-experiment stability was important because the CEAS approach requires a stable I_0 that is valid for the whole experiment. The temperature of the room usually increased during

experiments due to the equipment running in the lab. The building's air-conditioning system was powerful enough to keep the room stable to within a few degrees, but this meant that the air from the HVAC vents could vary from 15 to 28 °C. The possible effects of temperature changes on the setup are explored below.

3.4.1   Temperature stability of CEAS system

Optical mounts

The aluminium that makes up most of the mounts has an expansion coefficient of 22×10^{-6} K^{-1}. During cold experiments there was difference of 30 K between the posts inside and outside the insulated box. For posts 200 mm long this temperature difference results in a vertical displacement of 4.4 µm, which is not enough to cause the beam to wander out of the ≈ 300 µm entrance of the fibre. Both the lens and fibre were outside the insulation. Nevertheless, materials at either end of the chamber were matched to avoid potential issues with beampath alignment.

Another issue was the alignment of the mirrors relative to each other. The gimbal mounts used to hold the mirrors appeared to be immune to temperature changes. The NO$_2$ calibrations were very similar at all temperatures and across many temperature cycles—usually within 10%. The repeatability of the calibration was evidence that the setup was mechanically stable.

Optics

The properties of thin film optical coatings change with temperature. Most of the effect is a shift of spectral features to longer wavelengths on heating, due to the thermal expansion or contraction of the dielectric layers making up the coating. The mirrors were subject to a large temperature shift, as they were placed within the chamber. During each experiment, however, the temperature change was only around 5 °C, so the mirror calibration remained valid within each temperature point (provided there was no loss of alignment on cooling and rewarming, which was not seen).

The transmission of the bandpass filter and mirror as measured by a UV-Vis spectrometer (Perkin-Elmer Lambda 9) are shown in Figure 3.14. The bandpass filters were located just outside the chamber in an aluminium lens tube that passed into

(a) Mirror

(b) Bandpass filter

(c) Reflectance of coating
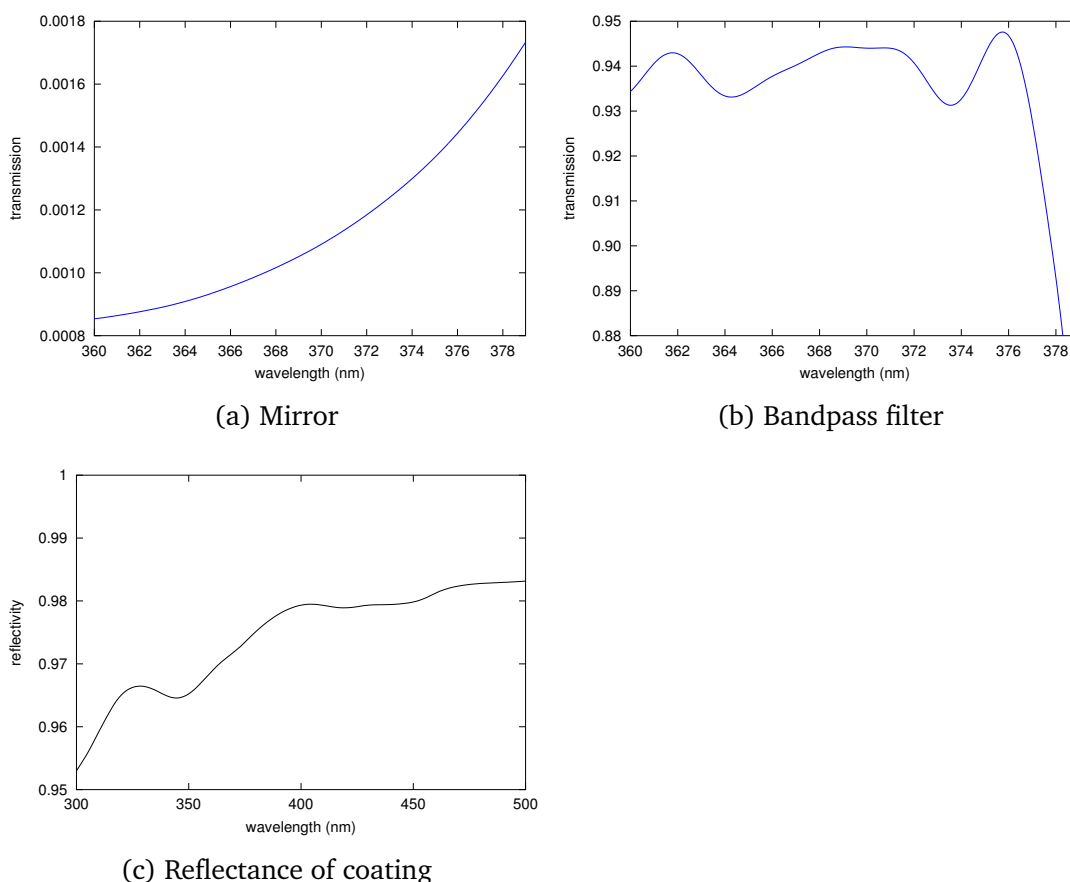
FIGURE 3.14: Transmissions of (a) cavity mirror and (b) bandpass filter used in UV cavity. (c): Reflectance of Avian B coating used to couple LED into spectrometer for I_{LED} measurement. Note different wavelength ranges.

the chamber. These optics would not experience the same temperature shifts as the mirrors.

The relatively flat transmission of the mirrors (Figure 3.14(a)), and the temperature stabilising effect of the chamber and heavy (260 g) mounts meant that mirror heating within each experiment was probably unimportant. The absorption spectrum imparted by the mirrors was however very similar to Br_2, so could be a source of the $[Br_2]$ artefact.

Unlike the mirrors, the bandpass filter (Figure 3.14(b)) does have structure. The response of the coating to temperature changes is difficult to measure, and the filter manufacturer refused to divulge this information. However, CVI–MellesGriot specify a sensitivity of between 0.016 and 0.027 nm K^{-1} at 400 and 820 nm respectively, which extrapolates to about 0.015 nm K^{-1} at 365 nm. Assuming this value to be representative of the coatings used on our mirrors and filters, we can attempt to find the residual spectra caused by a temperature shift.
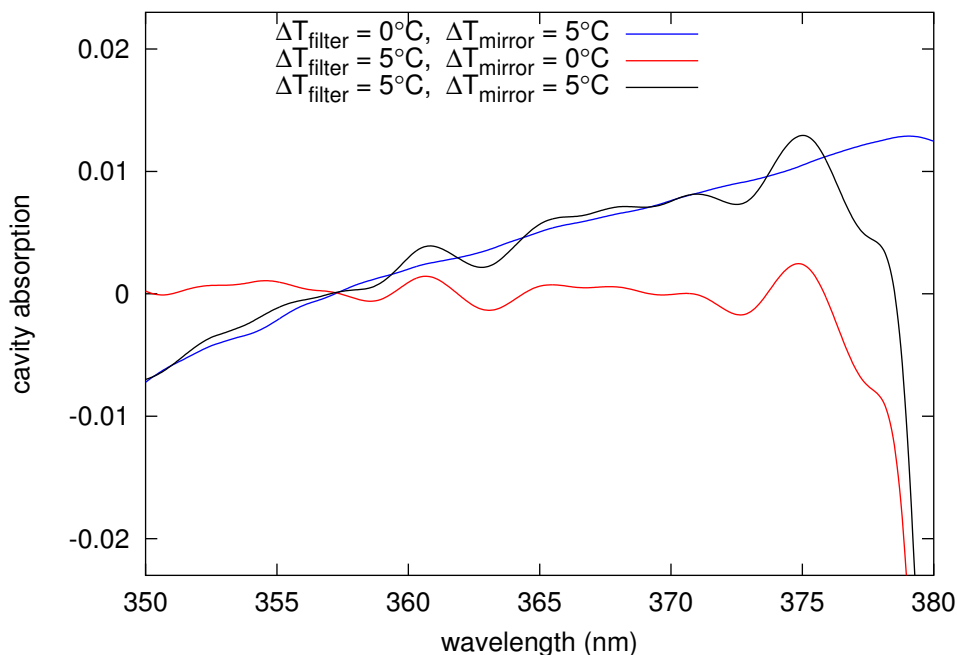
FIGURE 3.15: Calculated cavity absorption based on shifting the optical transmissions of the UV mirror and filter according to a temperature rise of 5 °C and a sensitivity of 0.015 nm K^{-1}.

Figure 3.15 shows the resulting apparent absorption seen when the transmissions of the optics are shifted by 5 °C. This temperature shift is larger than that measured by the thermocouples inside the chamber, but it is similar to the variation in the HVAC air. The large trough at 380 nm is present only when the spectrum of the bandpass filter shifts, while the Br_2-like slope is due to the mirror. The effective spectrum where both are shifted compares poorly to that observed in Figure 3.13, although the filter does seem responsible for the drop at 380 nm. As long as the fit range is restricted to below 375 nm, the filter would have a negligible effect on the apparent $[Br_2]$. The mirror shift is unavoidable however, and in this example a 5 °C shift imparts an apparent $[Br_2]$ of 18 ppb. Including a baseline offset allows the $[Br_2]$ to increase to 19 ppb.

Another contributing factor is the reflectivity of the white coating used to sample the emission of the LED. The coating was made from Avian-B highly reflective coating (Avian Technologies) mixed with black carbon soot to bring the signal down into range. This mixture had to be replaced every few weeks to maintain appropriate signal so its exact spectrum is unknown. The manufacturer's reflectance curve is shown in Figure 3.14(c). There is also more than likely a contribution from scattering within the reflective coating of the mirrors.

Even if all of these spectra were completely stable, the structure would still be seen
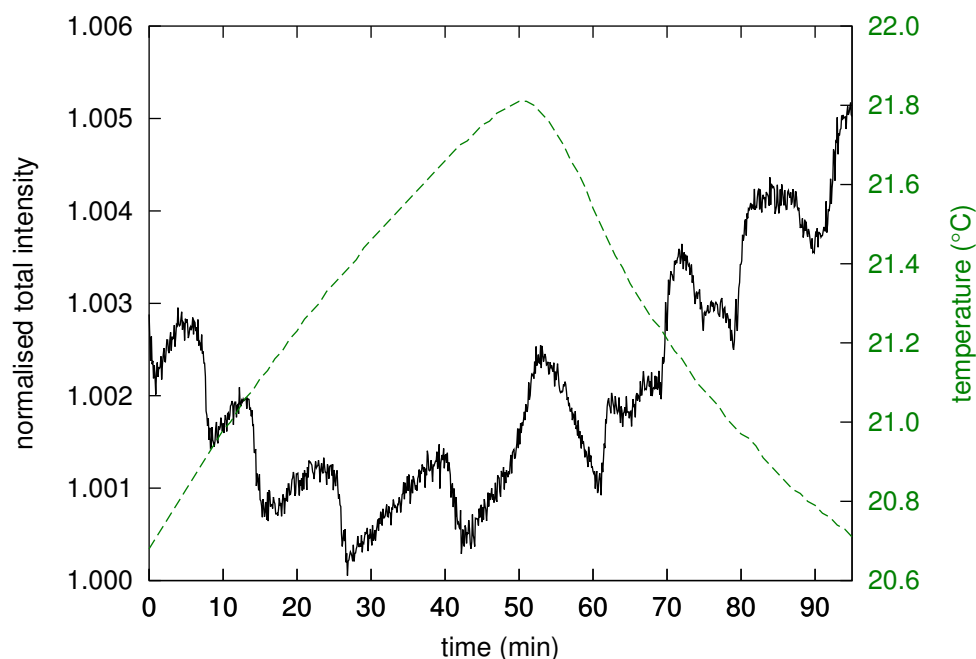
FIGURE 3.16: In black is the temporal change in the UV LED output, where all wavelength bands are summed and normalised to the lowest value. The dashed green line is the temperature of the lab. Change is on the order of 0.5% over 1 hour, and anti-correlates slightly with temperature.

to shift if the spectrograph were unstable. First we will look at the stability of the LED.

LED emission

The emission of the LED must be stable if small changes in the signal are to be attributable to genuine cavity absorptions. Figure 3.16 shows the change in the UV LED emission intensity where all wavelengths are summed together. Over 1 hour the total emission changed by 0.5%. The temperature profile matches the output only slightly, and the temperature does not show the same step changes every 10 min as the LED does. The non-smooth nature of the LED emission change indicates that it was probably caused by imperfect thermal compensation in the LED power supply or some other electronic effect (mechanical expansion tends to give smoother signals).

The intensity did not change uniformly across the emission spectrum. Figure 3.17(a) shows the change against wavelength. The change is small so it is easier to visualise it by plotting the ratio of spectra of the two, as shown in Figure 3.17(b). Below the peak emission at 365 nm the emission increased by 2%, and above, it decreased by

67
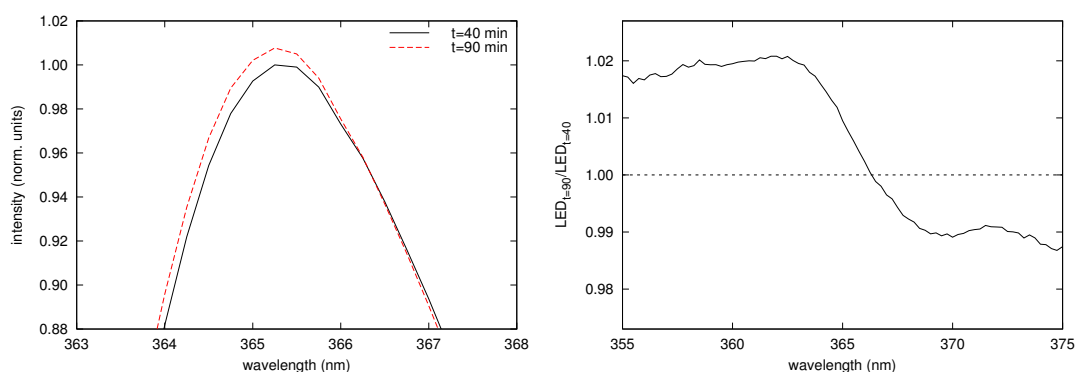
FIGURE 3.17: Change in the apparent emission of the UV LED. Times refer to Figure 3.16. (a) Spectra of LED output at t =40 and 90 min. Intensity normalised to maximum of $t = 40$ min. (b) Ratio of LED spectra at t =40 and 90 min. Dotted line at $y = 0$ is the no-change baseline

1% . This difference implies that the change is both a blue shift and a brightening. If the shift were due to power supply current changes, it would show a red-shift at higher intensities (as seen with the laser diode test in Section 2.3.3). The shift must therefore be due to another factor, which is almost certainly the spectrograph. The absolute changes in LED output are corrected for by the I_{LED} channel, whereas shifts in the spectrometer are more difficult to compensate for reasons outlined in the next section.

Etalon effects are a known issue with the use of LEDs in CEAS systems,[245] and shifting of the LED etalon structure can cause large artefacts. However the emission spectrum shown in Figures 3.17 3.7 (full spectrum) appears to be smooth at the resolution of the spectrograph.

Spectrograph

If certain parts of the spectrograph expand with increasing temperature then the diffracted light will land on a different part of the sensor. A Mitutoyo micrometer controls the position of the spectrograph's grating. It is helpfully designed so that a one micron movement causes the centre wavelength to shift by one nanometre. To measure the temperature shift an accurate wavelength standard is required, and the 406.5 nm Hg line from a pencil lamp was well suited to this task. The observed shifts (Figure 3.18) were similar in appearance to those of the LED shown in Figure 3.17, except that the atomic line is sharper and can be modelled more precisely. The shift is less than one pixel so cannot be read off directly, but by fitting a Gaussian curve to the emission line and plotting the mode wavelength the the temporal profile is easily seen (Figure 3.18). It is clear that the wavelength shift is a delayed response
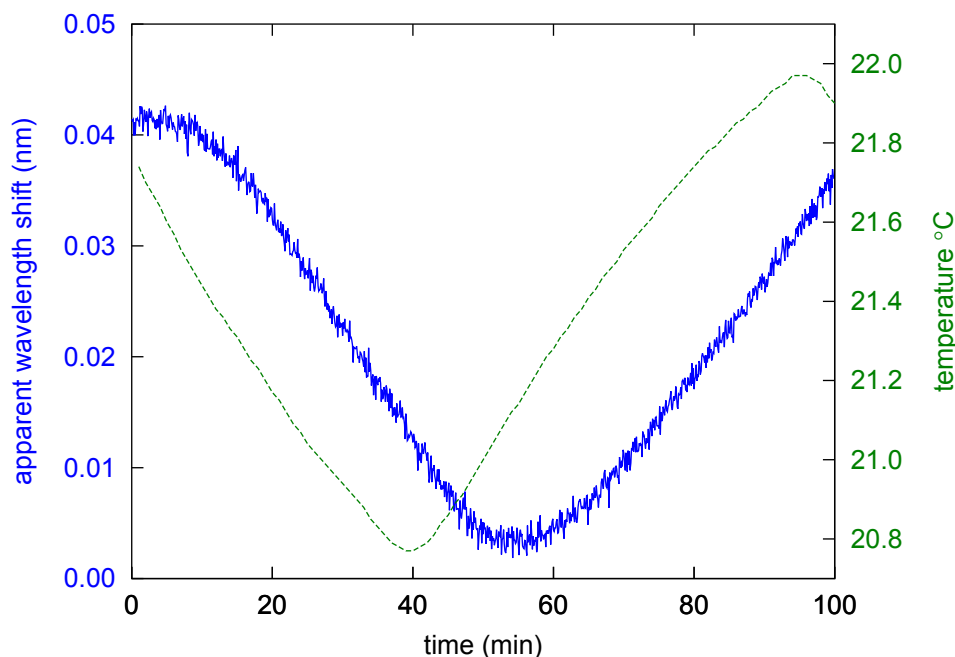
Figure 3.18: Plot of wavelength shift of spectrometer with temperature on the optical bench.

to room temperature changes, measured about 2 m away from the spectrometer. The apparent wavelength shift in Figure 3.18 is 0.04 nm, which is equivalent to 0.16 pixels and much smaller than the ±1 pixel shifts in calibration seen from day-to-day. This small change is equivalent to a movement of the micrometer of only 0.04 μm, something which could be caused by the casing of the spectrometer warming by just 0.04 °C relative to the micrometer spindle (assuming 5 cm of Al with a temperature coefficient of $22.2 \times 10^{-6}\,\mathrm{m^{-1}\,K^{-1}}$). Another factor with similar sensitivity is the thermal expansion of the grating,[246] which could be be mitigated with insulation and use of expensive custom gratings made from Zerodur glass or similar.

Since the FWHM of the LED emission is only 32 nm (shown in Figure 3.8), the emission curve is steep and changes by a factor of 20 %/nm or 5 %/pixel on either side of the peak. A 0.16 pixel shift would therefore result in an apparent LED emission change of 0.8%, large enough to compromise the $[\mathrm{Br_2}]$ retrieval.

The emission of the LED was known, so by scaling the I_0 spectra with the new I_{LED} the shifts in the LED's spectrum—due to both actual emission changes and perceived wavelength shifts—were corrected for. However, there remains structure in the transmission of the optics that are not shifted to the same degree, and cannot be corrected unless the shift is known. In most cases the shift was so small that it could not be retrieved and corrected without introducing more error into the

measurement than was caused by the shift.

While use of the atomic line to recalibrate the wavelength scale for each spectrum would be feasible, it was not practical to inject an atomic line into the well-sealed beam path without interfering with the chamber measurements. In fact the shift shown in Figure 3.18 could only be detected with the 406.5 nm Hg line, the other lines were too weak or had too high background signals. The wavelength shift retrieved from the NO_2 spectra were not precise enough to determine a shift quantitatively, and the emission of the LED was not stable enough to use as a reference wavelength. Instead the spectrometer was insulated with polystyrene, taking care to pack it gently around the micrometer head. The stability was thereafter much improved.

3.4.2   Reproducing the artefact

The individually shifted transmissions of the optical components did not completely reproduce the structure in Figure 3.13.

To confirm that the structured artefact shown in Figure 3.13 was indeed the result of some optical component, the artefact is reproduced in this section by shifting the transmission of the whole cavity system.

Since $I = I_{LED} \times T$, where T is the total transmission of the cavity system from LED to camera, and if we assume that the LED emission I_{LED} is constant, then:

$$\alpha_{cav} = \frac{I_0 - I_t}{I_t} = \frac{I_{LED}T_0 - I_{LED}T_t}{I_{LED}T_t}$$
$$= \frac{T_0 - T_t}{T_t}. \tag{3.8}$$

In fact we need not assume that I_{LED} is constant as it is measured continuously. If I_{LED} were taken directly from the LED we would know the actual transmission. Instead it was scattered off a small area of white paint. This imparts a reflectance spectrum, which cancels out if we assume it is constant. We can then find a "scaled" transmission by simply dividing the measured I_{LED} by I. From the same data as in the initial artefact example in Figure 3.13, the measured transmissions at $t = 5$ and 60 min are shown in Figure 3.19(a).

The transmission of the cavity contains more structure than any of the individually measured optical components (Figures 3.14, 3.17). The structure has the appearance of an etalon with a spacing of 5.2 nm. At 360 nm this corresponds to an glass etalon
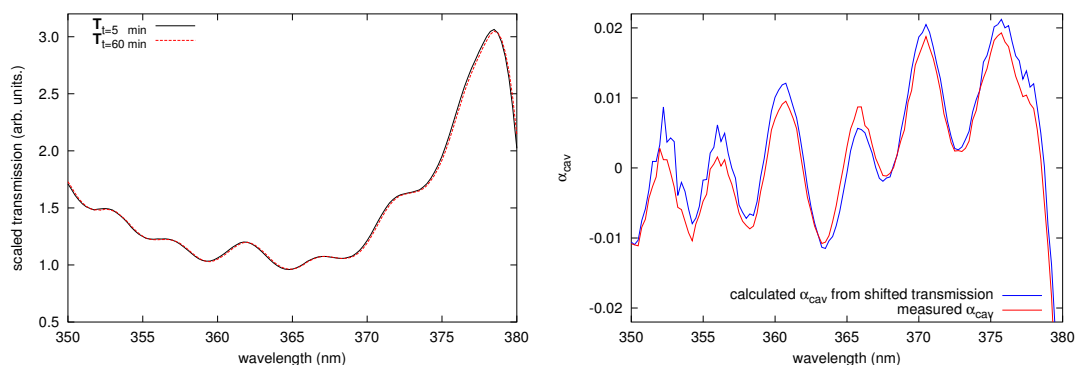
FIGURE 3.19: Measured transmission and derived α_{cav} from shifted transmission alone.

thickness ($n = 1.5$) of $8\,\mu$m. This etalon could arise from the multiple reflections in the mirror coating, something which might not be detected on a single pass.

The transmission at $t = 60$ min looks identical to that at $t = 5$ min, but is shifted slightly. Figure 3.19(b) shows α_{cav} calculated as usual from the corrected I in red, and also α_{cav} calculated from Equation 3.8 using only $T_{5\,min}$ as T_0, and $T_{5\,min}$ shifted by 0.09 nm as T_t. Such a shift could be caused by $2\,°$C of warming of the spectrometer. The spectra match very well, implying that the structured artefact is indeed caused by transmission shifts relative to the spectrometer. Other structures can be produced by shifting the single-pass transmission of each component, as was explored in Figure 3.15 above.

The spectrometer and optics were insulated after this effect was discovered. The fit range was restricted to wavelengths below 376 nm to avoid the structure in the bandpass filter, and $[Br_2]$ were determined within a few minutes of the I_0 to limit the spurious concentration to a few ppb.

This section provided an answer for why the $[Br_2]$ could not be measured for long periods in many of the experiments. Although this frustrated attempts to measure wall losses, the data could be trusted when temperatures were stable. Although numerous papers emphasise the need to insulate the spectrometer in field instruments, none are quantitative in the effects of temperature changes. Stutz and Platt[246] for instance note that "grating spectrometers usually show a temperature drift of one tenth of a pixel per Kelvin." Even so, in a whole section on the origin of residuals in the main textbook of DOAS techniques, no mention is made of temperature shifts.[247]

3.5   Photolytic flux measurement

Underneath the FEP floor of the chamber was a photodiode (Thorlabs PM100 with
S130VC UV-Si detector) that recorded the intensity of the photolysis lamps during
each experiment. Although this diode had a dissimilar spectral sensitivity to both
the Br_2 absorption and lamp emission, these differences were constant so it still
provided a precise measure of J_{Br_2} in the chamber. The output of the lamps took 3
minutes to reach 98% of full intensity, so they were warmed up for 3 minutes prior
to use. A large shutter made of cardboard wrapped in black cloth was kept between
the lamps and the chamber until ready for illumination. It was effective in blocking
all light, with an attenuation of around $\approx 10^6$. Most of the light leakage probably
occurred via scattering down the injection line feeding into the chamber. The lamps
dimmed by no more than around a few percent over the 5 months of use. Due to
the warm up period, within each experiment the intensity never changed by more
than 3%, and usually only 0.5%. As this change is considerably smaller than the
error in $[Br_2]$, it was ignored and the photolysis flux was regarded as constant. The
signal from the photodiode was only proportional to the J_{Br_2}. The actual photolysis
flux was determined in three ways:

3.5.1   Observation of $[Br_2]$ under photolysis

The photolysis rate of a Br_2, j_{Br_2}, is given by

$$j_{Br_2} = \phi \boldsymbol{\sigma} \boldsymbol{F} \tag{3.9}$$

where ϕ is the quantum yield, $\boldsymbol{\sigma}$ is the absorption cross section and $\boldsymbol{F}$ is the flux of
photons. Expressed in chemical terms, the photolysis of Br_2 creates $Br^{\cdot}$, which can
recombine back to Br_2:

$$Br_2 \xrightarrow[h\nu]{j_{Br_2}} Br + Br \tag{R 3.1}$$

$$Br + Br \xrightarrow[M]{k_{rec}} Br_2 \tag{R 3.2}$$

where j_{Br_2} is the photolysis we would like to know and k_{rec} is the recombination rate
taken from the literature. At steady state, the rates of these two reaction are equal
so, assuming k_{rec} incorporates $[M]$,

$$\frac{d[Br]}{dt} = 2j_{Br_2}[Br_2] - 2k_{rec}[Br]^2 = 0. \tag{3.10}$$

We are only able to measure $[Br_2]$, so we must express this in terms of $[Br_2]$ only. Since every Br atom comes from photolysis of Br_2:

$$[Br] = 2([Br_2]_{dark} - [Br_2]_{light}) \tag{3.11}$$

$$j_{Br_2} = \frac{2k_{rec}\big([Br_2]_{dark} - [Br_2]_{light}\big)^2}{[Br_2]} \tag{3.12}$$

where $[Br_2]_{dark}$ and $[Br_2]_{light}$ are the measured steady state concentrations in the dark and illuminated chamber. By measuring the change in the steady-state $[Br_2]$ when the photolysis lights are switched on j_{Br_2} can be determined. Although this approach has been used successfully for measuring photolysis of I_2,[248] it was not successful in this case as the fractional change in $[Br_2]$ was too small to quantify, and where a change was seen it was not easily distinguishable from background variation. Often there was some mechanical disturbance caused by removing the shutter, making the small signal change difficult to detect. An example can be seen in Figure 3.4(b) shown previously, where the lights come on after the wall loss determination at the end of the red line.

We can calculate what the change in $[Br_2]$ should have been. From Equation 3.10 it follows that for a given j_{Br_2} at equilibrium

$$[Br]_{light} = \sqrt{\frac{j_{Br_2}[Br_2]_{light}}{k_{rec}}}. \tag{3.13}$$

The initial $[Br_2]$ in the dark is simply the sum $[Br_2]_{light} + {}^{[Br]}/_2$. An example of the expected change in $[Br_2]$ is plotted against the initial $[Br_2]$ in Figure 3.20. The rate j_{Br_2} is taken from the measurements in Section 3.5.3 and k_{rec} is one of two literature values (Table 4.2). At an initial $[Br_2]$ of $10^{11}\,\mathrm{molec\,cm^{-3}}$ the expected drop in $[Br_2]$ on photolysis is approximately 20%. Since the noise level of the $[Br_2]$ retrieval was around $10^{11}\,\mathrm{molec\,cm^{-3}}$ only larger changes would have been visible. At higher $[Br_2]$ the change becomes smaller and more difficult to detect. The fact that no change was observed may be evidence that the k_{rec} in the chamber was faster than either literature rate (discussed later in Section 4.7.6) however the uncertainty of the $[Br_2]$ is probably sufficient to explain the lack of a detected change.
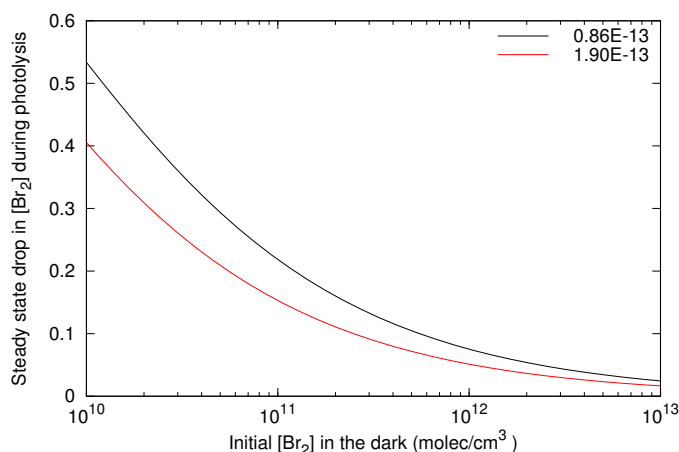
FIGURE 3.20: Calculated equilibrium drop of $[Br_2]$ on photolysis assuming j_{Br_2} of $0.0021\,s^{-1}$ and two literature k_{rec} in units of $cm^3\,molec^{-1}\,s^{-1}$. With an initial dark $[Br_2]$ of $10^{10}\,molec\,cm^{-3}$, the $[Br_2]$ will be reduced by 41% assuming a k_{rec} of 1.9 $cm^3\,molec^{-1}\,s^{-1}$, or by 53% if the k_{rec} is $0.86\,cm^3\,molec^{-1}\,s^{-1}$.

3.5.2 Standard reaction

Observing the $[Br_2]$ reduction directly was not a quantitative method of finding j_{Br_2}. Another technique to measure j_{Br_2} is to use an alkene to scavenge the Br during its formation, thereby preventing the Br recombination. Like most halogen radicals, Br react rapidly with alkenes to form Br-alkane radicals. These combine immediately with O_2 to form the bromoperoxy compound,[249] which can then deposit to walls or condense on aerosols. Due to the large excess of alkene, it is reasonable to assume that even if a small number of Br were reformed from the bromoperoxy alkane, they would be too dilute to recombine back to Br_2 in a significant degree. The alkene chosen was 2-methyl-2-butene (amylene), which we assume reacts thus:

$$Br + \xrightarrow{k_{amyl}} products \downarrow \tag{R 3.3}$$
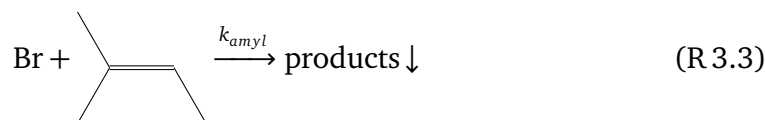
$$\tag{3.14}$$

The rate of change of $[Br]$ is then

$$\frac{d[Br]}{dt} = 2j_{Br_2}[Br_2] - 2k_{rec}[Br]^2 - k_{amyl}[Br] \cdot [\text{---}] \tag{3.15}$$

where k_{amyl} is available from literature.[250] Amylene was used at a concentration of 20 ppm, and $[Br_2]$ was at most 0.3 ppm. Looking at the magnitude of the terms in the above equation, the removal of Br due to amylene ($k_{amyl}[Br][\text{---}] \approx -10^{14}\,s^{-1}$)

74

is much faster than either its production ($2j_{Br_2}[\mathrm{Br_2}] \approx 10^{10}\,\mathrm{s^{-1}}$) or its recombination to $\mathrm{Br_2}$ ($2k_{rec}[\mathrm{Br}]^2 \approx -10^7\,\mathrm{s^{-1}}$). This means that $\mathrm{Br}^{\cdot}$ is removed by amylene as quickly as it is produced. The rate of decay of $[\mathrm{Br_2}]$ therefore yields directly j_{Br_2}:

$$\frac{\mathrm{d}[\mathrm{Br_2}]}{\mathrm{d}t} = -j_{Br_2}[\mathrm{Br_2}] \tag{3.16}$$

Integrating in the usual way results in

$$\ln[\mathrm{Br_2}]_t = j_{Br_2}t + \ln[\mathrm{Br_2}]_0 \tag{3.17}$$

so a plot of $\ln[\mathrm{Br_2}]_t$ against time gives a line whose gradient is j_{Br_2}, yielding the photolysis rate directly.

The experimental procedure was to first inject $1\,\mathrm{mL}$ $\mathrm{Br_2}$ vapour into the dark chamber, followed by $20\,\mathrm{\mu L}$ of liquid amylene introduced by evaporating it into a flow of zero air with the aid of a heat gun, yielding a concentration of $20\,\mathrm{ppm}$. The mixture was left in the dark for about 10 minutes to verify that there was no detectable dark reaction. The chamber was then illuminated by removing the shutter. After the $[\mathrm{Br_2}]$ had decayed—around 10 minutes—the chamber was flushed for at least a weekend to remove the reaction products from the chamber before the next experiment. This procedure was carried out 5 times over the course of the campaign. The j_{Br_2} measured in this way were 1.2, 2.6, 1.8, 2.1 and $2.0 \times 10^{-3}\,\mathrm{s^{-1}}$. All of these except the last suffered from a large broadband intensity change which was not well corrected for by a baseline offset. A first order decay did not closely match the actual decay in these instances. While there may have been a contribution from aerosol extinction, the major cause of the offset was almost certainly the effect of the heatgun on the optics, which could be observed by the change in I_{LED}. In the cramped setup it was difficult to avoid some interaction between the heatgun and the LED. The last four values are in reasonable agreement, and they have a mean$\pm 2\sigma$ of $2.1 \pm 0.7 \times 10^{-3}\,\mathrm{s^{-1}}$.

3.5.3 Calibrated spectroradiometer

To obtain a quantitative measure of the spectral irradiance in the chamber an ASD FS3-Max spectroradiometer was fitted with an integrating sphere to collect light from 2π steradians.[251] The instrument is manufacturer-calibrated for a certain fibre terminus, and the custom-made integrating sphere was calibrated separately. The calibration procedure used another integrating sphere illuminated at its entrance

3. CHAMBER SETUP FOR STUDY OF MERCURY
   OXIDATION KINETICS
3.5 Photolytic flux measurement
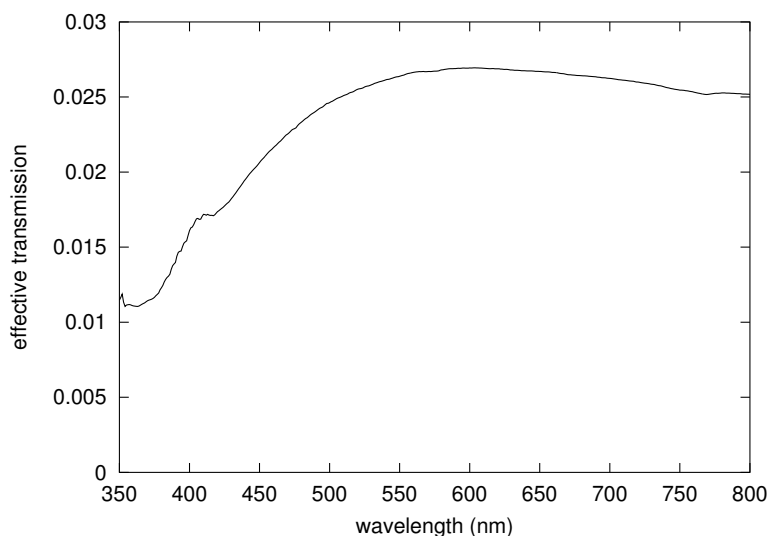
FIGURE 3.21: Effective transmission factor of the integrating sphere used to calibrate the chamber, including conversion from units of total incident flux to flux per 2π hemisphere.

aperture with the blue and UV LEDs used in the cavity and an ordinary halogen bulb in order to provide a flat-field radiance for each wavelength to be calibrated. The ratio of the measurements with the bare fibre at the exit of calibration sphere, to the measurements made with the first sphere attached to the fibre end is the transmission factor (Figure 3.21). This calibration curve was also checked by comparison to outdoor measurements referenced to a whole sky radiometer. Since the sphere was coated internally with Avian B (Avian Technologies, NH,USA), the transmission closely resembles the reflectivity of the Avian B coating shown in Figure 3.14(c).

The calibrated sphere-fibre device was placed at each point on a $3 \times 3 \times 3$ grid inside the chamber, where each point was at the centre of one of 27 imaginary, equal, boxes making up the chamber. The alignment of the integrating sphere was checked by removing the chamber insulation and lining up with markers. The panels were then replaced and the spectrum recorded (acquisition time $= 31\,\text{s}$). By orienting the sphere so that its aperture was directed upwards and then downwards, the downwelling and upwelling radiation at each point was obtained. All the collected spectra are shown together in Figure 3.22. The group of lower spectra correspond to the upwelling radiation from the sides and bottom of the chamber. These are all lower and closer to one another than the radiation downwelling directly from the lights.

Since the integrating sphere has an excellent cosine response, adding the upwelling and downwelling spectra together gives the total illumination at that point at each wavelength. The average of each of these points is then the total photon flux in the
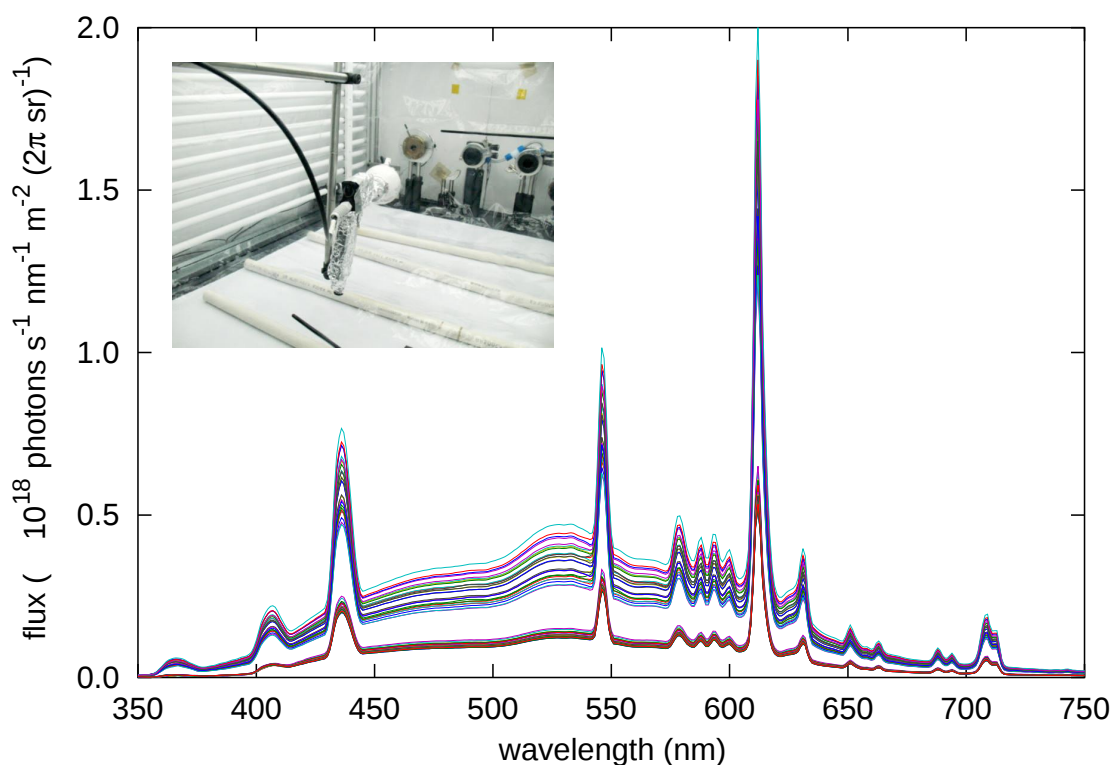
Figure 3.22: All 54 spectra of illumination measured at each point of the $3 \times 3 \times 3$ grid in the chamber facing up and down. The lower group of spectra are the upwelling measurements. The downwelling radiation is always larger but more variable. Inset is a photo of the pistol-shaped fibre holder with the integrating sphere attached.

chamber. To turn these spectra into a photolysis rate, they must be multiplied by the absorption cross-section and quantum yield (Equation 3.9). The Br_2 reference spectrum was convoluted with the slit function of the ASD spectrometer, which, from inspection of the spectra of the lamps, was estimated as a Gaussian curve with FWHM of 3 nm. The quantum yield of Br_2 photolysis into two atoms is approximately unity in the region 200–680 nm.[252] Since the Br_2 absorption is relatively small outside these wavelengths it is reasonable to assume that the photolytic quantum yield is unity across the whole Br_2 absorption spectrum in its measured range of 350–650 nm. The values of J_{Br_2}, calculated at each point of the grid, are shown in Figure 3.23.

Each level in the chamber is plotted as a surface. Since the top level is closest to the lights, j_{Br_2} was largest there so its layer in the plot is also displayed on top. The flux at the bottom of the chamber is 20% lower than at the top. This difference could have been reduced by coating the white paper at the bottom of the chamber in the same manner as the cooling pipes, but the homogeneity of j_{Br_2} was deemed sufficient. The flux at the north end is slightly lower than the south end. Since the north wall of the chamber had to be removed to allow the device access and could
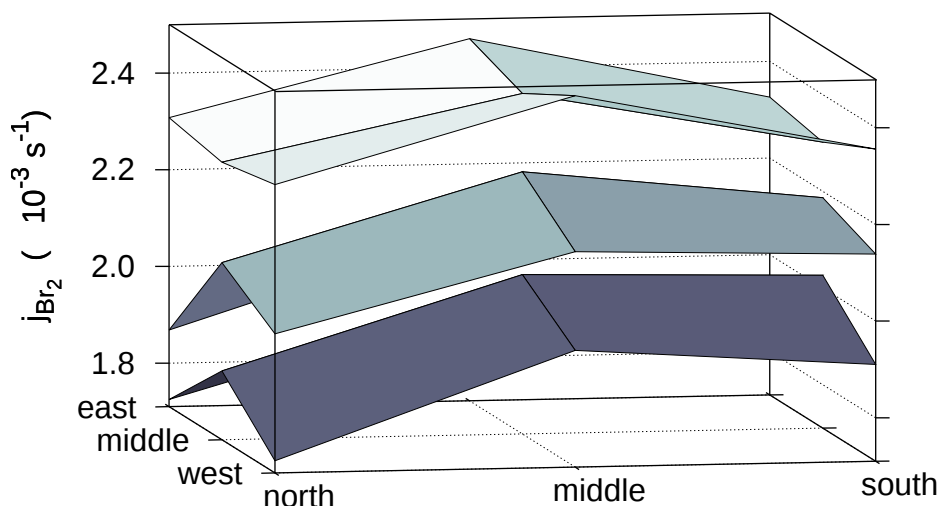
FIGURE 3.23: Plot of j_{Br_2} measurements at 27 points in the chamber. On the vertical axis is j_{Br_2}, which happens to coincide with height. The colours are also related to height arbitrarily.

only be re-covered by small pieces of polystyrene, which were not coated with a UV reflective material, j_{Br_2} at the north end was lower than the south end by a factor of 5%, but the impact on the overall mean is only 2%. Given the overall uncertainty in this determination no correction was made.

This calibration was carried out at the beginning and in the middle of the campaign. These yielded j_{Br_2} of 2.21 and $2.11 \times 10^{-3} \, \text{s}^{-1}$. The latter is 5% lower, consistent with the relative measurements of the photodiode during the two experiments. These values agree very well with the j_{Br_2} from the standard reaction of $2.1 \pm 0.7 \times 10^{-3} \, \text{s}^{-1}$. A value of $2.1 \times 10^{-3} \, \text{s}^{-1}$ was assumed in all simulations.

3.6 Experimental procedure

3.6.1 Chamber preparation

The chamber was flushed overnight with a Tekran 1100 zero air generator. This device is effective in removing Hg, but it does not scrub NO_x or H_2O. Before each experiment the chamber was flushed for at least 2 hours (6 chamber volumes) of UltraZero air (Airgas, Reno, NV, USA) reducing the concentration of any remaining contaminant by a factor of at least 400.

3.6.2   Typical experiment

Several different procedures were used throughout the campaign as the experiments were optimised. In a typical experiment, a sample of Br_2 vapour (20 μL–1 mL, 22 °C) was injected first (yielding a $[Br_2]$ of 1–100×10^{11} molec cm^{-3} or 5–500 ppb), followed by at least 10 minutes to establish a wall loss and ensure that the systems were working correctly. If the $[Br_2]$ injection failed to give a response in the CEAS system it was repeated. Then 2.5 mL Hg vapour was injected (19.1 °C, yielding an [Hg] of 100 ng m^{-3} or 2×10^8 atoms cm^{-3} or 10 ppt), followed by another 10 minutes to establish a background reaction rate arising from residual Br atoms remaining from Br_2 photolysis outside the chamber (the 'dark' reaction). The chamber lights were switched on to warm up and 3 minutes later the black shutter was removed to allow light into the chamber. The decay of Hg was followed until the [Hg] dropped below the detection limit (≈ 1 ng m^{-3}), taking between 30 s to 30 min. If time permitted then another injection of Hg was made to measure the reaction rate in a 'dirty' chamber, otherwise the chamber was flushed in preparation for the next experiment.

Overall there were 67 injections of Hg and 71 of Br_2 into the chamber. There were 17 experiments with NO_2 (4 of which also contained Hg and Br_2), 5 with O_3, 5 with extra FEP film, 3 with sea-salt aerosol and 5 with amylene. Most experiments were at room temperature (298±2 K), while 8 were at 279±1 K and 6 were at 266±2 K. Each experiment could have illumination on, off or both if there was no reaction detected in the dark. Some single experiments had multiple injections of Hg, with all but the first reaction analysed separately (Section 4.5.7). A total of 125 Hg depletion curve were fitted, including wall losses, dark reactions and commissioning tests.

3.6.3   Injection sequence

Most experiments used some combination of injecting Br_2, Hg and switching on the photolysis lamps. Of the six possible permutations of these events only three were used (the lights were never on during Br_2 injection). Most commonly, the order was Br_2 first, then Hg, then lights on. Primarily this was due to the unreliability of the Br_2 injections, and by injecting it first the $[Br_2]$ could be verified before proceeding. Hg was injected first when the CRDS needed to be recalibrated against the Tekran monitor, and also to measure a wall loss rate for Hg. In both these permutations the lights were switched on last, so there would not be a steady state [Br] in the

initial phase of the reaction. The analysis in Chapter 4 takes account of this non equilibrium [Br].

In the third permutation the lights were switched on after Br_2 injection but before Hg, allowing the formation of a steady-state of [Br]. The disadvantage of this order is that the Hg was not properly mixed for the first 30 s of reaction. Mixing effects are not easily quantifiable, so in these experiments the first 30 s of [Hg] data could not be used for analysis. At the higher [Br_2], with Hg lifetimes of <30 s, the Hg had to be introduced before photolysis to be able to measure some part of the decay in a well mixed chamber. Unfortunately at these higher [Br_2] the Hg would also react in the dark during mixing, so neither sequence was without drawbacks.

3.7 Uncertainty Budget

3.7.1 Calibration

The NO_2 calibration determined the enhancement factor of the cavity which provides the basis for all the [Br_2] measurements. Any error present in the calibration will also be present in every experiment using that calibration.

The accuracy of the NO_x box is stated by the manufacturer as 2.5%. The precision seen during each calibration point was around 5%. As this noise was random it tends to cancel out with longer averaging times and more [NO_2] calibration points. The fitting of the α_{cav} spectra with the reference introduced more uncertainties. Due to the highly structured absorption spectrum of NO_2 and a strong cavity absorption signal, these uncertainties did not exceed 1–2%. The narrowband fit residual also averaged out over the spectrum, and did not systematically affect E (Figure 3.10).

A more dubious assumption is that the E remained constant between days. The peak value of E changed by no more than 10% from one week to the next, despite temperature cycling and realignments. We therefore assume 10% uncertainty in [Br_2] arising from the calibration, which is systematic for each week but random between calibrations.

3.7.2 Br_2 Injection

[Br_2] was not determined from the volume of the injection as this method was

extremely unreliable. In cases where there were multiple failed injections, some Br_2 may have been injected below the detection limit. Such cumulative small amounts of Br_2 would only be visible in the spectra if I_0 were taken before the injections. In practice I_0 was taken immediately before the successful injection to avoid spectral drifts. The extra uncertainty of the invisible injections, equivalent to the detection limit of 10^{11} molec cm^{-3}, was added manually.

3.7.3 Br_2 Retrieval

The fit of the reference Br_2 spectrum to the measured spectra yielded the ±95% confidence interval directly. This interval only represents the fit uncertainty, and there are other sources of error to consider. The transmission shift artefact described in 3.4 could cause large offsets in $[Br_2]$, but these could be detected easily, and mostly avoided by using the zero-offset fit and choosing a smaller averaging time slot closer to the injection. The fit uncertainty accounted for any remaining error. In the earlier experiments that had no correction for I_{LED}, it might be supposed that artefact like that in Figure 3.13 would invalidate the results entirely. However, in the two cavity setup the spectrometer was placed underneath the optical table, surrounded by cardboard boxes and packaging materials. The spectrometer was somewhat insulated from the air temperature changes caused by the air conditioning system. The estimated $[Br_2]$ range encompasses the measurements derived from both cavities, incorporating much of the possible artefact. As a result we can be confident the actual concentration lies within the stated range.

Another source of error arises from the wavelength calibration of the spectrometer. The spectrum of Br_2 in the observed region is a steep slope of nearly constant gradient. Small shifts in wavelength affect the observed spectra and derived $[Br_2]$. There are no significant features in the Br_2 spectrum to realign the wavelength as there are in the spectrum of NO_2, so the wavelength calibration measured at the end of each day with the Hg lamp had to be used unadjusted. Fortunately the wavelength calibration was stable to within one CCD pixel and usually did not change between days. The minimum detectable λ-shift of one pixel (0.25 nm), would cause an apparent change in $[Br_2]$ of 4%. Although short term wavelength shifts could be detected and compensated by a timely I_0 as described in Section 3.4, the drift of the wavelength calibration results in a relative shift of the reference Br_2 spectrum that cannot be compensated without knowledge of that shift. The error from a potential shift was accounted for by adding 5% extra uncertainty to the $[Br_2]$ retrieval.

3.7.4 Wall loss

Wall losses were seen to be negligible when the signal was stable enough over a long time period. To be sure of including the actual $[Br_2]$ in the given value, the lower limit of the error margin was lowered by a further 5% of the $[Br_2]$.

In total, $[Br_2]$ uncertainty came from the 95% confidence interval of the spectral fit, plus extra contribution from the NO_2 calibration (10%) and the wavelength shift (5%). These latter two are likely to be random and independent so they impart together an extra 11%:

$$\sqrt{0.1^2 + 0.05^2} = 0.11 \tag{3.18}$$

The lower margin of the $[Br_2]$ was also extended downwards to incorporate any wall loss. The effect of these extra uncertainties is only to lengthen the appearance of the error bars accordingly, the actual data point is not shifted.

3.7.5 Hg Concentrations

The CRDS system was calibrated regularly against a Tekran 2537 unit. The $[Hg]$ were accurate to within $\pm 2\,\mathrm{ng\,m^{-3}}$ whenever the laser was operating correctly. The only parameter derived from the $[Hg]$ time series was the first order decay rate, which does not require an accurate calibration. However, any baseline offsets could affect the relative change and its derived rate. These offsets could feasibly occur through changes in laser linewidth and diminished performance of the wavelength locking system. The sensitivity of the decay rate calculation to baseline offsets was checked by adding an artificial offset to example data. The rate of first order decay changed by around 10% for every $1\,\mathrm{ng\,m^{-3}}$ extra offset. Due to noise in the laser signal, offsets could not be determined much better than to $1\,\mathrm{ng\,m^{-3}}$. However, since the first order fits always assumed decay to zero $[Hg]$, the fits had a larger uncertainty when there was a significant offset. The wider confidence interval always accommodated the value from an optimal fit. Wall losses of Hg were orders of magnitude slower than most of the reactions, so no correction was made. The uncertainty was taken to be 2σ of the linear fit to logged data. This uncertainty does not include any potential systematic bias caused by the reaction not being first order, which will be dealt with separately in Section 4.7.

Chapter 4

Chamber results

4.1 Overview of chemical kinetics

Chemical reactions seldom happen in one neatly defined step. There are often many intermediates, back reactions, side reactions and competing processes. Separating each elementary step of an experimental system may not be possible, and for this reason the rate equation is experimentally defined. The most general reaction of a substance A with a concentration [A] and stoichiometry of a:

$$a\text{A} \xrightarrow{k} \text{products} \tag{R 4.1}$$

has a rate defined as

$$-\frac{1}{a}\frac{\text{d}[\text{A}]}{\text{d}t} = k[\text{A}]^x \tag{4.1}$$

where x is the order of reaction, effectively a measure of the sensitivity of the rate to the concentration, and k is the rate coefficient. The order of the reaction is an experimentally observed parameter, but it is related to the number of molecules involved in the slowest step of the overall reaction.

In a zero order reaction, $x = 0$, the rate does not depend on the concentration of the species [A] at all. Zero order reactions arise when the rate is completely determined by the concentration of another species such as a catalyst or enzyme. The rate may well be first order in the concentration of the catalyst, but it is still zero order in [A].

In a first order reaction, $x = 1$, the rate is linearly dependent on the species. These reactions are most common and occur when only one molecule of the species is involved in the dominant step of the reaction. The photolysis of Br_2 is an example,

where the rate is determined by the photon flux.

Second order reactions, where $x = 2$ are also common. For example the recombination reaction $2\,\mathrm{Br} \xrightarrow{M} \mathrm{Br_2}$ is second order in Br˙. The overall order, that is the sum of the orders of all the reactants, is often second or third order.

In reality, complex reactions may not have a clearly defined rate limiting step. The order of complex reactions may be a non-integer or vary with reaction conditions. There are a few assumptions that can help in building a chemical mechanism. If a reagent has an active form in rapid equilibrium with the initial form, then we can assume that there is a constant ratio between the initial form and the active form. The photolysis and recombination of $\mathrm{Br_2}$ is an example. An extension to pre-equilibrium is the steady state approximation, where the concentration of any intermediate can be regarded as invariant. The analysis in this chapter relies partly on a steady-state of Br˙, despite the many different reactions Br˙ could undergo. If one of the reactants is in a large (> 50) excess then its concentration will hardly change even at completion. Thus the fixed concentration can be incorporated into the rate constant, and the overall order for the reaction reduced. In the experiments below the $[\mathrm{Br_2}]$ is in excess, and the individual reactions can be described as pseudo-first order in Hg. By comparing multiple $[\mathrm{Br_2}]$, all in excess, the order in $[\mathrm{Br_2}]$ can be measured.

The above assumptions are convenient, and were essential in the days before computerised numerical analysis. These days it is straightforward to model a system such as the chamber without making these assumptions. In this chapter the chamber data will be analysed with several different models, from a simple one step reaction to a model with seven reactions. Real world environmental data would require even more steps to model successfully, but a brief comparison between the chamber results and the consequences for existing environmental models is made at the end of the chapter. The rate coefficients for the model reactions were taken from the literature and adjusted to the chamber conditions, as outlined in the next section.

4.2   Review of rates

Numerous theoretical and experimental studies of Hg kinetics have been summarised in two recent reviews.[253,254] There have been additional, more recent studies, not included in the existing reviews, and the purpose of this section is to review the literature for all potential reactions that Hg could undergo in the chamber conditions,

Table 4.1: List of reactions reviewed. Reactions with a labelled k_N rate are explicitly included in the chamber simulations.

Bromine Equilibrium :
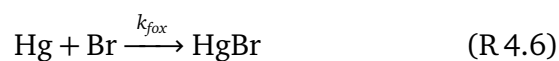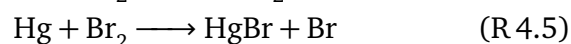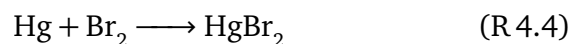
$$Br_2 \xrightarrow{j_{Br_2}} 2\,Br \tag{R 4.2}$$

$$2\,Br \xrightarrow[M]{k_{rec}} Br_2 \tag{R 4.3}$$

Hg^0 Oxidation :

$$Hg + Br_2 \longrightarrow HgBr_2 \tag{R 4.4}$$

$$Hg + Br_2 \longrightarrow HgBr + Br \tag{R 4.5}$$

$$Hg + Br \xrightarrow{k_{fox}} HgBr \tag{R 4.6}$$

HgBr Reduction :

$$HgBr \xrightarrow[\Delta]{k_{thm}} Hg + Br \tag{R 4.7}$$

$$HgBr \xrightarrow[h\nu]{} Hg + Br \tag{R 4.8}$$

$$HgBr + Br \xrightarrow{k_{abs}} Hg + Br_2 \tag{R 4.9}$$

Hg(1+) Oxidation :

$$HgBr + Br \xrightarrow{k_{cpa}} HgBr_2 \tag{R 4.10}$$

$$HgBr + Br_2 \xrightarrow{k_{cpm}} HgBr_2 + Br \tag{R 4.11}$$

$$HgBr + X \longrightarrow XHgBr \tag{R 4.12}$$

Reactions involving oxygen :

$$Hg + O_3 \longrightarrow HgO + O_2 \tag{R 4.13}$$

$$Hg + OH \longrightarrow HgOH \tag{R 4.14}$$

$$Hg + BrO \longrightarrow products \tag{R 4.15}$$

$$Hg + NO_2 \longrightarrow HgNO_2 \tag{R 4.16}$$

Other Reactions :

$$Hg + F_2 \,/\, Cl_2 \,/\, I_2 \longrightarrow products \tag{R 4.17}$$

$$HgBr + nH_2O \rightleftharpoons HgBr \cdot nH_2O \tag{R 4.18}$$
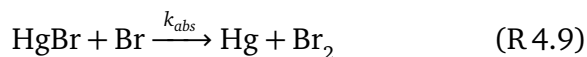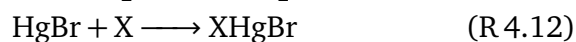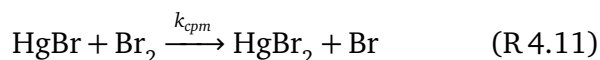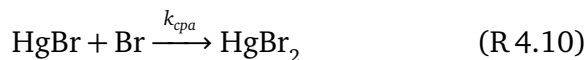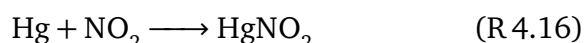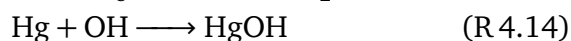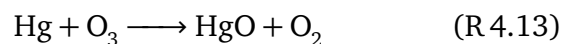
and collate the preferred values for each. Other reactions may be important in the environment, e.g. gas-liquid transitions, but these are neglected in this review as they were not important in the chamber conditions. Halogens are thought to constitute the most important species for Hg depletion,[107] and bromine is the only halogen present in large enough to cause AMDEs. Bromine is the main focus.

Some studies were excluded from this review. The experimental study of Greig

et al.[255] has been dismissed as having large systematic errors already,[256] and need not be considered further. The literature focussing on Hg reactions at the high temperature of coal combustion exhaust is somewhat separate from the environmental chemistry community. These industrial studies are typically concerned with efficiency of Hg removal rather than describing or measuring each reaction step, so are not directly comparable.[257–263] Two high temperature studies are included for comparison. Niksa et al.[264] extrapolated rates for bromine-mercury reactions from the analogous chlorine reactions, and did not consider some important processes such as HgBr dissociation. Wilcox and Okano[265] used reasonably high level *ab initio* methods to find rates at high temperatures. Their claimed range of validity is on the edge of the chamber temperature, but for comparison they are included anyway. As the authors themselves note however, the calculations in Balabanov et al.[266] are more accurate, whose values are preferred if there is a conflict.

Conversion of rates to chamber conditions

Many of the available studies are concerned with typical conditions in the Arctic or in coal combustion emission plumes. Neither of these are directly comparable to the conditions in the chamber, so often the published rate coefficients had to be extrapolated, sometimes beyond their stated range of validity. In particular, due to the altitude of 1500 m in Reno, the atmospheric pressure in the chamber was only 845 hPa, some 15% lower than standard atmospheric conditions.

Correcting for the pressure dependence is not straightforward as the observed rate does not always increase linearly with pressure. At low pressure the rate increases in a linear fashion, but at some pressure, known as the fall-off region, the rate levels out at a maximum known as the high pressure limit.[227] The actual pressures involved depend on the reaction, and extrapolating the rate to different conditions may not be accurate. A higher pressure will not always increase the rate but a lower pressure may reduce it to some extent.

Temperature also affects the reaction rate due to changes in buffer gas density. The density is proportional to $1/T$, so the air in the chamber is 13% more dense at 265 K than at 300 K. However, the molecules are moving more slowly so the collision frequency is reduced by a factor of $\sqrt{T}$, yielding a rate 6% slower (for a barrierless reaction).

The Troe expression can correct for pressure dependence,[267] but requires knowledge of the high and low pressure limits for each reaction. Other methods do not require

such information, but were beyond the scope of this work.[268,269] If an expression was not given in its 3rd body form, while other studies did, then the assumption was that the reaction was in the low pressure regime and so the rate coefficient was corrected by multiplying by the ratio of the density in the chamber to the air density for which the rate was defined. When a reaction was stated as being in the high-pressure limit no additional pressure adjustment was made.

Most theoretical studies use a noble gas as it much simpler to model. Air is 99% diatomic gas, so it is more efficient at supplying or removing the energy of reaction. As there is no simple way to correct quantitatively for the different gases, the rate was not adjusted and the identity of the gas noted.

4.2.1   Br source

R 4.2 $Br_2 \xrightarrow[h\nu]{j_{Br_2}} Br + Br$
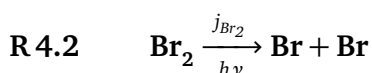
The photolysis of Br_2 has been reviewed by the IUPAC sub-committee on gas phase kinetics.[252] Their recommended photolysis cross-section was used in this study. As described in Section 3.5, the measurements of j_{Br_2} from the spectral irradiance in the chamber and the decay of $[Br_2]$ in the presence of a $Br^\cdot$ scavenger yielded similar photolysis rates. A j_{Br_2} value of $0.0021\,s^{-1}$ is assumed throughout this study.

R 4.3 $Br + Br \xrightarrow[M]{k_{rec}} Br_2$
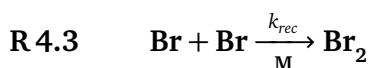
There are several studies on the recombination of $Br^\cdot$, which have been reviewed in Donohoue et al.[256] and some of the rates are listed in Table 4.2. In many of the older studies there is a lack of standardisation in the expression for the rate coefficient. The modern standard is to define the rate for the change in a single stoichiometric unit,[270] whereas the work of Ip and Burns[271] uses a rate based on the stoichiometry as it appears in the equation used. Concerning $Br^\cdot$ recombination, this leads to a rate twice as fast if reported as the decay in $[Br]$ rather than $0.5[Br]$. This factor is corrected for in applying the rates to the chamber. As has been noted,[256] DeGraff and Lang[272] reported rates that were close to twice that of the others. The simplest explanation for this is an accidental miscalculation or misprint.

All the reactions in the chamber are carried out in air, which could lead to faster recombination than the pure N_2 used in much of the literature. In the one study that used both N_2 and O_2, the ratio k_{O_2}/k_{N_2} was 1.7–1.8, so k_{AIR} would be about 15%

faster than k_{N_2}. However, the efficiencies of Br_2 or CCl_4 as the third bodies give rates on the order of ten times faster than for Ar,[272] and the recombination of I is twice as fast in a pure O_2 atmosphere as in N_2.[273]

While this reaction is almost irrelevant in the environment (Br˙ reaction with O_3 is much faster), it is important to the chamber work. The uncertain effect of the third body will be reconsidered later.

4.2.2 Oxidation of Hg

R 4.4 $\mathbf{Hg + Br_2 \longrightarrow HgBr_2}$
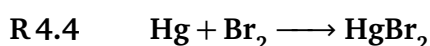
Table 4.3 shows the rates of k_{dir}, the direct insertion in one step. Ariya et al.[159] found that Hg had a lifetime of 20 s at a $[Br_2]$ of 20 ppm in a 650 mL flask. However, the authors noted very strong wall effects and that their derived rate of $10^{-17}\,cm^3\,molec^{-1}\,s^{-1}$ was only an upper limit. Sumner et al.[239] saw no reaction at all with 1-2 ppb Br_2 inside a large 17.3 m^3 chamber. From other experiments in that chamber it appears that the dilution rate was so high that no reaction could have been detected if were slower than about $10^{-17}\,cm^3\,molec^{-1}\,s^{-1}$. The high-level theoretical study of Balabanov et al.[266] found the reaction to be essentially impossible.

R 4.5 $\mathbf{Hg + Br_2 \longrightarrow HgBr + Br}$

The rates for this reaction are listed in Table 4.4. Balabanov et al.[266] found this reaction as unlikely as the direct insertion, which is not surprising as the two reactions share the same large barrier of breaking apart the Br_2 molecule. This reaction is not included in the chamber simulations. The difference between the *ab intio* rates and those extrapolated from the analogous Cl reactions indicates that extrapolation may not be reliable method, and this may apply to other rates of the same study.

R 4.6 $\mathbf{Hg + Br \xrightarrow{k_{fox}} HgBr}$
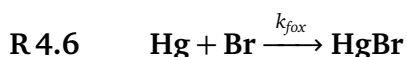
Since the direct insertion and abstraction reactions are virtually impossible, the oxidation by Br˙ is likely the first step in Hg oxidation in the chamber. The reaction has been central to many experimental and theoretical studies. Table 4.5 lists

the available rates. The two experimental studies of Ariya et al.[159] and Spicer et al.[274] measured relative rates. This method is likely to be influenced by secondary chemistry, and the derived rates are unreliable. The rate of Donohoue et al.[256] is the most widely used in models, however an updated rate with lower uncertainty is also available.[158]

The theoretical rate of Shepler et al.[275] used the largest basis set and most advanced level of theory of the rates surveyed, however their use of Ar as the third body may mean their rate is too slow for the chamber. An experimental study using both He and N_2 found that N_2 is yields a rate 3.6 times faster than He.[256] The theoretical studies give rates that are generally faster than the experimental studies, although the agreement between them is reasonable when compared to the orders of magnitude difference for other reactions.

4.2.3   Reduction of HgBr

R 4.7 $\mathbf{HgBr} \xrightarrow[\Delta]{k_{thm}} \mathbf{Hg + Br}$
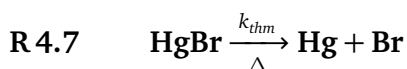
The thermolysis of HgBr is regarded as a critical process that impedes the oxidation of $Hg^0(g)$. Table 4.6 summarises the known rates. The PhD dissertation of Donohoue[158] describes the only known experimental measurements of the thermolysis of HgBr, based on direct measurements of [HgBr]. To create a measurable [HgBr] the [Hg] was in excess, which meant that temperatures were higher than those used in our chamber, and the extrapolation to our conditions is somewhat dubious. The rate of Dibble et al.[106] is used in the model here, but the effect of a much faster rate is discussed later.

R 4.8 $\mathbf{HgBr} \xrightarrow{h\nu} \mathbf{Hg + Br}$

The photolysis of HgBr is mentioned briefly by Goodsite et al.[276] as an alternative HgBr loss process, and calculations[277] have shown that HgBr is vulnerable to photolysis. Krauss and Stevens[278] calculated the photolysis cross-section of HgBr. Though the computational study dates from 1981 the methods should be qualitatively accurate (K Petersen, Pers. Comm.). Using this cross section and the photolytic flux measurements of Section 3.5 yields a photolysis rate of $2 \times 10^{-3}\,s^{-1}$. This rate is not included explicitly in the chamber model, as it is equivalent to modifying the thermolysis rate.

R 4.9 $\mathbf{HgBr + Br} \xrightarrow{k_{abs}} \mathbf{Hg + Br_2}$
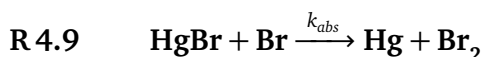
There is only a tiny barrier to HgBr reacting with a radical. It can go onto form HgBr$_2$ (R 4.10) or, in this reaction, return to the elements. The rates are listed in Table 4.7, and are two orders of magnitude faster than the completion to HgBr$_2$. This is not surprising as the extra product makes the reaction more favourable, and is probably at its high pressure limit. The reaction has been neglected from most models, yet the process could be important if there is a high [Br] and no other sink of HgBr.

4.2.4   Oxidation of Hg(1+)

R 4.10 $\mathbf{HgBr + Br} \xrightarrow{k_{cpa}} \mathbf{HgBr_2}$
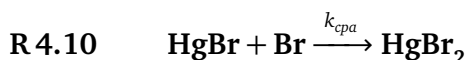
The second oxidation step is important to stabilise the HgBr. The rates are summarised in Table 4.8. Goodsite et al. [276] states that this reaction is close to its high-pressure limit at 1 atmosphere, therefore no correction is made for the lower air pressure of the chamber. There is no record of what the rate from Calvert and Lindberg [279] was based on (S Lindberg, Pers. Comm.). It is mentioned here only because it was included in the MECCA box model, [280] and used in several modelling studies [281,282] despite more accurate calculations being available. In simulations where there is little other than Br$_2$ to quench the unstable intermediate, this reaction is important in determining the overall rate and its temperature dependence. The rate of Balabanov et al. [266] is used here, but the effect of slower rates is discussed in Section 4.8.

R 4.11 $\mathbf{HgBr + Br_2} \xrightarrow{k_{cpm}} \mathbf{HgBr_2 + Br}$

The high [Br$_2$] in the chamber could make completion bv the Br$_2$ molecule important. The rates are summarised in Table 4.9. This reaction has not been included in environmental mechanisms as there is virtually no Br$_2$ in the atmosphere. It is thought to be important in coal stack emissions control, where Br$_2$ is used to oxidise Hg in the dark. However there are only two theoretical studies, both of which show large discrepancies with more accurate studies when comparing rates of the other reactions.

R 4.12   HgBr + X $\longrightarrow$ BrHgX

Thermodynamic calculations show that the second oxidation by BrO, NO_2, HO_2, ClO and O_3 is favourable.[106,275] Some of these radicals are abundant in the atmosphere—up to ppb levels—and it now seems likely that the second oxidation of Hg will occur exclusively with these rather than an extra Br atom. Since the barrier to radical reactions is typically low the rate is likely to be fast, and one estimate[283] is of the order $10^{-11}\,cm^3\,molec^{-1}\,s^{-1}$. This reaction pathway has not been considered until recently, and there is a lack of detailed studies on the kinetics.

4.2.5 Reactions involving Oxygen

Oxygen chemistry is quite well understood. Ozone and the hydroxyl radical oxidise the bulk of organic pollutants and it is natural to assume they might have a role in Hg oxidation. However, there has been much confusion over the stability of the main purported product, HgO(g). JANAF data tables show a large, stable binding energy with respect to its ground state atoms of $268\,kJ\,mol^{-1}$, and a mass-spectrometric study found a value of $221\,kJ\,mol^{-1}$.[284,285] However, the JANAF data apparently came from extrapolating the behaviour of similar compounds[284] and it is thought that the mass-spectrometric values actually measured a dimer or oligomer of HgO, which would be more stable.[286]

One theoretical study showed that the molecule HgO(g) does not exist,[286] and more extensive high level calculations found the binding energy to be only 17 $kJ\,mol^{-1}$.[284] It is therefore not known whether the species HgO(g) is important to Hg depletions.

R 4.13   Hg + O_3 $\longrightarrow$ HgO + O_2

Since ambient O_3 levels are relatively high, if there were a fast reaction between Hg and O_3 there would be have to be very large emissions or re-emissions of Hg to maintain the observed atmospheric [Hg], which makes a fast reaction unlikely. The theoretical studies discussed above found that HgO(g) is probably unstable, and that HgO will decompose rapidly unless stabilised by some other reaction. The reaction as written is thought to be endothermic by $90\,kJ\,mol^{-1}$.[285] The mechanism may involve the van der Waals complex HgO_3 rather than the molecule HgO.[286,287] Nevertheless some reaction is observed, and there is broad consistency between rates shown in Table 4.10. The presence of carbon monoxide accelerates the reaction,

probably due to the stabilisation of the HgO(g) or HgO$_3$ intermediates. Where a surface is available, the HgO can be deposited and aggregates of HgO(s) have been observed.[288] One theoretical study[289] found that the reaction is around 10^6 times faster with the involvement of two water molecules compared to just one, albeit using only small basis sets. An experimental test of the humidity dependence found only a weak correlation between humidity and rate, with only condensed water on the walls giving a large acceleration in the latter half of the reaction.[288]

R 4.14   Hg + OH ⟶ HgOH
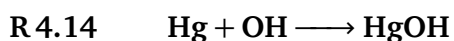
HO$^{\cdot}$ is the most important oxidant in the atmosphere. Subir et al.[253] reviewed its role in Hg oxidation. Theoretical studies have shown that the oxidation of Hg by HO$^{\cdot}$ is unlikely. This reaction is not studied here and HO$^{\cdot}$ would be almost absent from the chamber.

R 4.15   Hg + BrO ⟶ HgOBr / HgO / BrHgO / HgBr

The direct oxidation by BrO has long been speculated as the primary mechanism of Hg depletion. BrO is known to cause ozone depletion events, and these often occur at the same time as Hg depletion events. Despite early assumptions that the reaction with BrO was the main driver of Hg depletion, no theoretical study has been able to find a feasible reaction trajectory. Both addition products HgOBr and HgBrO are unstable,[106,290] and both abstraction products HgO and HgBr can only be created endothermically.[291] The insertion product BrHgO is stable, however the barrier for direct Hg insertion into BrO is too high for a feasible reaction, similar to the direct insertion into Br$_2$ (R 4.4).

Nevertheless, experimental rates for the reaction have been reported, and they are summarised in Table 4.11. In experimental studies it is very difficult to separate the reactions of BrO and Br, since there will always be a lot of Br in the presence of BrO due to photolysis and self-reaction of BrO. Without detailed information on photolytic fluxes, [O$_3$] and analysis including a complete BrO chemical model, it is not possible to determine what reaction was actually being measured. Raofie and Ariya[160] analysed solid deposits of the reaction with BrO with MALDI-TOF and found m/z peaks corresponding to HgO, HgBr and HgOBr. None of these species were necessarily formed in the gas phase during the reaction. Due to the lack of theoretical justification for a direct reaction, it is likely that Hg oxidation is always

initiated by Br˙ rather than BrO.

R 4.16 $\mathbf{Hg + NO_2 \longrightarrow HgNO_2}$
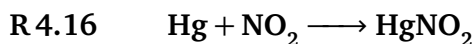
Similar to the reaction with BrO, the direct addition is very unlikely. Atmospheric and chamber evidence suggests it is unimportant.[285] Like many other abundant radicals however, there is a strong possibility that NO_2 takes part in the second oxidation step $HgBr + NO_2 \longrightarrow BrHgONO$.[106]

4.2.6   Other reactions

R 4.17 $\mathbf{Hg + F_2\ /\ Cl_2\ /\ I_2 \longrightarrow products}$
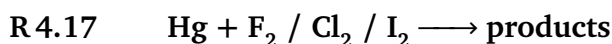
Fluorine gas can react with Hg, but only in the dark as fluorine atoms react with water much more quickly than with Hg.[239] It is unlikely that any reactive fluorine species would be long lived enough to contribute to Hg depletion.

Chlorine has been studied extensively as it is the key radical driving stratospheric ozone depletion. There are many theoretical and experimental studies of its participation in Hg oxidation.[253,254] Chlorine may be a significant driver of Hg depletion in the stratosphere where Cl˙ can be abundant, but the tropospheric [Cl˙] is too low for this route to be significant. It is not considered further in this study.

Iodine has been found to react slowly with Hg.[292] In marine environments there are commonly several ppt of I_2,[293] and due to the large photolytic cross-section many of those molecules will be photolysed. The initial product of Hg oxidation, HgI, is even more unstable than HgBr so it is not likely that I˙ can initiate the Hg oxidation.[294] I˙ or IO may assist with the second oxidation like other radicals (R 4.12). One model of field data fitted better when including iodine chemistry.[283] These reactions were not studied in our chamber, although in principle I_2 and IO are easier to detect with CEAS than Br_2 and BrO due to the highly structured absorption spectra of I_2 and IO at visible wavelengths.[216]

R 4.18 $\mathbf{HgBr + nH_2O \rightleftharpoons HgBr \cdot nH_2O}$
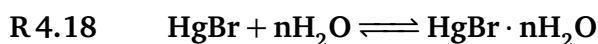
The effect of water vapour is believed to underlie some of the uncertainties of Hg depletion reactions. If HgBr were to dissolve in water on aerosol it could be further oxidised by many aqueous species. The interaction of HgBr with water has been

proposed as a mechanism that would extend its lifetime, giving it further opportunity to react before decaying back to its elements. The only study of such micro-solvation is a high level theoretical calculation, finding that the reaction

$$Hg + Br + n \cdot H_2O \longrightarrow HgBr \cdot nH_2O \tag{R 4.19}$$
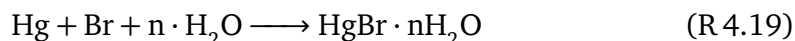
has an enthalpy of -68, -74, -83 and $-77\,kJ\,mol^{-1}$ with 0,1,2 and 3 water molecules present respectively. While water certainly makes the reaction more favourable the difference is not enormous, and in the dry environment of the chamber very few HgBr molecules would be hydrated. Using an estimated entropy of condensation of $-3R$, then for $n = 2$ at 280 K $\Delta G = 8\,kJ\,mol^{-1}$, and $K_p = 30\,bar^{-1}$. The ratio of hydrated to non-hydrated HgBr is then

$$\frac{[HgBr \cdot 2\,H_2O]}{[HgBr]} \approx 30 \times [H_2O] \tag{4.2}$$

Since the chamber was flushed with UltraZero air there would have been only trace quantities of water present. The measured humidity of lab air was around 4000 ppm (Dew point $-5\,°C$, or RH of 15%). Flushing with dry air (UltraZero air is rated to $< 2\,ppm$) would not reduce the humidity to less than a few ppm. At 10 ppm water vapour the proportion of hydrated HgBr would be only 3×10^{-4} (T Dibble, Pers. Comm.). In humid air with $[H_2O] = 10\,000\,ppm$, the hydration of HgBr may be important.

TABLE 4.2: R 4.3 $Br + Br \xrightarrow[\text{M}]{k_{rec}} Br_2$
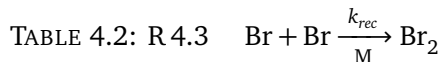
Units are **A**: $L^2\,mol^{-2}\,s^{-1}$, **B**: $cm^6\,molec^{-2}\,s^{-1}$

Reference	Rate (**Unit**)	T (K)	chamber range $(\times 10^{-13}\,cm^3\,molec^{-1}\,s^{-1})$	third body (Torr)
Ip and Burns[271]	$(9.767 \pm 0.021) - (1.583 \pm 0.057)\log(^T/_{300})$ **A**	300–2985	2.4(0.2)–1.6(0.1)	$O_2 \approx 100$
Ip and Burns[271]	$(9.499 \pm 0.034) - (2.208 \pm 0.253)\log(^T/_{300})$ $+(0.889 \pm 0.405)\log^2(^T/_{300})$**A**	300–1275	1.4(0.1)–0.89(0.05)	$N_2 \approx 100$
DeGraff and Lang[272]	$(3.3 \pm 0.3) \times 10^9$ **A**	$\approx$300–400	2.1(0.2)–1.9(0.2)	$N_2 \approx 10$–400
DeGraff and Lang[272]	$(4.2 \pm 0.4) \times 10^9$ **A**	$\approx$300–400	2.7(0.3)–2.4(0.3)	$CO \approx 10$–400
Donohoue et al.[256]	$4.31 \pm 0.21 \times 10^{-33} \times {^T/_{298}}^{-2.77\pm0.30}$**B**	243–298	1.5(0.1)–0.86(0.04)	$N_2 \approx 200$–600

TABLE 4.3: R 4.4 $Hg + Br_2 \longrightarrow HgBr_2$
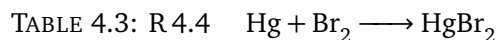
‡Reported units are actually $cm^3\,mol^{-1}\,s^{-1}$ but it is clear that the authors are misusing the SI symbol mol to mean molecule.

Reference	Rate ($cm^3\,molec^{-1}\,s^{-1}$)	T (K)	chamber range $(\times 10^{-31}\,cm^3\,molec^{-1}\,s^{-1})$	Method
Ariya et al.[159]	$< 1 \times 10^{-17}$	298	27(4)	Direct Br_2 UV absorption
Sumner et al.[239]	no reaction	NA	none	Direct, Lumex extraction
Balabanov et al.[266]	2.74×10^{-31} ‡	298	2.7	icMRCI+Q/AVTZ/CBS +SO/ μVT

Table 4.4: R 4.5 $\quad$ Hg + Br$_2$ $\longrightarrow$ HgBr + Br

Units **A**: cm^3 molec^{-1} s^{-1} (again, the authors used mol to mean molecules rather than moles),
B: cm^3 mol^{-1} s^{-1} and R has units of kcal mol^{-1}.

Reference	Rate (**unit**)	T (K)	chamber range ($\pm$) ($\times 10^{-31}$ cm^3 molec^{-1} s^{-1})	Method
Balabanov et al.[266]	3.9×10^{-31} **A**	298	3.9	icMRCI+Q/AVTZ/CBS +SO/ QCT
Niksa et al.[264]	$1.15 \times 10^{14} \cdot e^{31.8/RT}$ **B**	$\approx$400-1400	0.0000038–0.014	Extrapolation from Cl rxns
Wilcox and Okano[265]	$9.76 \times 10^{14} \cdot e^{(26.49/RT)}$ **B**	298–2000	0.88–810	CCSD(T) /AVTZ / VTST

TABLE 4.5: R 4.6 $Hg + Br \xrightarrow{k_{fox}} HgBr$

‡Overall rate for whole depletion, assumed here to apply to this step only as all products removed to walls.
Units: **A**: $cm^3 \, molec^{-1} \, s^{-1}$, **B**: $cm^6 \, molec^{-2} \, s^{-1}$, **C**: $cm^3 \, mol^{-1} \, s^{-1}$

Experimental studies

Reference	Rate (**unit**)	T (K)	chamber range (±) ($\times 10^{-13}$**A**)	Method
Ariya et al. [159]‡	$3.2 \pm 0.4 \times 10^{-12}$ **A**	298	27(4)	relative CH_3Br photolyisis, UV absorption
Spicer et al. [274], via [256]	9.7×10^{-13} **A**	298	9.3–8.0	relative, Luminex extractive [Hg]
Donohoue et al. [256]	$(1.46 \pm 0.34) \times 10^{-32}$ $\times (T/298)^{-(1.86 \pm 1.49)}$ **B**	243–293	4.4(1.6)–2.9(0.6)	flash photolysis of Br_2, LIF, N_2
Donohoue [158]	$1.49 \pm 0.12 \times 10^{-32}$ $\times (T/298)^{-(1.76 \pm 0.5)}$ **B**	243–420	4.5(0.6)–3.0(0.3)	flash photolysis of Br_2, LIF, N_2

Theoretical studies

Reference	Rate (**unit**)	T (K)	chamber range (±) ($\times 10^{-13}$**A**)	Method
Khalizov et al. [295]	$1.01 \times 10^{-12} \cdot e^{209.03/T}$ **A**	not recorded	23–20	CCSD(T)/ ECP60MWB/ CBS+SO/ Langevin
Goodsite et al. [276]	$1.1 \times 10^{-12} \cdot (T/298)^{-2.37}$ **A**	180–400	13–9.1	B3LYP/ CEP-121G/ RRKM
Goodsite et al. [296]	$1.5 \times 10^{-32} \cdot (T/298)^{-1.76}$ **B**	200–300	4.5–3.0	B3LYP/ CEP-121G/ RRKM
Shepler et al. [275]	$4.07 \times 10^{-32} \cdot e^{(112(1/T - 1/298))}$ **B**	200–400	10.1–8.3	CCSD(T)/ AVTZ/ CBS+CV+SO+LS/ QCT
Niksa et al. [264]	$6.94 \times 10^{14} \cdot T^{0.5}$ **C**	≈400-1400	7.3–6.8	Extrapolation from Cl rxns
Wilcox and Okano [265]	$4 \times 10^{11} \cdot (T/298)^{-0.859}$ **C**	298–2000	6.3–5.6	CCSD(T) /AVTZ / RRKM

TABLE 4.6: R 4.7 $\quad HgBr \xrightarrow[\Delta]{k_{thm}} Hg + Br$

Units **A**: s^{-1}, **B**: $cm^3\,molec^{-1}\,s^{-1}$, **C**: s^{-1} and R has units of $kcal\,mol^{-1}$

†Upper uncertainty margin allows for error $> 100\%$, if all errors acted in the same direction, lower bound used here.

‡as no equation is provided, these are the experimental data under the conditions listed.

Reference	Rate (**unit**)	T (K)	chamber range ($\pm$) ($\times 10^{-3}\,s^{-1}$)	Method
Goodsite et al. [276]	$1.2 \times 10^{10} \cdot e^{(-8357/T)}$ **A**	180–400	0.13–9.6	B3LYP/CEP-121G/RRKM
Goodsite et al. [296]†	$4.0 \times 10^{9} \cdot e^{(-7292/T)}$ **A**	200–300	2.2–94	B3LYP/CEP-121G/RRKM
Shepler et al. [275]	$1.95 \times 10^{-20} \cdot e^{(-7670(1/T - 1/298))}$ **B**	200–4000	10.6–471	CCSD(T)/ AVTZ/ CBS+CV+SO+LS/ QCT
Dibble et al. [106]	$(1.6 \pm 0.37) \times 10^{-9}$ $\times (T/298)^{-(1.86\pm1.49)} \times e^{-(7801\pm201)/T}$ **B**	243–293	4.5(2.6)–164(100)†	detailed balance with k_{fox} from Donohoue et al. [256]
Wilcox and Okano [265]	$4.57 \times 10^{10} \cdot e^{(15.64/RT)}$ **C**	298–2000	2.8–160	CCSD(T) /AVTZ / RRKM
Donohoue [158]	‡375(50) and 500(120) **A**	360 and 420	$\approx 200\,000$–$300\,000$	600 Torr N_2

TABLE 4.7: R 4.9 $\quad HgBr + Br \xrightarrow{k_{abs}} Hg + Br_2$

Units **A**: $cm^3\,molec^{-1}\,s^{-1}$, **B**: $cm^3\,mol^{-1}\,s^{-1}$ and R has units of $kcal\,mol^{-1}$.

Reference	Rate (**unit**)	T (K)	chamber range ($\pm$) ($\times 10^{-11}\,cm^3\,molec^{-1}\,s^{-1}$)	Method
Balabanov et al. [266]	4.52×10^{-11} **A**	298	4.52	icMRCI+Q/AVTZ/CBS +SO/ QCT
Wilcox and Okano [265]	$1.38 \times 10^{14} \cdot e^{(\approx 0/RT)}$ **B**	298–2000	23	CCSD(T) /AVTZ / VTST

Table 4.8: R 4.10 $\quad HgBr + Br \xrightarrow{k_{cpa}} HgBr_2$

Units **A**: $cm^3\,molec^{-1}\,s^{-1}$, **B**: $cm^3\,mol^{-1}\,s^{-1}$, R in $kcal\,mol^{-1}$
†no equation given, these are experimental data at the given conditions
‡no record exists of the method of estimation (S. Lindberg, Pers Comm.)

Reference	Rate (**unit**)	T (K)	chamber range ($\pm$) ($\times 10^{-10}\,cm^3\,molec^{-1}\,s^{-1}$)	Method
Donohoue [158]	$3.5(1.0)$–$3.0(1.0) \times 10^{-10}$ **A**	360 and 420	5–4	600 Torr N_2
Calvert and Lindberg [279]	3×10^{-12} **A**	273	0.03	Estimation‡
Goodsite et al. [276]	$2.5 \times 10^{-10}\,(T/298)^{-0.57}$ **A**	180–400	2.7–2.4	B3LYP/CEP-121G/RRKM
Balabanov et al. [266]	1.05×10^{-10} **A**	298	1.05	icMRCI+Q/AVTZ/CBS +SO/ QCT
Niksa et al. [264]	$8.83 \times 10^{14} \cdot T^{0.5}$ **B**	$\approx$400-1400	0.0092–0.0086	Extrapolation from Cl rxns
Wilcox and Okano [265]	$2.00 \times 10^{12} \cdot e^{9.18/RT}$ **B**	298–2000	0.0095–0.035	CCSD(T) /AVTZ / RRKM

Table 4.9: R 4.11 $\quad HgBr + Br_2 \xrightarrow{k_{cpm}} HgBr_2 + Br$

Reference	Rate ($cm^3\,mol^{-1}\,s^{-1}$)	T (K)	chamber range ($\pm$) ($\times 10^{-13}\,cm^3\,molec^{-1}\,s^{-1}$)	Method
Niksa et al. [264]	$1.11 \times 10^{14} \cdot e^{0.5/RT}$	$\approx$400–1400	120–160	Extrapolation from Cl rxns
Wilcox and Okano [265]	$4.02 \times 10^{11} \cdot e^{0.87/RT}$	298–2000	1.2–1.5	CCSD(T) /AVTZ / VTST

Table 4.10: R 4.13 $Hg + O_3 \longrightarrow HgO + O_2$

Reference	Rate ($cm^3\,molec^{-1}\,s^{-1}$)	T (K)	Method
Hall[297]	$3 \pm 2 \times 10^{-20}$	293	0.5, 1 and 2L FEP bags, absolute
Pal and Ariya[298]	$7.5 \pm 0.9 \times 10^{-19}$	298	2 and 5 L wax coated flasks, relative and absolute
Sumner et al.[239]	$6.4 \pm 2.3 \times 10^{-19}$	NA	17.3 m^3 chamber, absolute
Snider et al.[288]	$6.2 \pm 1.1 \times 10^{-19}$	298	3.1 and 5.5L wax coated flasks,variable RH% and [CO]
Vahedpour et al.[289]	4.8×10^{-20}	298	H2O present B3LYP/MP2/SDD/RRKM

Table 4.11: R 4.15 $Hg + BrO \longrightarrow HgOBr$ / HgO / $BrHgO$ / $HgBr$

Reference	Rate ($cm^3\,molec^{-1}\,s^{-1}$)	T (K)	Method
Raofie and Ariya[160]	10^{-13}–10^{-15}	293	3 L flask, Br_2 or CH_2Br_2 photolysis with O_3, relative rate
Spicer et al.[274],via[285]	3.0–6.4×10^{-14}	298	17 m^3 chamber, Br_2 photolysis with O_3, relative rate

4.3   Simulation of chamber results

By simulating a full chemical model of the Hg depletion in the chamber we can have not only a benchmark to compare the observations to, but also verify that the data analysis procedure functions as intended. The rate of change of each species in the chamber can be represented by a differential equation. Under the assumption of a perfectly mixed chamber, the equations together are a system of ordinary differential equations, commonly described as a zero dimensional box model. Research into solving such systems goes back to Newton and Leibniz so methods to solve these are well developed and available for virtually any language or platform. All the simulations here were carried out in Octave[299] using KPP[300] to generate the equation system from the reaction scheme. KPP uses, by default, Matlab's order 1:5 Runge-Kutta method. The closest implementation to this was the order 2:3 Rosenbrock method which converged in around one second for a single reaction. It turns out that both these methods are slow and not very accurate,[301] so the gold-standard Radau5 solver was used instead (`ode5r`). Although KPP can be configured to generate code to use any integrator, for convenience of data manipulation and plotting it was overall faster to use Octave's interface rather than the KPP generated one. A balance between speed and accuracy was found at $0.2\,$s per decay, integrating about 200 steps. These calculated Hg decays had a total square deviation from a much longer, more accurate integration of $< 1\%$. This integration time was quick enough that the data visualisation and analysis took longer, so no further effort was put into increasing the integrator efficiency.

The preferred rates chosen from the literature review are listed in Table 4.12. This system will be referred to as the default mechanism, and example Hg decays calculated from it are shown in Figure 4.1. On the same plot are fits of first order exponential decay to the simulated reaction. Later on the lifetime of the experimental reactions will be measured in the same way, and the value of the lifetimes from the experiments and simulations will be compared directly as crude measure of similarity. At the end of this chapter a more accurate comparison will also be carried out by comparing the differences between the whole curve of the experimental and simulated reactions, thereby distinguishing the importance of the different reaction steps in determining the overall Hg depletion.

TABLE 4.12: Preferred rates of the default mechanism, chosen from the literature review.

Reaction Rate	Rate expression
$\dot{j}_{Br_2}$	$0.0021 \ \mathrm{s}^{-1}$
k_{rec}	$8.84 \times 10^{-14} \cdot (T/298)^{-3.77} \ \mathrm{cm^3 \, molec^{-1} \, s^{-1}}$
k_{fox}	$2.99 \times 10^{-13} \cdot (T/298)^{-2.86} \ \mathrm{cm^3 \, molec^{-1} \, s^{-1}}$
k_{thm}	$3.28 \times 10^{10} \cdot (T/298)^{-2.86} \cdot e^{(-7801/T)} \ \mathrm{s}^{-1}$
k_{cpa}	$2.5 \times 10^{-10} \cdot (T/298)^{-0.57} \ \mathrm{cm^3 \, molec^{-1} \, s^{-1}}$
k_{abs}	$4.5 \times 10^{-11} \ \mathrm{cm^3 \, molec^{-1} \, s^{-1}}$
k_{cpm}	$1.5 \times 10^{-13} \ \mathrm{cm^3 \, molec^{-1} \, s^{-1}}$
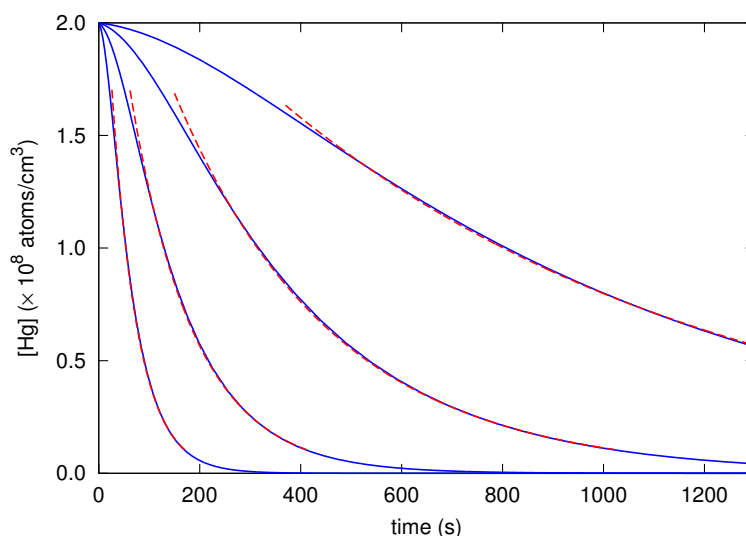
FIGURE 4.1: Example of simulated [Hg] decays (blue) with best fit exponential decays to the simulation (dashed red), with 4 different, constant $[Br_2]$. In this example the exponential decay is a good fit to the simulations, especially in the latter part of the reaction.

4.4 Reactions in the dark

4.4.1 Data Analysis

As was described in Section 4.2.2, no dark reaction between Hg and Br_2 was expected. However, we observed a complete depletion of Hg in the dark within minutes, well above the wall loss rate. If there were a direct insertion reaction,

$$\mathrm{Hg} + \mathrm{Br_2} \xrightarrow{k_{dir}} \mathrm{HgBr_2,} \tag{R 4.20}$$
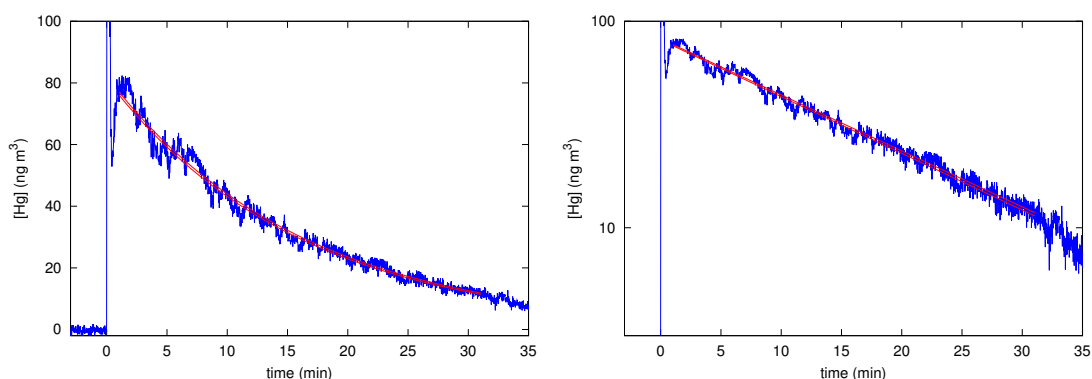
FIGURE 4.2: Example of exponential decay fitting to [Hg], showing the linear plot and the straight line fitted to the log transformed data.

then it would be first order in [Hg]:

$$-\frac{\text{d}[\text{Hg}]}{\text{d}t} = k_{dir}[\text{Hg}][\text{Br}_2].\tag{4.3}$$

During each Hg decay the [Br_2] is assumed to be constant so on integration we get:

$$\ln[\text{Hg}]_t = k_{dir}[\text{Br}_2]t + \ln[\text{Hg}]_0.\tag{4.4}$$

A plot of $\ln[\text{Hg}]_t$ against t will therefore have a gradient of $k_{dir}[\text{Br}_2]$, from which k_{dir} at that concentration can be found trivially. Figure 4.2 shows an example of the first order Hg decay fitting on both log and linear axes.

There are more advanced algorithms that also fit an exponential decay, however the straight line to log transformed data was chosen as it weights the data at the end of the decay, unweighting any non equilibrium period at the beginning. The effectiveness of this simple fitting is seen more clearly with simulated data in Figure 4.1. The extra relative noise at low [Hg], seen in the log plot, makes the fit slightly more uncertain but probably more accurate than the fit based on the initial few seconds. The decay of Hg fits well ($R^2 > 0.98$) to a first order exponential decay. The k_{dir} found by Equation 4.4 at each [Br_2] are plotted in Figure 4.3. If the direct insertion happened in one step then the rates would not depend on [Br_2] at all, but it is clear from the graph that this is not the case. In fact k_{dir} calculated in this way varied between $3.4{\times}10^{-16}$ to $1.3{\times}10^{-14}\,\text{cm}^3\,\text{molec}^{-1}\,\text{s}^{-1}$ smoothly over the [Br_2] range tested (from $1.2{\times}10^{13}$ to $8{\times}10^{10}\,\text{molec}\,\text{cm}^{-3}$). The presence of the curve in Figure 4.3 indicates that the order of the reaction is not unity, and the actual reaction
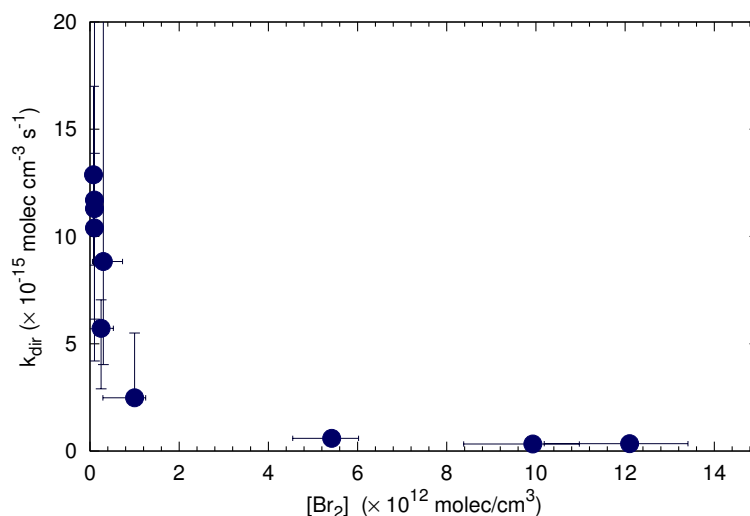
FIGURE 4.3: Calculated k_{dir} for different $[Br_2]$. Despite large error bars, the points do not fit a straight line.

is more complex than direct insertion. For the more general reaction

$$-\frac{d[Hg]}{dt} = k_{overall}[Hg][Br_2]^a \tag{4.5}$$

the rate equation gives after integration

$$\ln[Hg]_t = k_{overall}[Br_2]_t^a + \ln[Hg]_0. \tag{4.6}$$

This time the gradient of the plot $m = k_{overall}[Br_2]^a$. To find the order, a, in $[Br_2]$ we take the log of this expression:

$$\ln m = \ln k_{overall} + a\ln[Br_2] \tag{4.7}$$

Thus the log-log plot of the data in Figure 4.3 will yield a line where the gradient a is the order of reaction in $[Br_2]$. Each experiment measures the gradient of the decay of $\ln[Hg]$, but in practice it is more convenient to use the the inverse of the rate, the reaction lifetime τ. The lifetime is the time it takes for the $[Hg]$ to decrease by a factor of e. After 4 lifetimes the reaction is practically complete as the $[Hg]$ falls into the range of the limit of detection.

Figure 4.4 shows on logarithmic scale the measured lifetimes of each reaction. In this plot the lifetime, τ, of the $[Hg]$ decay is plotted against the fixed, excess $[Br_2]$ during that decay along with the associated uncertainties calculated according to Section 3.7. The reactions are divided into two categories: those where the $[Br_2]$
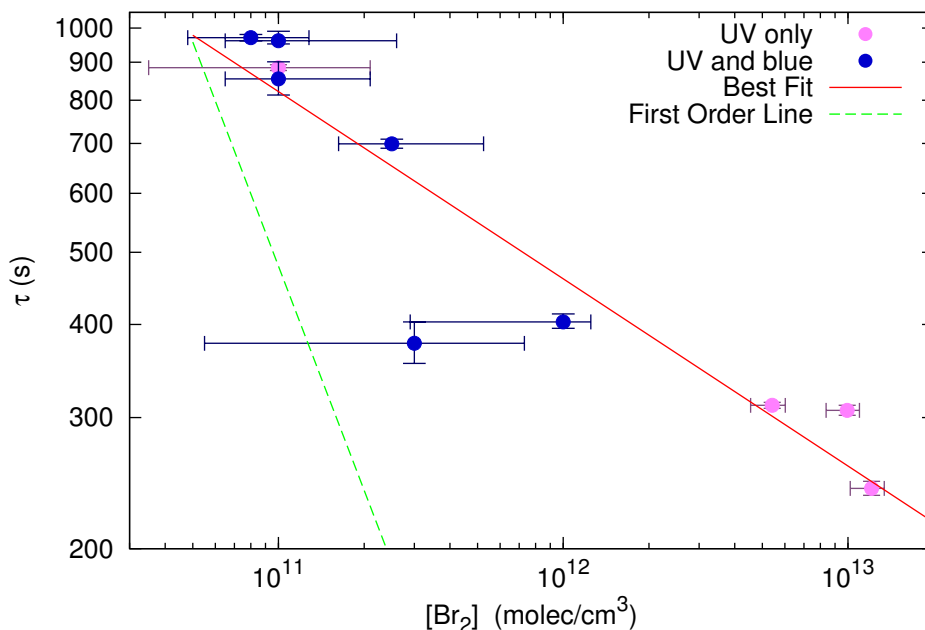
FIGURE 4.4: Observed reaction lifetimes of Hg and Br_2 in the dark. Each dot is one experiment, the UV and blue refers to the detection cavities in operation at the time. The two lines are a best fit line of gradient -0.25 (red) and an example reference line of gradient -1 (dashed green).

was retrieved from both the blue and UV cavities (pink), and those from later on in the campaign when the blue cavity was disabled and the UV cavity was used alone with a background correction channel (blue). It is clear from the plot that the uncertainties associated with using both the UV and blue cavities are much larger than those from the background corrected UV channel.

The lifetimes vary between 241 and 971 s, whereas there should be no reaction at all. The lifetime is also dependent on $[Br_2]$, indicating that the depletion of Hg was indeed caused by Br_2 and not some other factor. Results from both categories lie more or less on the same trend line with two of blue points being faster. A straight line fit of this data (red) has a gradient of -0.25 ± 0.7 and intercept of $13 \pm 2 \, (\ln s)$. We therefore could naively write that the reaction $Hg + 0.25 \, Br_2 \longrightarrow HgBr_x \downarrow$ has a rate of $2 \times 10^{-6} (\, cm^3 \, molec^{-1} \, s^{-1})^{-0.25}$. The non-integer order implies a more complex mechanism. The direct insertion, Reaction R 4.4, would have an order of one, and a line corresponding to this order with an arbitrary rate is plotted in green dashes. This line does not fit the data at all, and any rate derived with a gradient of one would be heavily dependent on whichever particular $[Br_2]$ happened to be sampled. The gradient of 1 almost fits the blue-and-UV category, this will be explored again later. Numerous experiments were therefore conducted to find the
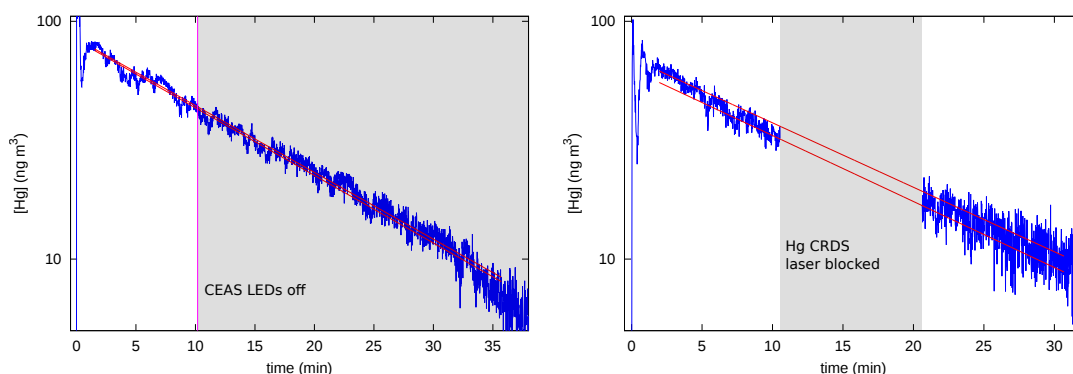
FIGURE 4.5: Effect of blocking (a)CEAS LEDs and (b) CRDS laser on [Hg] decay. No change in gradient is seen.

cause of this dark reaction.

4.4.2   Photolysis from LEDs and laser

There was a concern that the photolysis from the CEAS LEDs would be sufficient to allow Reaction R 4.2 and R 4.6 to proceed. To test this hypothesis, the LEDs and the laser were switched off mid-experiment to see the effect on the [Hg] decay.

LEDs   Figure 4.5(a) shows the effect of switching off the LEDs during the reaction. There is no detectable change in gradient. Additional experiments were conducted where the LEDs were blocked before the Br_2 or Hg injections and then switched on during the reaction. These variations also did not alter the [Hg] decay gradient. The photolysis cross-section of Br_2 in the blue cavity was 4.5 times larger than in the UV. Even after the blue cavity was disabled the reaction proceeded at a similar rate (Figure 4.4). If there were a large difference, the UV-only points would have much longer lifetimes. Instead they all follow roughly the same trend, with two, rather uncertain, blue points being much faster than the others.

Laser   There was also the possibility of another reaction involving an excited Hg atom ($^3P_1$) reacting directly with a ground or excited state Br_2 molecule. The intensity of the laser—around 5 nW—would be sufficient to maintain a small excited population in the volume of the laser beam. Irradiation at 254 nm excites Hg atoms into a more chemically reactive state, an effect studied extensively through the first half of the 20th century. Though chiefly used to activate saturated alkanes by abstraction of H˙, excited Hg can also form O_3 from O_2, which would not normally

106

FIGURE 4.6: Photograph of extra FEP surface suspended within chamber

happen at wavelengths longer than 246 nm.[242] Because the lifetime of $Hg(^3P_1)$ is very short (100 ns), any reaction caused by the laser should stop immediately after blocking it from the chamber. Figure 4.5(b) shows the effect of blocking the laser during the reaction. Despite the lack of [Hg] data for the period when the laser is blocked, it can be seen that there is little change in the steepness of the curve. What small difference in steepness there is would be expected from a slight deviation from 1st order decay.

4.4.3   Surface reaction

Surface reactions have been used to explain the observed dark reaction previously.[159] While zero and first order wall losses were measured on Br_2 and Hg individually (see Section 3.2.4) and found insignificant, a possible surface reaction between Hg and Br_2 was not accounted for. For this to occur, a reaction proceeds only when one or both of Br_2 and Hg are adsorbed onto the chamber wall. Such a surface-mediated reaction is particularly interesting as it is thought to have some role in depletion events, due to the detection of high levels of particle bound Hg during these events.[302] To test for this surface reaction, $1\,m^2$ of extra foil (surface area of $2\,m^2$) was cut in a lattice pattern and inserted into the chamber. Care was taken to avoid interference with the beam paths and maintain mixing through the extra surface. A photograph of this is shown in Figure 4.6.

The observed lifetimes of reactions with extra surface are shown in Figure 4.7, together with the dark reactions shown already. Instead of a faster reaction as would be expected from a surface process, the reaction was considerably slower. At the
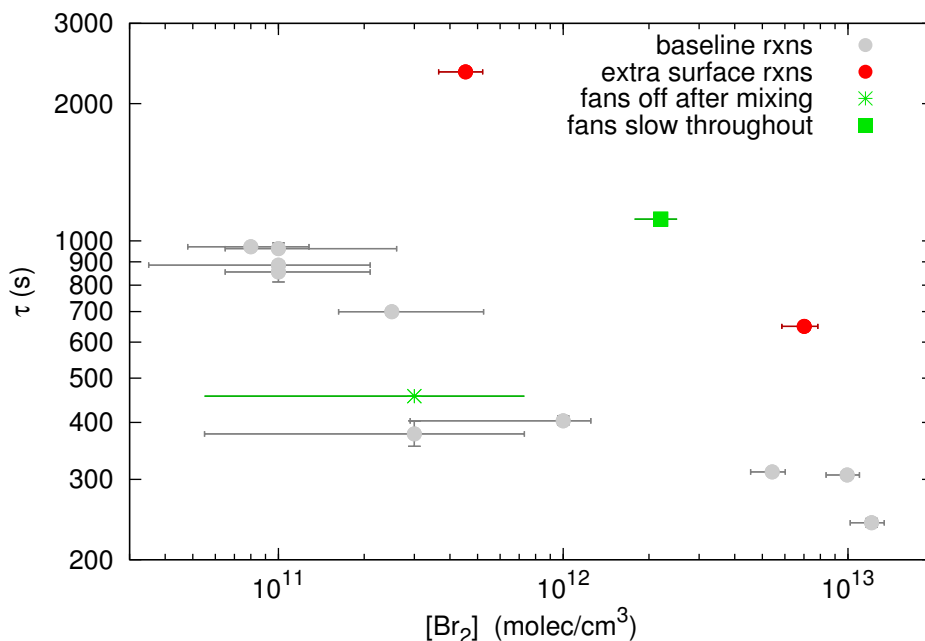
FIGURE 4.7: Reaction lifetimes of Hg and Br_2 in the dark. Baseline experiments (grey) are compared with reactions in the presence of extra surface (red), or with a slower mixing speed (green).

two $[Br_2]$ measured, the lifetime was more than doubled.

The cause of the slower reaction was probably slower mixing in the chamber. Also plotted in Figure 4.7 are reactions carried out in the normal chamber with alterations in the fans' speeds. The green star corresponds to a reaction where the fans were switched off after reagent injection and mixing. It is unchanged amidst the baseline reactions. The square point corresponds to a reaction where one fan was off and the other fan was at half voltage during the whole experiment. The mixing time in this reaction was several times slower, 2–3 minutes. The slowly mixed reaction happens to lie on the same line as the extra surface experiments. This line may represent the effective rate of reaction when the reagents are diffusing through the chamber rather than being homogeneously mixed. We can conclude that the effect of the extra surface can be at least reproduced by increasing the mixing time.

Another effect of extra surface could be quenching of some activated intermediate, such as Br˙. This would also slow down the overall [Hg] decay. However, if the surface removed Br˙ without regenerating Br_2, then depletion of Br_2 would be rapid and this was not observed.
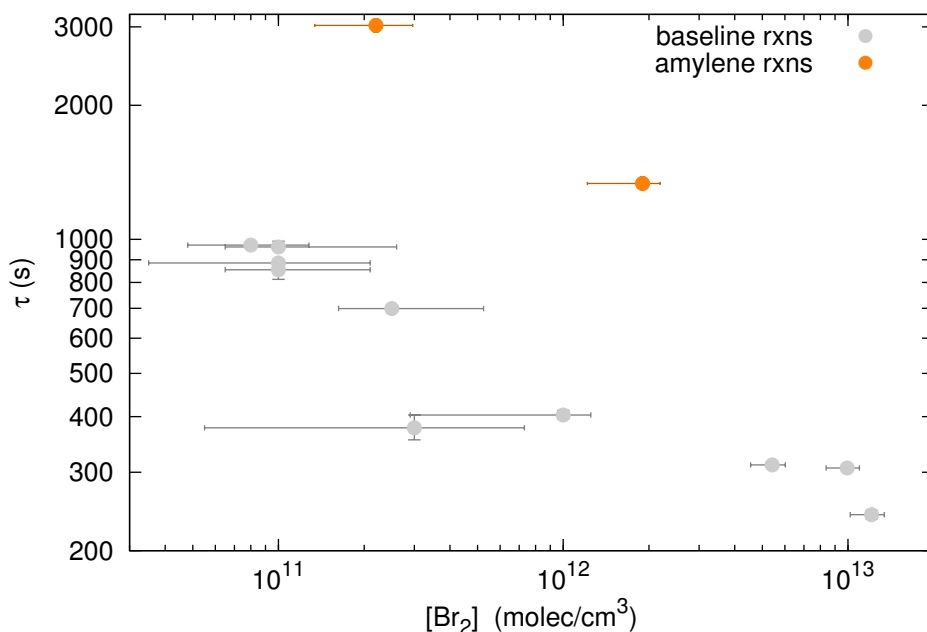
FIGURE 4.8: Reaction lifetimes of Hg and Br_2 in the dark, comparing the baseline reactions (grey) with the slower reactions in the presence of amylene (orange).

4.4.4   Dark reaction in the presence of amylene

The cause of the dark reaction was now established to be something other than the FEP surface, the laser and LEDs. To test whether the reaction was due to Br˙ as opposed to Br_2, the same reaction was carried out with the addition of $19\,\mu L$ liquid amylene. When evaporated into the chamber in a stream of hot air the concentration of amylene in the chamber would be 3.6×10^{14} molec cm^{-3} or 18 ppm. This concentration is 200 times greater than $[Br_2]$, and several orders of magnitude larger than $[Br]$. Due to the very fast reaction between amylene and Br˙ (2×10^{-11} cm^3 molec^{-1} s^{-1}), and subsequent quenching with O_2, amylene effectively removes Br˙ from the system (Section 3.5). Figure 4.8 shows the effect of adding amylene to the reaction mix. The lifetimes measured are some 5 times longer. The presence of such a large excess of amylene should remove all Br˙ and stop the Hg depletion. The observed depletion is probably due to a reaction between Hg and the amylene-bromine-peroxyl intermediate. With only amylene there was no noticeable depletion. These experiments are further evidence that the depletion of Hg in the dark is caused by un-recombined Br˙.
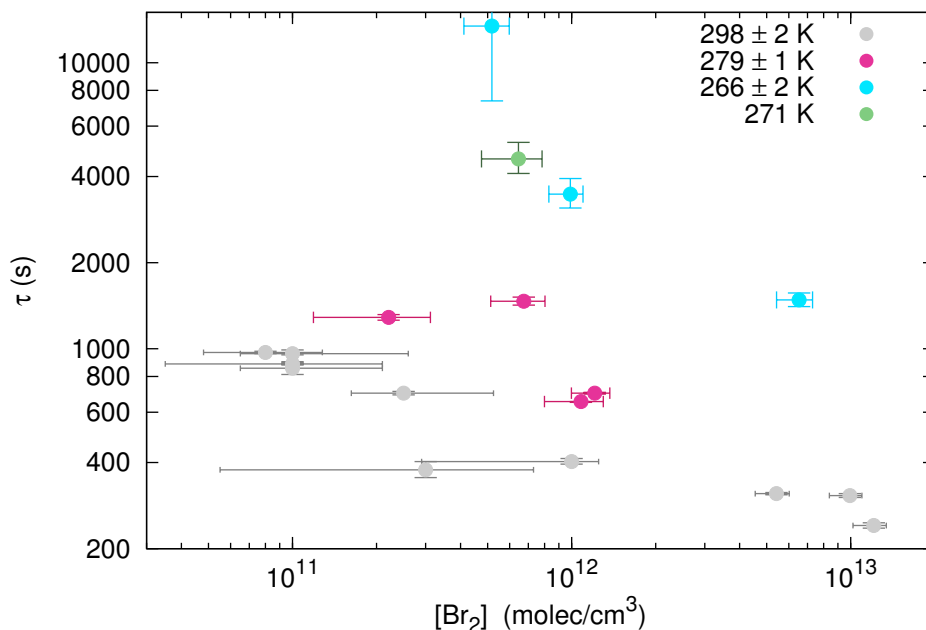
FIGURE 4.9: Reaction lifetimes of Hg and Br_2 in the dark, comparing the baseline reactions at 300 K with reactions carried out at 280 and 265 K. Lower temperatures increase the Hg lifetime significantly.

4.4.5   Temperature effect on dark reaction

Recombination reactions typically have a strong negative temperature dependence. Bromine atom recombination is no exception, as it almost twice as fast at 265 K than at 300 K (Table 4.2). Since un-recombined Br˙ was suspected to be the source of the reaction, at lower temperatures the recombination would be faster and there would be a lower [Br], slowing the dark oxidation of Hg.

Figure 4.9 shows the effect of colder temperatures on the apparent dark reaction. The reactions all proceed much slower in the colder conditions. The slowest of these reactions, with a lifetime of over 10 000 s, was actually not distinguishable from Hg wall loss, i.e. there was no change in the (somewhat noisy and flat) trend in [Hg] after injecting Br_2 in the dark. If the slower reactions were due to faster wall loss of Br˙, a considerable decay in $[Br_2]$ would be expected. Such a $[Br_2]$ depletion was not observed.

The reaction of Br˙ with Hg, R 4.6, is also thought to be faster at lower temperatures, which should shorten the lifetime (Table 4.5). Given that the lifetimes were longer, the dominant effect was the Br˙ recombination.
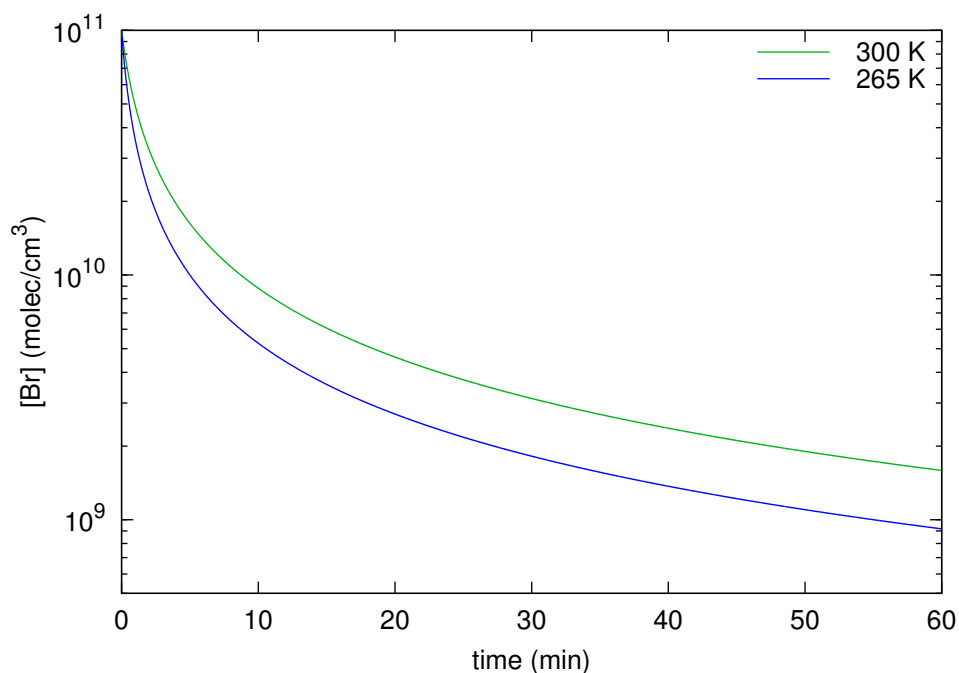
FIGURE 4.10: Calculated recombination of Br· at 300 K and 265 K using the recombination rates of 0.86 and 1.5 cm^6 molec^{-2} s^{-1} respectively, assuming 845 mbar [N$_2$], with no photolysis of Br$_2$.

4.4.6 Source of Dark reaction

The experiments at cooler temperatures and with a Br· scavenger strongly indicated that the observed depletion of Hg in the dark was due entirely to Br·. These radicals could have been produced by a very small light source, but thus far it is not clear why turning off the LEDs had no impact. The recombination of Br· was simulated using the methods outlined in Section 4.3. Figure 4.10 shows the simulated decay of [Br] in the dark for a nominal initial concentration of 1×10^{11} molec cm^{-3}, which is the equilibrium [Br] formed under normal photolysis conditions in the chamber with an initial [Br$_2$] of 5×10^{12} molec cm^{-3}.

The simulation shows that even after some 30 minutes in the dark, a relatively high [Br] remains. As the recombination is a pseudo-second order process the lifetime is not constant but increases as the radicals become more scarce. To reduce [Br] to 10% of its initial value takes only a few minutes, but to reach 1% takes an hour. This means that some residual Br· would always be present in the chamber, regardless of how dark it was kept. It also explains why blocking the cavity LEDs had no discernible effect—there was insufficient time for the Br· to recombine. The observed lifetimes of Hg in the dark—between 1000 and 300 s^{-1}—would need a [Br] of 3–11$\times10^9$ molec cm^{-3}, assuming a simple one step reaction of R 4.6 (see

111

simple model in next Section). This [Br] could easily be created with the small photolysis from the LEDs.

The photolytic flux from the LEDs was difficult to measure directly as detecting the light intensity in the cavity also destroys the cavity. A maximum value for the intensity inside the cavity can be estimated by taking the intensity before the first mirror (I_{LED}) because the reflectivity of the two mirrors is essentially the same. The same amount of light lost by back-reflection off the first mirror will be regained by reflection between the two. By using the same spectrometer as for the calibration noted in Section 3.5, the upper limit for the intra-cavity j_{Br_2} were 7 and $0.2 \times 10^{-3}\,\mathrm{s}^{-1}$ in the blue and UV cavities respectively, and $3 \times 10^{-5}\,\mathrm{s}^{-1}$ from the UV led after the configuration change. The beam path occupies $^1/_{1000}$ of the chamber volume, but because the recombination times are an order of magnitude longer than the mixing time, it is likely that the equilibrium [Br] in the whole chamber is not far below the equilibrium in the beam. These 3-dimensional mixing and recombination effects in the chamber may explain the low reaction order (0.25) in Br_2, and why the order with the higher photolysis of the blue cavity was larger (i.e. the steeper gradient of the blue points in Figure 4.4). A more detailed model of the background photolysis will be shown in 4.7.6.

From these experiments it was clear that Br˙ were slow to recombine after photolysis, especially when diluted from the syringe into the chamber. All sources of light were therefore minimised prior to injection. The lab was thereafter as dark as practical with only red LEDs used for illumination, and the blue cavity was disabled. These measures minimised the number of Br˙ injected into the chamber. Dilution into the chamber volume of 300 L reduced their concentration further. Since the dark reaction observed was actually the same reaction as R 4.6, its rate was not subtracted from the overall rate as a wall loss would be.

The dark reaction reported by Ariya et al.[159] had a lifetime of a few seconds with a [Br_2] of 20 ppm, which was explained as a surface reaction (flask size was only 0.65 L). The rate would also result from a [Br] of 6 ppb, which could be caused by a continuous photolysis rate of $1 \times 10^{-5}\,\mathrm{s}^{-1}$. In addition to the stated surface process, a contribution from residual Br˙ is probable. There is still no evidence of a fast direct insertion, so it was not included in the default model.

4.5   Reactions under illumination

4.5.1   Data analysis

For reactions under chamber illumination the data analysis procedure was the same as for the dark reactions described in Section 4.4.1. The reaction expected to dominate is the first oxidation step of Hg by Br$^\cdot$ to give the unstable intermediate HgBr (R 4.6). If we start by making the assumption that this is the rate determining step, then the reaction should be first order in Br$^\cdot$. Since we can only measure [Br$_2$] and not [Br], we apply a pre-equilibrium to [Br], and since [Br]$\gg$[Hg] by a factor of 1000, the consumption of Br$^\cdot$ is negligible and the pre-equilibrium is then equivalent to the steady state approximation described earlier in Equation 3.10, i.e.

$$[\text{Br}] = \sqrt{\frac{j_{Br_2}[\text{Br}_2]}{k_{rec}}}. \tag{4.8}$$

Thus the simple, one step, model of the whole Hg depletion is

$$-\frac{\text{d}[\text{Hg}]}{\text{d}t} = k_{fox}[\text{Hg}]\sqrt{\frac{j_{Br_2}[\text{Br}_2]}{k_{rec}}}. \tag{4.9}$$

Integrating and taking logs we get

$$\ln \tau = \ln k_{fox}\sqrt{\frac{j_{Br_2}}{k_{rec}}} - 0.5\ln[\text{Br}_2]. \tag{4.10}$$

A plot of $\ln[\text{Br}_2]$ against $\ln \tau$ would have an intercept of $\ln k_{fox}\sqrt{\frac{j_{Br_2}}{k_{rec}}}$. In the same way as the direct dark insertion plotted in Figure 4.3, this simple model did not fit the experimental data at all. It assumes an order in [Br$_2$] of 0.5, whereas a simulation of the full default mechanism (Table 4.12) yields a higher order (0.53) due to the thermolysis of HgBr (R 4.7). Instead the more general Equation 4.5 is used where the order in [Br$_2$] is fitted from the gradient of the log-log plot, as was done for the dark reaction.

Figure 4.11 shows the measured lifetimes of Hg in conditions of constant [Br$_2$] and under a photolysis of $0.0021\,\text{s}^{-1}$. As with the dark reaction the Hg lifetime is shorter at higher [Br$_2$]. Also similar to the dark reaction is that the earlier data points collected with both UV and blue cavities operating follow the same trend. This is
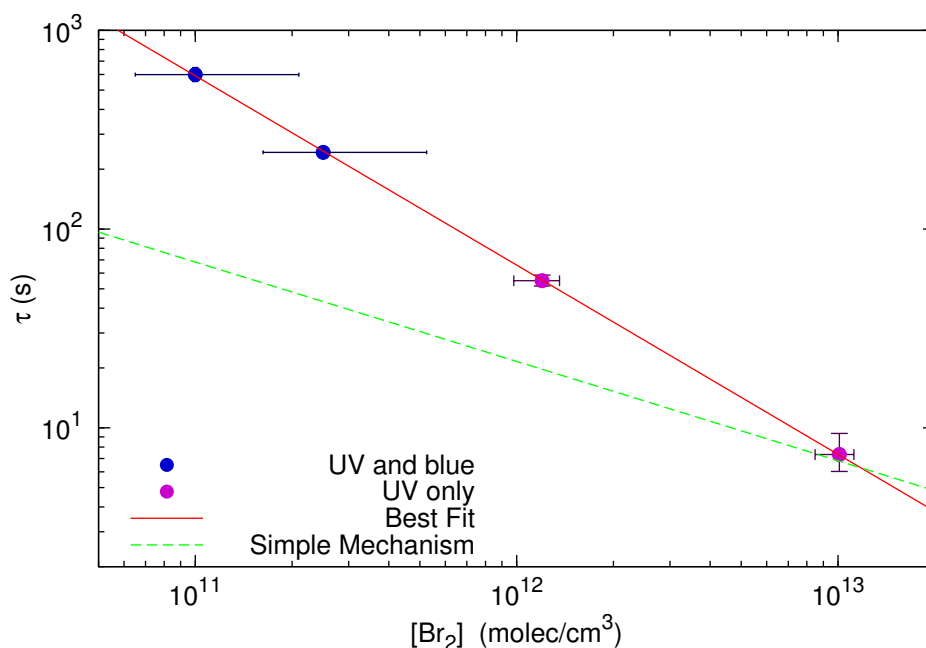
FIGURE 4.11: Lifetime of Hg vs $[Br_2]$ for reactions conducted at room temperature under photolysis, with the UV only (purple) or both UV and blue cavities (blue) in operation. The red line is fitted to the data and the green dashed line is calculated from Equation 4.10

despite that in one of these points the LEDs had been switched off when the Br_2 was injected. The agreement between these indicates that the residual $Br^{\cdot}$ that had caused the dark reaction were not important for the light reaction. The uncertainties for the blue-LED points are much higher than for the others, but they are included as they feature the lowest $[Br_2]$ sampled during the campaign. The best fit line has a gradient of -0.95 ± 0.02, meaning the order of the reaction in $[Br_2]$ is 0.95, with an effective overall rate of $3.9 \times 10^{-19} (cm^3\, molec^{-1}\, s^{-1})^{-0.95}$. The order of 0.95 is higher than the 0.5 expected from the simple, one step mechanism (Equation 4.9), and indeed the line produced from the simple model (green dashes) calculated with the rates from Table 4.12, does not fit the data at all. If the gradient of the best fit is fixed to -0.5 and fitted to the data anyway—equivalent to shifting the simple mechanism line upwards without changing the gradient, the rate would be equal to $1.2 \times 10^{-13}\, cm^3\, molec^{-1}\, s^{-1}$. This value depends on whichever $[Br_2]$ happened to be sampled, and does not describe the data properly.

The cause of larger order in Br_2 will be explored in Section 4.7.5. In the next sections the effect of changing various parameters will be investigated.
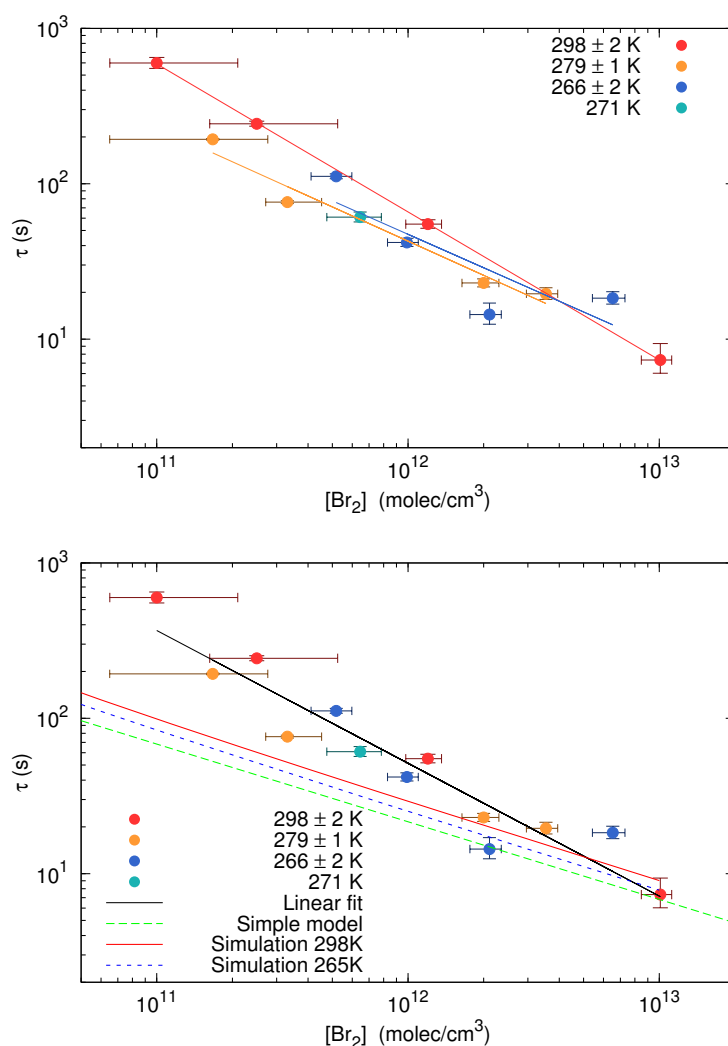
FIGURE 4.12: Hg lifetime vs $[Br_2]$ for reactions conducted at different temperature under photolysis. (a) Best fit lines to each temperature group. (b) Model lines and a best fit line to the pooled data. Gradients are listed in Table 4.13

4.5.2   Temperature effect on illuminated reaction

The unstable intermediate HgBr is thought to decompose back to its elements faster in warmer temperatures. The overall lifetime of Hg should therefore be shorter in cold conditions, as the reactive intermediate HgBr will be stabilised and have more opportunity to react further to a stable form. The chamber was designed to investigate this temperature dependence. Under the conditions in the chamber however, the HgBr reacted to the stable $HgBr_2$ so quickly that the temperature effect was only modest. Figure 4.12(a) shows the measured lifetimes of Hg at different temperatures. Overall the lifetimes at lower temperatures have the same $[Br_2]$ dependence, with roughly the same gradient, as at ambient temperature (Table

Table 4.13: Table of the order of reaction in Br_2 for illuminated reactions within each temperature group, pooled together, and of a simulation of the default mechanism at 298 K. The uncertainty in the simulation order arises because the line is not straight but slightly curved, i.e. the order is not quite constant over the $[Br_2]$ studied.

Temperature (K)	order in Br_2
298	0.95 ± 0.02
280	0.7 ± 0.4
265	0.7 ± 1.4
overall	0.85 ± 0.17
Models	
Simple	0.5
Default 298	0.53 ± 0.01
Default 265	0.52 ± 0.01

4.13). There is not enough data to quantitatively measure the difference in gradient, but nearly all the cooler temperatures have shorter lifetimes than the same $[Br_2]$ at 300 K.

Figure 4.12(b) shows the same data together with the line calculated from the simple model (Equation 4.10) and the lines calculated from the lifetimes extracted from the default model simulation. None of the simulations match the data well. The simulations show only slight changes in overall rate between temperatures, and the reaction order (gradient) is practically identical between them.

To derive a reaction rate from the data requires that the order be fixed, because otherwise the uncertainty in the $\ln y$-intercept is several orders of magnitude, and the derived rate meaningless. It is not appropriate to fix the order to 0.5, as this line does not match the data. There is so much uncertainty in the order of each temperature group that no value can be fixed for each one, but pooling all the temperatures together gives an order of 0.85 ± 0.17 (black line 'Linear fit'), which is well outside both the simple one step reaction with an order of exactly 0.5 (green dashes), and the simulation of the default mechanism with an order of 0.53 ± 0.01 (red line and blue dashes). No rate can be given from this analysis, but later in Section 4.7.3 some semi-quantitative rate information is extracted.

It was anticipated that we should have observed a much faster Hg depletion at low temperature than at room temperature, due to the strong negative temperature dependence of k_{thm}. The initial simulations used for the project design had employed a slow, fixed k_{cpa} of $3 \times 10^{-12}\,\mathrm{cm^3\,molec^{-1}\,s^{-1}}$ (from the MECCA model, see Section 4.2.4) which led to an overall temperature dependence that was 10% larger than the default mechanism, due to the increased lifetime of HgBr.

4.5.3 NO$_x$

It has been hypothesised that NO$_x$ can participate in Hg depletion by oxidising HgBr to a more stable species.[106] Alternatively, Br radicals react with NO and NO$_2$ to form a reservoir of Br, which may also react with Hg. NO$_2$ reacts rapidly with Br to form BrONO, which can also be photolysed,[252] The concentration of BrONO would have been too low to detect with the Br$_2$ cavity, especially since there is overlapping absorption from NO$_2$.

Reaction of Hg and NO$_2$ The direct oxidation of Hg by NO$_2$ is thought to be slow to non-existent, especially since atmospheric Hg has a long lifetime in polluted environments with a large ambient [NO$_2$]. No change in Hg wall loss was observed with addition of NO$_2$ or NO. With typical Hg lifetimes of $\approx 10\,000$ s in the chamber and an [NO$_2$] of 1.2×10^{12} molec cm^{-3} this corresponds to an upper limit for the rate of 1×10^{-16} cm^3 molec^{-1} s^{-1}. The maximum rate determined in larger chambers was 10^7 times slower than this, so there is no contradiction with the literature.

Reactions of NO$_2$ and Br$_2$ NO$_2$ and Br are likely to react in the chamber to form BrONO which may oxidise Hg. Using a BrONO photolysis rate of 10^{-4} s^{-1} and a formation of 3.7×10^{-12} cm^3 molec^{-1} s^{-1} (estimated from the photolytic flux from Section 3.5 and a literature data[252]) the equilibrium constant is 3.7×10^{-8} cm^3 molec^{-1}. With 10^{12} molec cm^{-3} NO$_2$, the ratio $^{[BrONO]}/_{Br}$ would be 3.7×10^4 meaning that at equilibrium nearly all the Br would be in the form of BrONO, and Br$_2$ would be depleted quickly. The overall transmission of the cavity increased on illumination of Br$_2$ and NO$_2$, but due to spectral noise the depletion of neither [NO$_2$] nor [Br$_2$] could be quantified. There are in addition possible reactions such as $BrONO + Br \longrightarrow Br_2 + NO_2$, which complicates the chemistry further.

Hg, NO$_x$ and Br$_2$ Figure 4.13 shows the effect of adding NO$_2$ or NO to the chamber. NO$_2$ was always introduced before Hg and Br$_2$, as this allowed for the calibration of the CEAS mirrors with the NO$_2$. All the NO$_x$ data occur roughly together with the baseline data, so there is no large systematic deviation from the baseline case. Three cases had slightly longer lifetimes than the baseline, while the one test of NO and one NO$_2$ case both had a lifetime twice as long as the baseline. As the results with cooler temperatures (Figure 4.12) above showed similar variability, the deviation is probably more indicative of the systematic uncertainties present with the chamber
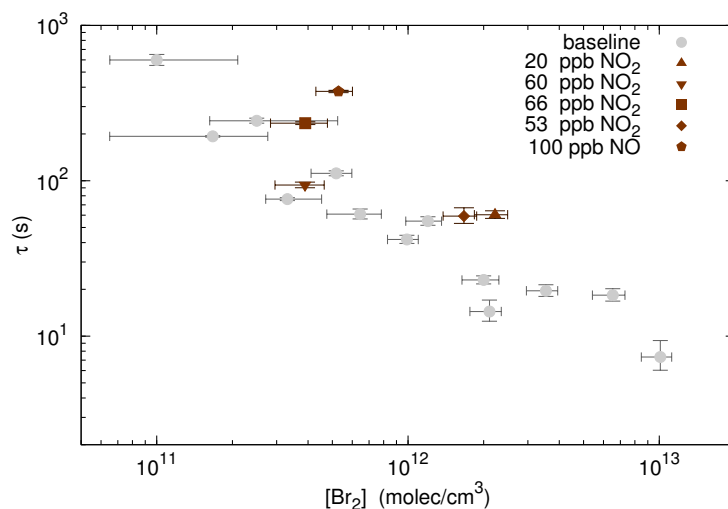
FIGURE 4.13: Hg lifetime vs $[Br_2]$ under illumination at room temperature with various concentrations of NO_x (brown). There is no consistent deviation from the baseline reactions (grey).

than the chemistry of Hg and BrONO. On average however the presence of NO_x slowed the oxidation of Hg, but there is not enough good quality data to confirm this as a real effect. Previous studies in conditions of coal combustion flue gas found that NO had a non linear effect[259] or no effect[260] on Hg oxidation by Br_2.

4.5.4   BrO

BrO and O_3 were once purported to be the primary oxidants of Hg in the atmosphere. To test this hypothesis, BrO was produced in the chamber by adding O_3 to the usual mixture of Br_2 and Hg. Any Br· formed on photolysis would react with the O_3 to form BrO, which quickly reacts with itself to reform O_2 and Br_2. Overall there is a loss of one O_3 per cycle, leading to rapid depletion of O_3:

$$Br + O_3 \xrightarrow{k_{prod}} BrO + O_2 \qquad (R\,4.21)$$

$$BrO + BrO \xrightarrow{k_{dest}} 2\,Br + O_2 \qquad (R\,4.22)$$

$$\text{net}: \quad Br + O_3 \longrightarrow {}^1/_2 Br_2 + {}^3/_2 O_2 \qquad (R\,4.23)$$
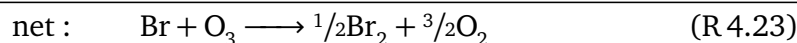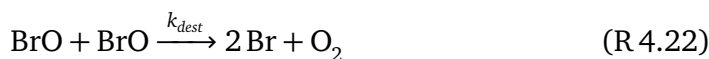
As there is already a reaction between Br and Hg the aim was to see an increase in rate, and possibly a change in shape of the curve as the oxidation of HgBr should occur more quickly. Using rates of 1.2×10^{-12} and $2.7 \times 10^{-12}\ cm^3\,molec^{-1}\,s^{-1}$ for the k_{prod} and k_{dest} respectively[252] and the measured $[Br_2]$ and $[O_3]$ in the chamber, the
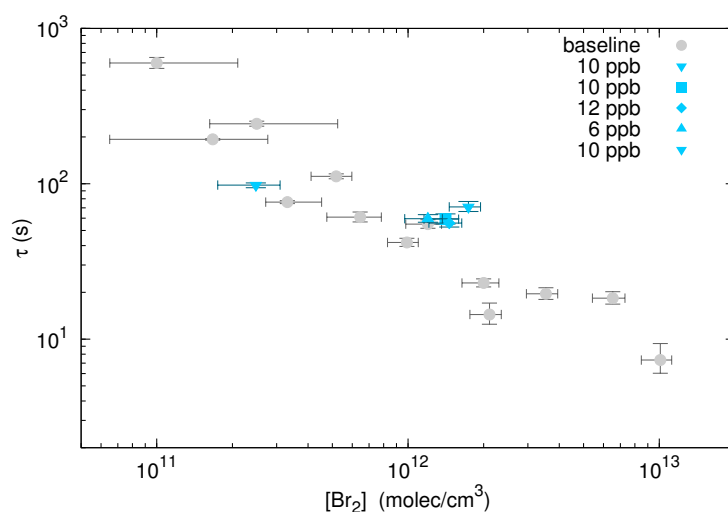
FIGURE 4.14: Hg lifetime vs $[Br_2]$ under illumination at room temperature with various concentrations of O_3 (blue). Most of the O_3 are slower compared to the baseline reactions (grey).

production of BrO was simulated with the methods in Section 4.3. In the simulations, the maximum $[BrO]$ produced was between 2 and 4 $\times 10^{10}$ molec cm^{-3} depending on $[Br_2]$ and $[O_3]$. At least 1 molec cm^{-3} of BrO was maintained for around a minute before the O_3 became exhausted—long enough for a small $[BrO]$ to be sustained during the Hg depletion. Including an estimated photolysis of BrO and O_3 arising from the laser and LED did not affect the $[BrO]$ greatly.

BrO detection

BrO has a structured absorption in the UV which is ideal for CEAS detection. It was hoped that one of the large absorption bands would overlap enough with the lower end of the LED range at 355 nm LED to detect BrO specifically. Even then the expected $[BrO]$ was at the detection limit of the CEAS setup. By setting the I_0 immediately before the lights were switched on Br_2 was eliminated from the fit. Under photolysis the only species to change significantly is BrO, resulting in greater sensitivity. However, the shape of the typical thermal-shift artefact (Section 3.3.3) was very similar to the BrO spectrum, so detection of BrO was not particularly convincing. Even fitting only BrO to a period 10–30 s after photolysis when the $[BrO]$ should be at a maximum did not help the sensitivity. As the O_3 was indeed depleted—as seen by the CRDS laser at 254 nm—there is no doubt that BrO was formed, but was below the detection limit of the setup.

BrO When the lamps where switched on the Hg was depleted quickly, but no more so than expected from the reaction with Br only. Figure 4.14 shows the lifetimes of reactions with about 10 ppb O_3, and 1 ppb BrO. No large or consistent increase in reaction rate was seen. Due to the speed of oxidation of by Br·, the influence of BrO would have to be large to have a noticeable effect. A BrO oxidation of Hg at 10^{-13} cm^3 $molec^{-1}$ s^{-1} may have been about the slowest detectable rate. This upper limit is above those already in the literature (10^{-15}–10^{-13} cm^3 $molec^{-1}$ s^{-1}, Table 4.11).

Ozone only Due to the very strong interference of ozone with the Hg measurement, only small quantities of ozone could be used in the chamber, and they had to be introduced first to establish a new baseline for the Hg instrument and make sure it was operating correctly without excessive noise. It was therefore not possible to routinely measure both a wall loss of Hg in the empty chamber and a dark reaction of just O_3 and Hg in the same experiment. In the one experiment where O_3 was added after Hg, there was no change whatsoever in the nearly flat trend of [Hg]. Typical lifetimes were no different to the wall losses—around 10 000 s. With up to 12 ppb O_3 in the chamber this would imply an upper limit on the rate of 4×10^{-16} cm^3 $molec^{-1}$ s^{-1} which is not lower than existing literature rates of 1×10^{-20}–1×10^{-17} cm^3 $molec^{-1}$ s^{-1} (Table 4.10).

4.5.5   Reactions with larger surface area

Reactions under illumination were carried out when FEP film was placed inside the chamber to investigate the dark reaction (Section 4.4.3). Figure 4.15 shows the difference in lifetime of two reactions in the presence of extra FEP film. One point is indistinguishable from the baseline reactions and the other, at higher $[Br_2]$, has a longer lifetime. This confirms that the observed reaction is not predominantly a surface one, but is does not exclude some interfering role of the surface.

4.5.6   Sea Salt Aerosol

Sea Salt Aerosol (SSA) is a potentially important surface as it is abundant in the marine and coastal environments where Hg depletion events have been observed. It is thought that it has an important role in Hg oxidation.[285] Indeed, in commercial Hg monitors KCl denuders are used to adsorb the oxidised Hg and their efficiency,
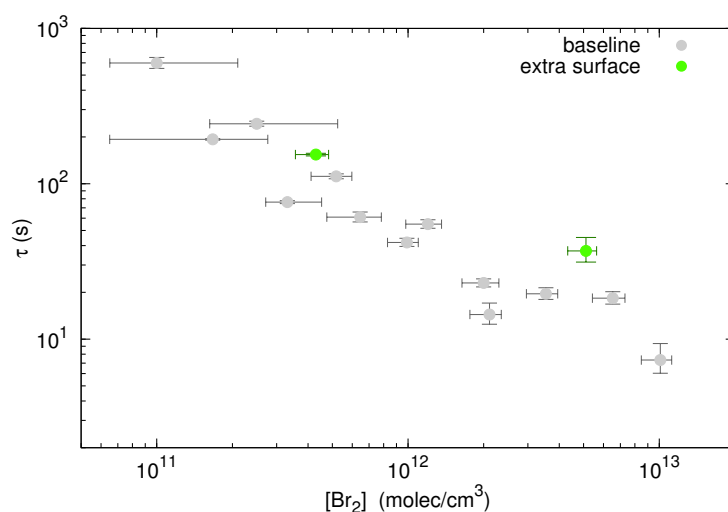
FIGURE 4.15: Hg lifetime vs $[Br_2]$ under illumination at room temperature with extra FEP foil (light green). Reactions are generally slower than the baseline reactions (grey).

although not perfectly quantitative, is always more than 20%.[84,85] SSA was generated by an ultrasonic transducer submerged in a small depth of water to which consumer Californian sea salt was added to 3.5% by mass. The ultrasound produced dense clouds of aerosols which were accumulated in a 10 L bucket. Samples of the aerosol were drawn through an aerosol dryer by a venturi pump and blown into the chamber. Conductive tubing was used throughout. A TSI SMPS 3081 DMA and CPC 3775 were used to check the output of the aerosol generation system. Accurate size distributions were not obtained, but all measured particles were between 10 and 500 nm, and the total particle concentrations in the chamber were $500 \pm 50 / cm^3$ at the beginning of the experiment, decreasing to around $100 / cm^3$ by the end. No particles were otherwise detected in the clean chamber.

Figure 4.16 shows the results of the three experiments with SSA. All were slower than the baseline reactions by a factor of about 2. The effect of aerosols on the $[Br_2]$ retrieval was shown in Figure 3.12. The potential bias would be to lower $[Br_2]$ than actually present, which is the wrong direction to explain the data. The slower rate may be due to quenching of $Br^{\cdot}$, or possibly some artefact arising from the scattering of the aerosols in the the CRDS laser. The aerosol was rather dilute and would not increase the absolute surface area in the chamber greatly, so no large effect on the reaction should be expected.
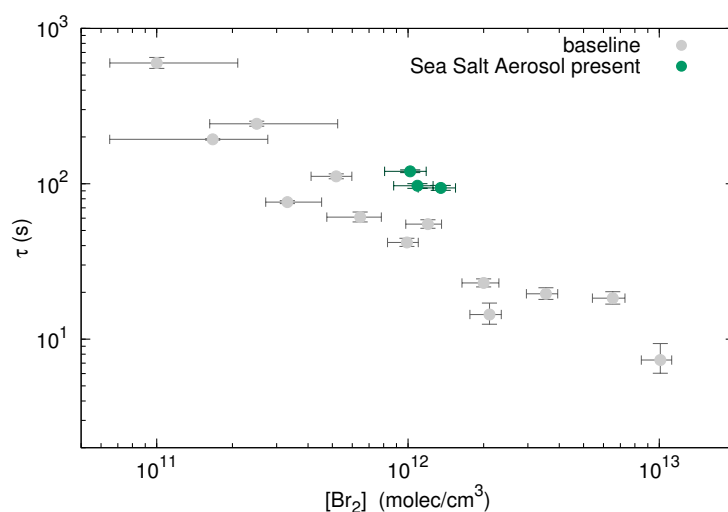
FIGURE 4.16: Hg lifetime vs $[Br_2]$ under illumination at room temperature with sea salt aerosol (dark green). Reactions are generally slower than the baseline reactions (grey).

4.5.7   Reactions in contaminated air

On several occasions more than one Hg aliquot was injected during the same experiment to obtain a second decay. It has been noted previously that reactions carried out in the presence of products from a previous reaction are faster, lending support to the hypothesis of a surface catalysed process.[159] A similar effect was observed here. When two sequential reactions were identical (i.e. same illumination, fan speed, temperatures etc) the Hg lifetimes can be compared directly. Figure 4.17 shows the relative speed of the second reaction compared to the first. Uncertainties bars are estimated from the sum of relative errors in the two reaction. Positive values, above the green line at $y = 0$ indicate a faster second reaction, while negative values below the green line are slower. The mean value is 0.43, and it is clear from the plot that indeed most repeated reactions were about 40% faster. Some repeated reactions were more than twice as fast, and in only four cases were they slower. There is only a weak correlation with $[Br_2]$ ($R^2 < 0.1$, line not shown), which is probably spurious. Since repeat injections were carried out opportunistically, these data points were not collected in a systematic way. They are a mixture of light and dark reactions, surface area, $[NO_2]$, temperatures, time elapsed between Hg injections and whether the chamber was dark or light between the two reactions. There is not enough of any one set of conditions to compare them effectively. For example, of the 4 slower reactions (those below the green line), the slowest is a dark reaction in NO_2 (-0.43), while the others are colder reactions under photolysis at 7 °C (-0.40), 6 °C (-0.08) and in the dark at -7 °C (-0.15), and the elapsed time

122
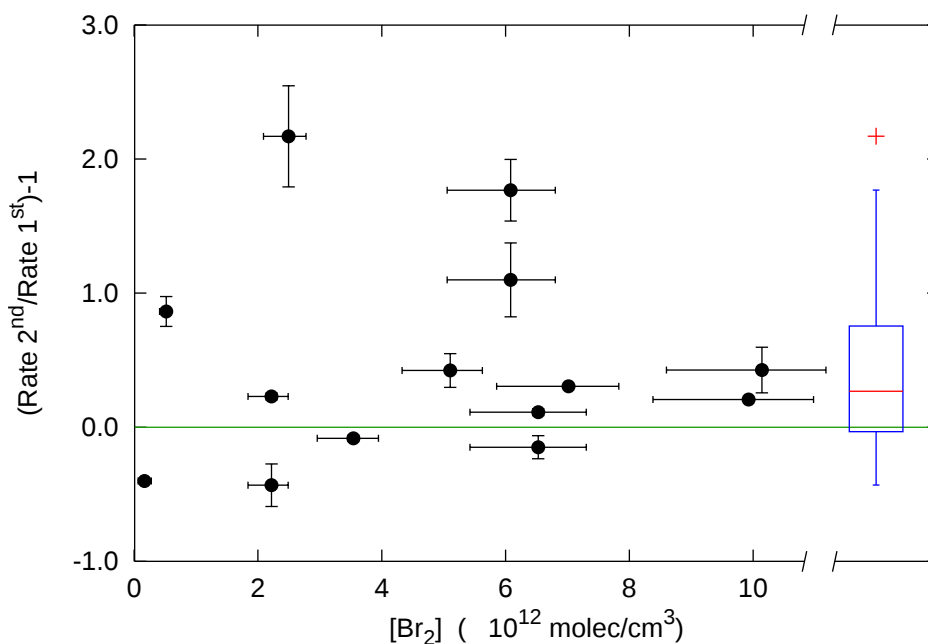
FIGURE 4.17: Scatter plot of speed up of repeated reaction against $[Br_2]$, with a boxplot showing the distribution of the values. Green line marks $y = 0$, meaning the second reaction had the same rate as the first.

between the two injections varied from 9.1–30.5 minutes. Other reactions with NO_2 or below 0 °C were speeded up.

However, the fact that the reaction is nearly always faster across a wide range of conditions does support the existence of a different mechanism involving reaction products. The lack of a strong correlation with $[Br_2]$ indicates that the limiting step does not involve Br_2 or Br. Hg deposition directly to an aggregate may be an explanation. Because the starting $[Hg]$ was always the same there should be similar numbers of these aggregates across all experiments. Evidence for the formation small Hg containing aggregates already exists.[160,292] However, the concentration of reaction products is limited by the initial $[Hg]$ so would always be lower than Br· or Br_2. It is not clear how such a low concentration of $HgBr_x$ could affect the reaction to any large extent. More detailed analysis of whole Hg decay curve was carried out for the repeated reactions but the difference could not be isolated to a single reaction.

One of the consequences of this finding is that some of the illuminated reaction data acquired earlier in the campaign could not be used, as it was gathered as a second Hg injection after a complete depletion in the dark. As these illuminated reactions were in the presence of reaction products, they were not comparable to the rest of the illuminated data.

4.6   Fate of Reaction Products

None of the anticipated reaction products are volatile so must deposit somewhere. Three different methods were used to gain some insight into the fate of these products.

4.6.1   Scavenge from chamber air

Two attempts were made to collect reaction products directly from the chamber air. A Tekran KCl coated annular denuder fitted with the standard elutriator extracted from the chamber with a flow rate of 10 L/min. To avoid chamber collapse it was refilled simultaneously with UltraZero air. On the first occasion the denuder was connected to the chamber with a PFA fitting after the reaction had completed. On the second occasion, the whole denuder was inserted into the chamber through a hole in the wall to a depth of around 10 cm when the reaction was at around 50% completion. The denuder was heated in a clamshell furnace and the emitted Hg collected and quantified by a Tekran 2537. The mass of Hg collected was 13.6 and 19.5 pg for sampling volumes of 15 and 180 L respectively. If all the Hg from the reaction remained airborne and of a form that the denuder could collect, we should have recovered over 1 and 10 ng respectively.

The performance of KCl coated annular denuders has been investigated.[84,85,303] While some discrepancies between the various collection efficiencies were found, the studies established that the denuders could collect $HgBr_2$ with an efficiency of at least 20% under non-ideal conditions (high humidity and O_3). The chamber air (low humidity and O_3-free) should have favoured near total scavenging. Low collection efficiency cannot explain the 1% recovery found here. Additionally, the picogram loadings are much lower than the nanograms such denuders usually collect, so saturation is not an issue. Alternative explanations are that final product did not consist of $HgBr_2$ but of something not scavenged by the denuder. This could include very large particles caught by the elutriator, or small ones that would otherwise continue to the particulate trap (not available at the time). Another possibility is that the product deposited to the chamber walls within a few seconds, but even in that case a larger proportion should have been collected in the denuder.

4.6.2   Heating walls

After flushing with Hg-free air from the Tekran generator for 2 days the walls of the chamber were heated to 40–50 °C with a heat gun. At this point during the campaign approximately 140 ng of Hg had been injected into the chamber. A Tekran monitor continuously extracted air from the chamber its gold trap. The measured [Hg] was barely above zero, equivalent to much less than a nanogram baking off the walls. This means that the deposited products were heat stable, with only a small amount of adsorbed Hg^0.

4.6.3   Swabbing walls

Two-thirds of the way through the campaign the walls were wiped with damp kim wipes. Around 940 ng Hg had been injected into the chamber by this point and most of it had been oxidised by Br_2. The wipes were collected and processed by Ashley Pierce and Chris Moore. Three fresh wipes had blank Hg loadings of 0.18, 0.19 and 0.25 ng each. Wipes were taken from a 15×15 cm area from each internal wall of the chamber in triplicate. The Hg loadings of the wiped areas extrapolated to 1.6 ± 0.6 μg over the whole internal surface. Wipes were taken again at the end of the campaign, from areas offset from those previously wiped, after flushing with Hg-free air for a month. This time the loading was equivalent to 2.0 ± 0.5 μg Hg. These findings are consistent with all of the Hg depositing to the walls. The coverage on the walls was probably not large enough to affect the surface chemistry. A monolayer of $HgBr_2$ covering the inside of the chamber to a depth of 0.1 nm would have a mass of 1.6 mg. Therefore the microgram quantity deposited would cover at most 0.1% of the internal surface, an area smaller than the surface area of the mirrors.

4.7   Analysis of whole Hg decay profile

4.7.1   Order in Hg

The preceding analysis assumed that the Hg decay was always first order due to the straight line fit to log transformed [Hg]. In principle this assumption is not required as the order can be derived from the whole decay curve. An algorithm was developed for finding the order. The order of the simulated Hg decays was found to

be slightly less than one, but at low $[Br_2]$, towards 5×10^{11} molec cm^{-3}, the profiles were nearly straight lines with $[Hg]$ orders close to zero. The best fit $[Hg]$ orders to the observed decays were influenced by noise or baseline offsets. The mean order found was 0.8 ± 0.1 for dark reactions and 0.5 ± 0.1 for reactions under illumination, with the poorer fits excluded. Overall the $[Hg]$ order analysis gave no quantitative insight, and a more advanced fitting procedure was developed.

4.7.2   Simulation of whole decay curve

In Section 4.5 the difference between the results of the simulations and experiments was described, but no conclusion could be drawn as to what led the experiments to deviate from the simulations. The approach taken in this section is to alter each simulation parameter in turn to find what adjustments are necessary to explain the chamber results.

Automated fitting method   One software package with automated fitting of complex reactions is in the form of a Matlab toolbox called Potter's Wheel.[301] The only observables in the chamber were the $[Hg]_t$, j_{Br_2}, and $[Br_2]_0$. The parameters with no direct measurement and had to be fitted are $[Br]_0$, $[Hg]_0$, k_{rec}, k_{fox}, k_{thm}, k_{abs}, k_{cpa} and k_{cpm}. Using Potter's Wheel it became apparent that the only parameter that could be fitted with low uncertainty was the $[Hg]_0$, which is not surprising as $[Hg]$ was being measured. Without accurate concentration data for the intermediates or products, there is little constraint on the model. Even the $[Br_2]$ was constrained only by the experimental uncertainties, as without these limits the reactions rates could adjust to virtually any $[Br_2]$. In fact the reaction scheme did not require any photolysis or Br_2 in the chamber at all, as excellent fits could be obtained with just residual Br· and a faster oxidation. Including several experiments in one optimisation did not constrain the parameters better, as there are some reactions, according to the measured data, with near identical conditions but yet had different rates.

It became clear that a completely automated approach using Potter's Wheel would not produce meaningful results. Instead a more methodical technique was developed whereby only one model parameter was optimised at a time. Rather finding a particular solution the goal of such a 'sloppy model'[304] is to find which parameters are important and which do not affect the fit however they are altered.

126

Semi-automated fitting method   Automatic fitting of all the parameters at once was ineffective due to the multitude of parameters and lack of constraint. The procedure for semi-automated fitting was to start with the default mechanism (Section 4.3) and alter only one parameter at a time to find the best fit. The initial parameters were the rates in Table 4.12 using the temperature measured in the chamber, $[Br_2]_0$ and $[Hg]_0$ were as measured in each experiment. The initial $[Br]$ was, in cases where the Br_2 was photolysed before Hg injection, set to the $[Br]$ expected after the elapsed time assuming the default j_{Br_2} and k_{rec}. Otherwise it was set arbitrarily to 10^8 molec cm^{-3} to account for the background photolysis (see next Section). The quality of fit was calculated for each simulation against the experiment, and the model was then run again with different values for one parameter spanning a range of several orders of magnitude. This was then repeated for nine parameters (seven rate coefficients and initial $[Br]$ and $[Br_2]$) each time beginning with the default values. This procedure was then repeated for every experiment.

The fit deviation was calculated as

$$\sum_t \frac{(model_t - expt_t)^2}{\sum_t (expt_t - \overline{expt})^2 \cdot n} \tag{4.11}$$

where $model_t$ is each time point of the simulated decay, $expt_t$ is each time point of the experimentally measured decay, and n is the number of points in the time series. This measure is effectively the total of the squared deviations of each point in the experiment, normalised to the total deviation of each experiment. This definition is similar to other measures of goodness-of-fit such as adjusted R^2, but with the advantage that in these simulations it gave numbers that were easy to visualise when plotted over the many orders of magnitude studied, something which was important when quickly checking through thousands of fit qualities.

Figure 4.18(a) shows a typical experimental decay of $[Hg]$ with three simulations. This particular example is at $-9\,°C$ with an initial $[Br_2]$ of 5×10^{11} molec cm^{-3}. The only parameter being varied is k_{thm}. Figure 4.18(b) shows how the goodness-of-fit measure changes with the different values of k_{thm}. At the presumed literature rate (red dashed line) the fit is very poor, and this is shown with a large fit deviation. At a much faster thermolysis (dark green line) the fit is better but the decay too slow. At the optimum value of k_{thm} the fit deviation is lowest and the optimum fit achieved. The value of the optimised parameter is not necessarily realistic, but nonetheless provides insight into the reaction. Neither is the optimum fit necessarily a good fit, but it is the best achievable by tuning this one parameter. For instance the optimum

127
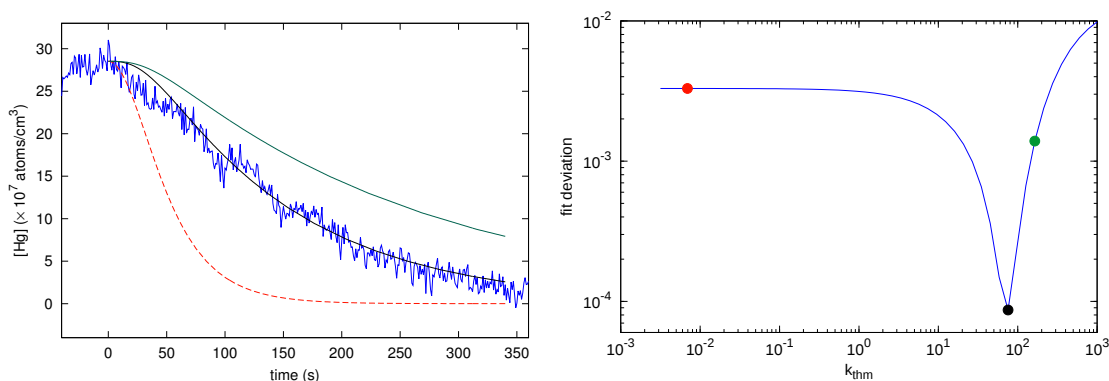
FIGURE 4.18: Demonstration of fitting procedure where k_{thm} is optimised. In (a) the blue line is the experimental [Hg], the other lines are trial fits whose fit deviation are shown in (b). Lowest fit deviation, and the best fit, is in black.

fit in Figure 4.18(b) (black line) begins less steeply than the experimental decay line (blue). The fit deviation with the optimised parameter is therefore an important metric.

The optimisation could in principle be achieved by Levenburg-Marquardt fitting as used in the NO_2 calibration earlier (Section 3.3.1), or indeed any optimisation technique,[301] but in practice for learning about the system the trend had to be visualised. In Figure 4.18(b) for example it can be seen that changes of a factor of 10 or even 100 to the default k_{thm} have no effect on the fit quality, due to the reaction being an insignificant pathway at lower rates. Each optimisation is based on sampling 200 parameter values, which, over the orders of magnitude studied yields a resolution no worse than 6%.

4.7.3   Influence of each parameter

Figures 4.19 and 4.20 show examples of the best fits produced by changing each parameter. As noted in Section 4.5, the experimental decays were generally slower than the default model These plots show that for some parameters the optimum fit is quite poor which indicates that an alteration of these parameters alone cannot explain the chamber results. Each of the parameters will now be discussed in turn.

j_{Br_2} Even though j_{Br_2} was well characterised by two independent techniques (Section 3.5), the effect of changing j_{Br_2} in the simulation was used for analysing the dark reaction, which is discussed later (Section 4.7.6). For illuminated experiments, changing the photolysis rate alone could allow the simulation to fit the observed

(a) j_{Br_2}

(b) k_{rec}

(c) k_{fox}

(d) k_{thm}

(e) k_{cpa}

(f) k_{abs}
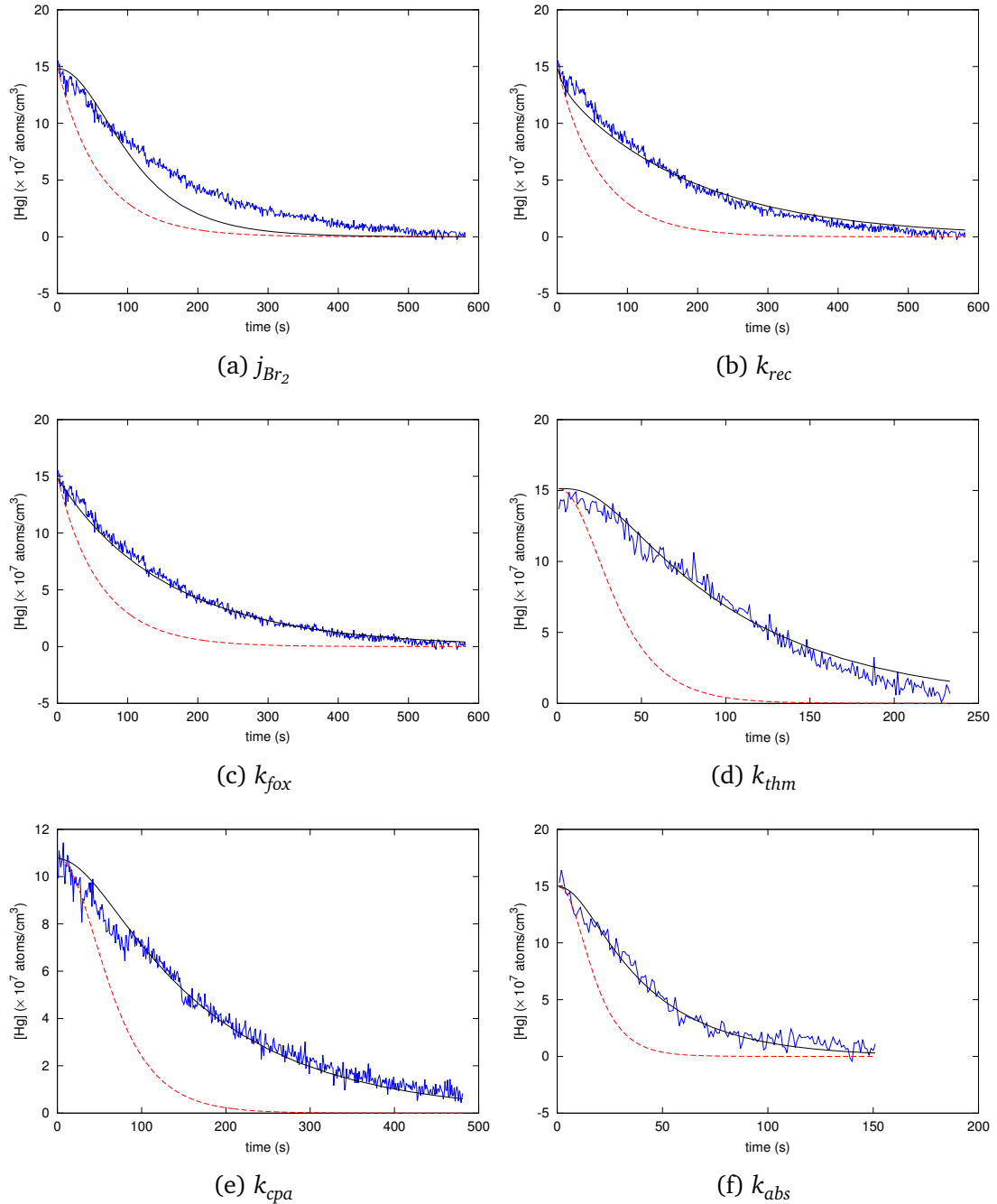
FIGURE 4.19: Examples of the type of fit produced by varying j_{Br_2}, k_{rec}, k_{fox}, k_{thm}, k_{cpa} and k_{abs} individually. The red dashed line is produced by the default mechanism, the black line is the fit

decay, although the shape did not always match well. The fact the photolysis has to be slowed down is an indication that other parameters had to be adjusted.

k_{rec} Changing the rate of Br˙ recombination led to good fits on nearly all reactions, but typically it had to accelerated by a factor of 10. This is well outside the range of uncertainty of all the literature rates. In Section 4.7.6 there will be some discussion of how the k_{rec} may indeed be faster than the literature.

k_{fox} Changing the rate of the first oxidation step also produced excellent fits, when it was slower than the default k_{fox} by a factor of around 3. The relationship of the optimum change of k_{rec} to k_{fox} is not surprising as, if the steady-state approximation for [Br] is valid, the decay of [Hg] is proportional to $k_{fox}/\sqrt{k_{rec}}$ (Equation 4.9) and the two rates are indistinguishable. Since the default rates for k_{fox} and k_{rec} came from the same study, there is no reason to prefer one more than the other.

k_{thm} Changing the rate of the thermolysis of HgBr could also make good fits, but only when 490 to 1700 times faster than the literature values. The difference is most noticeable in the latter part of the decay which is more sensitive to [Hg] offsets. The goodness-of-fit measure is normalised to the absolute deviation rather than the relative (as is χ^2), so the deviation does not overly influence the overall fit. As noted in Figure 4.18(b), small changes in k_{thm} did not improve the fit, as the recycling of Hg atoms is insignificant when k_{thm} is too slow. The photolysis of HgBr is not explicitly included as a separate reaction, but k_{thm} acts as a proxy for it. This is discussed in more detail later (Section 4.7.5).

k_{cpa} The completion by the Br˙ atom is another reaction whose optimisation could fit the chamber results well. The optimum fits were at ratios to the default rate of between 0.04 to 0.1. The literature rates cover a very large range but as the reaction is practically barrierless, it is not likely to proceed more slowly than the more accurate calculations suggest.

k_{abs} The abstraction of Br from HgBr may be an important reverse process in the high [Br] of the chamber. To explain the experimental data this rate needed to be faster by a factor of between 7 and 21. As the literature data is sparse compared to the other rates, there is a larger probability that the existing rates may be incorrect.

(a) k_{cpm}

(b) $[Br_2]_0$

(c) $[Br]_0$
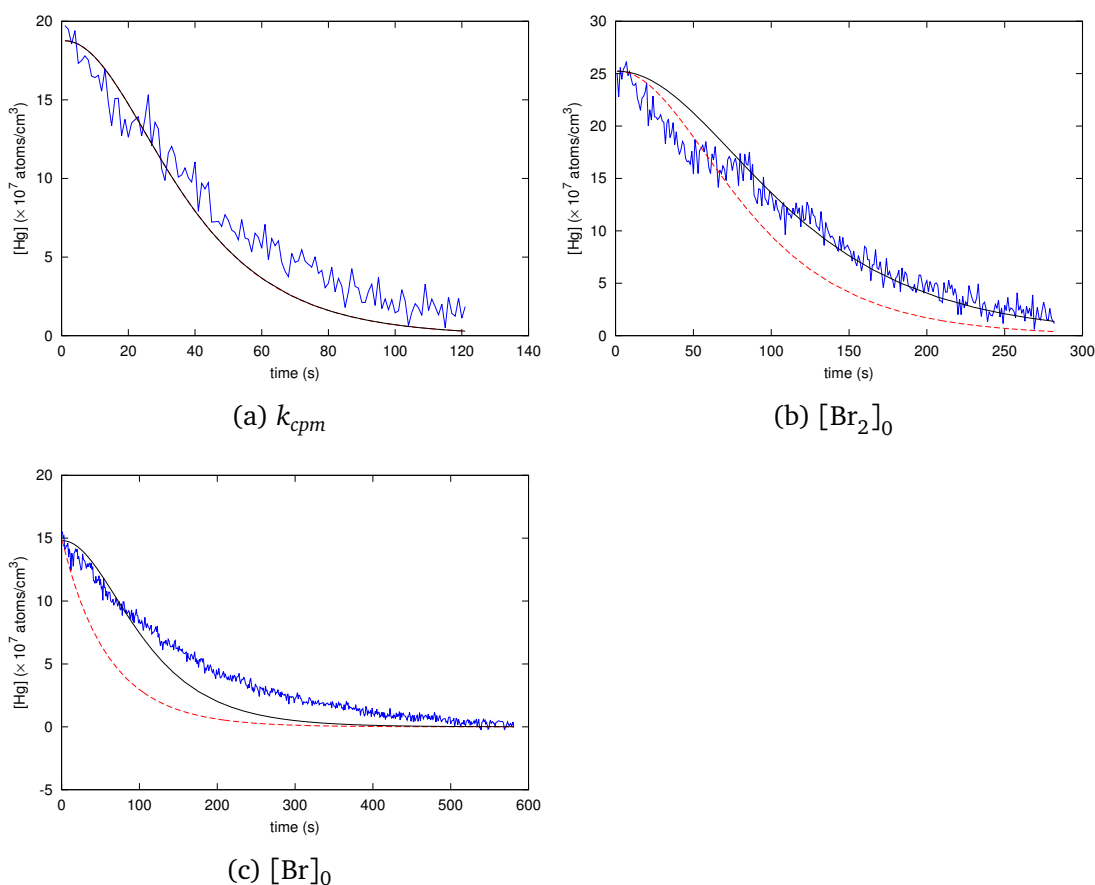
FIGURE 4.20: Examples of the type of fit produced by varying k_{cpm}, $[Br_2]_0$ and $[Br]_0$ individually. The red dash line is produced by the default mechanism, the black line is the fit

k_{cpm} The completion step by molecular Br_2 could have been important in the chamber due to the high $[Br_2]$. However, the completion by atomic $Br^{\cdot}$ was so rapid that slowing or stopping the completion by the molecular Br_2 had virtually no impact on the overall rate, so altering k_{cpm} did not improve the fits. The optimised rate was usually the minimum boundary of the range tested.

$[Br_2]_0$ Much effort was put into quantifying the uncertainties and biases that the retrieved $[Br_2]$ could have. If there were a further unknown systematic bias in the $[Br_2]$ retrieval it would become visible when optimising the $[Br_2]$ of the simulation. However, in order to fit the experiments the $[Br_2]$ would have to be 0.1 to 0.3 of its measured value, and even then the fits are not as good as could be achieved by other parameter manipulations. At very low $[Br_2]$, the simulations become too curved due to the long time needed to produce the $Br^{\cdot}$. It is very unlikely that all the retrieved $[Br_2]$ were too high by a factor as large as 3–10, and together with

the relatively poor fits this indicates that the $[Br_2]$ is not the source of the slower reactions in the chamber.

$[Br]_0$ Changing the initial $[Br]$ only altered the curve in the first few seconds of the decay and did not improve the fit except in a few isolated cases. Good fits required much larger changes in the curve shape than altering the initial $[Br]$ could provide. For the dark reaction the $[Br]_0$ was an important parameter, but was calculated in different way (Section 4.7.6).

Summary   The large quantity of data generated by the fitting procedure is challenging to interpret, but already we can see that good fits are obtained by altering any of k_{rec}, k_{fox}, k_{cpa} or k_{abs}. The other parameters j_{Br_2}, k_{thm}, k_{cpm}, $[Br_2]$ and $[Br]_0$ either did not help the fit or are known accurately enough that significant deviation was unlikely. In the next sections the distribution of the optimised values across the experiments will be visualised.

4.7.4   Reactions under illumination

Figure 4.21 is a representation of all the optimised parameters of each experiment of the temperature series that was shown previously in Figure 4.12. Experiments with O_3, NO_2, aerosol and extra FEP surface are excluded. In this plot the values of each optimised parameter are plotted in a column above the label as grey circles. The value of the parameter is represented as the ratio to its default value in order to visualise the range of values spanning nearly 30 orders of magnitude, and to remove the temperature dependence of the default rates. The quality of each fit is represented by the width of the grey circle. Poor fits are very small points so are easily ignored, while good fits are represented by larger circles that can overlap. Thus the darker regions correspond to numerous overlapping points, where the best fits from most experiments were of good quality and had similar values, indicating some kind of consensus on the ideal rate. The median optimised parameters are listed in Table 4.14.

Many of the general points made about each parameter in Section 4.7.3 can be seen more clearly in this plot. The most prominent dark patch, representing the optimum fits of k_{fox}, shows that across all the experiments a similar change in k_{fox} leads to good fits. For no other parameter are the optimum fits so close together. Since k_{fox} and k_{rec} are closely linked they produce the same fit quality, but k_{rec} has
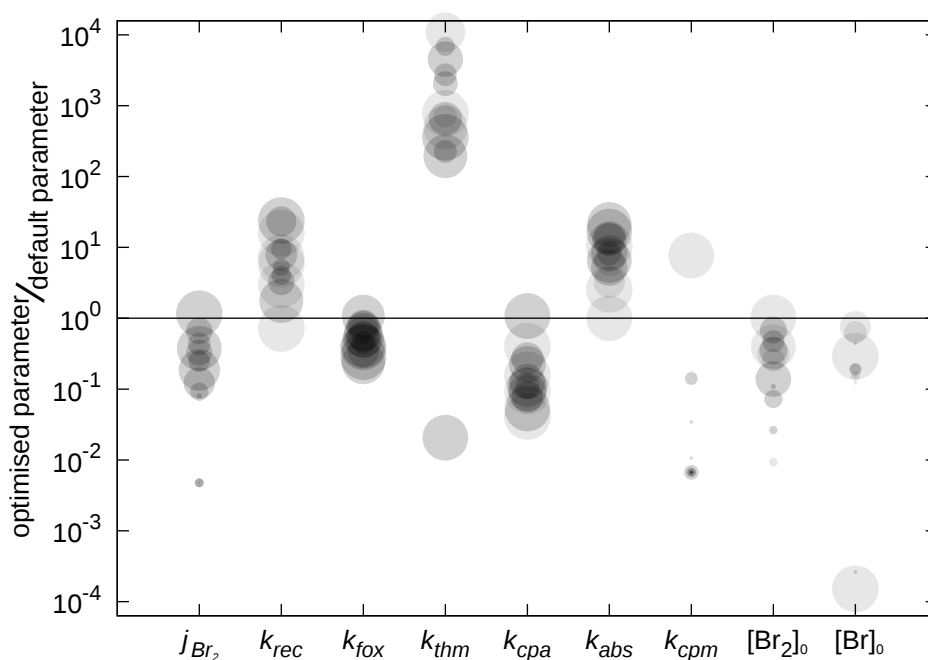
FIGURE 4.21: Scatter plot of the fits achieved by changing each parameter in isolation. All points are transparent grey circles, and the width of the circle is proportional to the fit quality. The distance from the 10^0 line represents how large a change from the default rate was necessary to fit the data. Darker regions arise where multiple points overlap, indicating consensus between experiments.

to be changed by twice as much. Neither of the required adjustments are within range of the literature rate uncertainties in Tables 4.2 and 4.5. Moderate fits can also be obtained from slowing k_{cpa} or speeding up k_{abs}, and these adjustments are far outside the range of the best quality literature rates.

The default rate of k_{fox} from the literature was determined in a carefully designed laser experiment, but the data analysis assumed that once HgBr was formed the Hg was removed from the system.[256] By extracting and re-analysing the data from one of the plots of the original study it was found that the Hg decays were noticeably slower when simulated with the default model including k_{abs}. However, the difference was fully compensated by an increase in k_{fox} of just 10%. This indicates that if the dataset behind the paper were to be completely re-analysed including these reactions, there is a possibility that the resulting k_{fox} would be around 10% faster. The difference is greater than stated uncertainty range, but the change is too small and in the wrong direction to explain the results here.

Also notable on Figure 4.21 is that k_{cpm}, $[Br_2]_0$ and $[Br]_0$ are not useful in fitting the experiments, as indicated by the wide scatter and small circles (poor fits). This is evidence that the poor fit of the default mechanism to the experiments was not solely due to inaccurate $[Br_2]$.

Table 4.14: Table of the median of the rate ratios optimised at all temperatures simultaneously, calculated for 280 K. The order in $[Br_2]$ was calculated from the gradient of the best fit straight line to the simulated points as in Section 4.5.

	Median Rate ratio $^{\text{optimised}}/_{\text{default}}$	Rate coefficient at 280 K	Order
j_{Br_2}	0.18	3.9×10^{-4} s^{-1}	0.512(0.004)
k_{rec}	5.8	6.5×10^{-13} cm^3 molec^{-1} s^{-1}	0.513(0.004)
k_{fox}	0.49	1.8×10^{-13} cm^3 molec^{-1} s^{-1}	0.526(0.008)
k_{thm}	720	22 s^{-1}	0.75(0.05)
k_{cpa}	0.11	2.8×10^{-11} cm^3 molec^{-1} s^{-1}	0.538(0.006)
k_{abs}	8.3	3.7×10^{-10} cm^3 molec^{-1} s^{-1}	0.526(0.007)

4.7.5 Order of reaction in Br2

To put the above results back into the broader context of the experiments, we can plot the optimised rates on the same graph initially used to visualise the experimental data (Section 4.5). In those graphs one of the first observations made about the results was that the gradient of the best fit line gave an reaction order in Br_2 of roughly 0.8, not the 0.53 predicted from the default model. Figure 4.22 shows the same experimental data together with the lines produced sampling 20 $[Br_2]$ points with default model and the simulations with each individually optimised parameter. The experiments were at different temperatures, but the optimum rate was evaluated as the ratio to the (temperature-dependent) default rate, so the rates at different temperatures can be compared on the same plot. The median of the optimised rate-ratios is then used to calculate the optimised rate at the median temperature of 280 K. The order line calculated from simulations at 280 K can be compared to data collected at other temperatures because temperature did not affect the gradient of the line, and made only a slight difference to its position (Figure 4.12(b)). The optimum rate at 280 K and resulting order in $[Br_2]$ are listed in Table 4.14. The parameters k_{cpm}, $[Br_2]_0$ and $[Br]_0$ are neglected because they were already shown to have little use in explaining the data.

It is clear from both Figure 4.22 and Table 4.14 that the only parameter that strongly affects the $[Br_2]$ order in this model is k_{thm}. Due to the order mismatch of the other optimised parameters the simulations are systematically too fast at low $[Br_2]$ and too slow at high $[Br_2]$. This trend in the rate with $[Br_2]$ was invisible in Figure 4.21. If the experiments at the far ends of the sampled $[Br_2]$ are to be trusted then a faster k_{thm} is necessary. The HgBr decomposition need not be due to thermolysis alone, as the same reaction could be caused by photolysis or some other mechanism. The

(a) j_{Br_2} order = 0.512

(b) k_{rec} order = 0.513

(c) k_{fox} order = 0.526

(d) k_{thm} order = 0.75

(e) k_{cpa} order = 0.538

(f) k_{abs} order = 0.526
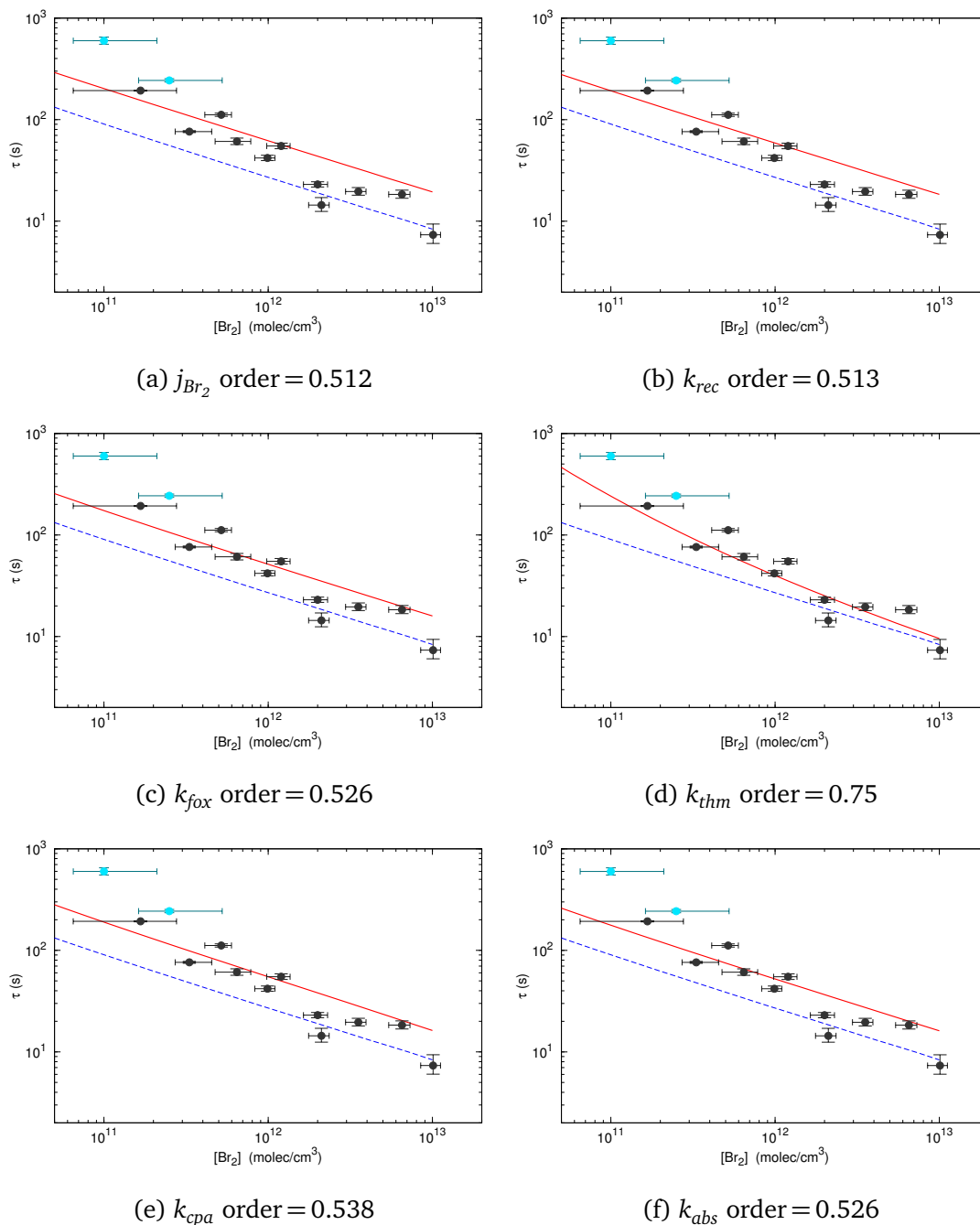
FIGURE 4.22: Examples of the overall fit to the experiments produced by varying each parameter individually. The blue dashed line is produced by the default mechanism, the red line is the median best fit of that parameter. The cyan points were measured with no I_{LED}, and are less reliable than the other points.

optimised rate of over $20\,s^{-1}$ is however several orders of magnitude faster than the calculated values of HgBr thermolysis (Table 4.6) and photolysis (Section 4.2.3).

There are plausible reasons why the data may be inaccurate at the extremes of $[Br_2]$. The two cyan points at the lowest $[Br_2]$ in Figure 4.22 were collected at the beginning of the campaign, with the older two cavity setup and before the experimental protocols were optimised. Although there is no specific feature that indicates they should be rejected, if they are ignored the gradient mismatch is much smaller, although it does not completely disappear. The gradient of the pooled experiments without the two cyan points is 0.8 ± 0.2. Additionally, at high $[Br_2]$ the reaction was faster than the mixing time which may have caused systematic bias, and at low $[Br_2]$ there may have been increased importance of Br wall losses that were not otherwise detectable. The gradient of the pooled experiments without the two cyan points or the highest $[Br_2]$ is 0.7 ± 0.2, which encompasses all the simulated orders.

More detailed statistical analysis of the same experiments is beyond the scope of this work, and it is not clear that it would be helpful in dealing with the possibility of systematic errors. Only more experiments at the extremes of $[Br_2]$ could confirm or rule out a much faster effective k_{thm}.

Figure 4.21 did not suggest k_{thm} as a parameter that could produce good fits because the optimum rates are much less temperature dependent than the default rate. The difference in temperature gives the rate ratio a large spread. Figure 4.23(a) shows the correlation of optimum k_{thm} with temperature. The data is scattered relatively evenly across the temperature range, without any correlation with temperature. When expressed in terms of the ratio to the default rate (Figure 4.23(b)) a strong temperature correlation emerges due to the temperature dependence of the default k_{thm}— a factor of 36 over the range studied. This implies that the temperature dependence in the default k_{thm} was too strong. However, k_{thm} is only a proxy for all HgBr decomposition processes. Photolysis would be largely temperature independent, but the estimated photolysis rate of HgBr was only $0.002\,s^{-1}$ (Section 4.2.3). Furthermore the overall temperature dependence of the Hg decay is not due to k_{thm} alone but is the result of a combination of all the dependences of every reaction together.

The only known experimental measure of k_{thm} also found rates faster than expected and with a smaller temperature dependence.[158] The rates at 420 and 360 K were 500 and $375\,s^{-1}$, which are faster than the default rate by factors of 5 and 53. However, the analysis procedure did not include k_{abs}, k_{cpm}, HgBr photolysis or the possibility
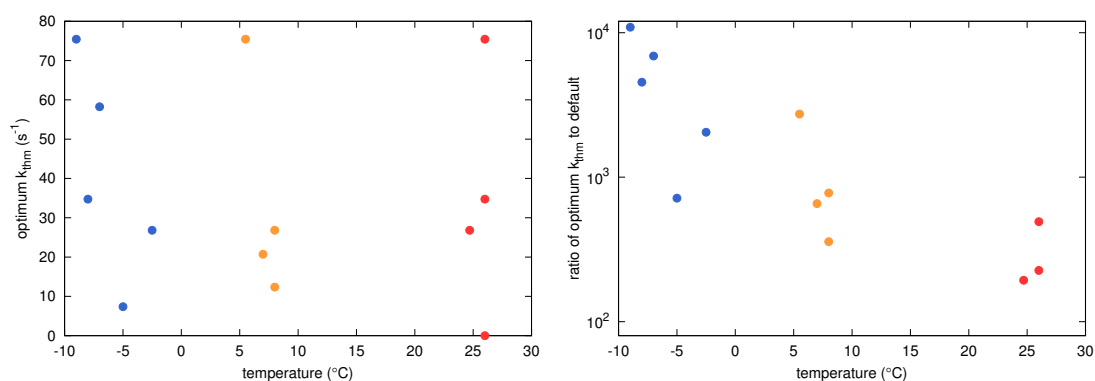
FIGURE 4.23: Scatterplot of ratios of optimal k_{thm} to the standard model k_{thm} against temperature. Slight correlation indicates standard model has too high temperature dependence: low temperatures must be speeded up and high temperatures slowed down. Colours correspond to 265, 279 and 298K categories used in earlier plots.

of HgBr self-reactions, all of which could be expected to increase the apparent k_{thm} in a temperature independent manner. The HgBr self-reaction was the factor cited as the most likely to have caused the fast decomposition, but this loss process would not be relevant to the very low [HgBr] of our chamber. Both k_{abs} and k_{cpm} were included in the chamber model here, and neither was able to explain all the data.

Another possibility is that HgBr may be vulnerable to decomposition by a route not previously considered. Due to the speed of the decomposition ($\tau_{HgBr} < 0.1\,\text{s}$), surface reactions are unlikely, except when sea salt aerosol was present in the chamber. The chamber air was otherwise almost certainly free of particulates. Such a surface reaction would have to release $Hg^0(g)$ back into the chamber to slow the overall oxidation kinetics. If the surface also immediately released Br˙ there would be a conflict with the thermodynamic stability of HgBr, as any such surface process would also catalyse the formation of HgBr and have no effect on the position of the equilibrium. The decomposition route would therefore have to be non-reversible, e.g. Hg-catalysed deposition of Br.

An abstraction of Br from HgBr by O_2, $HgBr + O_2 \longrightarrow Hg + BrOO$ is also unlikely as BrOO is not bound with respect to Br and O_2.[305] Abstraction by trace species such as O_3, NO_2 or NO would have become more noticeable when these were added to the chamber deliberately. The same analysis as in Figure 4.21 was carried out for all the reactions that had NO_x, O_3, aerosol, or extra FEP surface to find which parameters could explain the differences in overall rate, using both the default mechanism and multiple optimised parameters. Just as in Figure 4.21, it was not possible to distinguish the effects of the different parameters and the plots are not shown here.

If the data at the extremes of [Br_2] are discounted as untrustworthy then k_{thm}
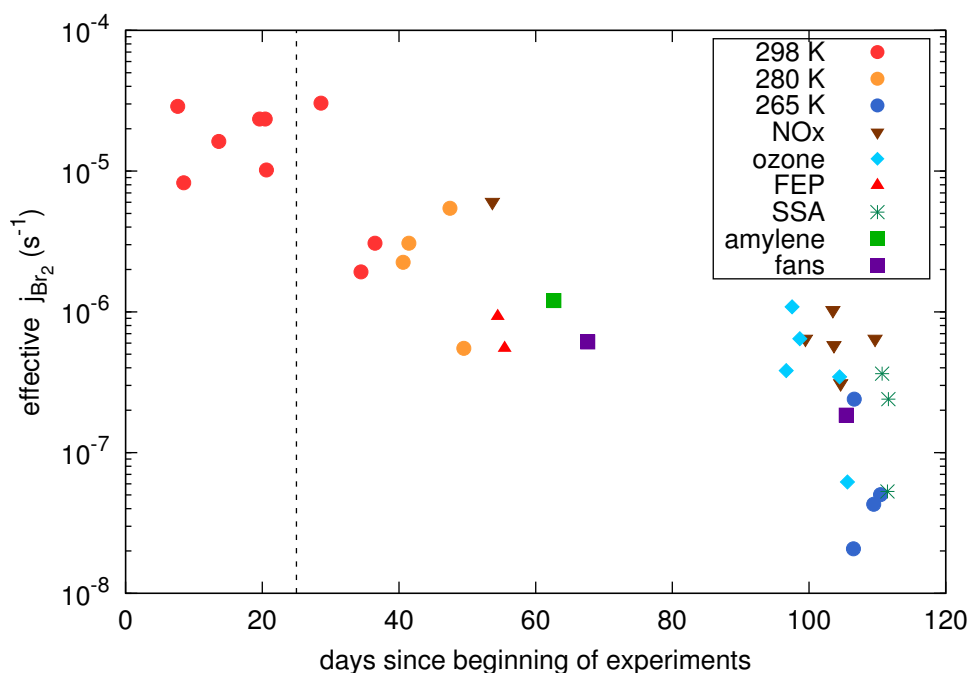
FIGURE 4.24: Trend of effective j_{Br_2} required to drive dark reaction over the course of the campaign. Dashed line on day 25 is when blue cavity was disabled. Empty period between days 68–95 corresponded to laser maintenance time.

adjustment is not required, and some combined adjustment to the rest of the rates could explain most of the data. In the next section, an attempt to measure k_{rec} in dark chamber conditions is described.

4.7.6   Reaction in the dark

The same fitting procedure was carried out on all the dark reactions. It was found that the dark reactions measured earlier in the campaign at 300 K could not be fitted without a large $[Br]_0$. The $[Br]_0$ was therefore initialised to the steady state defined by $[Br_2]$, k_{rec}, and j_{Br_2} (Equation 3.10). While this equilibrium may not be established in reality, the assumption allows the optimised j_{Br_2} to provide a measure of the level of un-recombined Br˙, whether due to photolysis inside the chamber from the LEDs or outside from the lab lights. The fit quality achieved with this method was always good. The j_{Br_2} that gave the best fit for the dark reactions of the whole campaign are shown in Figure 4.24.

The first weeks show a high j_{Br_2}, which was earlier determined to be caused by the CEAS LEDs (Section 4.4.6). The blue cavity was disabled on day 25, yet an abrupt reduction in the effective j_{Br_2} did not occur until after day 30. The point measured

with only the UV cavity on day 30, with a j_{Br_2} of $3 \times 10^{-5}\,s^{-1}$, was also the lowest dark $[Br_2]$ measured, and it is probable that the Br_2 was photolysed as it was being injected by some external light source. As it became clear that residual photolysis was a problem, the main lab was kept dark and the only illumination was from a small red LED and the various computer screens. The exact details of the photolytic flux incident on the Br_2 syringe during the journey from the fume hood in the room adjacent to the chamber were not recorded, as well as other variables such as in the early days a white LED may have been used for illumination, or the light may have been directed into the chamber during Br_2 injection instead of switching it off as soon as the needle was in position. The CEAS cavities were also re-aligned every few weeks, which may have increased or decreased the light in the chamber. After experiments resumed on day 96 after a period of laser maintenance, the protocol was more or less fixed. Unfortunately the only room temperature reactions with only Br_2 carried out in the latter part of the campaign were reactions with altered fan speed, so are not suitable as a room temperature reference. If we assume that the background k_{thm} was about $10^{-6}\,s^{-1}$ throughout the latter period of the campaign, we can calculate how changes in k_{rec} could explain the variation.

Figure 4.25 shows the effective k_{rec} required to fit the dark reaction assuming a constant j_{Br_2} of $10^{-6}\,s^{-1}$, plotted against temperature of reaction (if plotted against date the pattern is simply the inverse of Figure 4.24). A significantly faster k_{rec} was cited as possible explanation for the results in Section 4.7.3, and Figure 4.25 shows how k_{rec} may have changed throughout the campaign. The red and blue lines are the default values for k_{rec} at 298 and 265 K, yet almost none of the results lie within those bounds. The cold reactions are described by a much faster k_{rec}, and the warmer reactions by a slower one, indicating that k_{rec} was substantially more temperature dependent than the literature suggests.

However, the assumptions underlying Figure 4.25 are dubious or incorrect. The 298 K data all had much higher LED photolysis than the value assumed in this calculation, and there are likely higher wall losses of Br˙ at cold temperatures. The point on this graph with the coldest temperature ($-9\,°C$) is the same experiment as the point in Figure 4.9 with the lowest $[Br_2]$ at 265 K, and it was described there as not distinguishable from Hg loss to walls. The addition of extra gases and surfaces would also provide more loss mechanisms for Br˙, so it is not surprising these reactions show an increased effective k_{rec}. Clearly there are far too many variables to measure k_{rec} in this way.

Overall, the trends in effective k_{rec} or j_{Br_2} cannot be attributed to a specific cause.
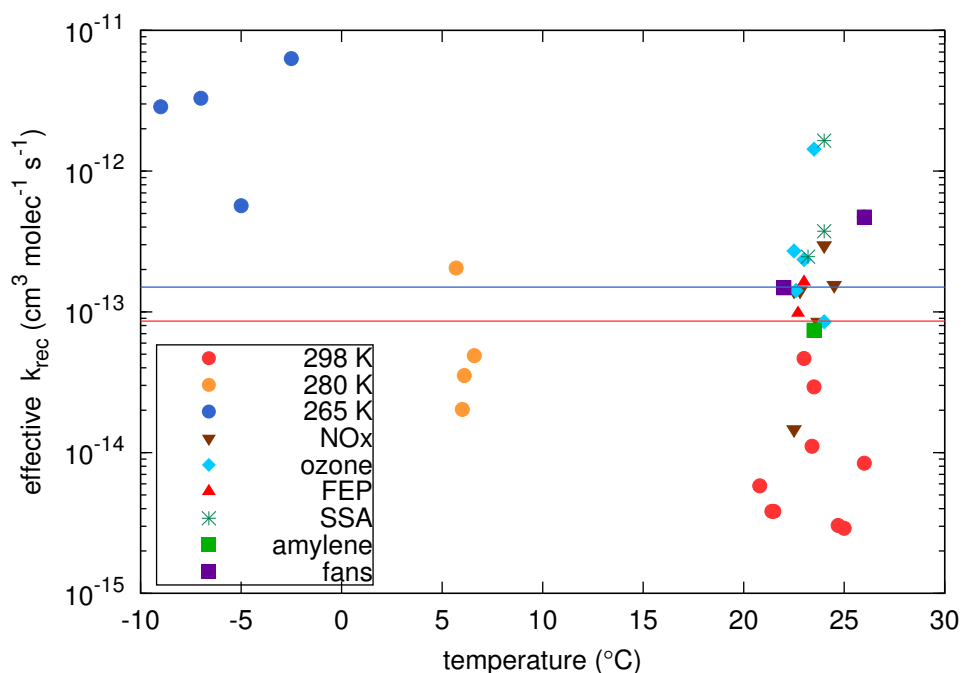
FIGURE 4.25: Trend of effective k_{rec} required to model the dark reaction with temperature, assuming constant j_{Br_2} of $10^{-6}\,\mathrm{s}^{-1}$. The blue and red lines are the literature rates for k_{rec} at 265 and 298 K.

There were likely contributions from further protocol development, differing wall losses as the chamber conditions changed. Actual differences in k_{rec} are unlikely to have contributed significantly to the observed changes in the dark reaction.

4.7.7 Conclusions

The oxidation of Hg in the chamber was generally slower than predicted by the most reliable literature data. The stepwise adjustment of each parameter of the model was a promising method of using all of the [Hg] decay data to separate the different reactions. However, without any measurements of the reaction intermediates or products the model was overdetermined so no unique solution exists.

If the poorer quality data at the extremes of [Br$_2$] are discounted then altering any of k_{fox}, k_{rec}, k_{cpa} or k_{abs} would fit most of the data. Of these parameters a reduction in k_{fox} by a factor of two was the smallest adjustment of a single parameter that could fit most of the data.

If the high and low [Br$_2$] are included then only an extremely fast, temperature-independent k_{thm} could fit all the points. There is no known mechanism that could produce such a fast HgBr dissociation that is consistent with the thermodynamics

140

of the HgBr bond. In the final section of this chapter the relevance of a fast HgBr dissociation to environmental studies is considered.

4.8   Application to environmental studies

In the environment, the timescale for Hg depletion is much longer than in the chamber, so it is reasonable to assume a steady state of HgBr, and that recombination of Br· is negligible. This simplifies the kinetics such that Hg decay is given by

$$-\frac{d[Hg]}{dt} = k_{fox}[Hg][Br] - k_{thm}[HgBr] \tag{4.12}$$

$$[HgBr] = \frac{k_{fox}[Hg][Br]}{k_{thm} + k_{sox}[X]} \tag{4.13}$$

where the second oxidation step by the arbitrary species [X] has the rate k_{sox}. The [X] includes Br· and any other species thought to be capable of completing the Hg oxidation.[106] The Hg lifetime is then

$$\tau_{Hg} = \frac{k_{thm} + k_{sox}[X]}{k_{fox}[Br]k_{sox}[X]} \tag{4.14}$$

If k_{thm} is much smaller than k_{sox} [X], then Hg is not recycled and goes straight to stable HgBrX. Under these conditions, $\tau_{Hg} = (k_{fox}[Br])^{-1}$ and HgBr thermolysis does not influence the Hg lifetime. This situation may arise in cold environments with a large [Br] or [X].

On the other hand, if k_{thm} is larger than k_{sox} [X], then Hg is recycled many times and k_{thm} becomes important. The lifetime is then proportional to $k_{thm}/k_{sox}[X]$. This would be the situation in most environments as [X] is generally low. Therefore we can say that for a given τ_{Hg}, an increased k_{thm} can be balanced by an increased [X].

The study of Hg depletion in the Dead Sea is particularly interesting as it is a warm environment with high levels of BrO and Br·.[94,282,306] The ambient temperature of 37 °C was expected to give a k_{thm} of 0.02 s^{-1}according to the old, incorrect, rate expression of Goodsite et al.[276] The corrected rate expression[296] gives a rate of 0.2 s^{-1}, whereas more accurate calculations[275] yield an even faster rate of 0.4 s^{-1}. These rates are still two orders of magnitude slower than the k_{thm} suggested here. However, the models of the Dead Sea Hg depletion included only BrO and Br as the secondary oxidants, and the k_{cpa} used was 2 orders of magnitude slower than

it likely is, due to the use of an estimated rate[279] rather than a calculated one (Section 4.2.4). As the ambient $[NO_2]$ and $[O_3]$ at the Dead Sea were several orders of magnitude higher than the $[Br]$, it is plausible that the second oxidation of Hg would be fast enough to compensate for the increased k_{thm}. Additionally, the effective k_{thm} suggested by the chamber experiments is not temperature dependent, so the effect of the hot environment would be less than it would with a literature k_{thm}. However, if our fast k_{thm} is due to photolysis, then it too may be an order of magnitude faster at the Dead Sea.

Another field study situated on tropical islands in the Pacific ocean[283] measured a diurnal cycle in which the RGM concentration began to increase at sunrise, peaked around midday then decreased again. They tested several models including some with more than just Br for the second oxidation step. The model that used the same k_{thm} as the default rate here required the secondary oxidation chemistry for a good fit, and the most likely candidates for the second oxidant were identified as NO_2 or HO_2. Since their best fit model already included secondary oxidation chemistry, there is no parameter that could adjust to accommodate a faster k_{thm}. The suggestion of a faster k_{thm} is therefore not consistent with these field observations.

Chapter 5

Conclusions and Further Work

Field measurements of atmospheric Hg depletion have been ongoing for more than 20 years, yet the chemical species resulting from the Hg oxidation have not yet been determined. [120] This work aimed to address this issue, first by designing a new Hg monitor, and then studying the gas phase oxidation reactions of Hg in a simulation chamber.

5.1   Hg Detector

The original project plan was to construct a 254 nm diode laser to use as the light source for a LIF or CEAS system. However, UV emission of the laser system was not achieved so an atomic line source was used instead in a simple CEAS setup to make measurements of $Hg^0(g)$. This was the first published example of an atomic line source being used for CEAS. [121] The [Hg] detection limit was 66 ng m^{-3} for an acquisition time of 10 s, which is not much better than conventional single pass instruments. The instrument could have been improved with a correction signal for lamp intensity variations. Measurement of another wavelength could also correct for broadband extinction from aerosols or O_3. The CEAS mirrors were also sensitive to humidity changes, which would complicate its use as a practical Hg monitor.

5.1.1   Future Work

For future work it is worth re-investigating diode lasers as a light source for Hg detection. Although many laser based systems have been developed for Hg detection,

all have been based on large, complex and delicate lasers that are very difficult to employ in field studies. A diode laser based system could give a marked improvement over existing systems.

Another approach would be to adapt the Zeeman-corrected method used by the Lumex Hg monitor. If the internal multi-pass cell was set up to cross a simulation chamber, it could potentially accomplish the same goal as the CRDS system. Long path field measurements based on this principle may be feasible.

Further development of field instrumentation is needed to better understand the atmospheric redox processes. No instrument can yet measure RGM quantitatively or with chemical speciation. Accurate flux measurements of $Hg^0(g)$ would also help to fill in many of the gaps in our understanding of environmental mercury cycles.

5.2   Hg Chamber Reactions

The atmospheric simulation chamber—built in the Desert Research Institute in Reno, NV, USA equipped with the Hg CRDS system of Pierce et al. [128]—afforded an opportunity to study Hg/Br chemistry at concentrations closer to environmental conditions than in previous studies. A typical experiment followed the decay of $[Hg]$ from $100\,ng\,m^{-3}$ to zero over a few seconds to several minutes, with $[Br_2]$ varied from 10^{10} to $10^{13}\,molec\,cm^{-3}$. Several experimental problems were encountered. Background photolysis of Br_2 caused an apparent dark reaction, which was solved by keeping the lab as dark as practical during Br_2 injection. Temperature changes induced artefacts in the spectrally-derived $[Br_2]$, so the spectrometer and cavity optics were insulated, and the Br_2 was determined as soon as possible after injection. Towards the end of the project laser failure became an issue as the beam quality degraded, and the dye had to be changed increasingly frequently.

5.2.1   Main Results

The Hg depletion observed in the chamber was slower than could be explained by current literature rates. The difference was greatest at low $[Br_2]$. A model of the chamber chemistry composed of 7 reactions was used to attempt to find which reactions could be responsible for the slow overall decay of Hg. It was not possible to determine exactly which rate was responsible as there were too many indistinguishable possibilities. Data on the concentration of the reaction

intermediates could help to separate the influence of the different reactions, but such measurements were unavailable.

The initial analysis of each chamber experiment individually suggested either k_{rec}, k_{fox}, k_{abs} or k_{cpa} differed from literature values by median factors of 6, 0.5, 8 and 0.1 respectively. None of the literature data were directly comparable as they used N_2 or Ar as opposed to air, and were at different temperatures and pressures to those in the chamber. Although k_{abs} and k_{cpa} required large adjustments, they are not relevant to the very low [Br] in the environment and their literature values are not well constrained. The fits achieved with the optimised rates to the individual reactions were acceptable, but the optimum values of all these parameters showed a dependence on [Br_2]. The only rate that could explain the reaction order in Br_2 was HgBr decomposition of $20\,s^{-1}$, some 700 times faster than suggested by the literature.

For the faster HgBr decomposition to be consistent with the thermodynamic stability of HgBr, the decay route cannot be the same as the formation. The lack of temperature dependence of the optimum k_{thm} suggested a non-thermal decomposition route, such as photolysis or collision with other molecules or surfaces. A calculated photolytic cross section suggested a rate that was 4 orders of magnitude smaller than the optimised k_{thm}. A much faster decomposition may have been measured in a previous study, although the results were highly uncertain and may have been influenced by analysis with an incomplete model.[158]

Although every effort was made to remove systematic biases, some may still remain. Removal of the earliest, most uncertain data points brings the measured Br_2 order much closer to the modelled order. There may have been additional variation caused by trace contamination in the chamber by H_2O, NO_2 etc.

Other gases such as O_3, NO_2 did not accelerate the oxidation but hindered it, possibly by reacting with Br·, or helping HgBr to dissociate. The extra noise and experimental variation introduced by the extra oxidant made quantitative measurements difficult. If the oxidation of HgBr was faster in these experiments it would not have been visible, as the second oxidation by Br· was fast enough that the completion step was not rate limiting.

The presence of extra surface in the form of FEP film or sea salt aerosol appeared to slow the reaction. This was probably due to the influence of the altered mixing rate or faster removal of Br·. Reactions were, however, nearly always faster in the presence of reaction products. This rate increase was highly variable but seen over

a wide range of conditions. Since the concentration of the reaction products was so low compared to the other species present the rate acceleration may be an artefact of the experiment, such as an increase of adsorbed Br_2 on the walls. There was no significant correlation of the acceleration with Br_2.

What is perhaps more significant is what was not observed. A large wall loss of Hg to the FEP wall was not observed, neither did the wall losses accelerate despite the build up of $HgBr_x(s)$ during the campaign. Re-emission of Hg deposited to the wall during heating or visible light photolysis was not observed.

The inability of the model to distinguish the effects of these different reactions underlines the need for measurements of the intermediates Br and HgBr. This work has demonstrated that a more detailed quantitative understanding of $Hg^0(g)$ oxidation can only be realised with these measurements.

5.2.2   Future work

Further studies with the same chamber setup should focus on repeating the initial baseline reactions with only Br_2, Hg and at room temperature. Increased temperatures would be relatively easy to achieve, and would provide more information on k_{thm}. Flushing the chamber with N_2 would aid comparisons to literature, and humidifying the chamber would provide even more environmentally relevant conditions. Reconfiguration of the $[Br_2]$ CEAS system and Br_2 injection system would take more work but may ultimately extend the measurements to much lower $[Br_2]$, where the differences between the possible Br_2 orders are larger.

Future studies of Hg chemistry must include measurements on the intermediates. Much of the uncertainty in this work was due to a lack of quantitative $[Br]$. There is now a lot of interest in the oxidation of HgBr, which can only be studied effectively if its concentration can be measured. LIF techniques often need reduced pressure, which requires more complex chamber design, or a much larger chamber that would not suffer excessive extraction losses. Reduced pressure would also be relevant to Hg oxidation in the stratosphere.

The transboundary nature of Hg pollution makes it a global problem. Knowledge of the oxidation pathways is only one step of the biogeochemical cycle.[2] Reduction processes are what allow Hg to be continuously re-emitted back to the environment, and methylation allows it to bioaccumulate up the food chain. Managing the impact of Hg requires progress not only in understanding of the chemistry, but also in

many diverse areas of international development, diplomacy, emissions regulations etc. The Minamata convention on mercury now provides a political framework to address these broader issues.[47] Better chemical understanding of biogeochemical cycles is just one part in a large and complex picture.

References

[1] UNEP Chemical Branch, *Technical Background Report for the Global Mercury Assessment*; 2013.

[2] UNEP Chemical Branch, *Global Mercury Assessment 2013, Sources, Emissions, Releases and Environmental Transport*; 2013.

[3] Czerwinski, F.; Richardson, A. C.; Oddershede, L. B. Quantifying Noise in Optical Tweezers by Allan Variance. *Opt. Express* **2009**, *17*, 13255–13269, doi:10.1364/OE.17.013255.

[4] Maric, D.; Burrows, J. P.; Moortgat, G. K. A study of the UV–visible absorption spectra of Br2 and BrCl. *J. Photochem. Photobiol. A Chem.* **1994**, *83*, 179–192, doi:10.1016/1010-6030(94)03823-6.

[5] Keller-Rudek, H.; Moortgat, G. K.; Sander, R.; Sörensen, R. The MPI-Mainz UV-VIS Spectral Atlas of Gaseous Molecules of Atmospheric Interest. *Earth Syst. Sci. Data* **2013**, *5*, 365–373, doi:10.5194/essd-5-365-2013.

[6] Gajić-Kvaščev, M.; Stojanović, M. M.; Šmit, v.; Kantarelou, V.; Karydas, A. G.; Šljivar, D.; Milovanović, D.; Andrić, V. New evidence for the use of cinnabar as a colouring pigment in the Vinča culture. *J. Archaeol. Sci.* **2012**, *39*, 1025–1033, doi:10.1016/j.jas.2011.11.023.

[7] Martín-Gil, J.; Martín-Gil, F. J.; Delibes-de Castro, G.; Zapatero-Magdaleno, P.; Sarabia-Herrero, F. J. The first known use of vermillion. *Experientia* **1995**, *51*, 759–761, doi:10.1007/BF01922425.

[8] UNESCO World Heritage Centre, Heritage of Mercury – Almadén, Idrija. 2011; `whc.unesco.org/uploads/nominations/1313rev.pdf`.

[9] Serrano, O.; Martínez-Cortizas, A.; Mateo, M.; Biester, H.; Bindler, R. Millennial scale impact on the marine biogeochemical cycle of mercury from early mining on the Iberian Peninsula. *Glob. Biogeochem. Cycles* **2013**, *27*, 21–30, doi:10.1029/2012GB004296.

[10] Hernández, A.; Jébrak, M.; Higueras, P.; Oyarzun, R.; Morata, D.; Munhá, J. The Almadén mercury mining district, Spain. *Miner. Depos.* **1999**, *34*, 539–548, doi:10.1007/s001260050219.

[11] Streets, D. G.; Devane, M. K.; Lu, Z.; Bond, T. C.; Sunderland, E. M.; Jacob, D. J. All-Time Releases of Mercury to the Atmosphere from Human Activities. *Environ. Sci. Technol.* **2011**, *45*, 10485–10491, doi:10.1021/es202765m.

[12] Dietz, R.; Outridge, P. M.; Hobson, K. A. Anthropogenic contributions to mercury levels in present-day Arctic animals–A review. *Sci. Total Environ.* **2009**, *407*, 6120–6131, doi:10.1016/j.scitotenv.2009.08.036.

[13] Dietz, R.; Sonne, C.; Basu, N.; Braune, B.; O'Hara, T.; Letcher, R. J.; Scheuhammer, T.; Andersen, M.; Andreasen, C.; Andriashek, D.; Asmund, G.; Aubail, A.; Baagøe, H.; Born, E. W.; Chan, H. M.; Derocher, A. E.; Grandjean, P.; Knott, K.; Kirkegaard, M.; Krey, A.; Lunn, N.; Messier, F.; Obbard, M.; Olsen, M. T.; Ostertag, S.; Peacock, E.; Renzoni, A.; Rigét, F. F.; Skaare, J. U.; Stern, G.; Stirling, I.; Taylor, M.; Wiig, Ø.; Wilson, S.; Aars, J. What are the toxicological effects of mercury in Arctic biota? *Sci. Total Environ.* **2013**, *443*, 775–790, doi:10.1016/j.scitotenv.2012.11.046.

[14] Holmes, C. D.; Jacob, D. J.; Corbitt, E. S.; Mao, J.; Yang, X.; Talbot, R.; Slemr, F. Global atmospheric model for mercury including oxidation by bromine atoms. *Atmos. Chem. Phys.* **2010**, *10*, 12037–12057, doi:10.5194/acp-10-12037-2010.

[15] Steffen, A.; Douglas, T.; Amyot, M.; Ariya, P.; Aspmo, K.; Berg, T.; Bottenheim, J.; Brooks, S.; Cobbett, F.; Dastoor, A.; Dommergue, A.; Ebinghaus, R.; Ferrari, C.; Gardfeldt, K.; Goodsite, M. E.; Lean, D.; Poulain, A. J.; Scherz, C.; Skov, H.; Sommar, J.; Temme, C. A synthesis of atmospheric mercury depletion event chemistry in the atmosphere and snow. *Atmos. Chem. Phys.* **2008**, *8*, 1445–1482, doi:10.5194/acp-8-1445-2008.

[16] Gochfeld, M. Cases of mercury exposure, bioavailability, and absorption. *Ecotoxicol. Environ. Saf.* **2003**, *56*, 174–179, doi:10.1016/S0147-6513(03)00060-5.

[17] Clarkson, T. W.; Magos, L. The Toxicology of Mercury and Its Chemical Compounds. *Crit. Rev. Toxicol.* **2006**, *36*, 609–662, doi:10.1080/10408440600845619.

[18] Hunter, D.; Bomford, R. R.; Russell, D. S. Poisoning by Methyl Mercury Compounds. *QJM* **1940**, *9*, 193–226.

[19] Ahlmark, A. Poisoning by Methyl Mercury Compounds. *Br J Ind Med* **1948**, *5*, 117–119.

[20] Nierenberg, D. W.; Nordgren, R. E.; Chang, M. B.; Siegler, R. W.; Blayney, M. B.; Hochberg, F.; Toribara, T. Y.; Cernichiari, E.; Clarkson, T. Delayed Cerebellar Disease and Death after Accidental Exposure to Dimethylmercury. *N. Engl. J. Med.* **1998**, *338*, 1672–1676, doi:10.1056/NEJM199806043382305.

[21] Stock, A. Die Gefährlichkeit des Quecksilberdampfes. *Angew. Chemie* **1926**, *39*, 461–466, doi:10.1002/ange.19260391502.

[22] Jonas, L.; Jaksch, H.; Zellmann, E.; Klemm, K. I.; Andersen, P. H. j. Detection of Mercury in the 411-year-old Beard Hairs of the Astronomer Tycho Brahe by Elemental Analysis in Electron Microscopy. *Ultrastruct Pathol* **2012**, *36*, 312–319, doi:10.3109/01913123.2012.685686.

[23] Johnson, L. W.; Wolbarsht, M. L. Mercury Poisoning: A Probable Cause of Isaac Newton's Physical and Mental Ills. *Notes Rec. R. Soc. Lond.* **1979**, *34*, 1–9.

[24] Fiedler, N.; Udasin, I.; Gochfeld, M.; Buckler, G.; Kelly-McNeil, K.; Kipen, H. Neuropsychological and stress evaluation of a residential mercury exposure. *Env. Heal. Perspect* **1999**, *107*, 343–347.

[25] Li, M.; Sherman, L. S.; Blum, J. D.; Grandjean, P.; Mikkelsen, B.; Weihe, P.; Sunderland, E. M.; Shine, J. P. Assessing Sources of Human Methylmercury Exposure Using Stable Mercury Isotopes. *Environ. Sci. Technol.* **2014**, *48*, 8800–8806, doi:10.1021/es500340r.

[26] Mergler, D.; Anderson, H. A.; Chan, L. H. M.; Mahaffey, K. R.; Murray, M.; Sakamoto, M.; Stern, A. H. Methylmercury Exposure and Health Effects in Humans: A Worldwide Concern. *AMBIO: J. Hum. Environ.* **2007**, *36*, 3–11, doi:10.1579/0044-7447(2007)36[3:MEAHEI]2.0.CO;2.

[27] Zhang, H.; Feng, X.; Larssen, T. r.; Qiu, G.; Vogt, R. D. In Inland China, Rice, Rather than Fish, Is the Major Pathway for Methylmercury Exposure. *Environ. Health Perspect.* **2010**, *118*, 1183–1188, doi:10.1289/ehp.1001915.

[28] Sonne, C. Health effects from long-range transported contaminants in Arctic top predators: An integrated review based on studies of polar bears and relevant model species. *Environ. Int.* **2010**, *36*, 461–491, doi:10.1016/j.envint.2010.03.002.

[29] Evers, D. C.; Savoy, L. J.; DeSorbo, C. R.; Yates, D. E.; Hanson, W.; Taylor, K. M.; Siegel, L. S.; Jr, J. H. C.; Bank, M. S.; Major, A.; Munney, K.; Mower, B. F.; Vogel, H. S.; Schoch, N.; Pokras, M.; Goodale, M. W.; Fair, J. Adverse effects from environmental mercury loads on breeding common loons. *Ecotoxicology* **2008**, *17*, 69–81, doi:10.1007/s10646-007-0168-7.

[30] Crump, K. L.; Trudeau, V. L. Mercury-induced reproductive impairment in fish. *Environ. Toxicol. Chem.* **2009**, *28*, 895–907, doi:10.1897/08-151.1.

[31] Bocharova, N.; Treu, G.; Czirják, G. A.; Krone, O.; Stefanski, V.; Wibbelt, G.; Unnsteinsdóttir, E. R.; Hersteinsson, P.; Schares, G.; Doronina, L.; Goltsman, M.; Greenwood, A. D. Correlates between Feeding Ecology and Mercury Levels in Historical and Modern Arctic Foxes (Vulpes lagopus). *PLoS One* **2013**, *8*, e60879, doi:10.1371/journal.pone.0060879.

[32] Mahaffey, K. R.; Sunderland, E. M.; Chan, H. M.; Choi, A. L.; Grandjean, P.; Mariën, K.; Oken, E.; Sakamoto, M.; Schoeny, R.; Weihe, P.; Yan, C.-H.; Yasutake, A. Balancing the benefits of n-3 polyunsaturated fatty acids and the risks of methylmercury exposure from fish consumption. *Nutr. Rev.* **2011**, *69*, 493–508, doi:10.1111/j.1753-4887.2011.00415.x.

[33] Karagas, M. R.; Choi, A. L.; Oken, E.; Horvat, M.; Schoeny, R.; Kamai, E.; Cowell, W.; Grandjean, P.; Korrick, S. Evidence on the Human Health Effects of Low-Level Methylmercury Exposure. *Environ. Health Perspect.* **2012**, *120*, 799–806, doi:10.1289/ehp.1104494.

[34] Axelrad, D. A.; Bellinger, D. C.; Ryan, L. M.; Woodruff, T. J. Dose-Response Relationship of Prenatal Mercury Exposure and IQ: An Integrative Analysis of Epidemiologic Data. *Env. Heal. Perspect* **2007**, *115*, 609–615, doi:10.1289/ehp.9303.

[35] Pichery, C.; Bellanger, M.; Zmirou-Navier, D.; Glorennec, P.; Hartemann, P.; Grandjean, P. Childhood lead exposure in France: benefit estimation and partial cost-benefit analysis of lead hazard control. *Environ. Heal.* **2011**, *10*, 44, doi:10.1186/1476-069X-10-44.

[36] Bellanger, M.; Pichery, C.; Aerts, D.; Berglund, M.; Castaño, A.; Čejchanová, M.; Crettaz, P.; Davidson, F.; Esteban, M.; Fischer, M. E.; Gurzau, A. E.; Halzlova, K.; Katsonouri, A.; Knudsen, L. E.; Kolossa-Gehring, M.; Koppen, G.; Ligocka, D.; Miklavčič, A.; Reis, M. F.; Rudnai, P.; Tratnik, J. S.; Weihe, P.; Budtz-Jørgensen, E.; Grandjean, P. Economic benefits of methylmercury exposure control in Europe: Monetary value of neurotoxicity prevention. *Environ. Heal.* **2013**, *12*, 3, doi:10.1186/1476-069X-12-3.

[37] Sundseth, K.; Pacyna, J. M.; Pacyna, E. G.; Munthe, J.; Belhaj, M.; Astrom, S. Economic benefits from decreased mercury emissions: Projections for 2020. *Journal of Cleaner Production* **2010**, *18*, 386–394, doi:10.1016/j.jclepro.2009.10.017.

[38] Rooney, J. P. K. The role of thiols, dithiols, nutritional factors and interacting ligands in the toxicology of mercury. *Toxicology* **2007**, *234*, 145–156, doi:10.1016/j.tox.2007.02.016.

[39] Broniatowski, M.; Dynarowicz-Łatka, P. Search for the Molecular Mechanism of Mercury Toxicity. Study of the Mercury(II)-Surfactant Complex Formation in Langmuir Monolayers. *J. Phys. Chem. B* **2009**, *113*, 4275–4283, doi:10.1021/jp810339e.

[40] Bergman, A.; Heindel, J. J.; Jobling, S.; Kidd, K. A.; Zoeller, R. T. *State of the science of endocrine disrupting chemicals - 2012*; UNEP, WHO: Geneva, Switzerland, 2013.

[41] Choi, A. L.; Budtz-Jørgensen, E.; Jørgensen, P. J.; Steuerwald, U.; Debes, F.; Weihe, P.; Grandjean, P. Selenium as a potential protective factor against mercury developmental neurotoxicity. *Environ. Res.* **2008**, *107*, 45–52, doi:10.1016/j.envres.2007.07.006.

[42] Harada, M. Minamata Disease: Methylmercury Poisoning in Japan Caused by Environmental Pollution. *Crit. Rev. Toxicol.* **1995**, *25*, 1–24, doi:10.3109/10408449509089885.

[43] Hachiya, N. The History and the Present of Minamata Disease–Entering the second half a century. *Japan Med. Assoc. J.* **2006**, *49*, 112–118.

[44] Bakir, F.; Damluji, S. F.; Amin-Zaki, L.; Murtadha, M.; Khalidi, A.; Al-Rawi, N. Y.; Tikriti, S.; Dahahir, H. I.; Clarkson, T. W.; Smith, J. C.; Doherty, R. A. Methylmercury poisoning in Iraq. *Science* **1973**, *181*, 230–241.

[45] Giles, J. Iraqis draw up blueprint for revitalized science academy. *Nature* **2003**, *426*, 484, doi:10.1038/426484b.

[46] Al-Damluji, S. F. Organomercury poisoning in Iraq: History prior to the 1971-72 outbreak. *Bull World Heal. Organ* **1976**, *53*, 9–13.

[47] UNEP, Minamata Convention on Mercury. 2013.

[48] Pavlish, J. H.; Sondreal, E. A.; Mann, M. D.; Olson, E. S.; Galbreath, K. C.; Laudal, D. L.; Benson, S. A. Status review of mercury control options for coal-fired power plants. *Fuel Process. Technol.* **2003**, *82*, 89–165, doi:10.1016/S0378-3820(03)00059-6.

[49] Clifford, M. J. Future strategies for tackling mercury pollution in the artisanal gold mining sector: Making the Minamata Convention work. *Futures* **2014**, *62, Part A*, 106–112, doi:10.1016/j.futures.2014.05.001.

[50] Selin, N. E. Global change and mercury cycling: Challenges for implementing a global mercury treaty. *Env. Toxicol Chem* **2014**, *33*, 1202–1210, doi:10.1002/etc.2374.

[51] Selin, N. E.; Jacob, D. J.; Yantosca, R. M.; Strode, S.; Jaeglé, L.; Sunderland, E. M. Global 3-D land-ocean-atmosphere model for mercury: Present-day versus preindustrial cycles and anthropogenic enrichment factors for deposition. *Glob. Biogeochem. Cycles* **2008**, *22*, GB2011, doi:10.1029/2007GB003040.

[52] Monbiot, G. *Yes, lead poisoning could really be a cause of violent crime*; Guardian, Jan, 2013.

[53] Nevin, R. Understanding international crime trends: The legacy of preschool lead exposure. *Environ. Res.* **2007**, *104*, 315–336, doi:10.1016/j.envres.2007.02.008.

[54] Wright, J. P.; Dietrich, K. N.; Ris, M. D.; Hornung, R. W.; Wessel, S. D.; Lanphear, B. P.; Ho, M.; Rae, M. N. Association of Prenatal and Childhood Blood Lead Concentrations with Criminal Arrests in Early Adulthood. *PLoS Med* **2008**, *5*, e101, doi:10.1371/journal.pmed.0050101.

[55] Mielke, H. W.; Zahran, S. The urban rise and fall of air lead (Pb) and the latent surge and retreat of societal violence. *Environ. Int.* **2012**, *43*, 48–55, doi:10.1016/j.envint.2012.03.005.

[56] McCall, P. L.; Land, K. C. Trends in environmental lead exposure and troubled youth, 1960-1995: an age-period-cohort-characteristic analysis. *Soc. Sci. Res.* **2004**, *33*, 339–359, doi:10.1016/j.ssresearch.2003.06.002.

[57] Broadwith, P. Tetraethyl lead bribery case ends with four executives convicted. 2014; `http://www.rsc.org/chemistryworld/2014/08/tetraethyl-lead-bribery-case-ends-four-executives-convicted`.

[58] Slemr, F.; Brunke, E.-G.; Ebinghaus, R.; Kuss, J. Worldwide trend of atmospheric mercury since 1995. *Atmos. Chem. Phys.* **2011**, *11*, 4779–4787, doi:10.5194/acp-11-4779-2011.

[59] Lamborg, C. H.; Hammerschmidt, C. R.; Bowman, K. L.; Swarr, G. J.; Munson, K. M.; Ohnemus, D. C.; Lam, P. J.; Heimbürger, L.-E.; Rijkenberg, M. J. A.; Saito, M. A. A global ocean inventory of anthropogenic mercury based on water column measurements. *Nature* **2014**, *512*, 65–68, doi:10.1038/nature13563.

[60] Pirrone, N.; Cinnirella, S.; Feng, X.; Finkelman, R. B.; Friedli, H. R.; Leaner, J.; Mason, R.; Mukherjee, A. B.; Stracher, G. B.; Streets, D. G.; Telmer, K. Global mercury emissions to the atmosphere from anthropogenic and natural sources. *Atmos. Chem. Phys.* **2010**, *10*, 5951–5964, doi:10.5194/acp-10-5951-2010.

[61] Amos, H. M.; Jacob, D. J.; Streets, D. G.; Sunderland, E. M. Legacy impacts of all-time anthropogenic emissions on the global mercury cycle. *Glob. Biogeochem. Cycles* **2013**, *27*, 410–421, doi:10.1002/gbc.20040.

[62] Pacyna, E. G.; Pacyna, J. M.; Steenhuisen, F.; Wilson, S. Global anthropogenic mercury emission inventory for 2000. *Atmos. Environ.* **2006**, *40*, 4048–4063, doi:10.1016/j.atmosenv.2006.03.041.

[63] Pirrone, N.; Cinnirella, S.; Feng, X.; Finkelman, R. B.; Friedli, H. R.; Leaner, J.; Mason, R.; Mukherjee, A. B.; Stracher, G.; Streets, D. G.; Telmer, K. In *Mercury Fate and Transport in the Global Atmosphere*; Mason, R., Pirrone, N., Eds.; Springer, 2009; pp 1–47.

[64] Horowitz, H. M.; Jacob, D. J.; Amos, H. M.; Streets, D. G.; Sunderland, E. M. Historical Mercury Releases from Commercial Products: Global Environmental Implications. *Environ. Sci. Technol.* **2014**, *48*, 10242–10250, doi:10.1021/es501337j.

[65] Schuster, P. F.; Krabbenhoft, D. P.; Naftz, D. L.; Cecil, L. D.; Olson, M. L.; Dewild, J. F.; Susong, D. D.; Green, J. R.; Abbott, M. L. Atmospheric Mercury Deposition during the Last 270 Years: A Glacial Ice Core Record of Natural and Anthropogenic Sources. *Environ. Sci. Technol.* **2002**, *36*, 2303–2310, doi:10.1021/es0157503.

[66] Obrist, D.; Pokharel, A. K.; Moore, C. Vertical Profile Measurements of Soil Air Suggest Immobilization of Gaseous Elemental Mercury in Mineral Soil. *Environ. Sci. Technol.* **2014**, *48*, 2242–2252, doi:10.1021/es4048297.

[67] Sunderland, E. M.; Mason, R. P. Human impacts on open ocean mercury concentrations. *Glob. Biogeochem. Cycles* **2007**, *21*, GB4022, doi:10.1029/2006GB002876.

[68] Pyykko, P.; Desclaux, J. P. Relativity and the periodic system of elements. *Acc. Chem. Res.* **1979**, *12*, 276–281.

[69] Calvo, F.; Pahl, E.; Wormit, M.; Schwerdtfeger, P. Evidence for Low-Temperature Melting of Mercury owing to Relativity. *Angew. Chemie Int. Ed.* **2013**, *52*, 7583–7585, doi:10.1002/anie.201302742.

[70] Cotton, F. A. *Advanced Inorganic Chemistry*, 5th ed.; John Wiley & Sons, 1988.

[71] Eichler, R.; Aksenov, N. V.; Belozerov, A. V.; Bozhikov, G. A.; Chepigin, V. I.; Dmitriev, S. N.; Dressler, R.; Gäggeler, H. W.; Gorshkov, V. A.; Haenssler, F.; Itkis, M. G.; Laube, A.; Lebedev, V. Y.; Malyshev, O. N.; Oganessian, Y. T.; Petrushkin, O. V.; Piguet, D.; Rasmussen, P.; Shishkin, S. V.; Shutov, A. V.; Svirikhin, A. I.; Tereshatov, E. E.; Vostokin, G. K.; Wegrzecki, M.; Yeremin, A. V. Chemical characterization of element 112. *Nature* **2007**, *447*, 72–75, doi:10.1038/nature05761.

[72] Dumarey, R.; Brown, R. J. C.; Corns, W. T.; Brown, A. S.; Stockwell, P. B. Elemental mercury vapour in air: the origins and validation of the 'Dumarey equation' describing the mass concentration at saturation. *Accred Qual Assur* **2010**, *15*, 409–414, doi:10.1007/s00769-010-0645-1.

[73] Huber, M. L.; Laesecke, A.; Friend, D. G. Correlation for the Vapor Pressure of Mercury. *Ind. Eng. Chem. Res.* **2006**, *45*, 7351–7361, doi:10.1021/ie060560s.

[74] Long, S. E.; Hendricks, J. H.; Schaedlich, F. Mercury Vapor Pressure Correlation. 2011; `www.nist.gov/mml/analytical/inorganic/hgvaporpressure.cfm`.

[75] Brown, A. S.; Brown, R. J. C.; Corns, W. T.; Stockwell, P. B. Establishing SI traceability for measurements of mercury vapour. *Analyst* **2008**, *133*, 946, doi:10.1039/b803724h.

[76] Brown, R. J. C.; Pirrone, N.; van Hoek, C.; Sprovieri, F.; Fernandez, R.; Toté, K. Standardisation of a European measurement method for the determination of total gaseous mercury: results of the field trial campaign and determination of a measurement uncertainty and working range. *J. Environ. Monit.* **2010**, *12*, 689, doi:10.1039/b924955a.

[77] Ent, H.; Inge van Andel,; Heemskerk, M.; Peter van Otterloo,; Bavius, W.; Baldan, A.; Horvat, M.; Brown, R. J. C.; Quétel, C. R. A gravimetric approach to providing SI traceability for concentration measurement results of mercury vapor at ambient air levels. *Meas. Sci. Technol.* **2014**, *25*, 115801–115811, doi:10.1088/0957-0233/25/11/115801.

[78] Quétel, C. R.; Zampella, M.; Brown, R. J. C.; Ent, H.; Horvat, M.; Paredes, E.; Tunc, M. International System of Units Traceable Results of Hg Mass Concentration at Saturation in Air from a Newly Developed Measurement Procedure. *Anal. Chem.* **2014**, *86*, 7819–7827, doi:10.1021/ac5018875.

[79] Sun, R.; Sonke, J. E.; Heimbürger, L.-E.; Belkin, H. E.; Liu, G.; Shome, D.; Cukrowska, E.; Liousse, C.; Pokrovsky, O. S.; Streets, D. G. Mercury Stable Isotope Signatures of World Coal Deposits and Historical Coal Combustion Emissions. *Environ. Sci. Technol.* **2014**, *48*, 7660–7668, doi:10.1021/es501208a.

[80] Mead, C.; Lyons, J. R.; Johnson, T. M.; Anbar, A. D. Unique Hg Stable Isotope Signatures of Compact Fluorescent Lamp-Sourced Hg. *Environ. Sci. Technol.* **2013**, *47*, 2542–2547, doi:10.1021/es303940p.

[81] Bergquist, B. A.; Blum, J. D. The Odds and Evens of Mercury Isotopes: Applications of Mass-Dependent and Mass-Independent Isotope Fractionation. *Elements* **2009**, *5*, 353–357, doi:10.2113/gselements.5.6.353.

[82] Blum, J. D. In *Handbook of Environmental Isotope Geochemistry*; Baskaran, M., Ed.; Advances in Isotope Geochemistry; Springer, 2012; pp 229–245.

[83] Lyman, S. N.; Jaffe, D. A.; Gustin, M. S. Release of mercury halides from KCl denuders in the presence of ozone. *Atmos. Chem. Phys.* **2010**, *10*, 8197–8204, doi:10.5194/acp-10-8197-2010.

[84] Gustin, M. S.; Huang, J.; Miller, M. B.; Peterson, C.; Jaffe, D. A.; Ambrose, J.; Finley, B. D.; Lyman, S. N.; Call, K.; Talbot, R.; Feddersen, D.; Mao, H.; Lindberg, S. E. Do We Understand What the Mercury Speciation Instruments Are Actually Measuring? Results of RAMIX. *Environ. Sci. Technol.* **2013**, *47*, 7295–7306, doi:10.1021/es3039104.

[85] McClure, C. D.; Jaffe, D. A.; Edgerton, E. S. Evaluation of the KCl Denuder Method for Gaseous Oxidized Mercury using $HgBr_2$ at an In-Service AMNet Site. *Environ. Sci. Technol.* **2014**, *48*, 11437–11444, doi:10.1021/es502545k.

[86] Landis, M. S.; Stevens, R. K.; Schaedlich, F.; Prestbo, E. M. Development and Characterization of an Annular Denuder Methodology for the Measurement of Divalent Inorganic Reactive Gaseous Mercury in Ambient Air. *Environ. Sci. Technol.* **2002**, *36*, 3000–3009, doi:10.1021/es015887t.

[87] Jernelöv, A.; Landner, L.; Larsson, T. Swedish Perspectives on Mercury Pollution. *J. (Water Pollut. Control Fed.)* **1975**, *47*, 810–822.

[88] Ebinghaus, R.; Banic, C.; Beauchamp, S.; Jaffe, D.; Kock, H. H.; Pirrone, N.; Poissant, L.; Sprovieri, F.; Weiss-Penzias, P. S. In *Mercury Fate and Transport in the Global Atmosphere*; Mason, R., Pirrone, N., Eds.; Springer, 2009; pp 223–291.

[89] Schroeder, W. H.; Anlauf, K. G.; Barrie, L. A.; Lu, J. Y.; Steffen, A. Arctic springtime depletion of mercury. *Nature* **1998**, *394*, 16–17.

[90] Lindberg, S. E.; Brooks, S.; Lin, C.-J.; Scott, K. J.; Landis, M. S.; Stevens, R. K.; Goodsite, M.; Richter, A. Dynamic Oxidation of Gaseous Mercury in the Arctic Troposphere at Polar Sunrise. *Environ. Sci. Technol.* **2002**, *36*, 1245–1256, doi:10.1021/es0111941.

[91] Carignan, J.; Sonke, J. The effect of atmospheric mercury depletion events on the net deposition flux around Hudson Bay, Canada. *Atmos. Environ.* **2010**, *44*, 4372–4379, doi:10.1016/j.atmosenv.2010.07.052.

[92] Ebinghaus, R.; Kock, H. H.; Temme, C.; Einax, J. W.; Löwe, A. G.; Richter, A.; Burrows, J. P.; Schroeder, W. H. Antarctic Springtime Depletion of Atmospheric Mercury. *Environ. Sci. Technol.* **2002**, *36*, 1238–1244, doi:10.1021/es015710z.

[93] Sprovieri, F.; Pirrone, N.; Hedgecock, I. M.; Landis, M. S.; Stevens, R. K. Intensive atmospheric mercury measurements at Terra Nova Bay in Antarctica during November and December 2000. *J. Geophys. Res.* **2002**, *107*, 4722, doi:10.1029/2002JD002057.

[94] Obrist, D.; Tas, E.; Peleg, M.; Matveev, V.; Faïn, X.; Asaf, D.; Luria, M. Bromine-induced oxidation of mercury in the mid-latitude atmosphere. *Nat. Geosci.* **2010**, *4*, 22–26, doi:10.1038/ngeo1018.

[95] Brunke, E. G.; Labuschagne, C.; Ebinghaus, R.; Kock, H. H.; Slemr, F. Gaseous elemental mercury depletion events observed at Cape Point during 2007-2008. *Atmos. Chem. Phys.* **2010**, *10*, 1121–1131, doi:10.5194/acp-10-1121-2010.

[96] Lyman, S. N.; Jaffe, D. A. Formation and fate of oxidized mercury in the upper troposphere and lower stratosphere. *Nat. Geosci.* **2012**, *5*, 114–117, doi:10.1038/ngeo1353.

[97] Wright, G.; Gustin, M. S.; Weiss-Penzias, P.; Miller, M. B. Investigation of mercury deposition and potential sources at six sites from the Pacific Coast to the Great Basin, USA. *Sci. Total Environ.* **2014**, *470*, 1099–1113, doi:10.1016/j.scitotenv.2013.10.071.

[98] Huang, J.; Gustin, M. S. Evidence for a Free Troposphere Source of Mercury in Wet Deposition in the Western United States. *Environ. Sci. Technol.* **2012**, *46*, 6621–6629, doi:10.1021/es3005915.

[99] Bartels-Rausch, T.; Huthwelker, T.; Jöri, M.; Gäggeler, H. W.; Ammann, M. Interaction of gaseous elemental mercury with snow surfaces: laboratory investigation. *Environ. Res. Lett.* **2008**, *3*, 45009, doi:10.1088/1748-9326/3/4/045009.

[100] Schroeder, W. H.; Munthe, J. Atmospheric mercury–An overview. *Atmos. Environ.* **1998**, *32*, 809–822, doi:10.1016/S1352-2310(97)00293-8.

[101] Amos, H. M.; Jacob, D. J.; Holmes, C. D.; Fisher, J. A.; Wang, Q.; Yantosca, R. M.; Corbitt, E. S.; Galarneau, E.; Rutter, A. P.; Gustin, M. S.; Steffen, A.; Schauer, J. J.; Graydon, J. A.; Louis, V. L. S.; Talbot, R. W.; Edgerton, E. S.; Zhang, Y.; Sunderland, E. M. Gas-particle partitioning of atmospheric Hg(II) and its effect on global mercury deposition. *Atmos. Chem. Phys.* **2012**, *12*, 591–603, doi:10.5194/acp-12-591-2012.

[102] Boudries, H.; Bottenheim, J. W. Cl and Br atom concentrations during a surface boundary layer ozone depletion event in the Canadian High Arctic. *Geophys. Res. Lett.* **2000**, *27*, 517–520, doi:10.1029/1999GL011025.

[103] Barrie, L. A.; Bottenheim, J. W.; Schnell, R. C.; Crutzen, P. J.; Rasmussen, R. A. Ozone destruction and photochemical reactions at polar sunrise in the lower Arctic atmosphere. *Nature* **1988**, *334*, 138–141, doi:10.1038/334138a0.

[104] Simpson, W. R.; von Glasow, R.; Riedel, K.; Anderson, P.; Ariya, P.; Bottenheim, J.; Burrows, J.; Carpenter, L. J.; Frieß, U.; Goodsite, M. E.; Heard, D.; Hutterli, M.; Jacobi, H.-W.; Kaleschke, L.;

Neff, B.; Plane, J.; Platt, U.; Richter, A.; Roscoe, H.; Sander, R.; Shepson, P.; Sodeau, J.; Steffen, A.; Wagner, T.; Wolff, E. Halogens and their role in polar boundary-layer ozone depletion. *Atmos. Chem. Phys.* **2007**, *7*, 4375–4418, doi:10.5194/acp-7-4375-2007.

[105] Halfacre, J. W.; Knepp, T. N.; Shepson, P. B.; Thompson, C. R.; Pratt, K. A.; Li, B.; Peterson, P. K.; Walsh, S. J.; Simpson, W. R.; Matrai, P. A.; Bottenheim, J. W.; Netcheva, S.; Perovich, D. K.; Richter, A. Temporal and spatial characteristics of ozone depletion events from measurements in the Arctic. *Atmos. Chem. Phys.* **2014**, *14*, 4875–4894, doi:10.5194/acp-14-4875-2014.

[106] Dibble, T. S.; Zelie, M. J.; Mao, H. Thermodynamics of reactions of ClHg and BrHg radicals with atmospherically abundant free radicals. *Atmos. Chem. Phys.* **2012**, *12*, 10271–10279, doi:10.5194/acp-12-10271-2012.

[107] Mao, H.; Talbot, R. W.; Sive, B. C.; Kim, S. Y.; Blake, D. R.; Weinheimer, A. J. Arctic mercury depletion and its quantitative link with halogens. *J Atmos Chem* **2010**, *65*, 145–170, doi:10.1007/s10874-011-9186-1.

[108] Johnson, K. P.; Blum, J. D.; Keeler, G. J.; Douglas, T. A. Investigation of the deposition and emission of mercury in arctic snow during an atmospheric mercury depletion event. *J. Geophys. Res.* **2008**, *113*, D17304, doi:10.1029/2008JD009893.

[109] Lalonde, J. D.; Amyot, M.; Doyon, M.-R.; Auclair, J.-C. Photo-induced Hg(II) reduction in snow from the remote and temperate Experimental Lakes Area (Ontario, Canada). *J. Geophys. Res.* **2003**, *108*, 4200, doi:10.1029/2001JD001534.

[110] Lalonde, J. D.; Poulain, A. J.; Amyot, M. The Role of Mercury Redox Reactions in Snow on Snow-to-Air Mercury Transfer. *Environ. Sci. Technol.* **2002**, *36*, 174–178, doi:10.1021/es010786g.

[111] Dommergue, A.; Bahlmann, E.; Ebinghaus, R.; Ferrari, C.; Boutron, C. Laboratory simulation of Hg0 emissions from a snowpack. *Anal Bioanal Chem* **2007**, *388*, 319–327, doi:10.1007/s00216-007-1186-2.

[112] Allard, B.; Arsenie, I. Abiotic reduction of mercury by humic substances in aquatic system– an important process for the mercury cycle. *Water Air Soil Pollut* **1991**, *56*, 457–464, doi:10.1007/BF00342291.

[113] Xiao, Z. F.; Strömberg, D.; Lindqvist, O. Influence of humic substances on photolysis of divalent mercury in aqueous solution. *Water Air Soil Pollut* **1995**, *80*, 789–798, doi:10.1007/BF01189730.

[114] Si, L.; Ariya, P. A. Reduction of Oxidized Mercury Species by Dicarboxylic Acids (C2-C4): Kinetic and Product Studies. *Environ. Sci. Technol.* **2008**, *42*, 5150–5155, doi:10.1021/es800552z.

[115] Si, L.; Ariya, P. A. Aqueous photoreduction of oxidized mercury species in presence of selected alkanethiols. *Chemosphere* **2011**, *84*, 1079–1084, doi:10.1016/j.chemosphere.2011.04.061.

[116] Bartels-Rausch, T.; Krysztofiak, G.; Bernhard, A.; Schläppi, M.; Schwikowski, M.; Ammann, M. Photoinduced reduction of divalent mercury in ice by organic matter. *Chemosphere* **2011**, *82*, 199–203, doi:10.1016/j.chemosphere.2010.10.020.

[117] O'Concubhair, R.; O'Sullivan, D.; Sodeau, J. R. Dark Oxidation of Dissolved Gaseous Mercury in Polar Ice Mimics. *Environ. Sci. Technol.* **2012**, *46*, 4829–4836, doi:10.1021/es300309n.

[118] Toyota, K.; McConnell, J. C.; Staebler, R. M.; Dastoor, A. P. Air-snowpack exchange of bromine, ozone and mercury in the springtime Arctic simulated by the 1-D model PHANTAS - Part 1: In-snow bromine activation and its impact on ozone. *Atmos. Chem. Phys.* **2014**, *14*, 4101–4133, doi:10.5194/acp-14-4101-2014.

[119] Stauffer, R. M.; Morris, G. A.; Thompson, A. M.; Joseph, E.; Coetzee, G. J. R.; Nalli, N. R. Propagation of radiosonde pressure sensor errors to ozonesonde measurements. *Atmos. Meas. Tech.* **2014**, *7*, 65–79, doi:10.5194/amt-7-65-2014.

[120] Jaffe, D. A.; Lyman, S.; Amos, H. M.; Gustin, M. S.; Huang, J.; Selin, N. E.; Levin, L.; Ter Schure, A.; Mason, R. P.; Talbot, R.; Rutter, A.; Finley, B.; Jaeglé, L.; Shah, V.; McClure, C.; Ambrose, J.; Gratz, L.; Lindberg, S.; Weiss-Penzias, P.; Sheu, G.-R.; Feddersen, D.; Horvat, M.; Dastoor, A.; Hynes, A. J.; Mao, H.; Sonke, J. E.; Slemr, F.; Fisher, J. A.; Ebinghaus, R.; Zhang, Y.; Edwards, G. Progress on Understanding Atmospheric Mercury Hampered by Uncertain Measurements. *Environ. Sci. Technol.* **2014**, *48*, 7204–7206, doi:10.1021/es5026432.

[121] Darby, S. B.; Smith, P. D.; Venables, D. S. Cavity-enhanced absorption using an atomic line source: application to deep-UV measurements. *Analyst* **2012**, *137*, 2318–2321, doi:10.1039/C2AN35149H.

[122] Clevenger, W. L.; Smith, B. W.; Winefordner, J. D. Trace Determination of Mercury: A Review. *Crit. Rev. Anal. Chem.* **1997**, *27*, 1–26, doi:10.1080/10408349708050578.

[123] Schweitzer, W. G. Hyperfine Structure and Isotope Shifts in the 2537-Å Line of Mercury by a New Interferometric Method. *J. Opt. Soc. Am.* **1963**, *53*, 1055–1072.

[124] Lurio, A. Lifetime of the 6s6p $^1P_1$ State of Mercury. *Phys. Rev.* **1965**, *140*, A1505–A1508, doi:10.1103/PhysRev.140.A1505.

[125] Faïn, X.; Moosmüller, H.; Obrist, D. Toward real-time measurement of atmospheric mercury concentrations using cavity ring-down spectroscopy. *Atmos. Chem. Phys.* **2010**, *10*, 2879–2892, doi:10.5194/acp-10-2879-2010.

[126] Thiebaud, J.; Thomson, M. J.; Mani, R.; Morrow, W. H.; Morris, E. A.; Jia, C. Q. In situ optical absorption mercury continuous emission monitor. *Environ. Sci. Technol.* **2009**, *43*, 9294–9299, doi:10.1021/es902409t.

[127] Revalde, G.; Denisova, N.; Gavare, Z.; Skudra, A. Diagnostics of capillary mercury-argon high-frequency electrodeless discharge using line shapes. *J. Quant. Spectrosc. Radiat. Transf.* **2005**, *94*, 311–324, doi:10.1016/j.jqsrt.2004.09.014.

[128] Pierce, A.; Obrist, D.; Moosmüller, H.; Faïn, X.; Moore, C. Cavity ring-down spectroscopy sensor development for high-time-resolution measurements of gaseous elemental mercury in ambient air. *Atmos. Meas. Tech.* **2013**, *6*, 1477–1489, doi:10.5194/amt-6-1477-2013.

[129] Carter, C. *A Cavity Ring-Down Spectroscopy Mercury Continuous Emission Monitor*; Sensor Research and Development Corporation: Orono, Maine, USA, 2005; DOE Contract DE-FC26-01FT41221.

[130] Wang, C.; Scherrer, S. T.; Duan, Y.; Winstead, C. B. Cavity ringdown measurements of mercury

and its hyperfine structures at 254 nm in an atmospheric microwave plasma: spectral interference and analytical performance. *J. Anal. At. Spectrom.* **2005**, *20*, 638, doi:10.1039/b504318b.

[131] Tao, S.; Mazzotti, F. J.; Winstead, C. B.; Miller, G. P. Determination of elemental mercury by cavity ringdown spectrometry. *Analyst* **2000**, *125*, 1021–1023, doi:10.1039/b001879l.

[132] Spuler, S.; Linne, M.; Sappey, A.; Snyder, S. Development of a Cavity Ringdown Laser Absorption Spectrometer for Detection of Trace Levels of Mercury. *Appl. Opt.* **2000**, *39*, 2480–2486, doi:10.1364/AO.39.002480.

[133] Hadeishi, T.; Church, D. A.; McLaughlin, R. D.; Zak, B. D.; Nakamura, M.; Chang, B. Mercury monitor for ambient air. *Science* **1975**, *187*, 348–349, doi:10.1126/science.187.4174.348.

[134] Kocman, D.; Horvat, M. A laboratory based experimental study of mercury emission from contaminated soils in the River Idrijca catchment. *Atmos. Chem. Phys.* **2010**, *10*, 1417–1426, doi:10.5194/acp-10-1417-2010.

[135] Thoma, E. D.; Secrest, C.; Hall, E. S.; Lee Jones, D.; Shores, R. C.; Modrak, M.; Hashmonay, R.; Norwood, P. Measurement of total site mercury emissions from a chlor-alkali plant using ultraviolet differential optical absorption spectroscopy and cell room roof-vent monitoring. *Atmos. Environ.* **2009**, *43*, 753–757, doi:10.1016/j.atmosenv.2008.10.032.

[136] Somesfalean, G.; Sjöholm, M.; Persson, L.; Gao, H.; Svensson, T.; Svanberg, S. Temporal correlation scheme for spectroscopic gas analysis using multimode diode lasers. *Appl. Phys. Lett.* **2005**, *86*, 184102, doi:10.1063/1.1921351.

[137] Lou, X.; Somesfalean, G.; Svanberg, S.; Zhang, Z.; Wu, S. Detection of elemental mercury by multimode diode laser correlation spectroscopy. *Opt. Express* **2012**, *20*, 4927, doi:10.1364/OE.20.004927.

[138] Bauer, D.; Campuzano-Jost, P.; Hynes, A. J. Rapid, ultra-sensitive detection of gas phase elemental mercury under atmospheric conditions using sequential two-photon laser induced fluorescence. *J. Environ. Monit.* **2002**, *4*, 339–343, doi:10.1039/b111688f.

[139] Bauer, D.; Everhart, S.; Remeika, J.; Tatum Ernest, C.; Hynes, A. J. Deployment of a sequential two-photon laser induced fluorescence sensor for the detection of gaseous elemental mercury at ambient levels: fast, specific, ultrasensitive detection with parts-per-quadrillion sensitivity. *Atmos. Meas. Tech. Discuss.* **2014**, *7*, 5651–5693, doi:10.5194/amtd-7-5651-2014.

[140] Brophy, J. H.; Rettner, C. T. Laser two-photon ionization spectroscopy : a new method for real-time monitoring of atmospheric pollutants. *Opt. Lett.* **1979**, *4*, 337–339.

[141] Clevenger, W. L.; Matveev, O. I.; Cabredo, S.; Omenetto, N.; Smith, B. W.; Winefordner, J. D. Laser-Enhanced Ionization of Mercury Atoms in an Inert Atmosphere with Avalanche Amplification of the Signal. *Anal. Chem.* **1997**, *69*, 2232–2237, doi:10.1021/ac9702148.

[142] Dodge, W. B.; Allen, R. O. Trace analysis by metastable energy transfer for atomic luminescence. *Anal. Chem.* **1981**, *53*, 1279–1286, doi:10.1021/ac00231a034.

[143] McNerney, J. J.; Buseck, P. R.; Hanson, R. C. Mercury Detection by Means of Thin Gold Films. *Science* **1972**, *178*, 611–612, doi:10.1126/science.178.4061.611.

[144] Crenshaw, W. B.; Williams, S. N.; Stoiber, R. E. Fault location by radon and mercury detection at an active volcano in Nicaragua. *Nature* **1982**, *300*, 345–346.

[145] Sabri, Y. M.; Ippolito, S. J.; O'Mullane, A. P.; Tardio, J.; Bansal, V.; Bhargava, S. K. Creating gold nanoprisms directly on quartz crystal microbalance electrodes for mercury vapor sensing. *Nanotechnology* **2011**, *22*, 305501, doi:10.1088/0957-4484/22/30/305501.

[146] Rogers, B.; Manning, L.; Jones, M.; Sulchek, T.; Murray, K.; Beneschott, B.; Adams, J. D.; Hu, Z.; Thundat, T.; Cavazos, H.; Minne, S. C. Mercury vapor detection with a self-sensing, resonating piezoelectric cantilever. *Rev. Sci. Instrum.* **2003**, *74*, 4899, doi:10.1063/1.1614876.

[147] Sabri, Y. M.; Kojima, R.; Ippolito, S. J.; Wlodarski, W.; Kalantar-zadeh, K.; Kaner, R. B.; Bhargava, S. K. QCM based mercury vapor sensor modified with polypyrrole supported palladium. *Sensors Actuators B* **2011**, *160*, 616–622, doi:10.1016/j.snb.2011.08.038.

[148] McNicholas, T. P.; Zhao, K.; Yang, C.; Hernandez, S. C.; Mulchandani, A.; Myung, N. V.; Deshusses, M. A. Sensitive Detection of Elemental Mercury Vapor by Gold-Nanoparticle-Decorated Carbon Nanotube Sensors. *J. Phys. Chem. C* **2011**, *115*, 13927–13931, doi:10.1021/jp203662w.

[149] Keebaugh, S.; Kalkan, A. K.; Nam, W. J.; Fonash, S. J. Gold Nanowires for the Detection of Elemental and Ionic Mercury. *Electrochem. Solid-State Lett.* **2006**, *9*, H88–H91, doi:10.1149/1.2217130.

[150] Munthe, J.; Wängberg, I.; Pirrone, N.; Iverfeldt, A. Intercomparison of methods for sampling and analysis of atmospheric mercury species. *Atmos. Environ.* **2001**, *35*, 3007–3017.

[151] Swartzendruber, P. C.; Jaffe, D. A.; Finley, B. Development and First Results of an Aircraft-Based, High Time Resolution Technique for Gaseous Elemental and Reactive (Oxidized) Gaseous Mercury. *Environ. Sci. Technol.* **2009**, *43*, 7484–7489, doi:10.1021/es901390t.

[152] Ambrose, J. L.; Lyman, S. N.; Huang, J.; Gustin, M. S.; Jaffe, D. A. Fast Time Resolution Oxidized Mercury Measurements during the Reno Atmospheric Mercury Intercomparison Experiment (RAMIX). *Environ. Sci. Technol.* **2013**, *47*, 7285–7294, doi:10.1021/es303916v.

[153] Lauretta, D. S.; Klaue, B.; Blum, J. D.; Busek, P. R. Mercury abundances and isotopic compositions in the Murchison (CM) and Allende (CV) carbonaceous chondrites. *Geochim. Cosmochim. Acta* **2001**, *65*, 2807–2818, doi:10.1016/S0016-7037(01)00630-5.

[154] Tatum Ernest, C.; Donohoue, D.; Bauer, D.; Ter Schure, A.; Hynes, A. J. Programmable thermal dissociation of reactive gaseous mercury - a potential approach to chemical speciation: results from a field study. *Atmos. Chem. Phys. Discuss.* **2012**, *12*, 33291–33322, doi:10.5194/acpd-12-33291-2012.

[155] Lopez-Anton, M. A.; Yuan, Y.; Perry, R.; Maroto-Valer, M. M. Analysis of mercury species present during coal combustion by thermal desorption. *Fuel* **2010**, *89*, 629–634, doi:10.1016/j.fuel.2009.08.034.

[156] Feng, X.; Lu, J. Y.; Grègoire, D. C.; Hao, Y.; Banic, C. M.; Schroeder, W. H. Analysis of inorganic mercury species associated with airborne particulate matter/aerosols: method development. *Anal Bioanal Chem* **2004**, *380*, 683–689, doi:10.1007/s00216-004-2803-y.

[157] Dreiling, T. D.; Setser, D. W. Interpretations of the mercury halide chemiluminescence from reactive quenching of Hg($^3P_2$) by halogen containing molecules. *J. Chem. Phys.* **1983**, *79*, 5423.

[158] Donohoue, D. L. Kinetic Studies of the Oxidation Pathways of Gaseous Elemental Mercury. Ph.D. thesis, University of Miami, 2008.

[159] Ariya, P. A.; Khalizov, A.; Gidas, A. Reactions of Gaseous Mercury with Atomic and Molecular Halogens: Kinetics, Product Studies, and Atmospheric Implications. *J. Phys. Chem. A* **2002**, *106*, 7310–7320, doi:10.1021/jp020719o.

[160] Raofie, F.; Ariya, P. A. Product Study of the Gas-Phase BrO-Initiated Oxidation of Hg^0: Evidence for Stable Hg^{1+} Compounds. *Environ. Sci. Technol.* **2004**, *38*, 4319–4326, doi:10.1021/es035339a.

[161] Deeds, D. A.; Ghoshdastidar, A.; Raofie, F.; Guérette, E.-A.; Tessier, A.; Ariya, P. A. Development of a Particle-Trap Preconcentration-Soft Ionization Mass Spectrometric Technique for the Quantification of Mercury Halides in Air. *Analytical Chemistry* **2015**, doi:10.1021/ac504545w.

[162] Ariya, P. A.; Raofle, F.; Deeds, D.; Guerette, E. A. (McGill University). Methods and systems for the quantitative chemical speciation of heavy metals and other toxic pollutants. 2011; WO2011020187 A1.

[163] Huang, J.; Lyman, S. N.; Hartman, J. S.; Gustin, M. S. A review of passive sampling systems for ambient air mercury measurements. *Environ. Sci. Process. Impacts* **2014**, *16*, 374–392, doi:10.1039/C3EM00501A.

[164] Hollerman, W. A.; Glass, G. A.; Greco, R.; Liao, C.; O'Kelly, D. J. PIXE and NAA analysis of mercury in a standard set of southern magnolia wood samples. *Int. J. PIXE* **2003**, *13*, 107–114, doi:10.1142/S0129083503000154.

[165] Hutson, N. D.; Attwood, B. C.; Scheckel, K. G. XAS and XPS Characterization of Mercury Binding on Brominated Activated Carbon. *Environ. Sci. Technol.* **2007**, *41*, 1747–1752, doi:10.1021/es062121q.

[166] Fuente-Cuesta, A.; Diaz-Somoano, M.; Lopez-Anton, M. A.; Martinez-Tarazona, M. R. Oxidised mercury determination from combustion gases using an ionic exchanger. *Fuel* **2014**, *122*, 218–222, doi:10.1016/j.fuel.2014.01.030.

[167] Murphy, D. M.; Thomson, D. S.; Mahoney, M. J. In Situ Measurements of Organics, Meteoritic Material, Mercury, and Other Elements in Aerosols at 5 to 19 Kilometers. *Science* **1998**, *282*, 1664–1669, doi:10.1126/science.282.5394.1664.

[168] Murphy, D. M.; Thomson, D. S. Laser Ionization Mass Spectroscopy of Single Aerosol Particles. *Aerosol Sci. Technol.* **1995**, *22*, 237–249, doi:10.1080/02786829408959743.

[169] Gustin, M. S.; Lindberg, S.; Marsik, F.; Casimir, A.; Ebinghaus, R.; Edwards, G.; Hubble-Fitzgerald, C.; Kemp, R.; Kock, H.; Leonard, T.; London, J.; Majewski, M.; Montecinos, C.; Owens, J.; Pilote, M.; Poissant, L.; Rasmussen, P.; Schaedlich, F.; Schneeberger, D.; Schroeder, W.; Sommar, J.; Turner, R.; Vette, A.; Wallschlaeger, D.; Xiao, Z.; Zhang, H. Nevada

STORMS project: Measurement of mercury emissions from naturally enriched surfaces. *J. Geophys. Res.* **1999**, *104*, 21831–21844, doi:10.1029/1999JD900351.

[170] Sommar, J.; Zhu, W.; Lin, C.-J.; Feng, X. Field Approaches to Measure Hg Exchange Between Natural Surfaces and the Atmosphere–A Review. *Crit. Rev. Environ. Sci. Technol.* **2013**, *43*, 1657–1739, doi:10.1080/10643389.2012.671733.

[171] Lin, C.-J.; Zhu, W.; Li, X.; Feng, X.; Sommar, J.; Shang, L. Novel Dynamic Flux Chamber for Measuring Air-Surface Exchange of Hg^0 from Soils. *Environ. Sci. Technol.* **2012**, *46*, 8910–8920, doi:10.1021/es3012386.

[172] Pierce, A. M.; Moore, C. W.; Wohlfahrt, G.; Hörtnagl, L.; Kljun, N.; Obrist, D. Eddy Covariance Flux Measurements of Gaseous Elemental Mercury Using Cavity Ring-Down Spectroscopy. *Environmental Science & Technology* **2015**, doi:10.1021/es505080z.

[173] Skov, H.; Brooks, S. B.; Goodsite, M. E.; Lindberg, S. E.; Meyers, T. P.; Landis, M. S.; Larsen, M. R. B.; Jensen, B.; McConville, G.; Christensen, J. Fluxes of reactive gaseous mercury measured with a newly developed method using relaxed eddy accumulation. *Atmos. Environ.* **2006**, *40*, 5452–5463, doi:10.1016/j.atmosenv.2006.04.061.

[174] Bash, J. O.; Miller, D. R. A Relaxed Eddy Accumulation System for Measuring Surface Fluxes of Total Gaseous Mercury. *J. Atmos. Ocean. Technol.* **2008**, *25*, 244–257, doi:10.1175/2007JTECHA908.1.

[175] Sommar, J.; Zhu, W.; Shang, L.; Feng, X.; Lin, C.-J. A whole-air relaxed eddy accumulation measurement system for sampling vertical vapour exchange of elemental mercury. *Tellus B* **2013**, *65*, 1–18, doi:10.3402/tellusb.v65i0.19940.

[176] Edner, H.; Sunesson, A.; Svanberg, S.; Unéus, L.; Wallin, S. Differential optical absorption spectroscopy system used for atmospheric mercury monitoring. *Appl. Opt.* **1986**, *25*, 403–409, doi:10.1364/AO.25.000403.

[177] Nayuki, T.; Marumoto, K.; Fujii, T.; Fukuchi, T.; Nemoto, K.; Shirakawa, A.; Ueda, K. Development of a differential-absorption lidar system for measurement of atmospheric atomic mercury by use of the third harmonic of an LDS-dye laser. *Appl. Opt.* **2004**, *43*, 6487–6491, doi:10.1364/AO.43.006487.

[178] Mei, L.; Zhao, G.; Svanberg, S. Differential absorption lidar system employed for background atomic mercury vertical profiling in South China. *Opt. Lasers Eng.* **2014**, *55*, 128–135, doi:10.1016/j.optlaseng.2013.10.028.

[179] Edner, H.; Faris, G. W.; Sunesson, A.; Svanberg, S. Atmospheric atomic mercury monitoring using differential absorption lidar techniques. *Appl. Opt.* **1989**, *28*, 921–930.

[180] Edner, H.; Ragnarson, P.; Wallinder, E. Industrial Emission Control Using Lidar Techniques. *Environ. Sci. Technol.* **1995**, *29*, 330–337, doi:10.1021/es00002a008.

[181] Edner, H.; Ragnarson, P.; Svanberg, S.; Wallinder, E.; Ferrara, R.; Cioni, R.; Raco, B.; Taddeucci, G. Total fluxes of sulfur dioxide from the Italian volcanoes Etna, Stromboli, and Vulcano measured by differential absorption lidar and passive differential optical absorption spectroscopy. *J. Geophys. Res.* **1994**, *99*, 18827–18838, doi:10.1029/94JD01515.

[182] Obrist, D.; Conen, F.; Vogt, R.; Siegwolf, R.; Alewell, C. Estimation of Hg^0 exchange between ecosystems and the atmosphere using ^{2}22Rn and Hg^0 concentration changes in the stable nocturnal boundary layer. *Atmos. Environ.* **2006**, *40*, 856–866, doi:10.1016/j.atmosenv.2005.10.012.

[183] Alnis, J.; Gustafsson, U.; Somesfalean, G.; Svanberg, S. Sum-frequency generation with a blue diode laser for mercury spectroscopy at 254 nm. *Appl. Phys. Lett.* **2000**, *76*, 1234, doi:10.1063/1.125994.

[184] Anderson, T. N.; Magnuson, J. K.; Lucht, R. P. Diode-laser-based sensor for ultraviolet absorption measurements of atomic mercury. *Appl. Phys. B* **2007**, *87*, 341–353, doi:10.1007/s00340-007-2604-z.

[185] Carruthers, A. E.; Lake, T. K.; Shah, A.; Allen, J. W.; Sibbett, W.; Dholakia, K. Single-scan spectroscopy of mercury at 253.7nm by sum frequency mixing of violet and red microlensed diode lasers. *Opt. Commun.* **2005**, *255*, 261–266, doi:10.1016/j.optcom.2005.06.009.

[186] Swartzendruber, P. C.; Bauer, D.; Ter Schure, A.; Hynes, A. J. Development of a method to speciate gaseous oxidized mercury using thermal decomposition. *Geochim. Cosmochim. Acta* **2010**, *74*, A1014–A1014.

[187] Hoops, A. A.; Farrow, R. L.; Schulz, P.; Reichardt, T. A.; Bambha, R. P.; Schmitt, R. L.; Kliner, D. A. V. *Proceedings of SPIE*; SPIE, 2008; Vol. 6875; pp 68750K–10.

[188] Galbács, G. A Review of Applications and Experimental Improvements Related to Diode Laser Atomic Spectroscopy. *Appl. Spectrosc. Rev.* **2006**, *41*, 259–303, doi:10.1080/05704920600620378.

[189] Saliba, S. D.; Scholten, R. E. Linewidths below 100 kHz with external cavity diode lasers. *Appl. Opt.* **2009**, *48*, 6961–6966.

[190] Merimaa, M.; Talvitie, H.; Laakkonen, P.; Kuittinen, M.; I, Compact external-cavity diode laser with a novel transmission geometry. *Optics* **2000**, *174*, 175–180.

[191] Paschotta, R. *Encyclopedia of laser physics and technology*; Wiley-VCH: Weinheim, 2008.

[192] Hult, J.; Burns, I. S.; Kaminski, C. F. Wide-bandwidth mode-hop-free tuning of extended-cavity GaN diode lasers. *Appl. Opt.* **2005**, *44*, 3675, doi:10.1364/AO.44.003675.

[193] Saliba, S. D.; Junker, M.; Turner, L. D.; Scholten, R. E. Mode stability of external cavity diode lasers. *Appl. Opt.* **2009**, *48*, 6692–6700.

[194] Carruthers, A. E.; Lake, T. K.; Shah, A.; Allen, J. W.; Sibbett, W.; Dholakia, K. Microlensed red and violet diode lasers in an extended cavity geometry. *Rev. Sci. Instrum.* **2004**, *75*, 3360, doi:10.1063/1.1791311.

[195] Lancaster, G. P. T.; Sibbett, W.; Dholakia, K. An extended-cavity diode laser with a circular output beam. *Rev. Sci. Instrum.* **2000**, *71*, 3646, doi:10.1063/1.1288237.

[196] Smith, A. SNLO. 2009; `http://www.as-photonics.com/snlo`.

[197] Brown, S. S.; Stark, H.; Ciciora, S. J.; McLaughlin, R. J.; Ravishankara, A. R. Simultaneous in

situ detection of atmospheric NO_3 and N_2O_5 via cavity ring-down spectroscopy. *Rev. Sci. Instrum.* **2002**, *73*, 3291–3301, doi:10.1063/1.1499214.

[198] Gherman, T.; Venables, D. S.; Vaughan, S.; Orphal, J.; Ruth, A. A. Incoherent Broadband Cavity-Enhanced Absorption Spectroscopy in the near-Ultraviolet: Application to HONO and NO_2. *Environ. Sci. Technol.* **2007**, *42*, 890–895, doi:10.1021/es0716913.

[199] Kennedy, O. J.; Ouyang, B.; Langridge, J. M.; Daniels, M. J. S.; Bauguitte, S.; Freshwater, R.; McLeod, M. W.; Ironmonger, C.; Sendall, J.; Norris, O.; Nightingale, R.; Ball, S. M.; Jones, R. L. An aircraft based three channel broadband cavity enhanced absorption spectrometer for simultaneous measurements of NO_3, N_2O_5 and NO_2. *Atmos. Meas. Tech.* **2011**, *4*, 1759–1776, doi:10.5194/amt-4-1759-2011.

[200] Robert, C. Simple, stable, and compact multiple-reflection optical cell for very long optical paths. *Appl. Opt.* **2007**, *46*, 5408–5418, doi:10.1364/AO.46.005408.

[201] Berden, G.; Engeln, R. *Cavity ring-down spectroscopy: techniques and applications*; Wiley: Chichester, 2009.

[202] Fiedler, S. E.; Hese, A.; Ruth, A. A. Incoherent broad-band cavity-enhanced absorption spectroscopy. *Chem. Phys. Lett.* **2003**, *371*, 284–294, doi:10.1016/S0009-2614(03)00263-X.

[203] Engeln, R.; Berden, G.; Peeters, R.; Meijer, G. Cavity enhanced absorption and cavity enhanced magnetic rotation spectroscopy. *Rev. Sci. Instrum.* **1998**, *69*, 3763, doi:10.1063/1.1149176.

[204] O'Keefe, A.; Scherer, J. J.; Paul, J. B. cw-Integrated cavity output spectroscopy. *Chem. Phys. Lett.* **1999**, *307*, 343–349, doi:10.1016/S0009-2614(99)00547-3.

[205] Platt, U.; Meinen, J.; Pöhler, D.; Leisner, T. Broadband Cavity Enhanced Differential Optical Absorption Spectroscopy (CE-DOAS): applicability and corrections. *Atmos. Meas. Tech.* **2009**, *2*, 713–723, doi:10.5194/amt-2-713-2009.

[206] Thalman, R.; Volkamer, R. Inherent calibration of a blue LED-CE-DOAS instrument to measure iodine oxide, glyoxal, methyl glyoxal, nitrogen dioxide, water vapour and aerosol extinction in open cavity mode. *Atmos. Meas. Tech.* **2010**, *3*, 1797–1814, doi:10.5194/amt-3-1797-2010.

[207] Lis, G.; Wassenaar, L. I.; Hendry, M. J. High-Precision Laser Spectroscopy D/H and $^{1}8O/^{1}6O$ Measurements of Microliter Natural Water Samples. *Anal. Chem.* **2007**, *80*, 287–293, doi:10.1021/ac701716q.

[208] Sneep, M.; Hannemann, S.; van Duijn, E. J.; Ubachs, W. Deep-ultraviolet cavity ringdown spectroscopy. *Opt. Lett.* **2004**, *29*, 1378–1380, doi:10.1364/OL.29.001378.

[209] Méjean, G.; Kassi, S.; Romanini, D. Measurement of reactive atmospheric species by ultraviolet cavity-enhanced spectroscopy with a mode-locked femtosecond laser. *Opt. Lett.* **2008**, *33*, 1231–1233, doi:10.1364/OL.33.001231.

[210] Ball, S. M.; Langridge, J. M.; Jones, R. L. Broadband cavity enhanced absorption spectroscopy using light emitting diodes. *Chem. Phys. Lett.* **2004**, *398*, 68–74, doi:10.1016/j.cplett.2004.08.144.

[211] Thompson, J. E.; Spangler, H. D. Tungsten source integrated cavity output spectroscopy for the determination of ambient atmospheric extinction coefficient. *Appl. Opt.* **2006**, *45*, 2465–2473, doi:10.1364/AO.45.002465.

[212] Kiwanuka, S.-S.; Laurila, T.; Kaminski, C. F. Sensitive Method for the Kinetic Measurement of Trace Species in Liquids Using Cavity Enhanced Absorption Spectroscopy with Broad Bandwidth Supercontinuum Radiation. *Anal. Chem.* **2010**, *82*, 7498–7501, doi:10.1021/ac1012255.

[213] Laurila, T.; Burns, I. S.; Hult, J.; Miller, J. H.; Kaminski, C. F. A calibration method for broadbandwidth cavity enhanced absorption spectroscopy performed with supercontinuum radiation. *Appl. Phys. B* **2010**, *102*, 271–278, doi:10.1007/s00340-010-4044-4.

[214] Fiedler, S. E.; Hese, A.; Ruth, A. A. Incoherent broad-band cavity-enhanced absorption spectroscopy of liquids. *Rev. Sci. Instrum.* **2005**, *76*, 23107, doi:10.1063/1.1841872.

[215] Coburn, S.; Ortega, I.; Thalman, R.; Blomquist, B.; Fairall, C. W.; Volkamer, R. Measurements of diurnal variations and eddy covariance (EC) fluxes of glyoxal in the tropical marine boundary layer: description of the Fast LED-CE-DOAS instrument. *Atmos. Meas. Tech.* **2014**, *7*, 3579–3595, doi:10.5194/amt-7-3579-2014.

[216] Ashu-Ayem, E. R.; Nitschke, U.; Monahan, C.; Chen, J.; Darby, S. B.; Smith, P. D.; O'Dowd, C. D.; Stengel, D. B.; Venables, D. S. Coastal Iodine Emissions. 1. Release of I$_2$ by Laminaria digitata in Chamber Experiments. *Environ. Sci. Technol.* **2012**, *46*, 10413–10421, doi:10.1021/es204534v.

[217] Bogumil, K.; Orphal, J.; Homann, T.; Voigt, S.; Spietz, P.; Fleischmann, O. C.; Vogel, A.; Hartmann, M.; Kromminga, H.; Bovensmann, H.; Frerick, J.; Burrows, J. P. Measurements of molecular absorption spectra with the SCIAMACHY pre-flight model: instrument characterization and reference data for atmospheric remote-sensing in the 230-2380 nm region. *J. Photochem. Photobiol. A Chem.* **2003**, *157*, 167–184, doi:10.1016/S1010-6030(03)00062-5.

[218] Baumeister, P. *Optical coating technology*; SPIE Pub., 2004.

[219] Donohoue, D. L.; Bauer, D.; Hynes, A. J. Temperature and Pressure Dependent Rate Coefficients for the Reaction of Hg with Cl and the Reaction of Cl with Cl: A Pulsed Laser Photolysis-Pulsed Laser Induced Fluorescence Study. *J. Phys. Chem. A* **2005**, *109*, 7732–7741, doi:10.1021/jp051354l.

[220] Varma, R. M.; Venables, D. S.; Ruth, A. A.; Heitmann, U.; Schlosser, E.; Dixneuf, S. Long optical cavities for open-path monitoring of atmospheric trace gases and aerosol extinction. *Appl. Opt.* **2009**, *48*, B159–B171, doi:10.1364/AO.48.00B159.

[221] Etzkorn, T.; Klotz, B.; Sørensen, S.; Patroescu, I. V.; Barnes, I.; Becker, K. H.; Platt, U. Gas-phase absorption cross sections of 24 monocyclic aromatic hydrocarbons in the UV and IR spectral ranges. *Atmos. Environ.* **1999**, *33*, 525–540, doi:10.1016/S1352-2310(98)00289-1.

[222] Koch, J. D.; Gronki, J.; Hanson, R. K. Measurements of near-UV absorption spectra of acetone and 3-pentanone at high temperatures. *J. Quant. Spectrosc. Radiat. Transf.* **2008**, *109*, 2037–2044, doi:10.1016/j.jqsrt.2008.02.010.

[223] Waechter, H.; Bescherer, K.; Dürr, C. J.; Oleschuk, R. D.; Loock, H.-P. 405 nm Absorption Detection in Nanoliter Volumes. *Anal. Chem.* **2009**, *81*, 9048–9054, doi:10.1021/ac901696q.

[224] van der Sneppen, L.; Ariese, F.; Gooijer, C.; Ubachs, W. Liquid-Phase and Evanescent-Wave Cavity Ring-Down Spectroscopy in Analytical Chemistry. *Annu. Rev. Anal. Chem.* **2009**, *2*, 13–35, doi:10.1146/annurev-anchem-060908-155301.

[225] Seetohul, L. N.; Ali, Z.; Islam, M. Broadband Cavity Enhanced Absorption Spectroscopy as a Detector for HPLC. *Anal. Chem.* **2009**, *81*, 4106–4112, doi:10.1021/ac9004106.

[226] Haagen-Smit, A. J. Chemistry and Physiology of Los Angeles Smog. *Ind. Eng. Chem.* **1952**, *44*, 1342–1346, doi:10.1021/ie50510a045.

[227] Finlayson-Pitts, B. J. *Chemistry of the upper and lower atmosphere: theory, experiments, and applications*; Academic Press: San Diego, 2000.

[228] Becker, K. H. In *Environmental Simulation Chambers: Application to Atmospheric Chemical Processes*; Barnes, I., Rudzinski, K. J., Eds.; NATO Science Series: IV: Earth and Environmental Science 62; Springer, 2006; pp 1–26.

[229] Akimoto, H.; Hoshino, M.; Inoue, G.; Sakamaki, F.; Washida, N.; Okuda, M. Design and characterization of the evacuable and bakable photochemical smog chamber. *Environ. Sci. Technol.* **1979**, *13*, 471–475, doi:10.1021/es60152a014.

[230] Mentel, T. F.; Bleilebens, D.; Wahner, A. A study of nighttime nitrogen oxide oxidation in a large reaction chamber–the fate of NO_2, N_2O_5, HNO_3, and O_3 at different humidities. *Atmos. Environ.* **1996**, *30*, 4007–4020, doi:10.1016/1352-2310(96)00117-3.

[231] Saathoff, H.; Moehler, O.; Schurath, U.; Kamm, S.; Dippel, B.; Mihelcic, D. The AIDA soot aerosol characterisation campaign 1999. *J. Aerosol Sci.* **2003**, *34*, 1277–1296, doi:10.1016/S0021-8502(03)00363-X.

[232] Doyle, G. J. Design of a facility (smog chamber) for studying photochemical reactions under simulated tropospheric conditions. *Environ. Sci. Technol.* **1970**, *4*, 907–916, doi:10.1021/es60046a001.

[233] Duplissy, J.; Enghoff, M. B.; Aplin, K. L.; Arnold, F.; Aufmhoff, H.; Avngaard, M.; Baltensperger, U.; Bondo, T.; Bingham, R.; Carslaw, K.; Curtius, J.; David, A.; Fastrup, B.; Gagné, S.; Hahn, F.; Harrison, R. G.; Kellett, B.; Kirkby, J.; Kulmala, M.; Laakso, L.; Laaksonen, A.; Lillestol, E.; Lockwood, M.; Mäkelä, J.; Makhmutov, V.; Marsh, N. D.; Nieminen, T.; Onnela, A.; Pedersen, E.; Pedersen, J. O. P.; Polny, J.; Reichl, U.; Seinfeld, J. H.; Sipilä, M.; Stozhkov, Y.; Stratmann, F.; Svensmark, H.; Svensmark, J.; Veenhof, R.; Verheggen, B.; Viisanen, Y.; Wagner, P. E.; Wehrle, G.; Weingartner, E.; Wex, H.; Wilhelmsson, M.; Winkler, P. M. Results from the CERN pilot CLOUD experiment. *Atmos. Chem. Phys.* **2010**, *10*, 1635–1647, doi:10.5194/acp-10-1635-2010.

[234] Schnitzhofer, R.; Metzger, A.; Breitenlechner, M.; Jud, W.; Heinritzi, M.; De Menezes, L.-P.; Duplissy, J.; Guida, R.; Haider, S.; Kirkby, J.; Mathot, S.; Minginette, P.; Onnela, A.; Walther, H.; Wasem, A.; Hansel, A. Characterisation of organic contaminants in the CLOUD chamber at CERN. *Atmos. Meas. Tech.* **2014**, *7*, 2159–2168, doi:10.5194/amt-7-2159-2014.

[235] Zádor, J.; Turányi, T.; Wirtz, K.; Pilling, M. J. Measurement and investigation of chamber radical sources in the European Photoreactor (EUPHORE). *J Atmos Chem* **2006**, *55*, 147–166, doi:10.1007/s10874-006-9033-y.

[236] Apel, E. C.; Brauers, T.; Koppmann, R.; Bandowe, B.; Boß meyer, J.; Holzke, C.; Tillmann, R.; Wahner, A.; Wegener, R.; Brunner, A.; Jocher, M.; Ruuskanen, T.; Spirig, C.; Steigner, D.; Steinbrecher, R.; Gomez Alvarez, E.; Müller, K.; Burrows, J. P.; Schade, G.; Solomon, S. J.; Ladstätter-Weiß enmayer, A.; Simmonds, P.; Young, D.; Hopkins, J. R.; Lewis, A. C.; Legreid, G.; Reimann, S.; Hansel, A.; Wisthaler, A.; Blake, R. S.; Ellis, A. M.; Monks, P. S.; Wyche, K. P. Intercomparison of oxygenated volatile organic compound measurements at the SAPHIR atmosphere simulation chamber. *J. Geophys. Res.* **2008**, *113*, D20307, doi:10.1029/2008JD009865.

[237] Wang, X.; Liu, T.; Bernard, F.; Ding, X.; Wen, S.; Zhang, Y.; Zhang, Z.; He, Q.; Lü, S.; Chen, J.; Saunders, S.; Yu, J. Design and characterization of a smog chamber for studying gas-phase chemical mechanisms and aerosol formation. *Atmos. Meas. Tech.* **2014**, *7*, 301–313, doi:10.5194/amt-7-301-2014.

[238] Glowacki, D. R.; Goddard, A.; Hemavibool, K.; Malkin, T. L.; Commane, R.; Anderson, F.; Bloss, W. J.; Heard, D. E.; Ingham, T.; Pilling, M. J.; Seakins, P. W. Design of and initial results from a Highly Instrumented Reactor for Atmospheric Chemistry (HIRAC). *Atmos. Chem. Phys.* **2007**, *7*, 5371–5390, doi:10.5194/acp-7-5371-2007.

[239] Sumner, A. L.; Spicer, C. W.; Satola, J.; Mangaraj, R.; Cowen, K. A.; Landis, M. S.; Stevens, R. K.; Atkeson, T. D. In *Dynamics of Mercury Pollution on Regional and Global Scales*; Pirrone, N., Mahaffey, K. R., Eds.; Springer, 2005; pp 193–212.

[240] Grosjean, D. Wall loss of gaseous pollutants in outdoor Teflon chambers. *Environ. Sci. Technol.* **1985**, *19*, 1059–1065, doi:10.1021/es00141a006.

[241] Brown, R. J. C.; Wang, J.; Brown, A. S. Temperature propagation through a mercury vapour calibration source and assessment of possible analytical biases caused by measurement of temperature variations. *Measurement* **2010**, *43*, 1291–1298, doi:16/j.measurement.2010.07.004.

[242] Calvert, J. G.; Pitts, J. N. *Photochemistry*; John Wiley & Sons: New York, 1966.

[243] Fiedler, S. E.; Hese, A.; Heitmann, U. Influence of the cavity parameters on the output intensity in incoherent broadband cavity-enhanced absorption spectroscopy. *Rev. Sci. Instrum.* **2007**, *78*, 73104, doi:10.1063/1.2752608.

[244] Eilers, P. H. C. A Perfect Smoother. *Anal. Chem.* **2003**, *75*, 3631–3636, doi:10.1021/ac034173t.

[245] Kern, C.; Trick, S.; Rippel, B.; Platt, U. Applicability of light-emitting diodes as light sources for active differential optical absorption spectroscopy measurements. *Applied Optics* **2006**, *45*, 2077–2088, doi:10.1364/AO.45.002077.

[246] Stutz, J.; Platt, U. Numerical analysis and estimation of the statistical error of differential optical absorption spectroscopy measurements with least-squares methods. *Appl. Opt.* **1996**, *35*, 6041–6053, doi:10.1364/AO.35.006041.

[247] Platt, U.; Stutz, J. *Differential Optical Absorption Spectroscopy*; Springer: Berlin, 2008; pp 287–328.

[248] Ashu-Ayem, E. R. Development and application of a simulation chamber for the study of atmospheric iodine chemistry. Ph.D. thesis, 2012.

[249] Laine, P. L.; Sohn, Y. S.; Nicovich, J. M.; McKee, M. L.; Wine, P. H. Kinetics of Elementary Steps in the Reactions of Atomic Bromine with Isoprene and 1,3-Butadiene under Atmospheric Conditions. *J. Phys. Chem. A* **2012**, *116*, 6341–6357, doi:10.1021/jp212127v.

[250] Bierbach, A.; Barnes, I.; Becker, K. H. Rate coefficients for the gas-phase reactions of bromine radicals with a series of alkenes, dienes, and aromatic hydrocarbons at 298 ±2 K. *Int. J. Chem. Kinet.* **1996**, *28*, 565–577, doi:10.1002/(SICI)1097-4601(1996)28:8<565::AID-KIN2>3.0.CO;2-T.

[251] Arnold, I. J.; Moosmüller, H.; Sharma, N.; Mazzoleni, C. Beam characteristics of fiber-based supercontinuum light sources with mirror- and lens-based beam collimators. *Opt. Express* **2014**, *22*, 13860, doi:10.1364/OE.22.013860.

[252] Atkinson, R.; Baulch, D. L.; Cox, R. A.; Crowley, J. N.; Hampson, R. F.; Hynes, R. G.; Jenkin, M. E.; Rossi, M. J.; Troe, J. Evaluated kinetic and photochemical data for atmospheric chemistry: Volume III - gas phase reactions of inorganic halogens. *Atmos. Chem. Phys.* **2007**, *7*, 981–1191, doi:10.5194/acp-7-981-2007.

[253] Subir, M.; Ariya, P. A.; Dastoor, A. P. A review of uncertainties in atmospheric modeling of mercury chemistry I. Uncertainties in existing kinetic parameters - Fundamental limitations and the importance of heterogeneous chemistry. *Atmos. Environ.* **2011**, *45*, 5664–5676, doi:10.1016/j.atmosenv.2011.04.046.

[254] Ariya, P. A.; Peterson, K.; Snider, G.; Amyot, M. In *Mercury Fate and Transport in the Global Atmosphere*; Mason, R., Pirrone, N., Eds.; Springer, 2009; pp 459–501.

[255] Greig, G.; Gunning, H. E.; Strausz, O. P. Reactions of Metal Atoms. II. The Combination of Mercury and Bromine Atoms and the Dimerization of HgBr. *J. Chem. Phys.* **1970**, *52*, 3684–3690, doi:10.1063/1.1673544.

[256] Donohoue, D. L.; Bauer, D.; Cossairt, B.; Hynes, A. J. Temperature and Pressure Dependent Rate Coefficients for the Reaction of Hg with Br and the Reaction of Br with Br: A Pulsed Laser Photolysis-Pulsed Laser Induced Fluorescence Study. *J. Phys. Chem. A* **2006**, *110*, 6623–6632, doi:10.1021/jp054688j.

[257] Gao, Y.; Zhang, Z.; Wu, J.; Duan, L.; Umar, A.; Sun, L.; Guo, Z.; Wang, Q. A Critical Review on the Heterogeneous Catalytic Oxidation of Elemental Mercury in Flue Gases. *Environ. Sci. Technol.* **2013**, doi:10.1021/es402495h.

[258] Qu, Z.; Yan, N.; Liu, P.; Chi, Y.; Jia, J. Bromine Chloride as an Oxidant to Improve Elemental Mercury Removal from Coal-Fired Flue Gas. *Environ. Sci. Technol.* **2009**, *43*, 8610–8615, doi:10.1021/es901803s.

[259] Liu, S.-H.; Yan, N.-Q.; Liu, Z.-R.; Qu, Z.; Wang, H. P.; Chang, S.-G.; Miller, C. Using Bromine Gas To Enhance Mercury Removal from Flue Gas of Coal-Fired Power Plants. *Environ. Sci. Technol.* **2007**, *41*, 1405–1412, doi:10.1021/es061705p.

[260] Preciado, I.; Young, T.; Silcox, G. Mercury Oxidation by Halogens under Air- and Oxygen-Fired Conditions. *Energy Fuels* **2014**, *28*, 1255–1261, doi:10.1021/ef402074p.

[261] Van Otten, B.; Buitrago, P. A.; Senior, C. L.; Silcox, G. D. Gas-Phase Oxidation of Mercury by Bromine and Chlorine in Flue Gas. *Energy Fuels* **2011**, *25*, 3530–3536, doi:10.1021/ef200840c.

[262] Auzmendi-Murua, I.; Castillo, A.; Bozzelli, J. W. Mercury Oxidation via Chlorine, Bromine, and Iodine under Atmospheric Conditions: Thermochemistry and Kinetics. *J. Phys. Chem. A* **2014**, *118*, 2959–2975, doi:10.1021/jp412654s.

[263] Buitrago, P. A. Gas-Phase mercury oxidation: effects of bromine, chlorine and SO_2 under air firing and oxy-fuel conditions, experimental and modeling study. Ph.D. thesis, University of Utah, 2011.

[264] Niksa, S.; Padak, B.; Krishnakumar, B.; Naik, C. V. Process Chemistry of Br Addition to Utility Flue Gas for Hg Emissions Control. *Energy Fuels* **2010**, *24*, 1020–1029, doi:10.1021/ef901106t.

[265] Wilcox, J.; Okano, T. Ab initio-based Mercury Oxidation Kinetics via Bromine at Postcombustion Flue Gas Conditions. *Energy Fuels* **2011**, *25*, 1348–1356, doi:10.1021/ef101763r.

[266] Balabanov, N. B.; Shepler, B. C.; Peterson, K. A. Accurate Global Potential Energy Surface and Reaction Dynamics for the Ground State of $HgBr_2$. *J. Phys. Chem. A* **2005**, *109*, 8765–8773, doi:10.1021/jp053415l.

[267] Troe, J.; Ushakov, V. G. Revisiting falloff curves of thermal unimolecular reactions. *J. Chem. Phys.* **2011**, *135*, 54304, doi:10.1063/1.3615542.

[268] Glowacki, D. R.; Liang, C.-H.; Morley, C.; Pilling, M. J.; Robertson, S. H. MESMER: An Open-Source Master Equation Solver for Multi-Energy Well Reactions. *J. Phys. Chem. A* **2012**, *116*, 9545–9560, doi:10.1021/jp3051033.

[269] Allen, J. W.; Goldsmith, C. F.; Green, W. H. Automatic estimation of pressure-dependent rate coefficients. *Phys. Chem. Chem. Phys.* **2011**, *14*, 1131–1155, doi:10.1039/C1CP22765C.

[270] Nič, M., Jirát, J., Košata, B., Jenkins, A., McNaught, A., Eds. *IUPAC Compendium of Chemical Terminology: Gold Book*, 2nd ed.; IUPAC, 2009.

[271] Ip, J. K. K.; Burns, G. Recombination of Br Atoms by Flash Photolysis over a Wide Temperature Range. II. Br_2 in He, Ne, Ar, Kr, N_2, and O_2. *J. Chem. Phys.* **1969**, *51*, 3414–3424, doi:10.1063/1.1672530.

[272] DeGraff, B. A.; Lang, K. J. Gas-phase recombination of bromine atoms. *J. Phys. Chem.* **1970**, *74*, 4181–4187, doi:10.1021/j100718a002.

[273] Jenkin, M. E.; Cox, R. A.; Mellouki, A.; Le Bras, G.; Poulet, G. Kinetics of the reaction of iodine atoms with hydroperoxy radicals. *J. Phys. Chem.* **1990**, *94*, 2927–2934, doi:10.1021/j100370a036.

[274] Spicer, C.; Satola, J.; Abbgy, A.; Plastridge, R.; Cowen, K. *Kinetics of Gas-Phase Elemental Mer-*

cury Reactions with Halogen Species, Ozone, and Nitrate Radical under Atmospheric Conditions;
Florida Department of Environmental Protection, 2002.

[275] Shepler, B. C.; Balabanov, N. B.; Peterson, K. A. Hg+Br→HgBr recombination and collision-induced dissociation dynamics. *J. Chem. Phys.* **2007**, *127*, 164304, doi:doi:10.1063/1.2777142.

[276] Goodsite, M. E.; Plane, J. M. C.; Skov, H. A Theoretical Study of the Oxidation of Hg^0 to $HgBr_2$ in the Troposphere. *Environ. Sci. Technol.* **2004**, *38*, 1772–1776, doi:10.1021/es034680s.

[277] Tossell, J. A. Calculation of the Energetics for Oxidation of Gas-Phase Elemental Hg by Br and BrO. *J. Phys. Chem. A* **2003**, *107*, 7804–7808, doi:10.1021/jp030390m.

[278] Krauss, M.; Stevens, W. J. Photodissociation of HgBr, XΣ1/2. *Appl. Phys. Lett.* **1981**, *39,* 686–688, doi:10.1063/1.92869.

[279] Calvert, J. G.; Lindberg, S. E. A modeling study of the mechanism of the halogen-ozone-mercury homogeneous reactions in the troposphere during the polar spring. *Atmos. Environ.* **2003**, *37,* 4467–4481, doi:10.1016/j.atmosenv.2003.07.001.

[280] Sander, R.; Baumgaertner, A.; Gromov, S.; Harder, H.; Jöckel, P.; Kerkweg, A.; Kubistin, D.; Regelin, E.; Riede, H.; Sandu, A.; Taraborrelli, D.; Tost, H.; Xie, Z.-Q. The atmospheric chemistry box model CAABA/MECCA-3.0. *Geosci. Model Dev.* **2011**, *4*, 373–380, doi:10.5194/gmd-4-373-2011.

[281] Xie, Z.-Q.; Sander, R.; Pöschl, U.; Slemr, F. Simulation of atmospheric mercury depletion events ({AMDEs}) during polar springtime using the MECCA box model. *Atmos. Chem. Phys.* **2008**, *8*, 7165–7180, doi:10.5194/acp-8-7165-2008.

[282] Tas, E.; Obrist, D.; Peleg, M.; Matveev, V.; Faïn, X.; Asaf, D.; Luria, M. Measurement-based modelling of bromine-induced oxidation of mercury above the Dead Sea. *Atmos. Chem. Phys.* **2012**, *12*, 2429–2440, doi:10.5194/acp-12-2429-2012.

[283] Wang, F.; Saiz-Lopez, A.; Mahajan, A. S.; Gómez Martín, J. C.; Armstrong, D.; Lemes, M.; Hay, T.; Prados-Roman, C. Enhanced production of oxidised mercury over the tropical Pacific Ocean: a key missing oxidation pathway. *Atmos. Chem. Phys.* **2014**, *14,* 1323–1335, doi:10.5194/acp-14-1323-2014.

[284] Shepler, B. C.; Peterson, K. A. Mercury Monoxide: A Systematic Investigation of Its Ground Electronic State. *J. Phys. Chem. A* **2003**, *107,* 1783–1787, doi:10.1021/jp027512f.

[285] Hynes, A. J.; Donohoue, D. L.; Goodsite, M. E.; Hedgecock, I. M. In *Mercury Fate and Transport in the Global Atmosphere*; Mason, R., Pirrone, N., Eds.; Springer, 2009; pp 427–457.

[286] Tossell, J. A. Calculation of the Energetics for the Oligomerization of Gas Phase HgO and HgS and for the Solvolysis of Crystalline HgO and HgS. *J. Phys. Chem. A* **2006**, *110,* 2571–2578, doi:10.1021/jp056280s.

[287] Calvert, J. G.; Lindberg, S. E. Mechanisms of mercury removal by O_3 and OH in the atmosphere. *Atmos. Environ.* **2005**, *39,* 3355–3367, doi:10.1016/j.atmosenv.2005.01.055.

[288] Snider, G.; Raofie, F.; Ariya, P. A. Effects of relative humidity and CO(g) on the O$_3$-initiated oxidation reaction of Hg^0(g): kinetic & product studies. *Phys. Chem. Chem. Phys.* **2008**, *10*, 5616–5623, doi:10.1039/b801226a.

[289] Vahedpour, M.; Tozihi, M.; Nazari, F. Mechanistic Study on the Ozone-Mercury Reaction and the Effect of Water and Water Dimer Molecules. *J Chinese Chem. Soc* **2011**, *58*, 398–407, doi:10.1002/jccs.201190043.

[290] Dibble, T. S.; Zelie, M. J.; Mao, H. Corrigendum to "Thermodynamics of reactions of ClHg and BrHg radicals with atmospherically abundant free radicals" published in Atmos. Chem. Phys. 12, 10271-10279, 2012. *Atmos. Chem. Phys.* **2013**, *13*, 9211–9212, doi:10.5194/acp-13-9211-2013.

[291] Balabanov, N. B.; Peterson, K. A. Mercury and Reactive Halogens: The Thermochemistry of Hg + Cl$_2$, Br$_2$, BrCl, ClO, and BrO. *J. Phys. Chem. A* **2003**, *107*, 7465–7470, doi:10.1021/jp035547p.

[292] Raofie, F.; Snider, G.; Ariya, P. A. Reaction of gaseous mercury with molecular iodine, atomic iodine, and iodine oxide radicals - Kinetics, product studies, and atmospheric implications. *Can. J. Chem.* **2008**, *86*, 811–820, doi:10.1139/V08-088.

[293] McFiggans, G.; Bale, C. S. E.; Ball, S. M.; Beames, J. M.; Bloss, W. J.; Carpenter, L. J.; Dorsey, J.; Dunk, R.; Flynn, M. J.; Furneaux, K. L.; Gallagher, M. W.; Heard, D. E.; Hollingsworth, A. M.; Hornsby, K.; Ingham, T.; Jones, C. E.; Jones, R. L.; Kramer, L. J.; Langridge, J. M.; Leblanc, C.; LeCrane, J.-P.; Lee, J. D.; Leigh, R. J.; Longley, I.; Mahajan, A. S.; Monks, P. S.; Oetjen, H.; Orr-Ewing, A. J.; Plane, J. M. C.; Potin, P.; Shillings, A. J. L.; Thomas, F.; von Glasow, R.; Wada, R.; Whalley, L. K.; Whitehead, J. D. Iodine-mediated coastal particle formation: an overview of the Reactive Halogens in the Marine Boundary Layer (RHaMBLe) Roscoff coastal study. *Atmos. Chem. Phys.* **2010**, *10*, 2975–2999, doi:10.5194/acp-10-2975-2010.

[294] Shepler, B. C.; Balabanov, N. B.; Peterson, K. A. Ab Initio Thermochemistry Involving Heavy Atoms: An Investigation of the Reactions Hg + IX (X = I, Br, Cl, O). *J. Phys. Chem. A* **2005**, *109*, 10363–10372, doi:10.1021/jp0541617.

[295] Khalizov, A. F.; Viswanathan, B.; Larregaray, P.; Ariya, P. A. A Theoretical Study on the Reactions of Hg with Halogens: Atmospheric Implications. *J. Phys. Chem. A* **2003**, *107*, 6360–6365, doi:10.1021/jp0350722.

[296] Goodsite, M. E.; Plane, J. M. C.; Skov, H. Correction to A Theoretical Study of the Oxidation of Hg^0 to HgBr$_2$ in the Troposphere. *Environ. Sci. Technol.* **2012**, *46*, 5262, doi:10.1021/es301201c.

[297] Hall, B. The gas phase oxidation of elemental mercury by ozone. *Water Air Soil Pollut* **1995**, *80*, 301–315, doi:10.1007/BF01189680.

[298] Pal, B.; Ariya, P. A. Studies of ozone initiated reactions of gaseous mercury: kinetics, product studies, and atmospheric implications. *Phys. Chem. Chem. Phys.* **2004**, *6*, 572, doi:10.1039/b311150d.

[299] Octave community, GNU Octave 3.8.1. 2014; `www.gnu.org/software/octave/`.

[300] Sandu, A.; Sander, R. Technical note: Simulating chemical systems in Fortran90 and Matlab with the Kinetic PreProcessor KPP-2.1. *Atmos. Chem. Phys.* **2006**, *6*, 187–195, doi:10.5194/acp-6-187-2006.

[301] Maiwald, T.; Timmer, J. Dynamical modeling and multi-experiment fitting with PottersWheel. *Bioinformatics* **2008**, *24*, 2037–2043, doi:10.1093/bioinformatics/btn350.

[302] Subir, M.; Ariya, P. A.; Dastoor, A. P. A review of the sources of uncertainties in atmospheric mercury modeling II. Mercury surface and heterogeneous chemistry - A missing link. *Atmos. Environ.* **2012**, *46*, 1–10, doi:10.1016/j.atmosenv.2011.07.047.

[303] Finley, B. D.; Jaffe, D. A.; Call, K.; Lyman, S.; Gustin, M. S.; Peterson, C.; Miller, M.; Lyman, T. Development, Testing, And Deployment of an Air Sampling Manifold for Spiking Elemental and Oxidized Mercury During the Reno Atmospheric Mercury Intercomparison Experiment (RAMIX). *Environ. Sci. Technol.* **2013**, *47*, 7277–7284, doi:10.1021/es304185a.

[304] Brown, K. S.; Sethna, J. P. Statistical mechanical approaches to models with many poorly known parameters. *Physical Review E* **2003**, *68*, doi:10.1103/PhysRevE.68.021904.

[305] Grant, D. J.; Garner, E. B.; Matus, M. H.; Nguyen, M. T.; Peterson, K. A.; Francisco, J. S.; Dixon, D. A. Thermodynamic Properties of the XO_2, X_2O, XYO, X_2O_2, and XYO_2 (X, Y = Cl, Br, and I) Isomers. *J. Phys. Chem. A* **2010**, *114*, 4254–4265, doi:10.1021/jp911320p.

[306] Peleg, M.; Matveev, V.; Tas, E.; Luria, M.; Valente, R. J.; Obrist, D. Mercury Depletion Events in the Troposphere in Mid-Latitudes at the Dead Sea, Israel. *Environ. Sci. Technol.* **2007**, *41*, 7280–7285, doi:10.1021/es070320j.